Ice Crystal Icing in Gas Turbine Engines

Alexander Bucknell

St Catherine's College

University of Oxford

A thesis submitted for the degree of

Doctor of Philosophy

Trinity 2018

Ice Crystal Icing in Gas Turbine Engines

High altitude ice particles can accrete inside the core compression system of turbofan engines in cruise and descent. This can lead to severe in-flight events including blade damage, surge and flameout. This thesis describes the development and validation of a new comprehensive computational model to aid prediction of ice crystal icing in turbofan compressors. The Ice Crystal Icing ComputationaL Environment (ICICLE) delivers a step change in modelling of the phenomenon compared to the first generation of models in the open literature. Modelling of this multi-faceted problem is broadly divided into three strands: first, modelling of the ice particles in flight; second their interactions with solid surfaces; and third the thermodynamics of ice accretion. To aid development of models and provide validation data, three different experiments were also undertaken.

Treatment of particle size and shape distribution is considered first, and a particle trajectory model based on Lagrangian tracking is presented. A Nusselt number correlation for non-spherical particles is used to develop a phase change model for the particle in flight, incorporating sublimation, evaporation and melting. The model is then validated against measured particle melt data in an ice crystal facility. A model for the change in enthalpy and humidity of the airflow as a result of the particle phase change is proposed. Existing icing codes do not attempt to model these affects, but evidence from engine encounters with ice crystals indicate that they are significant.

It was assessed that experimentation was required to develop modelling capability in three areas: particle sticking, erosion and heat transfer. Two experimental campaigns were performed at the ice crystal wind tunnels of the National Research Council of Canada (NRC) using simple geometries (an inclined flat plate and a cone). Data was presented for the first time on heat transfer from a warm substrate under ice crystal conditions, and a method to predict the change in particle melt during surface impacts was proposed. New semi-empirical models were developed for sticking and erosion, with a substantially wider range of applicability than achieved in previous studies.

A new thermodynamic ice crystal accretion model was developed. A literature model for supercooled water icing was adapted to ice crystal and mixed phase conditions, and to substrates either above or below freezing. In the former case, an entirely novel three-layer accretion model was developed, which is a substantial advancement in modelling ice crystal growth on initially warm engine surfaces.

Finally, the complete model is validated against experimental accretions on the case of a compressor stator test article, also tested at the NRC. Agreement is seen generally to be good, with the transient behaviour of growth rates well predicted, typically within 20% of experimental measurements. It is shown that a substantial improvement in prediction accuracy may be attained by updating the fluid domain at discrete time points. This accounts for the influence of the growing accretion on the flowfield. The successful application of a quantitative code to a more complex, engine-realistic geometry is a significant step forward for the literature, as existing ice crystal codes have only been validated against simpler geometries.

Acknowledgements

I have enjoyed the support, guidance and friendship of many people during my years as a DPhil student.

Thanks firstly to my fellow students at the Oxford Thermofluids Insitute. It's been a wonderful few years, sharing ideas (some more on-topic than others), and travelling around the world for conferences. Thanks also to the technicians and support staff at the OTI, whose expertise and patience have been second to none.

To my friends at Catz, thank you for your unwavering support during my years there. Thanks also to the members of the Engine Environmental Protection team at Rolls-Royce plc, notably Geoff Jones, Alasdair Reed, Ben Collier and Rory Clarkson. Their support, both in programme management - enabling me to conduct experimentation at facilities around the world – and in technical expertise was truly invaluable.

Thanks to my supervisors, Prof. Matthew McGilvray and Prof. David Gillespie, whose sound guidance from the start has allowed me to grow as a researcher and pursue a truly fascinating project. Their support, particularly before and during the experimental campaigns, enabled me to get the very best out of my work.

Finally, thank you to my family for their steadfast support throughout my entire education, which has allowed me to reach this point.

Contents

This thesis has been written in the integrated thesis format (a combination of chapters and papers). Two papers written by the author are inserted in chapter 5 of the thesis. Page numbers in the main body of the thesis, excluding the papers, are contiguous.

List of Figures

In the following list, figures references that have a prefix ‘AI’ or ‘AS’ refer to figures in the AIAA and ASME papers respectively.

Nomenclature

a	Spheroid equatorial radius	m	L_v	Latent heat of vaporisation	J/kg
a_p	Acceleration (particle)	m/s^2	$\dot{m}$	Mass flux	$kg/(s.m^2)$
B	Ice thickness	m	m	mass	kg
c	Spheroid centre to pole radius	m	M	Molecular mass	kg/mol
C	Chord	m	$\dot{n}$	Molar flux	mol/s
C_D	Drag coefficient	-	N	Count (particles, layers, panels)	-
D_{va}	Diffusion coefficient of water vapour in air	m^2/s	P	Pressure	Pa
D	Diameter	µm	P_s	Sticking probability	-
$D_{v,xx}$	Diameter for which all particles with $D < D_{v,xx}$ constitute xx% of the total volume	µm	Q	Heat flux	W
e	Spheroid eccentricity	-	Q_s	Crack activation energy	J/(K.mol)
e_σ	Surface energy per unit area	J/m^2	q	Heat flux per unit area	W/m^2
E	Aspect ratio	-	r	Radial distance	m
F	Force	N	r_f	Recovery factor	-
g	Acceleration due to gravity	m/s^2	r_p	Radius	m
h	Water thickness	m	R_f	Specific gas constant of air	J/(kg.K)
h_f	Flow enthalpy	J/kg	s	Streamwise distance	m
H	Heat transfer coefficient	$W/(m^2.K)$	s_p	Displacement	m
H_m	Mass transfer coefficient	m/s	t	Time	s
$\dot{h}$	Ice growth rate	m/s	T	Temperature	K
J	Chilton-Colburn analogy factor	-	T_f	Freezing temperature of water	K
K_{ero}	Erosion model kinetic energy factor	$J/(kg.m^3)$	U_*	Friction velocity	m/s
K_t	Particle tracking timestep factor	-	U	Velocity	m/s
k	Thermal conductivity	W/(m.K)	V	Volume	m^3
$\mathcal{L}$	Ratio of particle kinetic energy to surface energy	-	x	Axial distance or direction	m
L	Characteristic length	m	y	Spanwise distance or direction	m

L_f	Latent heat of fusion	J/kg	y_+	Dimensionless wall distance = yU_*/ν	-
L_s	Latent heat of sublimation = $L_f + L_v$	J/kg	z	Vertical distance or direction	m
			Z	Mass loading fraction = TWC/ρ_f	-

Greek:

α	Thermal diffusivity = $k_f/\rho C_p$	m^2/s	μ_f	Dynamic viscosity	Pa .s
β	Collection efficiency	-	ν	Kinematic viscosity	m^2/s
γ	Angle between surface normal and axial direction	°	ρ	Density	kg/m^3
γ_f	Isentropic exponent of air	-	φ	Sphericity	-
δ	Mass averaged deflection angle	°	$\varphi_\perp$	Crosswise sphericity	-
Δ	Increment	-	τ_p	Particle relaxation time	s
ε	Mass averaged ballistic coefficient	-	$\tau_p{}^+$	Non-dimensional particle relaxation time = $\rho_f \tau_p {U_*}^2/\mu_f$	-
ϵ	Coefficient of restitution	-	τ	Relaxation time	s
η_s	Net sticking efficiency	-	τ_w	Wall shear stress	Pa
η_A	Erosion model constant	-	θ	Water temperature	K
η_C	Erosion model constant	-	ω	Vapour mass fraction	-

Subscripts/superscripts:

0	Total	m	Measured
∞	Freestream	$multi$	SEA multiwire probe
$\perp$	Normal projection	n	Normal direction
a	Air	p	Particle
acc	Accretion	r	Radial direction
B	Top of ice layer	ref	Reference condition
cl	Centreline	rel	Relative
$conv$	Convection	run	Runback
d	Drag	s	Secondary (particles)
e	Edge of boundary layer	sat	Saturation
eq	Equivalent (diameter)	$sens$	Sensible warming

evap	Evaporation	*sub*	Sublimation
exp	Experiment	*subs*	Substrate
f	Fluid	*surf*	Surface
g	Gravity	*t*	Timestep t, or tangential
h	Top of water layer	*vap*	Vapour
i	Ice	*w*	Wall or water
imp	Impinging	*x*	Axial direction
int	Internal (water)	*y*	Spanwise direction
kin	Kinetic	*z*	Vertical direction
loc	Local		

Dimensionless groups:

Bi	Biot number = HL/k_s
Ga	Galilei number = $U_g L/\nu$
Le	Lewis number = $k_f/D_{va}\,\rho C_p$
M	Mach number = $U/\sqrt{\gamma_f R_f T}$
Nu	Nusselt number = HL/k_f
Pe	Peclet number = UL/α
Pr	Prandlt number = $\mu/C_p k_f$
Re	Reynolds number = $\rho UL/\mu_f$
Re_p	Particle Reynolds number = $\rho U_{rel} D_p/\mu_f$
Sc	Schmidt number = $\mu/\rho\, D_{av}$
Sh	Sherwood number = $H_m L/D_{av}$
St	Stanton number = $H/\rho U C_p$
Stk	Stokes number = $\tau_p U/L$

Acronyms:

AC	Alternating Current
AGARD	Advisory Group for Aerospace Research & Development
AIWT	Altitude Icing Wind Tunnel
AoA	Angle of Attack °
CFD	Computational Fluid Dynamics
CIRA	Centro Italiano de Ricerche Aerospaziali
CIKP	Compact Iso-Kinetic Probe
D(E)RA	Defence (Evaluation) and Research Agency
DFDR	Digital Flight Data Recorder
EASA	European Aviation Safety Agency
EGT	Exhaust Gas Temperature (K)
EGV	Exit Guide Vane
EHWG	Engine Harmonization Working Group
EMM(-C)	Extended Messinger Model (-Crystals)
EMM-ICI	Ice Crystal Icing (warm substrate) EMM
ESS	Engine Section Stator
FEA	Finite Element Analysis
GLACIER	Global Aerospace Centre for Icing and Environmental Research
HAIC	High Altitude Ice Crystals
HIWC	High Ice Water Content
HP(C)	High Pressure (Compressor)
IATA	International Air Transport Association
ICC	Ice Crystal Consortium
ICICLE	Ice Crystal Icing Computational Environment
ICAO	International Civil Aviation Organisation
IGV	Inlet Guide Vane
IP(C)	Intermediate Pressure (Compressor)
IPHWG	Ice Protection Harmonization Working Group
ISA	International Standard Atmosphere
IWC	Ice Water Content (g/m^3)
LP(C)	Low Pressure (Compressor)
LWC	Liquid Water Content (g/m^3)
MCS	Mesoscale Convective weather System

MFR	Mass Flux Ratio = $\dot{m}_{melt}/\dot{m}_{evap}$
MMD	Median Mass Diameter (μm)
MR	Melt ratio = LWC/TWC (μm)
MVD	Median Volumetric Diameter
NACA	National Advisory Committee for Aeronautics
NASA	National Aeronautics and Space Administration
NRC	National Research Council of Canada
NTSB	National Transportation Safety Board
ONERA	Office National d'Etudes et de Recherches Aérospatiales
PIV	Particle Image Velocimetry
PSD	Particle Size Distribution
PSL	Propulsion Systems Laboratory
RA	Roughness Average (μm)
RAE	Royal Aircraft Establishment
RANS	Reynolds-Averaged Navier-Stokes
RATFac	Research Altitude Test Facility
RH	Relative Humidity
RR	Rolls-Royce
R-R	Rosin-Rammler
SEA	Science Engineering Associates
SF	Scale Factor
SH	Specific Humidity
SLD	Supercooled Liquid Droplets
SLW	Supercooled Liquid Water
SST	Shear Stress Transport
T30	Compressor delivery temperature (K)
TAT	Total Air Temperature (K)
TFG	Thin Film Gauge
TWB	Wet bulb temperature (K)
TWC	Total Water Content (g/m^3)

1 Introduction

In this chapter some background to the icing problems experienced by jet engines is presented, and the specific motivation for the current work discussed. The resulting research undertaken is outlined and its significance highlighted. Finally, the structure of the remainder of the thesis is set out.

1.1 Jet Engine Operation in Inclement Weather

The jet engine is used in the vast majority of powered flight – in regional, narrowbody and widebody commercial aircraft, and in transport and fast jet military aircraft. In 2016, the installed commercial fleet numbered some 60,000 engines, carrying around 4 billion passengers. The number of engines and passengers are forecast to grow to 103,000 (FlightGlobal, 2016) and to 7.8 billion (IATA, 2017) over the next twenty years respectively, with a market value for new aircraft in the region of $6.3 trillion (Boeing Commercial Airplanes, 2018).

Operation of turbofan engines in inclement atmospheric conditions – for example volcanic ash, sand, atmospheric pollution (e.g. sulphur), water or ice - has long been recognised as a risk to flight safety. Flights BA009 in 1982 (Chambers, 1985) and KLM867 in 1989 (Casadevall, 1994) suffered stall and flameout of all engines due to volcanic ash ingestion, leading to blockage of nozzle guide vane passages. In 2009, the believed blockage of aircraft probes by high-altitude ice crystals led to the loss of Air France flight 447. Recoverable engine power loss, such as a recoverable surge, may still result in extensive damage and the necessity for removal of the engine from service. Long-term engine damage, such as compressor cracking and erosion, film cooling hole blockage, and deposition on high pressure turbine components can lead to loss of efficiency, higher running cost and early retirement of components (Dunn, 2012). Applying overly-conservative flight rules is also economically damaging; following the 2010 eruption of Iceland volcano Eyjafjallayökull, over 100,000 flights were cancelled across Europe on the basis of poorly informed rules, with an estimated loss in revenue of €1.5 - 2.5 billion (Institute of Mechanical Engineers, 2010). Thus, research that informs safe atmospheric operating conditions may also provide economic benefit.

Fig. 1-1 (a) shows an indicative civil flight network, circa 1980, overlaid with regions of high atmospheric particulates (adapted from Forsyth, 2017). It is notable that the highest concentration of air traffic, skewed towards Europe and North America, largely does not coincide with these regions. The map, updated to the present, Fig. 1-1 (b), shows significant growth of domestic airline capacity and passenger numbers in the Gulf and Asia-Pacific regions: both operating in more hazardous atmospheric environments. Of particular interest to the current work is the Asia-Pacific region, as a high fraction of reported engine power loss events due to ice crystals have occurred in this area (Mason et al., 2006). A Boeing market outlook forecasts that traffic to the region will increase by 5.7% year-on-year until 2037 (compared to 1.5% in North America), and 40% of all new passenger aircraft deliveries will be to its airlines (Boeing Commercial Airplanes, 2018).

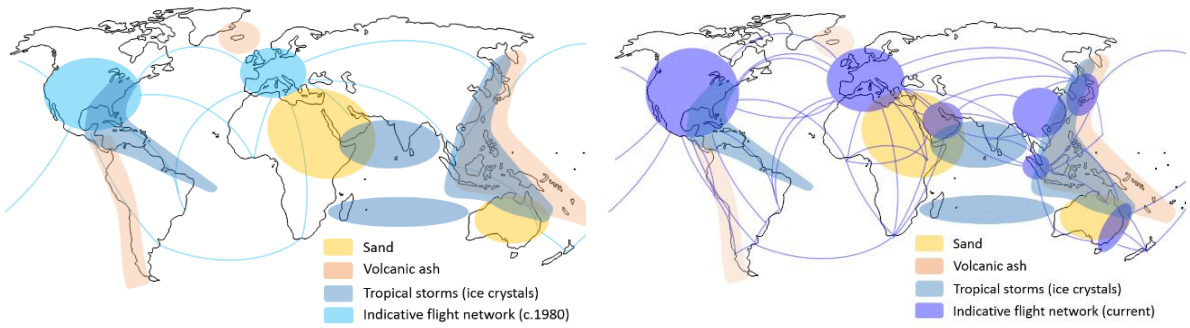

Fig. 1-1 Indicative flight network overlaid with regions of high atmospheric particles (adapted from Forsyth, 2017)

(a) c. 1980 (b) c. 2017

1.2 Aircraft and Engine Icing

Icing of wings, nacelles, fuselages and control surfaces can cause increased weight and drag, loss of lift, increased fuel burn and aircraft handling difficulties. Icing in these locations originates from supercooled liquid water (SLW) droplets (less than 50 µm diameter), or supercooled large droplets (SLDs, greater than 50 µm diameter). The former has been widely studied for over 40 years (Gent et al., 2000), and certification requirements for aircraft and engines are well defined, e.g. in Federal Aviation Agency report FAR Part 25 Appendix C (Jeck, 2002). Safe operation is effectively achieved through use of established techniques, such as electro-thermal or hot-air deicing, or deployment of deforming surfaces.

On 31st October 1994, an ATR 72 aircraft crashed near Roselawn, Indiana. Following an investigation by the National Transportation Safety Board (NTSB), the accident was attributed to an unrecoverable aircraft roll due to SLD icing of the control surfaces (NTSB, 1996). A renewed focus on certification requirements also led to increased interest in the possibility that high altitude solid ice particles could also cause engine power loss and/or corruption of probe readings. 62 turbofan power loss events that occurred since 1990 were attributed to encounters with ice crystal clouds by the Engine Harmonization Working Group (EHWG) (an industry consortium, Mason et al., 2006). With this and other evidence the EHWG proposed a certification envelope (ambient temperature *vs*. altitude operating space) where tolerance to 'glaciated' (ice only) and 'mixed phase' (ice and supercooled water) conditions must be designed for. In 2015, the European Aviation Safety Agency (EASA) adopted the new envelope, termed CS-25 Appendix P. The former EASA certification envelope for tests in 'ice-forming conditions' (EASA, 2010), the revised 2015 EASA (Appendix P) envelope, and known industry power loss events are shown in Fig. 1-2.

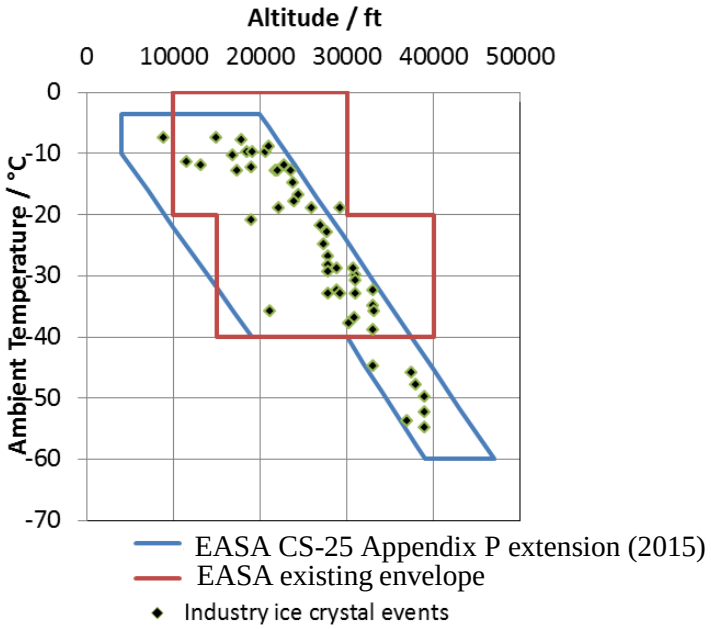

Fig. 1-2 Comparison of EASA engine icing certification envelopes: existing (pre-2015) in red, 2015 (Appendix P extension) definition for ice crystal conditions in blue. Known ice crystal icing events are overlaid (Jones, 2015a)

1.3 Ice Crystal Icing in Turbofans

Fig. 1-3 shows a generic two shaft turbofan engine, with areas susceptible to ice formation (Mason et al., 2006) highlighted. The nacelle, spinner, fan and core inlet stator are prone to icing due to supercooled liquid water and may be heated to mitigate the problem. The low pressure compressor booster (or intermediate pressure compressor for a three shaft engine) and inter-compressor duct are susceptible to ice crystal icing; here, however, active heating is currently not practical. On entry to the engine it may be surmised that large atmospheric ice particles are broken up by impact with the fan and are then ingested into the core. At cruise altitude static air temperatures in the IP compressor may rise from -15°C to +70°C under typical compression ratios. Particles which move through increasingly warm air begin to sublime, evaporate and melt. If the particles are in substantial concentrations, enthalpy removal from the air (evaporative cooling) and from surfaces will be sufficient that refreezing (ice accretion) will begin.

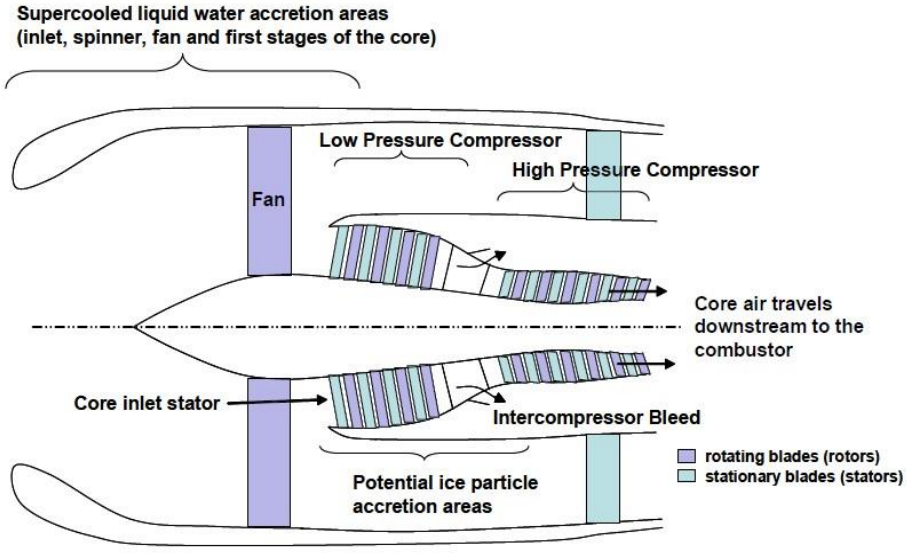

Fig. 1-3 Schematic of generic turbofan engine with areas at risk of icing highlighted (Mason et al., 2006)

There is evidence that in small (low bypass ratio) engines, the engine will run down (known as *uncommanded loss of thrust*) if there is sufficient blockage-induced reduction in mass flow rate and loss of compressor efficiency (Mason et al., 2006; Oliver, 2014). In high bypass ratio turbofans, accretion in the LP booster or IP compressor may lead to a reduction in compressor delivery temperature and pressure, but the engine will continue to run (Jones, 2015b). For large engines,

therefore, a potentially greater risk is that of ice shedding following accretion as this can cause blade damage, surge or flameout (Mason et al., 2006).

Rolls-Royce has had experience with in-service events due to ice crystal icing, most notably on their Trent 500 and Trent 800 engines. Typical damage experienced includes probe blockage, IP and HP compressor blade damage, compressor tip rubs and surge. For example, in November 2006, IP and HP compressor blade damage was incurred on four Trent 500 engines fitted to an Iberia Airbus A340 ('the Iberia event'). Other engine manufacturers face similar problems: Fig. 1-4 shows borescope images of HP compressor stage 1 rotor blades from a General Electric Aviation GEnx engine. The engine was fitted to an AirBridge Cargo Boeing 747-8 aircraft, which encountered ice crystal conditions in July 2013 near Chengdu, China. Three of the four engines incurred unacceptable damage due to ice shedding.

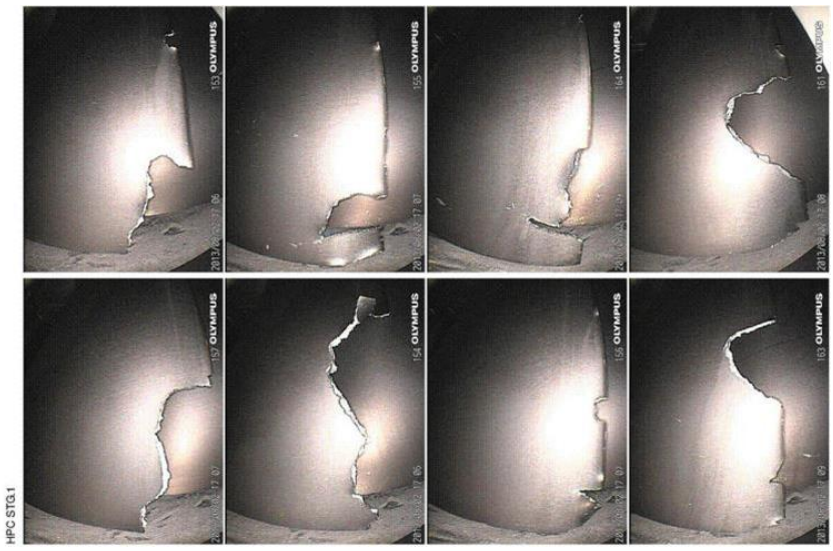

Fig. 1-4 Borescope images of damaged AirBridge Cargo GENx High Pressure Compressor stage 1 rotor blades in July 2013 (Federal Air Transport Agency of Russia, n.d.)

Clearly icing events can quickly lead to inoperable engines. Risk mitigation strategies for fleet engines include (i) opening intercompressor handling bleeds to draw centrifuged crystals into the bypass duct; (ii) circumnavigating deep tropical storm systems (which may be of the order of hundreds of kilometres in maximum dimension); (iii) running engines with increased descent idle speeds to raise interstage temperatures. All have the penalty of increased fuel burn. It is notable that this is a cost incurred by the operator, while the cost of reduced flight cycles between overhauls falls on the engine OEM.

1.4 Research Motivation: Physics-based Certification Compliance

The overarching aim of the research reported in this thesis is to develop a physics-based computational code, capable of predicting the rate of ice accretion on engine-realistic geometries as a function of operating and atmospheric conditions. This forms the necessary basis for developing a tool capable of predicting ice growth throughout the compression system of an engine of arbitrary architecture. To enable this, knowledge of the fundamental physical processes involved with ice formation, accretion and shedding, at engine representative conditions must be acquired and modelled with sufficient accuracy.

The research in this thesis has been conducted in close collaboration with Rolls-Royce plc, and builds on their existing certification techniques. These are twofold:

1. First a scaling approach is applied using data from the Iberia event. Using information from the digital flight data recorder, a threat window was identified for IPC locations with low dynamic pressure (typically below 14 kPa) and static air temperatures in the range 0 - 11°C, for altitudes below 33,000 feet (Jones, 2015b). For a new engine design, the estimated time spent at such a condition can be calculated. If an unacceptable mass of ice can form in that timeframe, a raised idle schedule or blade redesign may be specified. In spite of significant uncertainties associated with the underlying assumptions, application of these methods to recent engine certifications, such as the Trent 1000 and Trent XWB, has nevertheless given confidence that the susceptibility to accretion, damage and surge has been reduced.
2. Second, a phenomenological analysis method to predict an 'icing risk' has been developed (Mack, 2013a). The technique applies Lagrangian particle tracking with drag, particle-air heat transfer and phase change correlations to predict trajectories and the likelihood of accretion. Much of the physics (particle breakup, bouncing, splashing, erosion etc.) is neglected, but none the less, predictions of the stages at highest risk broadly match empirical evidence from in-service events.

New engine architectures, including geared designs, are likely to feature lower speed and low solidity fans (reducing particle breakup), an altered IP-HP work split (possibly increasing the risk to HPC), a

more pronounced swan-neck duct between LP and IP compressors, and lean-burn combustion (increased flameout risk). Thus, a step change in the predictive capability and flexibility of any model developed is now required. It is envisaged that the improved code could be used as a preliminary design tool, alongside simple meanline or throughflow flow solvers, to identify geometries and operating conditions which carry the highest and lowest risks of icing. The code will allow more radical design changes to be considered earlier in the design process. The enabling research describing the formation and growth of ice at a wide variety of atmospheric conditions is of interest to both the icing and wider scientific communities.

1.5 Research Strategy

To develop the aforementioned predictive code, termed the Ice Crystal Icing ComputationaL Environment (ICICLE), an initial assessment of existing research tools and knowledge was performed, along with an estimate of the research time required to improve understanding in each identified area. It was assessed that in some areas, this would involve experimentation to build numerical models.

The following strategy was used:

(1) Integrate 2D (planar or axisymmetric) flowfield solutions for engine-realistic geometries into a Lagrangian particle tracking code, under steady operating conditions.

(2) Develop models for two-way coupling between ice particles and flowfield, and assess their effect on the estimated ice growth rate.

(3) Incorporate particle-surface interaction models in the form of sticking, erosion, bounce and fragmentation, using experimentally-derived models where needed.

(4) Develop a new thermodynamic ice-accretion model for ice crystal conditions, using existing literature icing models for supercooled water as a framework.

1.6 Outline of Chapters

The contents of the remainder of this thesis is as set out below. In chapter 2, the open literature is reviewed, focusing on atmospheric ice particles, engine damage mechanisms, prior experimental

campaigns, and modelling techniques of other workers. Chapter 3 presents the proposed structure for the ice crystal icing model, as well as describing the experimental test articles used for code development and validation later in the thesis. Chapter 4 considers fluid-particle interaction in more detail, including the effects of particle size and shape, heat transfer and phase change. Methods for particle tracking and the necessity of two-way coupling are discussed. A sensitivity analysis is conducted to common input parameters. Chapter 5 focusses on particle-surface interaction, using an appropriate bounce-shatter model identified from literature, and results from two experimental campaigns conducted during the project. The first focuses on heat transfer during particle-surface impacts, the second on developing semi-empirical sticking and erosion models. Chapter 6 presents a new thermodynamic accretion model, developed by extending a model available in the literature to mixed phase and glaciated conditions. Chapter 7 reports results from the complete code with comparison to the validation test cases introduced in chapter 3. The sensitivity of the solution to aerodynamic and atmospheric conditions is assessed. Finally, chapter 8 summarises the findings and identifies necessary future research in the field.

1.7 Research Contributions

Several papers have already been published and presented from this research, resulting in the integrated thesis format chosen by the author. As these are presented in full in the thesis there is necessarily slight duplication in some of the information presented.

The major research contributions of this work and associated papers are:

- Development of a new thermodynamic icing code, applicable to ice crystal icing at ambient conditions both above and below 0 °C. The model extends an existing literature model for liquid water icing of airframes and wings to mixed-phase engine icing. The work presented in this thesis (chapter 6) is shortly to be written as a paper and submitted to the SAE International Conference on Icing of Aircraft, Engines and Structures (to be held in Minneapolis, June 2019)
- Investigation of heat transfer from warm engine surfaces under an ice crystal-laden flow. This is the first time heat transfer has been measured experimentally in an ice crystal cloud. The

work was written into (1) an ASME TurboExpo conference paper and (2) a paper for the ASME Journal of Engineering for Gas Turbines and Power:

(1) Bucknell A., McGilvray M., Gillespie D.H., Jones G., Reed A., Buttsworth D.R. *Heat Transfer in the Core Compressor Under Ice Crystal Icing Conditions.* Presented at ASME Turbo Expo 2017, 26th-30th June 2017, Charlotte, NC, USA. Paper GT2017-63077

(2) Bucknell A., McGilvray M., Gillespie D.H., Jones G., Reed A., Buttsworth D.R. *Heat Transfer in the Core Compressor Under Ice Crystal Icing Conditions.* ASME J. Eng. Gas Turbines Power. 2018; 140(7).

- Development of new, experimentally-derived semi-empirical models for ice crystal sticking and erosion, at a wide range of operating and atmospheric conditions. This was written into an AIAA Aviation Forum conference paper:

  Bucknell A., McGilvray M., Gillespie D.H., Jones G., Reed A. and Collier, B. "*Experimental Studies of Ice Crystal Accretion on an Axisymmetric Body at Engine-Realistic Conditions*", 2018 Atmospheric and Space Environments Conference, AIAA AVIATION Forum, June 25th-29th 2018, Atlanta, GA, USA. Paper 2018-4223.

  This paper won the 2018 AIAA Atmospheric and Space Environments Conference award for Best Student Paper. It is currently in submission to the AIAA Journal of Propulsion and Power.

- Integration of the novel elements listed above and additional literature models into a comprehensive end-to-end ice crystal icing model (ICICLE), validated against new experimental studies of ice accretion on engine-realistic components. The work presented in this thesis (chapters 3 & 6) is shortly to be written as a paper and submitted to the SAE International Conference on Icing of Aircraft, Engines and Structures (to be held in Minneapolis, June 2019).

2 Literature Review

This chapter is broadly divided into two sections. In the first, the characteristics of atmospheric ice particles and common observations during engine power loss events are summarised; experimental facilities dedicated to ice crystal icing are discussed, and findings pertinent to the current work highlighted. In the second part, approaches to modelling the phenomena involved in icing are investigated.

2.1 Atmospheric Ice Crystals

Depending on their altitude, atmospheric clouds may be 'glaciated' (entirely solid phase), entirely liquid or 'mixed phase'. High altitude atmospheric ice crystals are typically formed by mesoscale convective weather systems (MCSs), which loft moisture to sufficiently high altitudes that water can no longer remain liquid. Supercooled water may exist down to ~-40 °C, corresponding to an altitude of ~8,000 m (27,000 ft) for an International Standard Atmosphere (ISA) day. The anvil region of such weather systems – typically at the altitude of the tropopause (~18,000 m (60,000 ft) over the equator) - typically contains high concentrations of ice particles, may be hundreds of kilometres in width and have lifecycles of the order of hours. Prior to 2014, ice concentration measurements in weather systems pertinent to the icing problem remained sparse. Early flight trials were conducted by the Royal Aircraft Establishment (RAE) in 1958, resulting in the first recorded use of 'flight in ice crystal clouds' (Mason et al., 2006). A review of cloud microphysics and previous flight test campaigns is given in Lawson et al., (1998), where an upper estimate of ice water content (IWC) of 3.0 g/m^3 is given.

As part of the recent growth in research on ice crystal icing, two collaborative projects, termed High Ice Water Content (HIWC, US-led) and High Altitude Ice Crystals (HAIC, European-led), were conceived. Both had the purpose of advancing ice accretion modelling and improving understanding of the high-altitude ice crystal environment. In 2014 the two projects collectively conducted a flight test campaign out of Darwin, Australia, followed by a second campaign out of Cayenne, French Guiana in 2015. These campaigns had the aim of characterising ice concentrations and particle size and shape

parameters in high altitude convective weather systems. Particle size distributions were presented in Leroy et al. (2015) for three flights in high ice water content conditions. These flights are referred to by identifiers *Flight* 12, 13 and 16. Flights 12 and 13 sampled a single weather system of convective activity length 14 hours; while Flight 16 sampled a weather system four days later with convective activity of 8 hours. Fig. 2-1 shows the measured Median Mass Equivalent Diameter, MMD_{eq}, within specified Total Water Content (TWC) bands for the three flights. Here MMD_{eq} is defined as the particle diameter for which 50% of the sample of particles (by mass) have greater diameters, and 50% have smaller diameters. Since there is no liquid water at the altitudes tested, the TWC is equal to the ice concentration, given in grams of ice per cubic metre of air. The vertical height of the coloured boxes gives a rough idea of the extent of the MMD_{eq} distribution.

The time period of the convective weather event is shown to have a bearing on the ice distribution. In the younger weather system sampled in Flight 16, the bulk of the ice mass is close to a lower mean diameter, whereas in Flights 12 and 13 a (sparse) distribution of larger particles tends to increase the average MMD, attributed to the prolonged storm activity allowing agglomeration and vapour deposition.

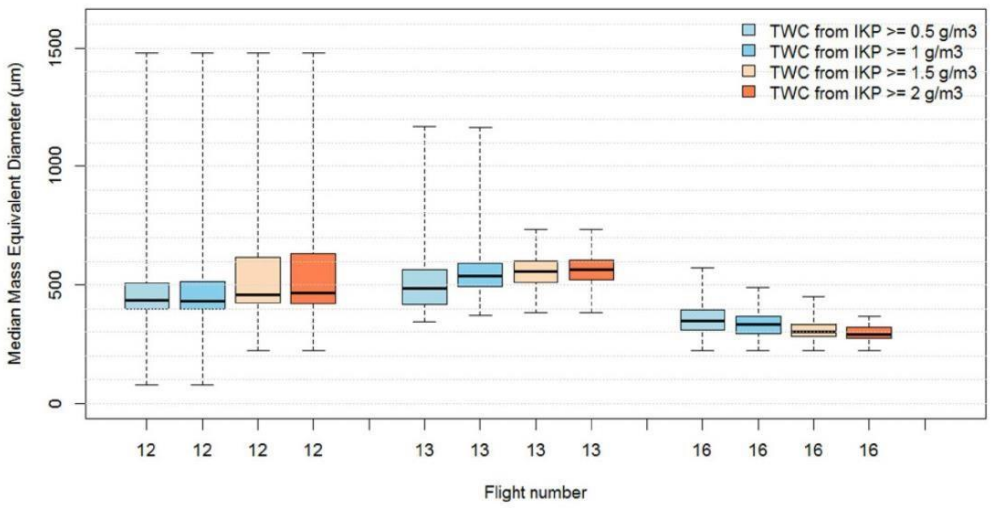

Fig. 2-1 Boxplot of MMD_{eq} for HAIC/HIWC flights 12, 13 and 16 (Leroy et al., 2015)

Fig. 2-2 shows the worldwide location of 46 engine power loss events attributed to ice crystals, between 1990 and 2003 (Mason et al., 2006). If the location of power loss is unknown, a location

halfway between the flight origin and destination has been plotted. There is a high frequency of events in the Asia-Pacific region, and most events occur within +/-45˚ latitude. The reduced frequency of events in the southern hemisphere may be partially explained by the significant skewing of all air traffic towards the northern hemisphere. However, air traffic in all regions – particularly in developing areas including Asia – will increase rapidly over the coming years. In 2013, the Asia-Pacific region had the largest worldwide annual growth in airline capacity (available seat kilometres), at 7.0% (ICAO, 2013). In the northern hemisphere, 72% of the events considered occurred between April and August, attributable to warm days enhancing convective transport of moisture to high altitudes.

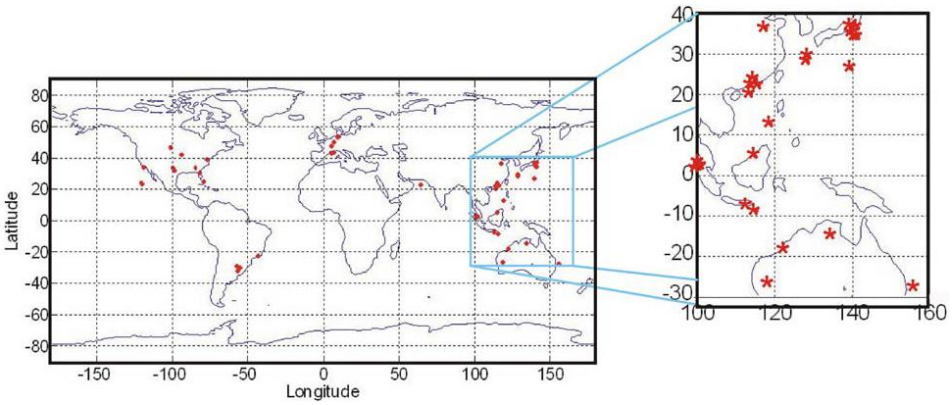

Fig. 2-2 Location of 46 engine power loss events analysed by Mason et al. (2006), with the Pacific Rim region inset

Pilot reporting and flight data from the 46 events analysed by Mason et al., (2006) identify common trends of ice crystal events. These trends may be summarised as

(i) High altitude. The median event altitude was 8,000 m (27,000 ft).

(ii) Aircraft above or in the vicinity of a tropical storm. This may be determined post-event from satellite data, or pilot reporting of heavy precipitation at lower altitudes.

(iii) An ambient temperature warmer than the International Standard Atmosphere (ISA) day. Thirteen events occurred at temperatures between ISA +11˚C and ISA +23˚C. Convective storms contain strong updraft cores that transport low altitude moisture to the high altitude anvil region. Higher day temperatures enhance convective transport thus producing higher concentrations of supercooled water and ice.

(iv) 'Precipitation' was observed on aircraft windscreen – attributed to ice crystals melting on the heated glass.

(v) Total Air Temperature (TAT) anomaly – where the reported TAT spuriously jumps in value, usually towards 0 ˚C. This has been attributed to ice crystals melting within heated probes.

(vi) No observed airframe icing – attributed to ice crystals bouncing off cold aircraft surfaces.

(vii) No evidence of ice crystals on cockpit radar. Ice crystal conditions may only be inferred from heavy precipitation at lower flight levels. This precipitation may lead pilots to climb, inadvertently entering ice crystal conditions. This is illustrated in Fig. 2-3.

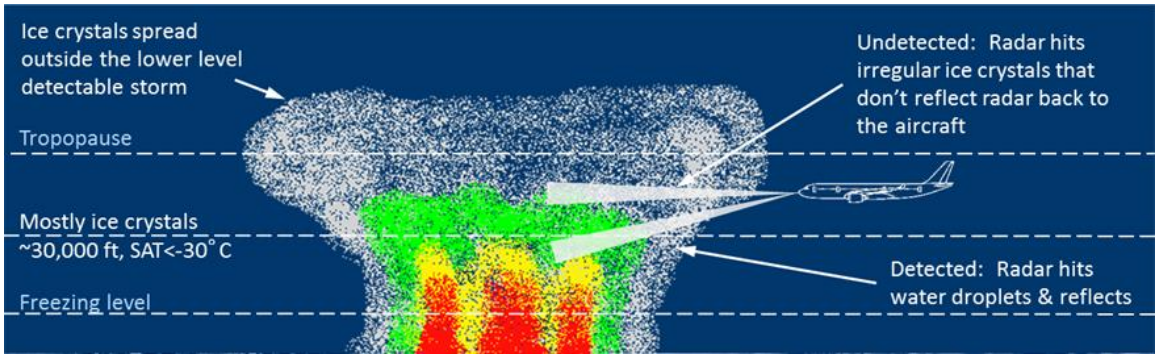

Fig. 2-3 Diagram of the radar reflectivity as a function of altitude for a convective tropical storm. Heavy rain at low altitudes gives a high reflectivity (coloured red). High altitude ice crystals give little (green) or no response (white) (Jones, 2015a)

2.2 Engine Damage Mechanisms and Response

In current-generation Rolls-Royce engines, the intermediate pressure compressor (IPC) has been shown to be susceptible to ice crystal accretion. Other ice crystal damage mechanisms that have been encountered (for example corruption of pitot probe measurements, rotor tip rubs due to cooling and contraction of the casing), are considered to fall outside of the scope of the current research.

In November 2006, all four Trent 500 engines on an Iberia Airbus A340 were damaged following descent through ice crystal conditions near Buenos Aires. Damage was reported on the second and fourth stage rotors of all four IP compressors, with multiple cases of entire blade release, as well as damage to high pressure compressor (HPC) rotor blades on multiple stages. The damage was detected

due to a surge in engine 4 on the aircraft's return flight to Madrid the following day. An event analysis was conducted using information provided from the Digital Flight Data Recorder (DFDR) and an engine strip (Jones, 2015b).

The three main outcomes of ice crystal accretion in high bypass ratio turbofans may be summarised as:

(i) Blade damage. Ice shedding from upstream blades may cause damage to rotor blades in both the IPC and high pressure compressor (HPC). This may be in the form of tip curl, or material release. Fragments of released metal may then cause more serious damage to downstream blade rows.

(ii) Compressor surge. Accreted ice sheds into the HPC, driving the compressor towards the stall line. This is due to (a) torque loss from the compressor shaft when the shed ice is accelerated circumferentially by a rotor row, (b) the loss of heat from a given stage due to melting, evaporation and sublimation of ice and (c) the loss of aerodynamic efficiency due to blades being coated with ice and water. An ice layer generally serves to increase surface roughness, promoting the early onset of transition, and if sufficiently thick may increase or decrease incidence onto neighbouring blades, increasing profile losses. Water layers in isolation typically collect in recirculation regions – for example the corner separation on stator blade suction surfaces near the endwalls. The resulting local increase in blockage has been shown to similarly affect incidence, promoting early stall (Day et al., 2008). The engine IP and HP shaft speeds reduce due to (a), and compressor delivery temperature T30 is reduced due to (b) and (c).

(iii) Flameout. The combustor flame is quenched due to ingestion of a large quantity of ice and water.

In low bypass ratio turbofans, in-service evidence suggests that rollback (uncommanded complete loss of thrust) is a likely outcome of ice crystal accretion (Mason et al., 2006; Oliver, 2014). This is typically as a result of severe blockage in the LP booster (measured as up to 60% in a recent whole-engine test

(Veres et al., 2016)) and significant increase in pressure loss coefficient in this region. The resulting reduction in core mass flow rate leads to decreasing compressor delivery pressure and temperature. Fuel flow initially rises to compensate, resulting in a rise in EGT and low-pressure shaft speed, but the reduction in core mass flow rate continues until all parameters decay entirely. Fig. 2-4 shows data from a Honeywell ALF502 engine, installed in the NASA PSL-3 ice crystal wind tunnel (Veres et al., 2016). The engine experienced a full rollback. The test condition was a simulated altitude of 8840 m (29,000 ft), a flight Mach number of 0.52, an inlet total temperature of 255 K and an inlet TWC of 1.4 g/m^3.

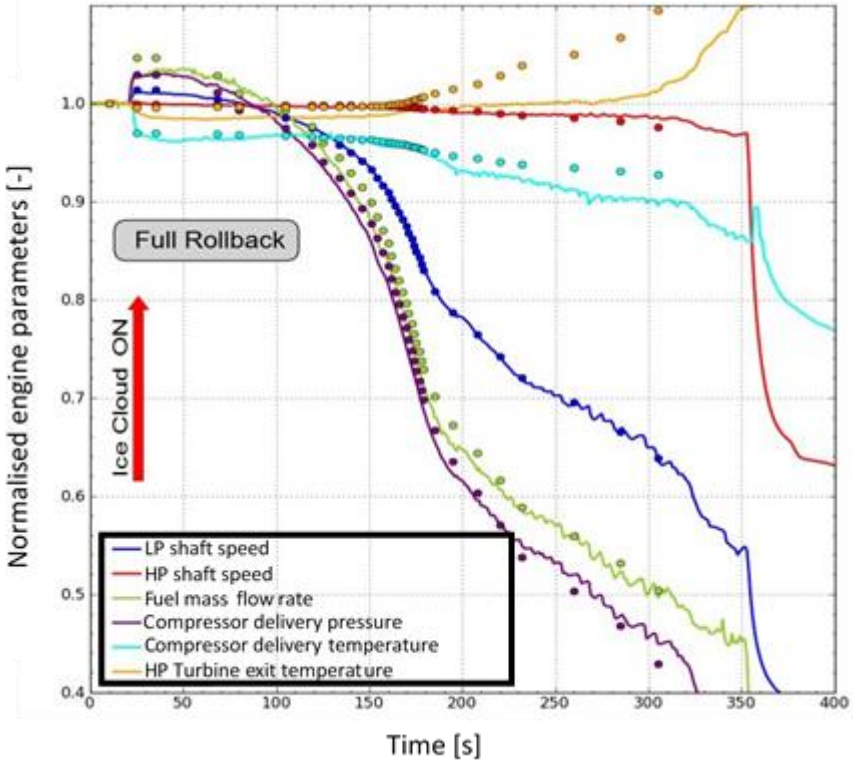

Fig. 2-4 Normalised engine parameters against time for Honeywell ALF502 test condition 093 (adapted from Veres et al., 2016). Solid lines are test data, circles are simulation of performance at discrete points.

2.3 Experimentation

In this section some major existing experimental facilities for ice crystal testing are described. The facilities are restricted to those likely available for current and future research collaboration with the Oxford Thermofluids Institute.

2.3.1 Experimental Facilities

Experimental facilities may be divided into engine-level test facilities, and component-level test facilities. The latter category may also refer to fundamental research on simple geometries such as flat plates or axisymmetric bodies.

Of engine-level test facilities, the most noteworthy is the Propulsion Systems Laboratory tunnel 3 (PSL-3) at NASA Glenn (Fig. 2-5). This tunnel features ice particle generation using freezeout of a liquid water spray. Full glaciation of particles is attained up to median mass diameters of 60 µm. The test section can house engines or cores with diameters of up to 2.13 m (Thomas, 2015). Therefore, small engines tests can and have been performed but high bypass ratio engines cannot be tested with a full fan. A rig-driven core compressor test is possible but without the presence of the fan and bypass duct, pre-conditioning of particles cannot be easily replicated.

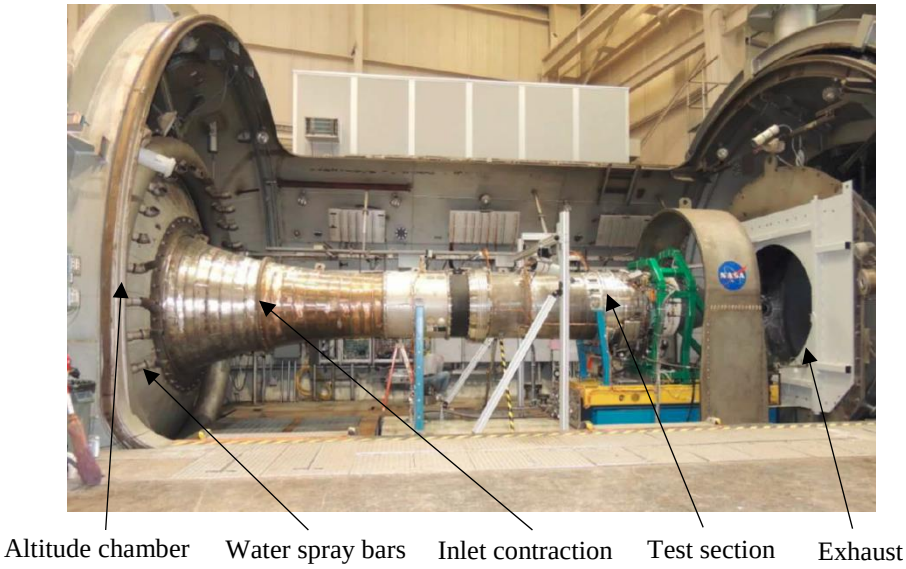

Fig. 2-5 NASA PSL-3 facility (adapted from Thomas, 2015)

The primary advantage of PSL-3 is that it is an altitude facility – and thus can replicate pressure-driven effects such as evaporative cooling. This may be compared to existing sea-level icing test facilities – such as the GLACIER facility in Manitoba, Canada – which can house high bypass ratio turbofans but cannot simulate either solid ice particles or pressure and temperature at altitude. In this thesis, more weight is given to fundamental (component-level) studies than module or engine-level studies since they are more conducive to extraction of quantitative data, thus facilitating model development. It is

the validation phase of the entire integrated code where qualitative and quantitative insight from whole-engine tests become invaluable.

Facilities for fundamental ice crystal research have undergone rapid development since the mid- 2000s when research interest began to become widespread. In 2006, the National Research Council of Canada initiated work to convert their Research Altitude Test Facility (RATFac) into an altitude ice crystal research tunnel (Fuleki and MacLeod, 2010). A schematic is shown in Fig. 2-6. The ice generation system and wind tunnel (termed the cascade rig) are housed inside an altitude chamber, pumped down to a target total pressure. Ice particles are generated by a grinder in the 'cold' side of the facility, and fed through into the 'warm' side of the facility. The ice-laden flow is mixed with warm air and steam to generate a jet of target ice concentration, total temperature and specific humidity. The jet passes into the bellmouth of the cascade rig and through the test section. Compressors draw on the outlet of the rig to achieve the desired Mach number. A probe plane sits ~50 mm upstream of the test article, where total water content (TWC), liquid water content (LWC), humidity, total temperature and total pressure are measured.

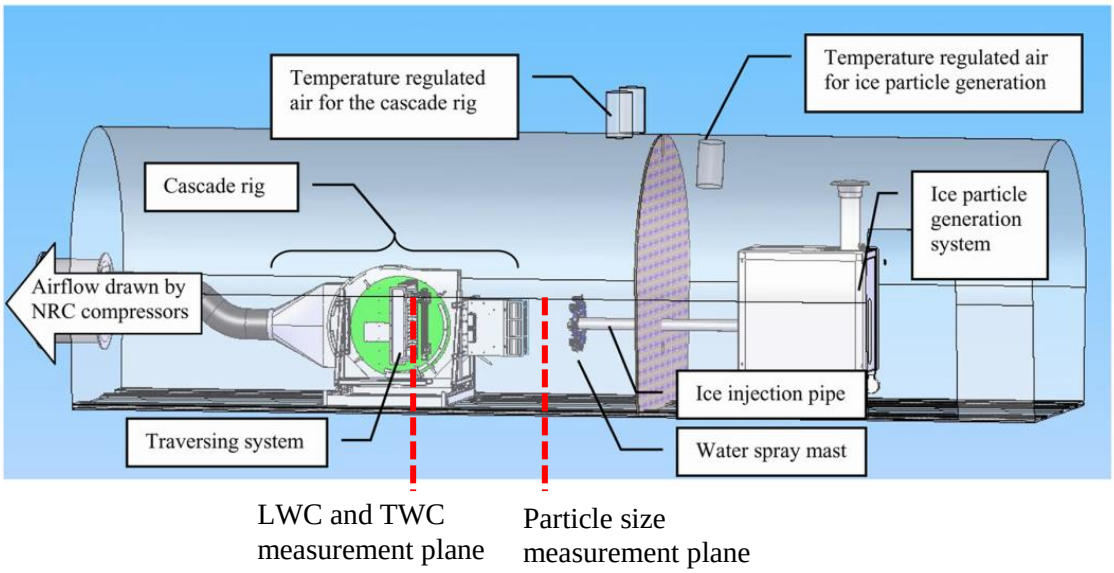

Fig. 2-6 Schematic of RATFac facility with particle size and ice/water measurement planes marked (adapted from Struk et al., 2011)

An additional fast turn-around atmospheric tunnel at the NRC is a modification of an existing supercooled water icing facility, the Altitude Icing Wind Tunnel (AIWT). In this facility ice particles

are generated by freezing water droplets in a liquid nitrogen cloud (Clark et al., 2018). Other rig-level facilities exist, such as the Icing Wind Tunnel at TU Braunschweig (Baumert et al., 2015), but the NRC facilities possess the advantages of altitude simulation and longest continuous development. The operating envelopes of both RATFac and AIWT are summarised in Table 2-1, along with a range of interest for typical operating conditions within the IP compressor at cruise or descent.

Table 2-1 Operating envelopes for RATFac and AIWT with ranges of interest for engine icing

Parameter	*RATFac*		*AIWT*		*Range of interest*	
	Min	*Max*	*Min*	*Max*	*Min*	*Max*
T_0 [℃]	-40	35	-30	45	-10	30
P_0 $[kPa]$	15.3	93.1	19.4	101	25.0	70.0
Mach number $[-]$	0.15	0.80	0.025	0.53	0.10	0.50
Relative humidity $[-]$	0.05	0.95	No control, typical 0.9-1.0		0.00	1.00
Injected ice D_{v50} [μm]	18	300	20	100	10	100
Injected water MVD [μm]	20	40	10	200	-	-
Injected ice IWC $[\mathrm{g/m^3}]$	2	12	No ice injection		4.0	12.0
Injected water LWC $[\mathrm{g/m^3}]$	0.5	4.0	0.1	3.5	-	-
Working section [m]	0.254 x 0.132		0.520 x 0.330		-	-
Ice generation system	Mechanical grinder		Water freezeout with liquid N_2		-	-

A key difference between the facilities is their ability to control humidity. RATFac is an open loop tunnel, where relative humidity (RH) is controlled through modulating steam injection. AIWT is a closed loop tunnel, whereby evaporation of recirculating ice particles results in a transient RH that approaches 100% sometime after test initiation. The result is that evaporative cooling may be regulated in RATFac, but is inhibited in AIWT. Both may be useful depending upon the test objectives.

2.3.2 Prior Experimental Studies

A number of fundamental experimental studies have been conducted at RATFac. In 2009, the NRC, NASA and Boeing performed experiments on an intercompressor ‘swan neck’ duct with an integral aerofoil strut (Mason et al., 2010). These tests were the first to demonstrate that ice crystal accretions

could form at temperatures above and below freezing provided a proportion of the impinging cloud was liquid. A wedge-shaped test article designed by NASA and the NRC showed in 2010 that the strength of the accretion was higher (more unlikely to shed) for thermodynamic wet bulb temperatures below 0 °C (Struk et al., 2011). Thermodynamic wet bulb temperature is defined as the temperature a control volume of air would attain if moisture was evaporated into it until saturation. The system is assumed adiabatic – i.e. the latent heat required for vaporisation is equal to the enthalpy lost from the volume of air. Both the 2009 and 2010 campaigns observed that there was a strong correlation between ice growth rate and bulk melt ratio, MR. This is defined as the ratio of the liquid water content (LWC) to total water content (TWC) in the icing cloud. Accretion growth rate was observed to be maximal within a specific band of melt ratio. In fully glaciated conditions ($MR = 0$), particles will bounce off surfaces unless heated. In wet conditions ($MR \rightarrow 1$), the rate of liquid run off is sufficiently high that no ice can stick.

Experiments with a NACA 0012 aerofoil (Struk et al., 2015a) demonstrated that accretions were largest for melt ratios in the range 0.06 – 0.12. Tests with two axisymmetric geometries (cone and hemisphere) and a planar half-cylinder (Currie et al., 2014) showed that the highest stagnation point growth rates were achieved when melt ratio was in the range 0.1– 0.2, termed by the authors the 'plateau region' or 'aggressive accretion range'. The difference between these two ranges indicates that this parameter is not a universal quantitative indicator of accretion. Both campaigns varied melt ratio by controlling the wet bulb temperature. At sub-freezing wet bulb temperatures, particle melting is inhibited, even if the dry bulb temperature is significantly above freezing. It was concluded that melt ratio was a key parameter to match between sea-level and altitude testing, and accretion size was almost independent of whether the bulk liquid water content was generated by particle melt or by supplemental water injection (Currie et al., 2013).

An industry group, the Ice Crystal Consortium (ICC), conducted a test campaign in RATFac in 2012 using a compressor stator cascade (Mack, 2013b). An icing severity was defined for each test condition based on the accretion quantity, location and propensity to shed. The primary accretion location was observed to be the pressure surface when the static wet bulb temperature was sub-freezing and the total

wet bulb temperature was above freezing; this tended to move to the leading edge once the total wet bulb temperature also fell below freezing. Accretions for (a) total and (b) static wet bulb temperatures around 0˚C are shown in Fig. 2-7. Accretions at the lowest wet bulb temperatures tended to be brittle with repeated partial sheds, whereas high wet bulb temperatures promoted slushy deposits. Increasing Mach number was observed to have a twofold effect – first it resulted in the static wet bulb temperature diverging from the total wet bulb temperature, shifting the accretion location; and second a reduced overall accretion severity which was attributed to increased erosion.

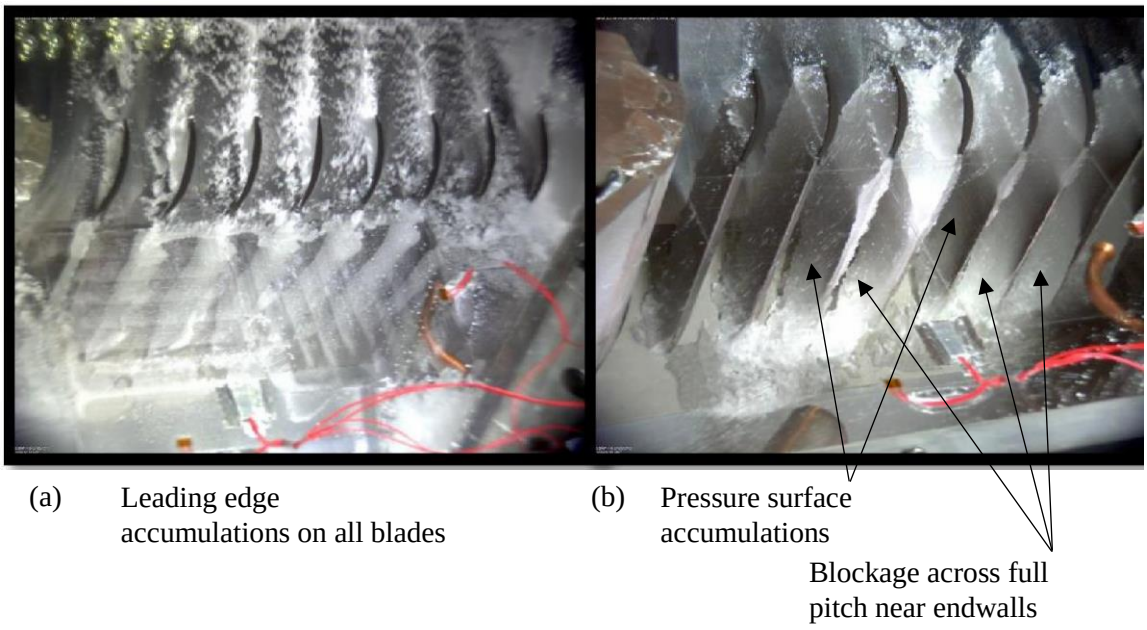

Fig. 2-7 Accretions in the ICC cascade in RATFac for (a) total and (b) static wet bulb temperatures near 0°C (Mack, 2013b)

It has been shown that erosion is strongly related to both particle velocity (Currie et al., 2014) and also particle size distribution, particularly the largest particles in the cloud, represented by the D_{v90} statistic (Knezevici et al., 2012). A particle sticking model was presented by the NRC (Currie et al., 2014), using a new erosion model. The erosion model assumed that ductile erosion was the primary mechanism of mass loss, whereby mass is sheared from an accretion due to highly oblique (i.e. near tangential) particle impacts (Neilson and Gilchrist, 1968; Tilly, 1973). The model considered the effect of particle velocity on erosion rate but neglected particle size due to a dearth of experimental data at differing size distributions. The overall particle sticking model defined the 'sticking efficiency' (η_s) as the sum of a sticking probability term and an erosive term, as shown in equation (2-1).

$$\eta_s = \frac{\dot{m}_{stuck}}{\dot{m}_{imp}} = P_s - E(\gamma) \tag{2-1}$$

where $\dot{m}_{stuck}$ is the sticking mass flux, easily obtainable from a measured growth rate, $\dot{m}_{imp}$ is the impinging mass flux, P_s is the sticking probability term and $E(\gamma)$ is a normalised erosion term at particle impact angle γ. Since the measured growth rate is the net effect of both sticking and erosion, it is difficult to decouple these terms using experimental data. The model was therefore only applied in the aggressive accretion regime ($MR \approx 0.1$-0.2), where it is assumed that $P_s = 1$. Empirically, it would be expected that P_s decreases for melt ratios either side of this range. A model for sticking probability that reflects the trends shown with melt ratio cannot be developed until sticking and erosion can be decoupled. In the remainder of the thesis, the measured sticking efficiency will be referred to as the 'net sticking efficiency', $\eta_{s,net}$, to emphasise this fact.

There is a continual drive to reduce the experimental uncertainty in ice crystal experiments. A method for calculating the uncertainty in ice growth rates extracted from video images was developed following tests on a NACA 0012 aerofoil (Struk and Lynch, 2012). This demonstrated that the accretion thickness uncertainty is typically small compared to that in water and ice concentration measurement. Historically, LWC has been measured using a hotwire device, where the power required to maintain wires exposed to the icing cloud at a fixed, elevated temperature is related to the water concentration. The Science Engineering Associates Inc. WCM-2000 multiwire probe ('the multiwire') has been shown to work to an acceptable degree of accuracy (within ~ 5%) in pure liquid clouds (Lilie et al., 2005). Significant research (Currie et al., 2014; Struk et al., 2015a, 2017) has been performed to understand if this probe can be used to measure liquid water content in mixed phase clouds, where liquid is generated either by supplemental water injection (the 'mixed phase regime') or by particle melt (the 'melting regime'). In fully glaciated conditions, it has been shown that the multiwire gives a false liquid reading due to ice crystals bouncing off the heated wires. This 'false response' has been shown to be in the region of 3 - 5 % of the total water content (Currie et al., 2014). The effect is believed to be somewhat counteracted in the melting regime by the water layer on partially melted particles not being fully shed onto the wires. Corrections have been proposed for taking measurements

in the mixed phase regime (Struk et al., 2015b) but interpreting readings in the melting regime remains an open question.

It is important to note that ice crystal icing codes will be incapable of predicting accretion profiles unless sticking and erosion models are well defined. The primary requirements for experimentation are therefore:

1. Parametrically study net sticking efficiency as a function of (at least) melt ratio, Mach number and particle size;
2. Studies on particle size should attempt to further investigate the effect of the shape of the PSD on erosion rate – e.g. independently studying the effect of D_{v50} and D_{v90};
3. Develop a method for decoupling sticking and erosion from net sticking efficiency measurements;
4. Develop a method for characterising the false response in LWC measurement as a function of condition.

A number of whole-engine studies have been performed in recent years at NASA PSL-3, most relevantly that of the Honeywell ALF502 R-5 engine. This engine has had several power loss events in service attributed to high altitude ice crystals, primarily due to ice blockage causing reduced thrust or complete rollback (Oliver, 2014). In the test campaign, particle size and humidity were parametrically varied to attain a range of melt ratios at the tandem Exit Guide Vane (EGV, upstream of the high pressure compressor), the location believed to be most susceptible to accretion. For a particle diameter range of 1 – 9.5 µm, a static wet bulb temperature range of 0.2 – 3.5 °C produced conditions where a complete rollback could occur (Veres et al., 2017). Using a melt prediction code, this was calculated to occur for melt ratios in the range 3 – 4%. The observations tend to support the theory of the existence of an 'aggressive accretion regime', albeit at lower (predicted) melt ratios than those measured in fundamental studies.

2.4 Ice Crystal Icing Modelling

Physics-based models for the growth of ice on aircraft surfaces have existed since the 1970s (Gent et al., 2000). Models were developed primarily to predict ice growth on aircraft wings, rotorcraft blades and engine nacelles when flying in supercooled liquid water (SLW) droplet conditions. The first generation of codes were developed by NASA Lewis Research Centre, the Office National d'Etudes et de Recherches Aérospatiales (ONERA) and the Royal Aircraft Establishment (RAE) (Wright et al., 1997). All three have common building blocks, comprising (a) an air flowfield solution, (b) particle tracking (in a Lagrangian or Eulerian framework), (c) a thermodynamic ice growth model and (d) prediction of the accretion profile and growth rate. This is shown in Fig. 2-8.

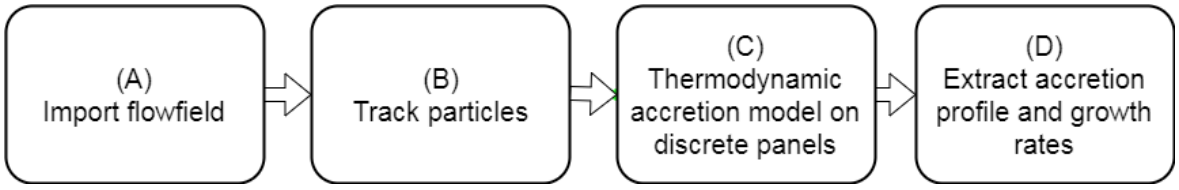

Fig. 2-8 Common building blocks of current aerospace icing codes

In the SLW problem, high-altitude supercooled water droplets freeze on impact with cold aircraft surfaces. Whilst this is materially different from the problem of ice crystal accretion inside turbofan engines, the model building blocks nevertheless remain the same.

Early efforts to adapt existing icing codes to glaciated and mixed phase conditions include the work of Mazzawy, (2007), and an adaptation to NASA Glenn's icing code GlennICE (Wright et al., 2010). The latter incorporated particle trajectory, breakup and heat transfer with a thermodynamic model based on the well-known Messinger model for aircraft icing (Messinger, 1953). The model was applied to thermodynamic cycle results for the NASA Energy Efficient Engine (E3), with qualitative predictions of possible accretion locations. Veillard et al., (2009) used a mixing-plane approach to integrate rotating turbomachinery into an existing 3D icing code, FENSAP-ICE (now owned by ANSYS). The Eulerian framework was used (defining the particulates as a second continuous phase), and the mass fluxes circumferentially averaged in mixing planes between blade rows. In the rotating stages, the system of equations is solved in the rotating frame of reference; equations are presented for application of centrifugal and Coriolis forces to the droplet cloud. The aerodynamic results were validated against the well-documented Aachen turbine, and the full model – using supercooled water

droplets only - applied to the NASA Stage 35 transonic compressor. It was later developed to incorporate mixed phase conditions, including non-spherical drag laws for ice crystals, and a simple particle bouncing model (Nilamdeen and Habashi, 2011). It does however neglect important phenomena such as particle evaporation and/or sublimation in-flight and erosion of previously-built ice accretions.

More recently, as part of the High Altitude Ice Crystal (HAIC) program, ONERA developed a comprehensive 2D model for ice crystal icing, as described in Trontin et al., (2016); Villedieu et al., (2014) (hereafter, 'the ONERA model'). The physics in the model was developed and influenced by concurrent fundamental experiments conducted by the Technical University of Darmstadt, the Central Aerohydrodynamic Institute and Airbus Group Innovation. Particles are treated in the Lagrangian framework, and are allowed to be non-spherical – introducing the need for non-spherical correlations of Nusselt number, Sherwood number and drag coefficient. Particle - surface heat transfer in bouncing or fragmenting impacts is neglected, which is likely to lead to an under-prediction of particle melt ratio. The model again uses the Messinger model for liquid water icing (Messinger, 1953), with the energy and continuity equations extended to mixed phase conditions. It has been validated using simple ice crystal icing experiments conducted at the NRC (Currie et al., 2014; Struk and Wright, 2012) and the Cox icing wind tunnel (Al-Khalil et al., 2003). Fig. 2-9 shows the level of agreement reached for ice accretion on a crowned cylinder test piece installed in the NRC (Currie et al., 2014). The model is yet to be applied to engine icing. As the most up-to-date and experimentally validated code at the time of writing, some of the component parts are incorporated or updated in the current work.

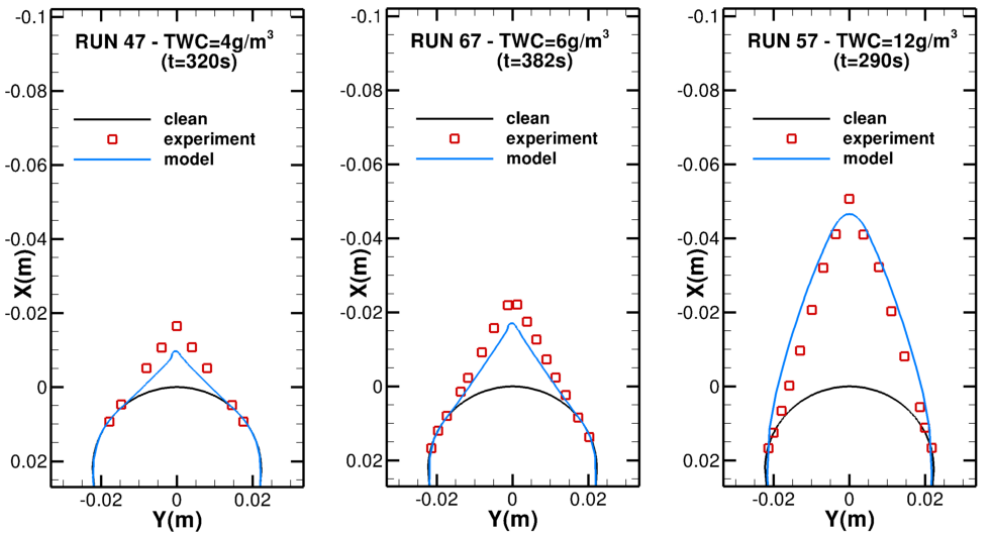

Fig. 2-9 Comparison of ONERA model predictions against NRC crowned cylinder results for varying TWC, at constant melt ratio and particle diameter (Trontin et al., 2016)

The framework presented in Fig. 2-8 will now be broken into its component parts and investigated in further detail.

2.5 Flowfield Modelling

Existing airframe icing codes typically use relatively low-fidelity embedded flow solvers. For example, LEWICE (Wright, 1995) and TRAJICE2 (Gent, 1994) use inviscid incompressible flow panel method solvers. Gas properties are calculated as a post-process operation, e.g. viscosity using Sutherland's law (Sutherland, 1893). An integral boundary layer solver is typically used to estimate heat transfer coefficients over clean and iced surfaces (Gent et al., 2000). It has been shown that these methods can give sufficient accuracy – as judged by comparison of predicted and experimental ice profiles – thereby negating the requirement for higher order methods (Gent et al., 2000). Codes are typically two-dimensional – which is generally considered acceptable for aircraft wing icing except for near the root or tip.

For turbomachinery, where flows are both highly unsteady and three-dimensional, it remains unclear how sensitive icing codes will be to flowfield fidelity. For the purposes of engine certification, it is likely that low-fidelity models will be run on multiple designs at a wide range of operating conditions, in order to identify a small number of critical regimes where icing is likely. These points may then be

re-examined using high-fidelity (e.g. full 3D Navier-Stokes) flow solvers to inform design choices. It may also be necessary to validate critical points experimentally to allow model tuning.

2.6 Discrete Phase Modelling

2.6.1 Particle Tracking Methods

Particle tracking models typically use an Eulerian (continuous secondary phase) or Lagrangian (discrete secondary phase) method. It is computationally more efficient to model the dispersed particles as a second Eulerian phase, as solutions may be generated with the addition of one extra set of mass, momentum and energy equations. The computational cost of Lagrangian particle tracking scales directly with the number of particles simulated; this in turn is dictated by the number required to achieve statistical convergence. The primary advantage of a Lagrangian approach is that since particles are treated individually, particle size distributions, application of particle-wall interaction models, and application of phase change and mass transfer models are straightforward (Guha, 2008). Eulerian tracking is more suitable for supercooled liquid water icing as droplets are assumed to be spherical, and evaporative mass transfer and complex surface interactions (e.g. splashing) are often neglected (Gent et al., 2000). Eulerian particle tracking has been applied to ice crystal trajectories (Iuliano et al., 2015) but restricted the cloud to mono-dispersed, fully glaciated and non-sublimating particles. All three caveats are severely limiting for modelling ice crystal accretion and so Eulerian particle tracking will not be considered further in the thesis.

The concept of collection or ‘catch’ efficiency is introduced at this point. Fig. 2-10 shows a schematic of two particle trajectories, moving from a far-field upstream location (left) to their respective impact locations (adapted from Gent et al., 2000).

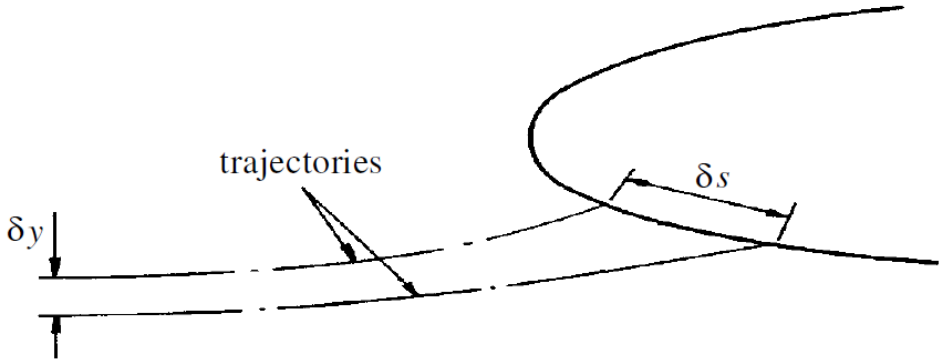

Fig. 2-10 Schematic of two particle trajectories for calculation of collection efficiency (adapted from Gent et al., 2000)

Local collection efficiency is given as the ratio of the particle separation in the freestream to that at impact:

$$\beta = \frac{\delta y}{\delta s} \tag{2-2}$$

It therefore takes into account the spreading of the impact locations due to the local surface angle, and also the divergence of trajectories due to the potential field of the body.

The local net sticking efficiency, introduced in equation (2-1), may be expressed in terms of collection efficiency:

$$\eta_{s,net} = \frac{\dot{m}_{stuck}}{\dot{m}_{imp}} = \frac{\dot{h}_{loc}\rho_{acc}}{\beta\ TWC\ U_{\infty}} \tag{2-3}$$

where $\dot{h}_{loc}$ is the local thickness growth rate, ρ_{acc} is the density of the accretion, TWC is the freestream total water content and U_{∞} is the freestream air velocity.

2.6.2 Lagrangian Particle Tracking

In Lagrangian tracking, Newton's second law of motion is calculated for each particle at each timestep to determine its trajectory in the next timestep:

$$\sum \vec{F}_{x,i} = m_p \frac{d\vec{U}_x}{dt} \tag{2-4}$$

where $\vec{F}_{x,i}$ is the i[th] force term in the $\vec{x}$ direction, and $\vec{U}_x$ is the velocity in the same direction.

It is therefore required to find the body forces pertinent to ice crystal motion. It is instructive at this point to consider whether particle motion is ballistic (inertia-dominated), or streamline-following (viscously dominated). This is typically described using Stokes number, given by

$$Stk = \frac{\tau_p}{\tau_f} \tag{2-5}$$

where τ_p is the characteristic particle relaxation time. Physically this is the time constant for the decay of a given slip velocity (the difference between the fluid and particle velocities) due to the drag force. Particle trajectories will be ballistic for a Stokes number much greater than unity, whereas trajectories will follow streamlines for a Stokes number much less than unity.

The relaxation time may be derived by considering the drag on a spherical particle in the Stokes regime:

$$\vec{F}_{d,Stk} = 3\pi\mu_f D_p(\vec{U}_p - \vec{U}_f) \tag{2-6}$$

where μ_f is the fluid dynamic viscosity and D_p is the particle diameter. Dividing through by the particle mass, $m_p = {}^{\pi}/_{6}\,\rho_p {D_p}^3$, the particle acceleration is given by

$$\vec{a}_{d,Stk} = \frac{18\mu_f}{\rho_p {D_p}^2}(\vec{U}_p - \vec{U}_f) \tag{2-7}$$

This equations assumes that particles are solid, not porous, thus tending to produce more ballistic trajectories. This assumption is likely acceptable for particles generated by freezeout of water, but for ice particles formed in the atmosphere by deposition and conglomeration, it may be limiting.

The particle relaxation time is given as the ratio of the relative velocity and Stokes flow acceleration

$$\tau_p = \frac{\left|\vec{U}_p - \vec{U}_f\right|}{\vec{a}_{d,Stk}} = \frac{\rho_p {D_p}^2}{18\mu_f} \tag{2-8}$$

The fluid characteristic time is given by

$$\tau_f = \frac{D}{\overline{U}_f} \tag{2-9}$$

where D is a characteristic length in the flowfield and $\overline{U}_f$ is a bulk flowfield velocity. An ice particle trajectory in a turbofan compressor may be used to get an expected approximate range. The data in the following analysis is taken from throughflow predictions of a Trent 500 IP compressor at top of descent, provided by Rolls-Royce Plc. In this case, the characteristic flow dimension is taken as the axial chord of a IP compressor stator vane, such that $D = C_x = 40$ mm. It is assumed that D_p is in the range $10 - 100$ μm, $\rho_p = 920$ kg/m^3, $\mu_f(T) = \mu_f(260\text{ K}) = 1.65x10^{-5}$ kg/m.s and $\vec{U}_f = 150$ m/s. Substituting these values into equations (2-8) and (2-9) yields Stokes number in the range $1.05 - 105$. This demonstrates that all but the smallest particles ($D_p < 10$ μm) will have near ballistic trajectories. Note that this calculation uses the stator chord to calculate fluid length scale, and the local static temperature to calculate viscosity and so is location-dependent in the compressor. If the conditions used here are representative of the front of the IPC, then conditions at the back, where $C_x \approx 20$ mm, $\mu_f(T) = \mu_f(340\text{ K}) = 1.98x10^{-5}$ kg/m.s, and $\vec{U}_f \approx 80$ m/s, then the same range of particle sizes gives a Stokes number range of $1.03 - 103$. However, sublimation, evaporation and breakup processes may mean that the particle size distribution at the front and back of the compressor are significantly different.

Particle Reynolds number is given by

$$Re_p = \frac{\rho_f \left|(\vec{U}_p - \vec{U}_f)\right| D_p}{\mu_f} \tag{2-10}$$

Taking a representative particle size of $D_p = 40$ μm, a slip velocity, $(\vec{U}_p - \vec{U}_f)$, in the range 10 – 100 m/s, a total pressure of 34.5 kPa and total temperature of 260 K gives a typical particle Reynolds number range of 11 – 111.

Both the values of Stk and Re_p indicate that motion is largely inertia-driven, meaning that diffusion-driven body forces such as Brownian motion may be neglected (Guha, 2008). It has been demonstrated that selection of forces most pertinent to particle motion and deposition can be formalised using a non-

dimensional particle relaxation time, τ_{p^+} (Guha, 2008; Young and Leeming, 1997). It is typically used with classical wall-bounded flow problems such as vertical pipe flow (Forsyth, 2017). However, it is nevertheless instructive when considering trajectories within a compressor where particles remain wall-bounded and freestream turbulence is significant. τ_{p+} is given by (Young and Leeming, 1997)

$$\tau_{p+} = \frac{\rho_f \tau_p {U_*}^2}{\mu_f} \tag{2-11}$$

where U_* is the wall friction velocity, defined as

$${U_*}^2 = \frac{\tau_w}{\rho_f} \tag{2-12}$$

Modelling a compressor stator blade as a flat plate, the laminar Blasius solution evaluated at 10% axial chord and the above bulk flow conditions ($Re_x \approx 10^5$) gives $\tau_w \cong 6.5$ Pa and $U_* \cong 3.8$ m/s. Once again taking D_p in the range $10 - 100$ μm, the particle relaxation time, τ_p, is in the range $3x10^{-4} - 0.03$ s. Using equation (2-11), τ_{p+} is in the range $110 - 1.1x10^4$. This is again indicative of the ballistic nature of particles at this flow condition. When $\tau_{p+} \ll 1$, particles follow streamline curvature closely and are diffusion-driven. For $\tau_{p+} \approx 1$, particles are more ballistic but motion is affected by acceleration imparted by turbulent eddies (advection-driven). As τ_{p+} increases, the effect of turbulence decreases until it has almost no effect (motion is inertia-driven) at $\tau_{p+} \approx 1000$ (Forsyth, 2017; Young and Leeming, 1997). Taking a laminar case may be seen as conservative – a turbulent boundary layer would lead to increased wall shear stress and thus increased τ_{p+}.

The body forces typically considered in particulate flows are gravity, drag, Brownian motion, Saffman's lift force, thermophoresis and turbophoresis. Saffman's lift force is the lift experienced on a particle due to a velocity imbalance across its surface, as a result of motion through a boundary layer or free shear layer. Thermophoresis refers to particle motion due to a temperature gradient, whereby bombardment of the particle from molecules in the continuous phase moving down the temperature gradient induces an acceleration. Turbophoresis is particle motion induced by non-homogeneous turbulence (i.e. particles are 'kicked' from an area of higher turbulence intensity to an area of lower

turbulence intensity). The above analysis indicates that $\tau_{p+} > 100$ for all the conditions considered, meaning that these three forces and Brownian motion may safely be neglected (Guha, 2008; Young and Leeming, 1997). Therefore, only drag and gravity will be considered in the remainder of the thesis.

2.7 Drag

The drag force in the $\vec{x}$ direction may be expressed as

$$\vec{F}_{d,x} = -\frac{1}{2}\rho_f C_D A_{p,\perp} \left|\vec{U}_{p,x} - \vec{U}_{f,x}\right| (\vec{U}_{p,x} - \vec{U}_{f,x}) \tag{2-13}$$

where $A_{p,\perp}$ is the particle area projected normal to the flow and C_D is the drag coefficient. Drag coefficient correlations for spherical particles are widely available, notably that of Clift and Gauvin, (1970). The shadowgraph images of atmospheric particles from the HAIC/HIWC flight trials show that application of spherical particle correlations is likely to be limiting for ice crystals.

2.7.1 Particle Shape & Drag Coefficient Correlations

Particle shape is commonly described through reference to a sphere of the same volume. Two definitions, sphericity, φ, (Wadell, 1935) and crosswise sphericity, $\varphi_\perp$, (Leith, 1987) are used, where

$$\varphi = \frac{6\, V_{eq}}{D_{eq} A_p} \tag{2-14}$$

where A_p is the surface area and $V_{eq} = V_p = {}^1\!/_6\, \pi {D_{eq}}^3$. Substituting this in to equation (2-14),

$$\varphi = \frac{\pi {D_{eq}}^2}{A_p} \tag{2-15}$$

Sphericity is independent of particle orientation, and therefore cannot take into account differing drag coefficients should a particle (such as a plate or column) travel in a lengthwise (head on) orientation rather than a crosswise (broadside) orientation. Lengthwise plates, discs and some high-aspect ratio spheroids can attain a lower drag coefficient than a sphere (at the same particle Reynolds number), which also cannot be captured through sole use of sphericity (Holzer and Sommerfeld, 2008).

Crosswise sphericity is defined as the ratio of the cross-sectional area of the volume-equivalent sphere and the actual area of the particle, projected normal to the flow direction ($A_{p,\perp}$):

$$\varphi_{\perp} = \frac{{}^{\pi}/_{4}\, {D_{eq}}^{2}}{A_{p,\perp}} \tag{2-16}$$

Since the particle orientation with respect to the flow is not known a-priori, an assumed orientation would need to be applied at the particle injection plane, and a tumbling model would then define the orientation at any timestep. Since a tumbling model is not included in the present work, it is assumed that particles adopt the (theoretically) most stable orientation, broadside to the flow. This is likely to be acceptable in steady flow cases, but in highly unsteady flows (such as the compressor environment) where perturbations knock particles from their stable orientations this may assumption may be limiting. Impacts with solid bodies (e.g. rotors) or regions of high flow curvature may also lead to particles being misaligned from the stable orientation.

Haider and Levenspiel, (1989) presented the first comprehensive drag coefficient correlation for non-spherical particles, given by

$$C_D = \frac{24}{Re}\left(1 + A{Re_p}^{B}\right) + \frac{C}{1 + {}^{D}/_{Re_p}} \tag{2-17}$$

where A, B, C and D are empirical functions of sphericity. Ganser, (1993) combined the work of Leith, (1987) and Thompson and Clark, (1991) to develop a drag coefficient applicable in both Stokes flow ($Re_p \ll 1$) and Newtonian flow ($Re_p \gg 1$). This is given by

$$\frac{C_D}{K_2} = \frac{24}{Re_p K_1 K_2}\left(1 + 0.112\left(Re_p K_1 K_2\right)^{0.6567} + \frac{0.4305}{1 + {}^{3305}\Big/_{\left(Re_p K_1 K_2\right)}}\right) \tag{2-18}$$

where K_1 is a Stokes-regime function of sphericity and crosswise sphericity and K_2 is a Newtonian-regime function of sphericity.

A comprehensive review of existing drag coefficient models and experimental data (Holzer and Sommerfeld, 2008) led to an updated correlation. This aimed to reduce the deviation between

equations (2-17) and (2-18) for non-isometric shapes with varying orientation relative to the flow. Fig. 2-11 shows experimentally measured drag coefficients for a range of shapes and orientations as a function of Reynolds number. Disks and plates orientated crosswise to the flow have a high drag coefficient for both low and high Reynolds numbers, as form drag dominates. In contrast, disks and plates orientated lengthwise to the flow (where skin friction drag becomes important) have a high drag coefficient at low Reynolds numbers, but low (almost spherical) drag coefficients at high Reynolds numbers. The effect of orientation – and hence crosswise sphericity – is clearly important across the Reynolds number range, something that neither equations (2-17) nor (2-18) can account for. The new correlation is given by

$$C_D = \frac{8}{Re_p}\frac{1}{\sqrt{\varphi_\perp}} + \frac{16}{Re_p}\frac{1}{\sqrt{\varphi}} + \frac{3}{\sqrt{Re_p}}\frac{1}{\varphi^{0.75}} + 0.42\left(10^{0.4(-log_{10}(\varphi))^{0.2}}\right)\frac{1}{\varphi_\perp} \qquad (2\text{-}19)$$

Equation (2-19) is applicable up to the critical particle Reynolds number (~100 - 300 for the particle shapes considered here (Chrust et al., 2010)) and the full range of particle sphericities. The mean error of this correlation from 2061 experimental datapoints, covering spheres, spheroids, isometric particles, disks and plates, is given as 14.4 %. The mean error in equations (2-17) and (2-18) from experimental results for disks and plates is estimated as 2000 % and 1800 % respectively. This is compared to 16.8 % difference for the same particles using equation (2-19). Equation (2-19) will therefore be used as the default correlation for the remainder of the thesis. A sensitivity analysis to particle shape and drag coefficient is given in chapter 3.

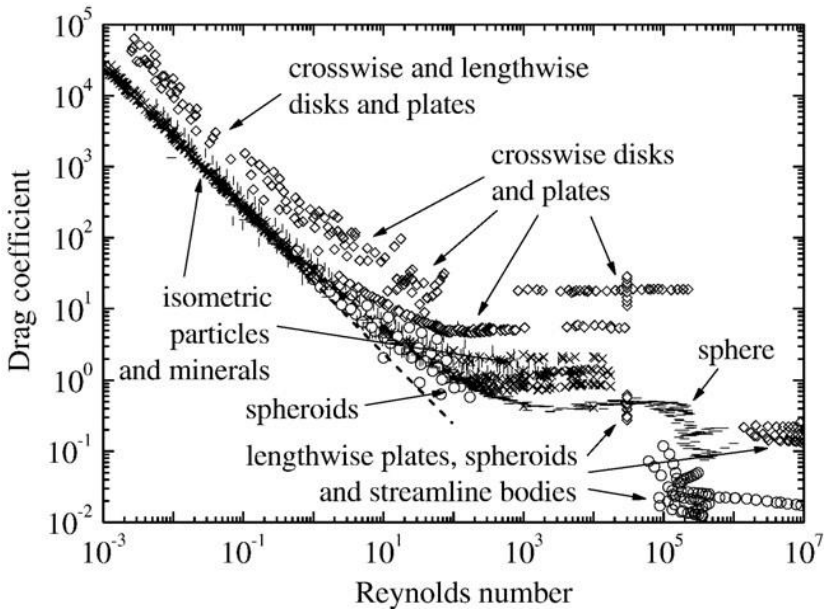

Fig. 2-11 Compilation of measured drag coefficients for a range of particle Reynolds numbers, shapes and orientations (Holzer and Sommerfeld, 2008)

2.8 Particle Impact, Sticking & Breakup

In supercooled liquid water icing codes all droplets are assumed to stick at the point of impact. Splashing is often neglected. The thermodynamic accretion model is then used to predict the proportion of the liquid water in the control volume that freezes. This is also commonly termed the 'freezing fraction'. In ice crystal icing, particle impacts with solid surfaces may lead to sticking, bouncing, fragmentation, melting, splashing and sliding / rolling. Modelling of these phenomena is therefore required as a pre-cursor to an accretion model.

The ice crystal icing model of ONERA (Villedieu et al., 2014) considers three distinct cases of surface interaction – sticking, bouncing and fragmentation. A sticking probability model based on empirical observations that partially melted particles and wetted surfaces are more likely to promote sticking was developed using the particle melt ratio and surface water film height. This approach was abandoned in an updated model (Trontin et al., 2016). The sticking probability was found to be highly sensitive to film height, which in turn relies on accurate modelling of skin friction and surface roughness. Instead, an empirical model is used based on experimental sticking efficiency data (Currie et al., 2014). This model captures the 'plateau effect' of sticking efficiency at surface temperatures

above freezing. However, the high experimental uncertainty and the small range of test conditions from which it is defined limits the applicability of the model.

Hail ingestion has long been seen as a threat to aircraft engines. As a result, several experimental studies have been performed to characterise impact and breakup behaviour. The Advisory Group for Aerospace Research and Development (AGARD) report AR-332 defines best practices for the assessment of the effect of atmospheric water, including hail. The report uses the concept of a 'critical' velocity, which is the minimum normal impact velocity required to cause fragmentation. This is based on the assumption that fragmentation occurs when the normal kinetic energy absorbed on impact exceeds the energy required for crack propagation. Guégan et al., (2012) conducted impact experiments at low speed (< 5 m/s) and angles between 45° and 90° for ice balls of 13 – 42 mm diameter. The critical velocity was measured and used to validate the hypothesis that the value of the ratio of the normal kinetic energy to particle surface energy, $\mathcal{L}$, could be used to predict the onset of fragmentation. This was formalised by Vidaurre and Hallett, (2008), who studied ice particles (diameters less than 1 mm) impacting at aircraft-realistic speeds. The ratio was given by

$$\mathcal{L} = \frac{Normal\ kinetic\ energy}{Particle\ surface\ energy} = \frac{\rho_p \frac{\pi}{6} {D_{eq}}^3 \frac{1}{2} {U_{p,n}}^2}{\pi {D_{eq}}^2 e_\sigma} = \frac{1}{12} \frac{\rho_p D_{eq} {U_{p,n}}^2}{e_\sigma} \tag{2-20}$$

where $U_{p,n}$ is the particle velocity normal to the wall and e_σ is the surface energy per unit area. This ratio may be seen as equivalent to a Weber number for solid particles.

Guégan et al., (2011) conducted experiments at high speed, where ice balls of 6 – 28 mm diameter were fired at an inclined surface at velocities between 60 and 200 m/s. This range was designed to be above the critical velocity for fragmentation so that the kinematics of the post-impact particle cloud could be studied. It was observed that there was significant absorption of normal kinetic energy, and that the angle between the leaving fragment cloud and surface was always less than ~2 °. These observations were later used by ONERA to develop empirical correlations for coefficients of restitution as a function of the ratio $\mathcal{L}$ (Villedieu et al., 2014). Studies of hail impact on flat plates and

fans (Pan and Render, 1996; Render and Pan, 1995) showed that a Rosin-Rammler particle size distribution was suitable for characterising secondary particles.

Under the European High Altitude Ice Crystals (HAIC) programme, studies on ice particle breakup were performed at Airbus Group Innovations (Hauk et al., 2014). Particles with maximum dimensions of several microns to ~1600 µm were fired at a tiltable aluminium plate with speeds up to 74 m/s, and the impact process recorded with a high speed camera. Over 200 impacts were recorded. Empirical correlations were defined for the critical velocity as a function of diameter for no, 'minor' and 'major' breakup. 'Minor' breakup was defined as cases where less than 20% of the particle was lost as fragments. Fig. 2-12 shows cases where no or minor breakup occurred. The experimental dataset was used by ONERA to estimate a value for $\mathcal{L}$ at the onset of fragmentation.

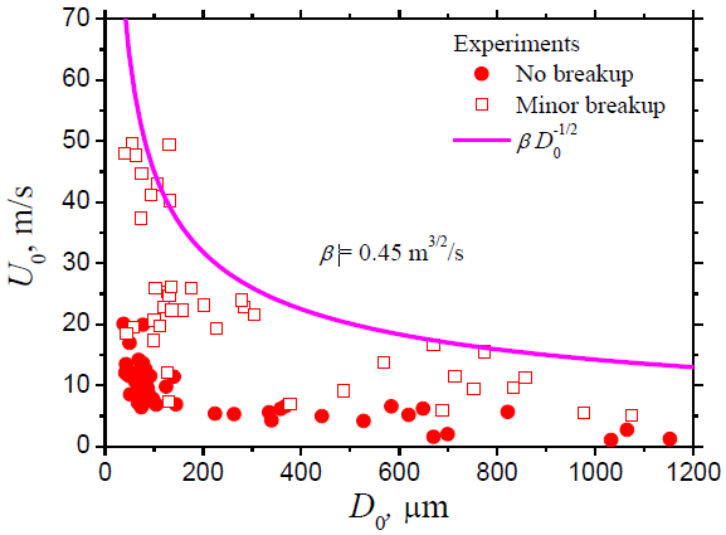

Fig. 2-12 Ice particle impact experiments with no or minor breakup. A correlation for the bound of minor breakup is also shown (Hauk et al., 2014)

Breakup models have been applied to simulations of ice particle ingestion into low bypass ratio turbofan engines. Safran S.A. (Aouizerate et al., 2018) tracked particle trajectory, breakup, melt and evaporation through the engine intake, fan, Inlet Guide Vane (IGV) and one stage booster. A Rosin-Rammler size distribution with 400 µm MMD was specified at inlet. The MMD after the Exit Guide Vane (EGV) was shown to be ~40 µm. Additional simulations with a monodisperse 80 µm particle cloud at inlet produced a 10 µm MMD after the EGV, demonstrating that the particle size at the booster exit was relatively insensitive to the inlet cloud. The study also showed that the atmospheric particles

were sufficiently inertia-driven through the inlet that trajectories were largely insensitive to sphericity, with a mean value of 0.2 (judged unrealistically low) required to generate significant deviation. Feulner et al., (2015) used the empirical correlations developed in the HAIC experiments to model particle breakup through the fan and four stages of LP booster. Particles of 150 μm diameter at inlet were reduced to 85 μm by the fan at a flight idle condition and 25 μm at a cruise condition. The resulting loss of inertia meant that there was significantly less breakup in the booster, with only 6% reduction in particle size through all four stages at the flight idle condition. The spatial distribution of ice concentration was also calculated. The IWC distribution in the spanwise direction was characterised by a spike at the casing primarily due to particles rebounding off the fan. A secondary, smaller spike was observed between 20% and 40% span, attributed to particles bouncing off the spinner. The radially inwards-curving hub wall was essentially in a shadow zone.

The ratio of IWC in the first stage to ambient IWC was observed to be greater than unity, due to the 'scoop effect'. At high flight speeds and low engine rotational speeds (for example at top of descent), the incident mass flow rate of air exceeds the mass flow rate drawn by the engine, resulting in air being pushed around the inlet lip of the nacelle (not ingested). Any secondary phase particles (e.g. rain or ice) are sufficiently ballistic to continue into the nacelle, therefore increasing the ratio of secondary phase mass flow rate to air mass flow rate.

2.9 Particle Heat & Mass Transfer

Modelling of particle phase change is crucial for ice crystal icing: the likelihood of particle sticking depends on the melted mass fraction; and refreezing of liquid water is driven by evaporative cooling of the airflow. An approach developed for the melting of hailstones (Mason, 1956) has been used in ice crystal codes (Lou and Hammond, 2011; Villedieu et al., 2014; Wright et al., 2010). In Mason's model, the particle is assumed to warm to its freezing temperature, melt at constant temperature and then warm again to equilibrium with the airflow. The change in enthalpy in each stage is balanced by convective and evaporative heat transfer. An experimental study by Rasmussen and Pruppacher, (1982) aimed to improve the model by accounting for an eccentric ice core and circulation inside the

external water film. These two effects were demonstrated to change the melting time by less than 10% for particles below 500 µm equivalent diameter.

The main challenge with these models is the prescription of a heat transfer coefficient (required in the convective term) and a mass transfer coefficient (required in the evaporative term), or, in their respective non-dimensional forms, Nusselt number and Sherwood number. A Chilton-Colburn heat-mass transfer analogy is typically used to calculate Sherwood number from Nusselt number (Villedieu et al., 2014). It then remains to find a suitable correlation for Nusselt number.

The Nusselt number correlation of Frossling, (1938) is commonly used for spherical particles. Comer and Kleinstreuer, (1995) proposed a Nusselt number correlation for non-spherical particles, applicable to oblate spheroids. The particles were assumed to be non-oscillating. It is applicable to relative Reynolds numbers in the range 40-120. The only shape parameter considered was aspect ratio, applicable in the range 0.2 - 1.0. Richter and Nikrityuk, (2012) developed a correlation for Nusselt number based on sphericity and crosswise sphericity. Similar to the studies of drag coefficient by Holzer and Sommerfeld, (2008), it is expected that particle orientation would affect the heat transfer coefficient distribution. Correlations for the two parameters may be formally similar though the Reynolds analogy. The correlation of Richter and Nikrityuk, (2012) is given by

$$\overline{Nu}_p = 1.76 + 0.55\varphi\sqrt{Re_p}\,\sqrt[3]{Pr}\,{\varphi_\perp}^{0.075} + 0.014\,{Re_p}^{2/3}\,\sqrt[3]{Pr}\left(\frac{\varphi}{\varphi_\perp}\right)^{7.2} \qquad (2\text{-}21)$$

It is applicable for prolate spheroids (aspect ratios in the range 1.0 -2.0) and cuboids, for particle Reynolds numbers up to 250. Chandarana et al., (1988) developed a correlation for cuboids, applicable up to $Re_p = 140$, where Re_p is based on the longest edge length of the cuboid.

ONERA developed a correlation with the aim of applicability to both prolate and oblate spheroids. The correlation used the Reynolds analogy, applied to the drag coefficient correlation of Holzer and Sommerfeld, (2008), to generate a formally similar correlation for Nusselt number. This was then tuned to match the equation of Frossling, (1938) for spherical particles ($\varphi = \varphi_\perp = 1$). It is given by

$$\overline{Nu}_p = 2\sqrt{\varphi} + 0.55\, Pr^{1/3}\varphi^{1/4}\sqrt{\overline{Re_p}} \tag{2-22}$$

The correlation was shown to agree within 5% with the results of Richter and Nikrityuk, (2012) for prolate spheroids in both lengthwise and broadside orientations. Agreement with Comer and Kleinstreuer, (1995) for oblate spheroids was within 6%. It will therefore be used in the current work. Equation (2-22) may be assumed applicable within the Reynolds number and aspect ratio ranges given above for the respective correlations.

As part of the European High Altitude Ice Crystals (HAIC) consortium, particle melting experiments were conducted by TU Darmstadt and Airbus Group Innovations (Hauk et al., 2016). Ice particles were extracted from a chest freezer and held in an acoustic levitator, whilst in a crossflow of warm air (low speed, typically below 2 m/s). Flow temperature, velocity and relative humidity were varied, as well as the initial ice particle temperature. The particles extracted from the freezer were invariably non-spherical, so a small number of spherical particles were generated by melting and then refreezing non-spherical particles with the same apparatus. The time for particles to fully melt was recorded. Predictions of melt time were generated using Mason's melting model, implementing equation (2-22) for Nusselt number. For non-spherical particles, the mean percentage difference between predicted and measured melt times was 9.7%. A sensitivity analysis to sphericity was performed. For the same set of tests, an additional predicted melt time was generated using an assumed sphericity of unity. The mean percentage difference between these predictions and the measured melt times increased to 19.9%. Fig. 2-13 shows an exemplary melting process, with the projected area (the area visible on the shadowgraph images) plotted against time.

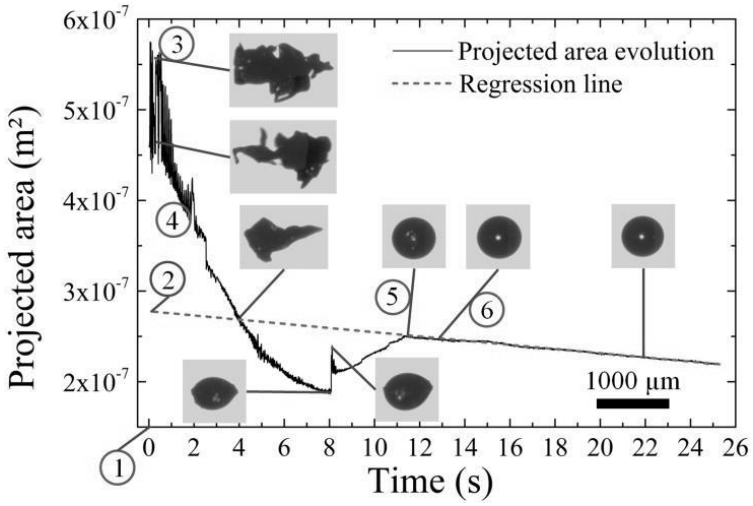

Fig. 2-13 Projected area against time for the melting process of a non-spherical particle. Numbers denote (1) test start; (2) extrapolated initial spherical area; (3) particle rotation; (4) particle shaking; (5) first spherical particle; (6) end of melting process (Hauk et al., 2016)

The experiments conducted here, as well as the bounce and shatter models given in 2.8, assume solid particles, or fragments. This may again be limiting for porous particles with internally trapped air.

All the ice crystal icing models discussed thus far neglect the effects of particle-surface heat transfer during bouncing or fragmentation. It is possible that impacts with warm surfaces contribute to the overall melt fraction of the particle, thus affecting the probability of sticking to surfaces. Therefore, this is the subject of further research reported later in this thesis.

2.10 Thermodynamic Accretion Model

A thermodynamic accretion model forms the third major component of any icing code. Energy and continuity equations are solved locally to predict the growth of ice and water layers using the mass flux of particles that have stuck. Accretion models have historically been developed for supercooled water icing - where water droplets impinge on sub-freezing engine components (Gent, 1994; Wright, 1995). Ice crystal accretion has been treated more simply as a continuity-based approach (Currie et al., 2014), if a sticking fraction at a given thermodynamic condition is known. The limitation of this approach is apparent – sticking fractions must be known empirically for every condition of interest and thus is highly inflexible. Given the current dearth of experimental data for ice crystal icing, the range of conditions for which this information is known to a good degree of accuracy is small. In

contrast, a thermodynamic approach provides a mechanism for modelling the necessary physical processes (evaporation, melting, runback etc.) at any condition. It also permits transience to be modelled – for example the temperature response of the underlying component.

Messinger, (1953) first formalised a thermodynamic accretion model for supercooled liquid droplets impinging on the wings of aircraft. This model still forms the basis of the most widely used icing codes today (Gent et al., 2000). It is a steady approach that assumes that the component surface (substrate) immediately adopts its equilibrium temperature, and holds it for the whole simulation time. Heat transfer normal to the surface is neglected (i.e. the accretion is at a uniform steady temperature). Similarly, the freezing fraction is constant at all time steps. The equilibrium temperature is calculated using an energy balance which considers evaporation, convection, melting, sensible warming of impinging droplets, and transfer of kinetic energy from impinging droplets. Careful consideration must be given to the calculation of the local heat transfer coefficient, for both clean and rough (iced) surfaces. An integral boundary layer model, which incorporates roughness using the equivalent sand grain height, is often used for airframe icing. The evaporative mass flux is estimated through a Chilton-Colburn heat mass transfer analogy, using the calculated heat transfer coefficient (Gent et al., 2000). The ONERA ice crystal icing code incorporates the Messinger model, adapted to mixed phase conditions using additional heat flux terms for the ice particle sensible warming, melting and kinetic energy transfer (Trontin et al., 2016).

Myers, (2001) proposed an improvement to the Messinger model, termed the 'Extended Messinger Model' (EMM). This model permits a linear temperature gradient normal to the icing surface, and thus heat flux from the substrate through the water and ice layers. This approach is therefore quasi-steady: time enters the problem through the changing accretion height - which due to the temperature gradient therefore produces a changing accretion surface temperature. The terms in the energy balance were maintained from the Messinger model. The assumed geometry is shown in Fig. 2-14. Ozgen and Canibek, (2008) further added to the temporal dependency by growing the accretion over multiple 'layers'. For each layer, the EMM is solved and the ice / water layers grown. After each layer, particle collection efficiency is updated. It may also be possible for the flowfield to be updated for further

improvement in accuracy. In theory, performing a multiple layer model also permits the incorporation of transient operating conditions (e.g. the transient from cruise to descent idle), as parameters may be updated between each layer calculation.

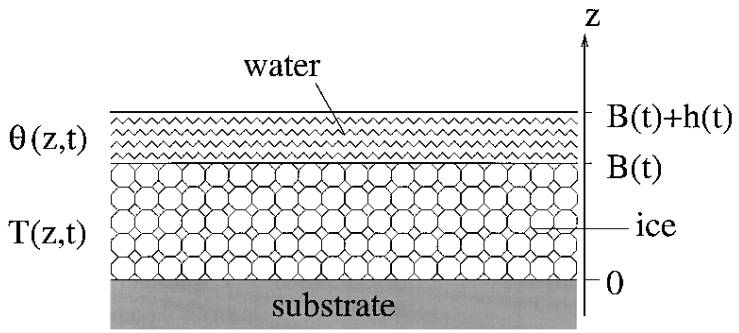

Fig. 2-14 Schematic of assumed geometry for the EMM applied to supercooled water droplet icing (Myers, 2001)

Qualitative experimental validation of the EMM was undertaken using leading edge accretion on a NACA 0012 aerofoil model, installed in the former Aerospace Composite Technology Icing Wind Tunnel (Artington). Agreement was within the experimental measurement uncertainty.

Overall, therefore, the EMM may be considered a suitable framework for a thermodynamic ice crystal accretion model. It does however require adaptation to mixed phase and glaciated conditions. Apart from the addition of energy source and sink terms, a number of simplifying assumptions – for example that any liquid film on a particle is immediately transferred into the surface liquid layer – is required. This assumption, and others, are introduced and justified in chapter 6.

2.11 Summary

From the literature review we may conclude that an ice crystal icing code incorporating the following elements will satisfy the research aims outlined in chapter 1:

(1) Flowfield importation and Lagrangian particle tracking;

(2) Particle-air heat and mass transfer using literature correlations for Nusselt and Sherwood numbers;

(3) Particle-surface interaction incorporating heat transfer, sticking and fragmentation;

(4) Thermodynamic accretion modelling based on a modified form of the EMM (Myers, 2001) to include mixed phase conditions;

(5) Erosion modelling and final accretion profile extraction

To fulfil this goal, a mixture of model development and baseline data generation through experimentation has been performed and is reported herein to generate each component. Due to the complexity in conducting ice crystal icing experiments (especially given that simulated altitude is required for accretion studies), only established research facilities were considered for use. It was quickly apparent that both the Research Altitude Test Facility (RATFac) and the Altitude Icing Wind Tunnel (AIWT) were suitable, these being facilities which can match conditions of interest accurately. They are also supported by an operating team with significant experience in mixed-phase measurement techniques.

The experiments to be performed were prescribed by gap analysis of the literature, with the number and scope limited by the cost of testing and the limited time slots available. Of the model components listed above, considerable prior modelling in the literature exist for (1) and (2). The same is also true for the first generation of bounce and fragmentation models. Similarly, while (4) requires significant model development, the EMM framework from literature exists. Section 2.3.2 highlights that literature sticking and erosion models were at very early stages of development at the start of the research programme, being defined from relatively few test conditions and with high experimental uncertainty. It was also apparent that there had also been no work undertaken to measure heat transfer from a surface under ice crystal impacting conditions. The areas targeted for experimentation were therefore sticking, erosion and particle - surface heat transfer.

It had been shown in previous campaigns (Currie et al., 2014; Struk et al., 2015a) that RATFac was ideally suited for sticking experiments, due to its ability to closely control relative humidity (evaporative cooling) and hence particle melt ratio. It was also best suited to erosion studies due to its superior control of particle size distribution, with near-independent variation of D_{v50} and D_{v90}.

For particle-surface heat transfer experiments, it was key to understand the behaviour of fully glaciated particles impacting on a warm, clean (de-iced) surface, representative of conditions early in the core compressor. For these experiments the NRC AIWT tunnel was suitable. This facility does not have humidity control, but this was deemed acceptable since neither accretion growth nor particle melt were the focus of the study. An additional benefit in using the facility was that because the humidity approaches 100%, effectively the evaporation term in the surface heat balance is removed from experimental analysis, considerably simplifying the post-processing and increasing confidence in the results obtained.

The test article design, instrumentation, test conditions and results of the experiments performed are reported in chapter 5.

3 Ice Crystal Icing Model & Test Cases

In this chapter, the proposed structure for a new ice crystal icing code is introduced. The elements of the code previously identified as requiring further experimentation are highlighted, and the experimental and numerical test cases used as validation are introduced.

3.1 Structure of Ice Crystal Icing Model

In chapter 2, the general structure of major historic and existing supercooled water icing codes was introduced, as shown in Fig. 3-1. This structure is used as the basis for the proposed ice crystal icing model, hereon referred to as the Ice Crystal Icing ComputationaL Environment (ICICLE). Additional functionality is however required to adequately adapt the modelling to mixed phase and glaciated conditions. These adaptations and their validation is the subject of chapters 4-6 of the thesis.

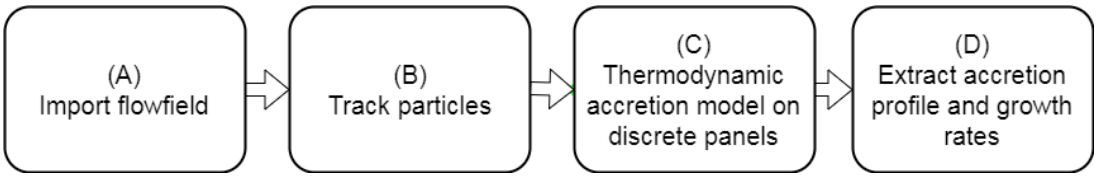

Fig. 3-1 Schematic of main components in aerospace icing codes

Fig. 3-2 shows the overall structure of ICICLE, using the same four-column representation as Fig. 3-1. Blocks are coloured by the chapter in which the enabling modelling is discussed and developed. The elements identified in chapter 2 as requiring further experimentation are outlined in blue.

Both Fig. 3-1 and Fig. 3-2 are termed ‘one-way coupled’ models: mass, momentum, and energy of the particles (discrete phase) are altered by the flowfield, but not vice versa. Flowfield and trajectories are solved only once. The accretion profile is generated by extrapolating the predicted growth rate over a fixed time period – the time for which the test article is ‘exposed’ to the icing cloud. It has been shown that this method can lead to inaccuracies for cases of ‘large’ accretions (of the same order of magnitude as the test article characteristic dimension) because (i) the area exposed to particles changes over time; and (ii) the assumption that the flowfield remains unchanged is unrealistic. Additionally, the effect of

particle sublimation and evaporation on the flowfield temperature and humidity (i.e. energy and mass coupling respectively) is neglected.

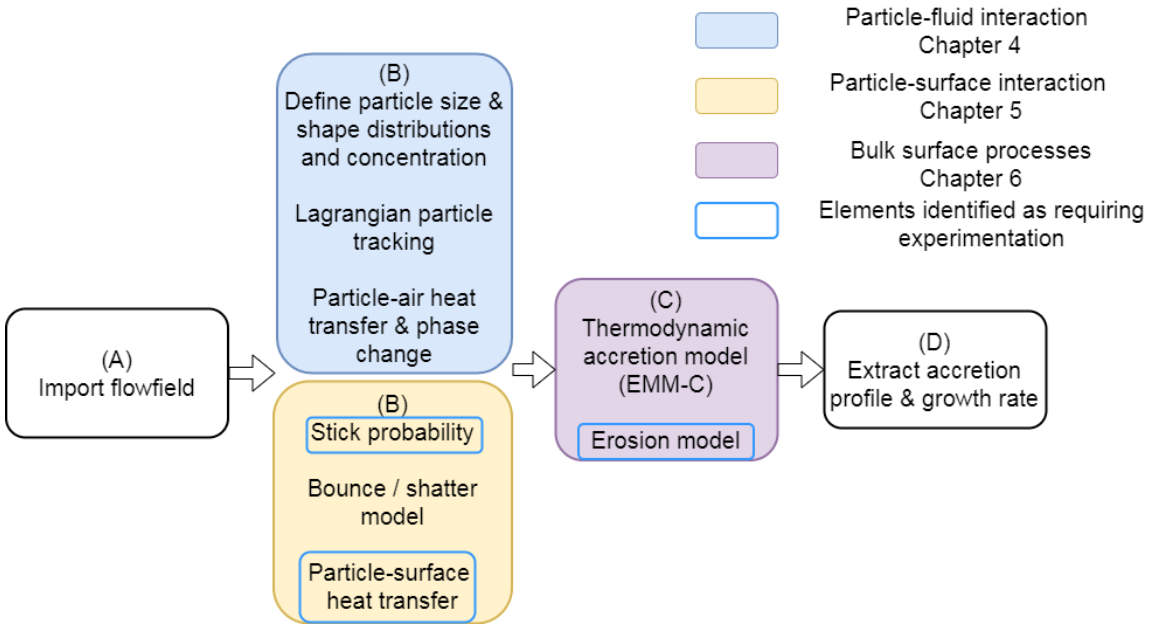

Fig. 3-2 Proposed structure of new ice crystal model (ICICLE) using the same building blocks as Fig. 3-1

Fig. 3-3 shows a schematic of one method of how two-way coupling can be implemented. The total exposure time is divided into discrete periods, and a 'layer' of ice grown within each period. Between periods, the new accretion profile is assumed into the test article geometry and is used to update the number of particles locally impinging (the collection efficiency). As the accretion elongates, surfaces may become increasingly oblique to the flow direction, reducing the exposed area. This is illustrated in Fig. 3-4 for a notional accretion on a cone.

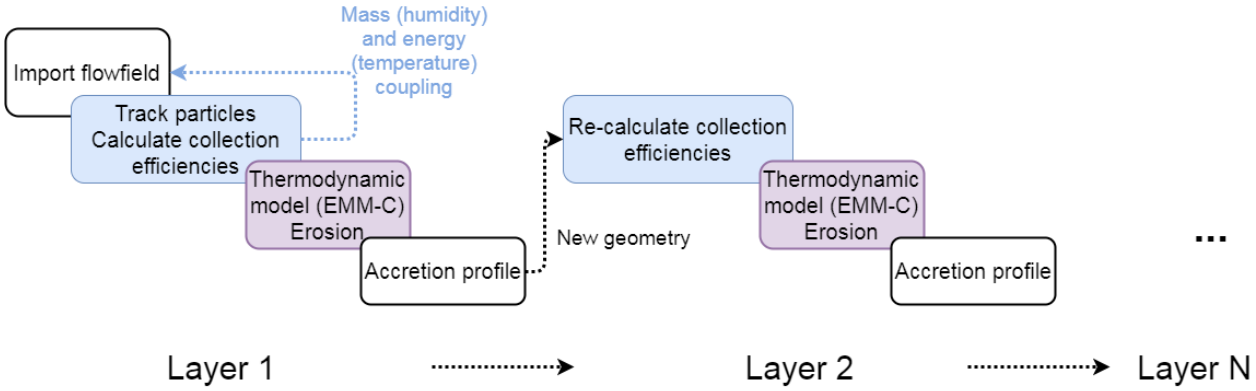

Fig. 3-3 Multi-layer accretion process using collection efficiency update, and two-way mass/energy coupling

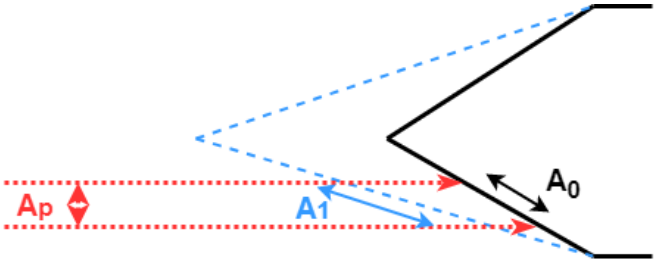

Fig. 3-4 Effect of accretion growth on collection efficiency, neglecting potential field effects. The initial collection efficiency is given by A_p / A_0, and the collection efficiency during accretion by A_p / A_1.

Fig. 3-5 shows a higher fidelity method of two-way coupling. The new geometry (test article plus accretion) is re-meshed and the flowfield re-solved inside a commercial CFD solver. Surface smoothing is typically required to aid mesh creation, and any gain in prediction accuracy is offset against an increased computational cost.

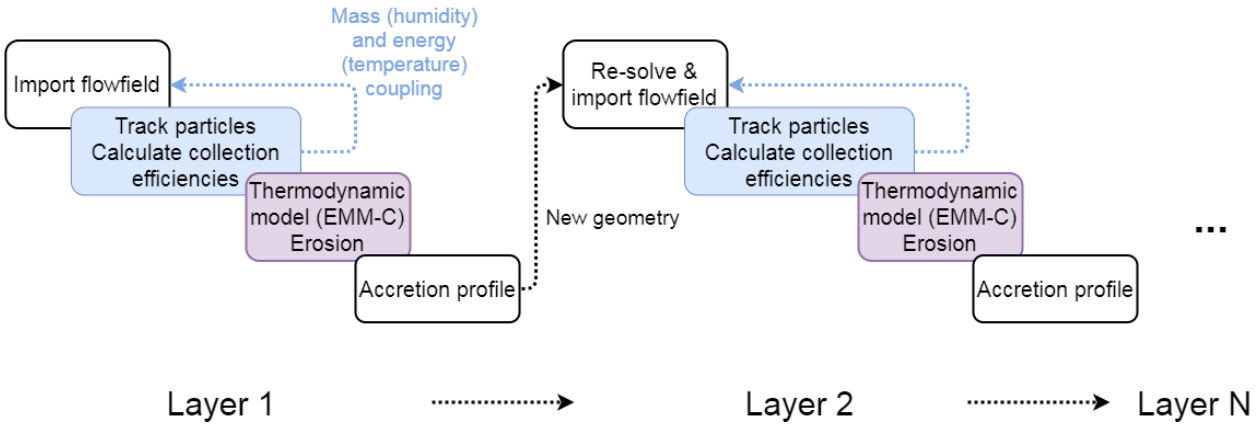

Fig. 3-5 Multi-layer accretion process using flowfield and trajectory update, and two-way mass /energy coupling

In both Fig. 3-3 and Fig. 3-5, two-way coupling of energy and mass is also implemented. Practically, this means that the flowfield temperature decreases and relative humidity increases if particles sublimate or evaporate. The underlying equations to model this effect are discussed in chapter 4.

3.2 Code Test Cases

Whilst the primary objective of the experimental campaigns was to generate fundamental data for model development, they also provided validation test data for the completed code. In this section, two test cases are introduced, referred to as ‘the cone’ and ‘the stator’. The test articles and experimental conditions are briefly introduced, as well as the numerical setup of CFD simulations of each. The

simulations were used during design of the test articles, but also provided the flowfield required by ICICLE to simulate the cases. Comparisons of the accretion profiles predicted by ICICLE and the experimentally measured profiles are given in chapter 7.

3.2.1 Experimental Facility & Conditions

The test facility used for both test articles was the Research Altitude Test Facility (RATFac) at the National Research Council of Canada (NRC) in Ottawa. This is a wind tunnel with altitude simulation and ice crystal injection capabilities, developed continuously since 2006. More detail on the facility commissioning and its previous campaigns is given in chapter 2.

RATFac has the ability to independently control altitude, Mach number, relative humidity, total temperature and particle size distribution. A summary of the test conditions used for both test articles is given in Table 3-1. Throughout the campaign, freestream total pressure was held at 34.5 kPa (ISA altitude of approximately 8.2 km / 27,000 ft) and total air temperature at 10 °C. The complete test matrix is given in Appendix B. Aerodynamic calibrations of the tunnel are available in Knezevici et al., (2011). Axial velocity was observed to be uniform within 95% of the centreline value over the central 60 mm x 60 mm portion – within which the measurement regions of both test articles sits. Non-uniformity in flow angularity was small, with a maximum deviation in the same region from the axial direction of 3°. The boundary layer thickness was estimated to be 25 mm at the test article plane.

Table 3-1 Summary of test conditions for the cone and stator test cases

Parameter	*Minimum*	*Baseline*	*Maximum*
Freestream Mach [-]	0.25	0.40	0.50 (cone only)
Relative humidity [-]	0.05	0.45	0.65
TWC [g/m^3]	4.0	8.0	12.0 (cone only)
Ice D_{v10} [µm]	18	18	35
Ice D_{v50} [µm]	34	34	68
Ice D_{v90} [µm]	54	54	131
Cone half angle [°]	20	35	45
Stator angle of attack [°]	-20	0	20

It has been shown in previous studies (Currie et al., 2014; Struk et al., 2011) that a wet bulb temperature above freezing promotes particle melt, whereas one below freezing inhibits it. Wet bulb temperature may be controlled by setting a target relative humidity at a fixed total pressure and temperature. In the experimental campaign, it was desired to systematically vary the bulk particle melt ratio, defined as the ratio of the measured LWC to the measured TWC. The former is measured using the Science Engineering Associates (SEA) multiwire probe (Lilie et al., 2005). It was discussed in chapter 2 that this probe suffers from a 'false response', whereby solid ice particles bouncing off the heated wires give a spurious LWC reading. Chapter 5 presents a new empirical correlation for the false response as a function of test condition.

TWC is measured using the NRC Compact Iso-Kinetic Probe (CIKP) (Davison et al., 2016a, 2016b). The CIKP evaporates the water and ice passing through an open-ended tube, and measures the difference in specific humidity between inlet and exit.

Ice particles are generated using a grinder system. Particle D_{v50} can be controlled in the range 20 – 300 μm, with additional near-independent control of D_{v90}. A Particle Imaging Velocimetry (PIV) system configured for shadowgraphy is used to estimate the particle size distribution, just upstream of the tunnel inlet. The grinder tends to produce angular, faceted particle shapes. A mean aspect ratio of 0.70 was reported following particle morphology studies in RATFac (Fuleki et al., 2015). Particles exit the grinder at a temperature of approximately -15°C.

Calibrations of the spatial uniformity of TWC and LWC were performed at test conditions of interest, as detailed in Appendix C. The calibration of TWC shows a diagonal non-uniformity across the test section, a trend which was repeatable (albeit to a greater or lesser degree of non-uniformity) for all test conditions. It was attributed to the non-uniform ice profile that exits the grinder on the 'cold side' of the rig. TWC calibrations were used in the data postprocessing to normalise the local measured growth rates by the approximate local TWC.

3.2.2 Test Article 1: The Cone

The cone is an axisymmetric test article with a conical icing surface. This simple geometry is not intended to be representative of an engine component, but was designed to provide ice growth rate data for both the sticking probability and erosion models. A cone was chosen due to the ease in imaging from multiple angles, and the reduced propensity for the accretion to droop under gravity, as may occur on other axisymmetric geometries such as hemispheres (Currie et al., 2014). The particle impact angle is also known accurately, and may be varied discretely by using multiple different half-angle cone 'noses'.

The test article is shown in Fig. 3-6 (a). A 60 mm diameter cone 'nose' is inserted into a cylindrical afterbody of the same diameter, with an aerodynamic conical tail downstream. Fig. 3-6 (b) shows the test article installed in RATFac, forward looking aft, and Fig. 3-6 (c) shows a side view, with side and isometric view cameras visible.

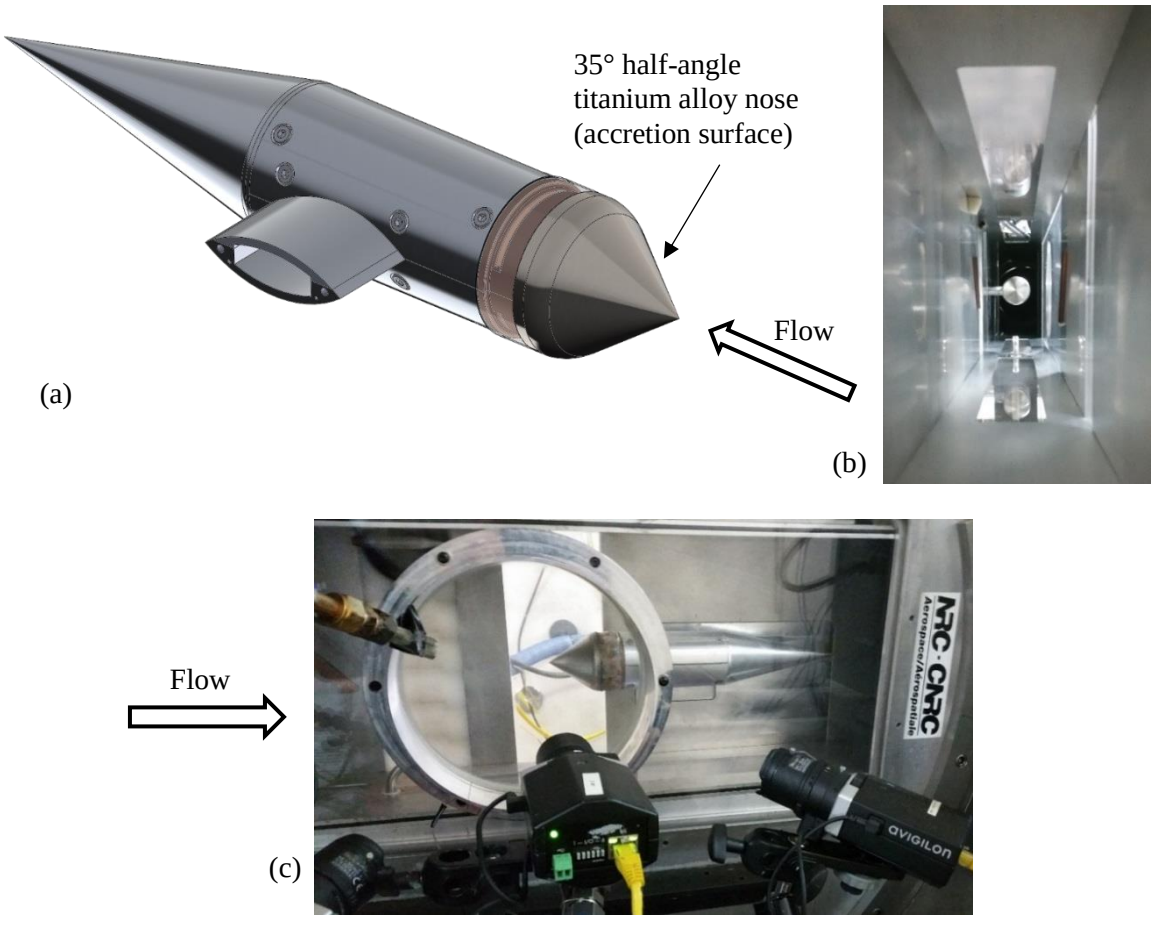

Fig. 3-6 (a) Isometric view of cone test article; (b) front view and (c) side view of the cone installed in RATFac

The cone nose was interchangeable with 20°, 35° and 45° half-angle versions. All noses had a ~400 µm thick titanium alloy (Ti90-Al6-V4) shell as the icing surface, bonded to a solid copper substrate. The alloy is representative of the material used in compressor components. The shells were 3D-printed using the Direct Metal Laser Sintering (DMLS) technique and polished to an RA representative of a compressor surface condition between entry into service and overhaul.

CFD simulations of the cone were run in a commercial solver, ANSYS Fluent. Solutions were used in the test article design, primarily to verify that the tunnel blockage was sufficiently low to allow the maximum target Mach number of 0.5 to be achieved. Data at the vertical midplane was also exported to MATLAB for use in ICICLE as the 2D flowfield. Fig. 3-7 shows the computational domain.

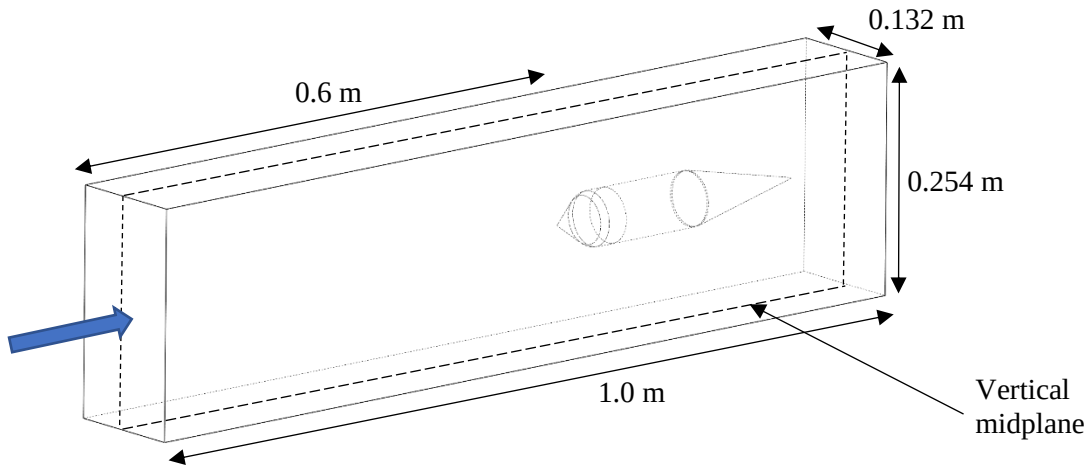

Fig. 3-7 Computational domain for cone test article. Flow is into the left boundary. The dashed line shows the vertical midplane, exported to MATLAB for use in ICICLE.

A mesh of 4.8M cells was used. A density-based RANS solver was used, in conjunction with the k-ω SST turbulence model. Full details of the mesh strategy and numerical setup, and results of a mesh independence study, are given in Appendix A-1.

Solutions were exported to ICICLE for the two primary aerodynamic conditions, freestream inlet Mach numbers of 0.25 and 0.40. All other aerodynamic conditions are as given in Table 3-1. Parameters exported comprise total and static temperature, total and static pressure, axial and radial velocity, density, dynamic viscosity, specific heat capacity at constant pressure and thermal conductivity. These were read into MATLAB and interpolated onto a coarser rectangular grid of 960,000 nodes.

Fig. 3-8 shows contours of normalised velocity magnitude at the vertical midplane, for (a) the M_∞ = 0.25 and (b) the M_∞ = 0.40 cases. Fig. 3-8 (c) shows the M_∞ = 0.40 case, windowed on the lower half of the conical icing surface. Since the tunnel blockage is ~ 11%, the maximum local Mach number at the edge of the boundary layer is significantly greater than that in the freestream, at 0.37 and 0.60 for cases (a) and (b) respectively. Compressibility effects are therefore potentially significant for the ice growth, as local static temperature, static pressure and vapour pressure will deviate from freestream values, all of which affect the energy balance in the thermodynamic model.

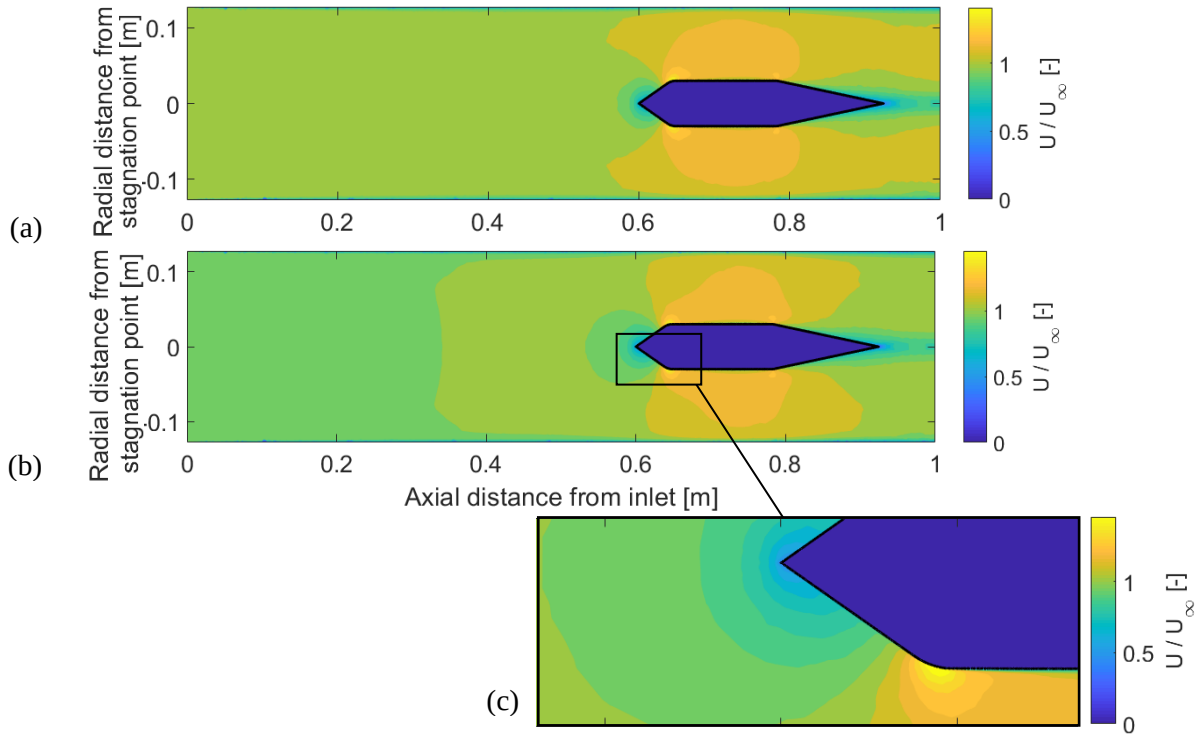

Fig. 3-8 Contours of normalised velocity magnitude at the vertical midplane for (a) the M_∞ = 0.25 and (b) the M_∞ = 0.40 cases. Flow is left to right. (c) shows the M_∞ = 0.40 case, windowed on the lower half of the icing surface.

The local heat transfer coefficient on the test article is also required as an input to ICICLE. It is used to calculate the convective, and evaporative heat fluxes on the icing surface. These terms are critical in determining whether ice will form, or whether complete melting (running wet conditions) will occur.

The heat transfer coefficient distribution was also extracted from the CFD simulations of the cone. A two-point approach was used: two simulations were run at the same aerodynamic condition, with

differing isothermal wall temperatures (280 K and 310 K). The local heat transfer coefficient may be calculated using both conditions as given in equation (3-1).

$$H(s) = \frac{q_{w,2}(s) - q_{w,1}(s)}{T_{w,2} - T_{w,1}} \tag{3-1}$$

where s is the streamwise distance from the cone tip, $q_w(s)$ is the predicted heat flux and T_w is the uniform wall temperature. Heat flux was circumferentially averaged. A Stanton number correlation for turbulent flow over a cone was also used to compare against the CFD. This is given by equation (3-2) (Crabtree et al., 1965).

$$H(s) = \rho U_e C_p St_s = \rho U_e C_p \left(0.176 \ (\log_{10} {Re_s}/{2})^{-2.45}\right) \tag{3-2}$$

where $Re_s = \frac{\rho_e U_e s}{\mu_e}$, where the subscript 'e' denotes conditions at the edge of the boundary layer.

The values are held constant over the exposure time and so do not take into account changes in surface roughness, shape or the presence of a water film. A fully turbulent boundary layer was assumed since (i) the turbulence intensity in RATFac was measured to be approximately 7.5% at the tunnel centreline on the traverse plane (Knezevici et al., 2011), and (ii) the tunnel Reynolds number based on hydraulic diameter was varied in the range 4.0 x10^5 to 6.4 x10^5.

Fig. 3-9 (a) shows velocity at the edge of the boundary layer normalised by freestream inlet velocity for the two Mach numbers tested. Local heat transfer coefficient values predicted by CFD and by the correlation in equation (3-2) are shown in Fig. 3-9 (b). The agreement between CFD and correlation is within 20% across the streamwise length. The integrated difference across the streamwise extent is 8.7 % of the mean.

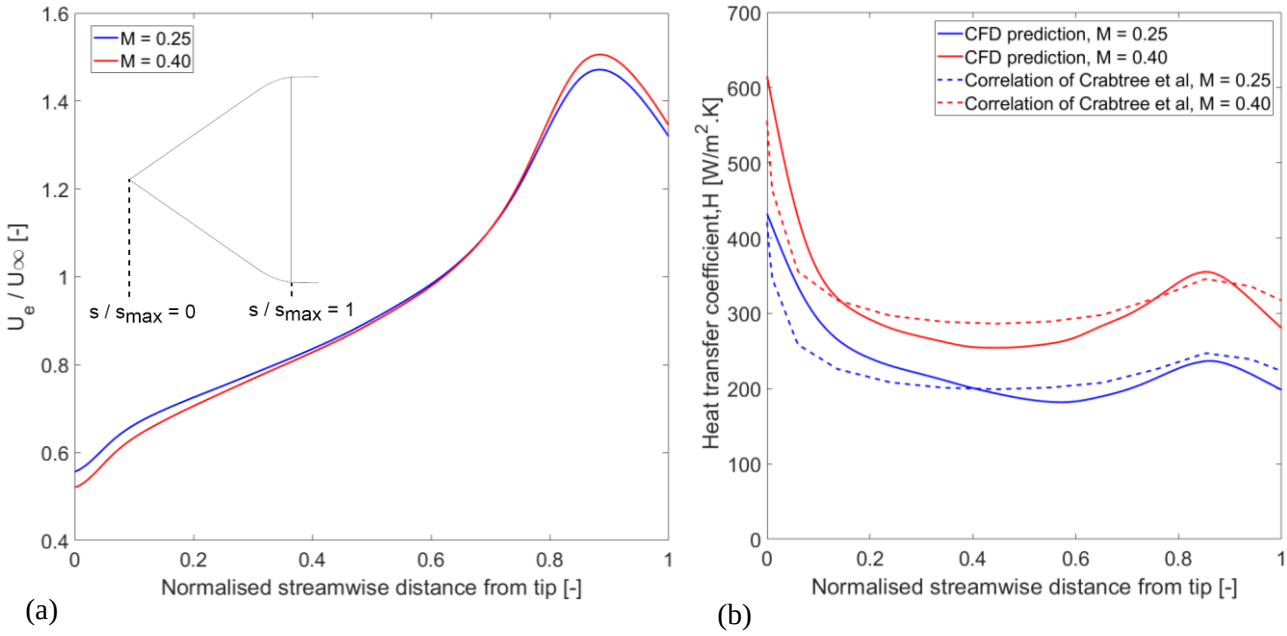

Fig. 3-9 (a) Normalised velocity distribution at edge of boundary level on the 35° cone. (b) Heat transfer coefficient distribution predicted by CFD and correlation against streamwise location

3.2.3 Test Article 2: The Stator

The prismatic stator test article was designed to be more pertinent to engine icing, albeit heavily simplified compared to a 'real' engine stator vane. Its sole purpose was to provide accretion profiles with which to validate ICICLE.

A prismatic stator was chosen as a validation test article as it contains geometric features – a leading edge and concave pressure surface – that are of interest from a modelling perspective. An ability to model particle catch and bounce on these continuously curving surfaces is a necessary precursor to more complex, and/or 3D geometries. The stator was not installed as part of a cascade. There is evidence from previous experimental campaigns at RATFac that high levels of ice blockage in the cascade passages can lead to image obscuration and can inhibit the extraction of quantitative data (Mack, 2013b), although excellent insight may be attained qualitatively.

Fig. 3-10 (a) shows the test article. The main body comprises a prismatic aerofoil, of 90 mm span, 42 mm chord and 27.5° camber angle. The profile was provided by Rolls-Royce plc, chosen to be

representative of an IP compressor stator vane at midspan, at 1-1 scale. The stator was mounted into a circular polycarbonate window, which itself was mounted into a rotatable frame, allowing angle of attack variation. The stator suction surface and the circular window are shown in Fig. 3-10 (b). The stator was backlit through this window and the free end (tip) imaged from a window on the opposite side of the tunnel, as shown in Fig. 3-10 (c). There was a ~ 30 mm gap between the tip and window to prevent ice buildup obscuring the image, as shown in Fig. 3-10 (d). Since the ice concentration decreases near the tunnel walls, the gap also ensured that the tip and central region were exposed to the icing cloud core.

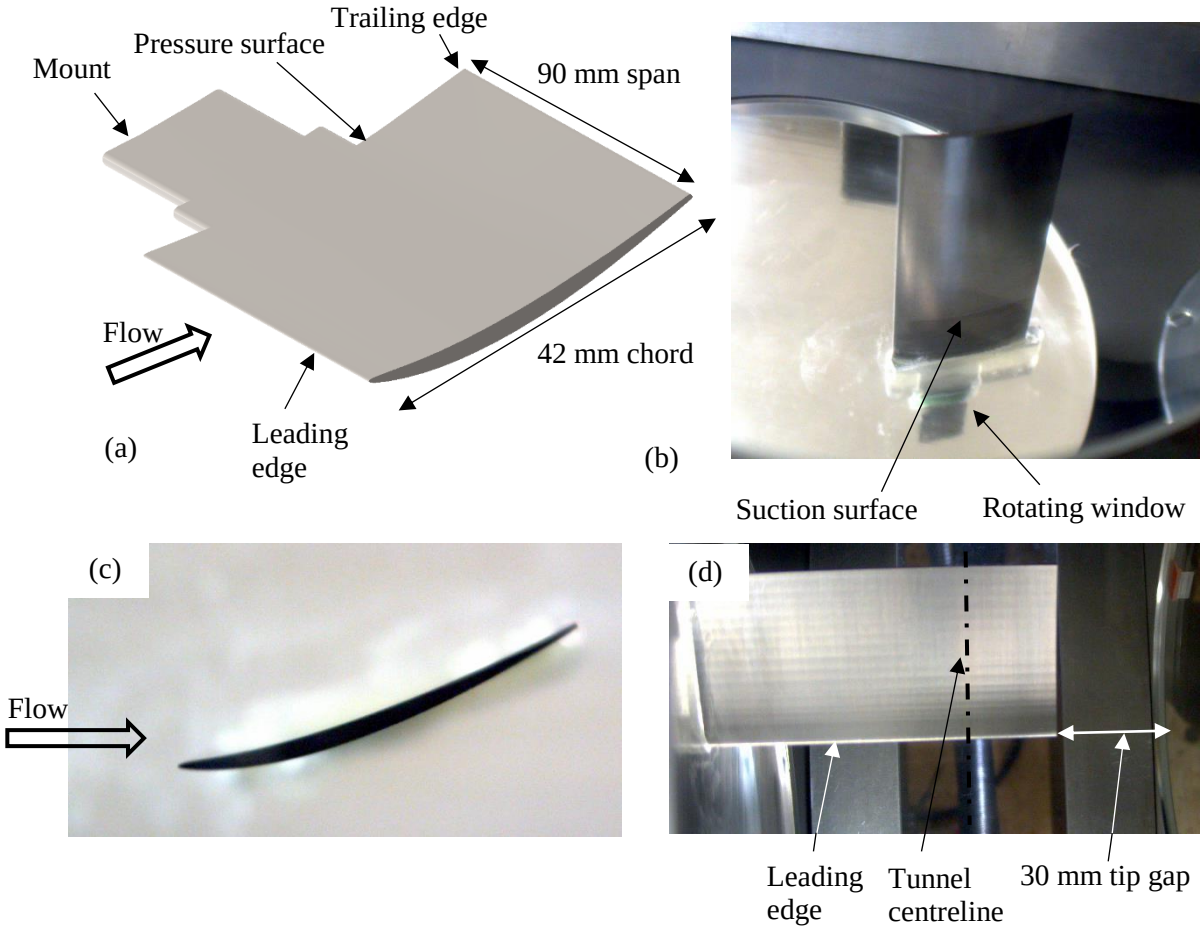

Fig. 3-10 (a) Isometric view of stator test article; (b) suction surface view when installed in RATFac; (c) side (tip) view and (d) top down view

A solid version and a version with a cutout on the suction surface were manufactured. The cutout was used to house thin film heaters and surface-mounted type-K thermocouples. The heaters were capable of delivering up to 60 kW/m^2 at 110 VAC, designed to be able to maintain the pressure surface at ~ 35

°C. Both versions were machined from solid Ti90-Al6-V4, with an as-machined roughness within the same RA range as the cone.

Simulations in ANSYS Fluent were again used to aid test piece design and to provide the necessary flowfield input to ICICLE. Fig. 3-11 shows the computational domain for the stator test article, and Fig. 3-12 contours of normalised axial velocity for a freestream inlet Mach number of =0.40. All other aerodynamic conditions are as given in Table 3-1. The meshing strategy, mesh independence study and numerical setup are given in Appendix A-2.

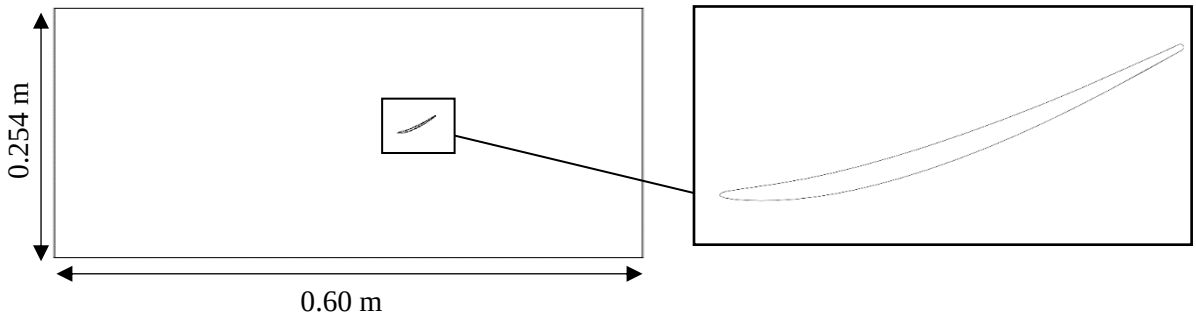

Fig. 3-11 Computational domain for stator test article, flow is left to right.

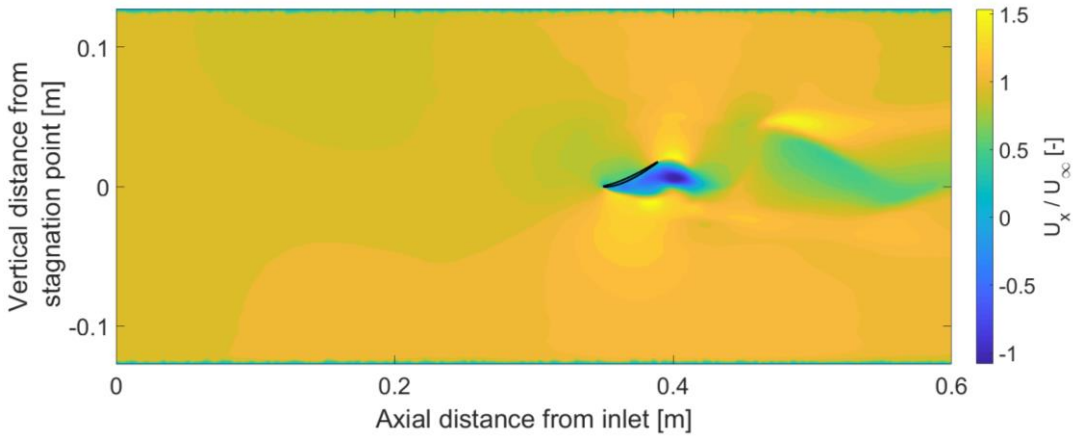

Fig. 3-12 Contours of axial velocity normalised by inlet freestream velocity

Since the stator is isolated (i.e. not in a cascade), it acts more as a bluff body, with early suction surface separation. This is not believed to be limiting for ice growth rate measurements since the leading edge and pressure surface are unaffected. Provided the flowfield and particle tracks can be predicted, then the stator can generate quantitative data for the geometric features of interest. Validation of the code with more realistic engine geometries – e.g. cascade or compressor module – will be more beneficial

after continued code development. It is further assumed that the two-dimensional flowfield presented here is representative of the real stator blade near midspan. Three-dimensional CFD was also performed using the correct tip gap to assess spanwise non-uniformities. Time-averaged spanwise velocity components did not exceed 5% of the axial component at the areas of interest (leading edge and pressure surface between midspan and the tunnel centreline).

Using the same two-point method as the cone, heat transfer coefficient data may be extracted from the simulations. Fig. 3-13 (a) shows the normalised axial velocity at the edge of the boundary layer over the stator surface for the Mach 0.40 simulation. Fig. 3-13 (b) shows the predicted heat transfer coefficient distribution. For the pressure surface, a correlation for an inclined flat plate with favourable pressure gradient (Motwani et al., 1985) is also plotted. The integrated difference is again within 10%.

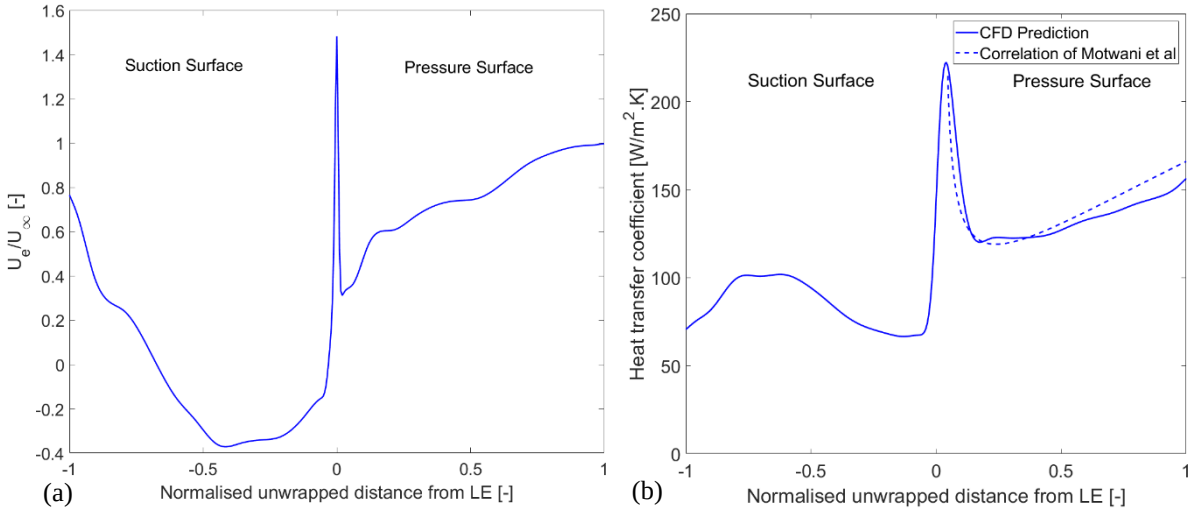

Fig. 3-13 (a) Normalised velocity distribution at edge of boundary level on the stator test piece. (b) CFD-predicted heat transfer coefficient distribution against streamwise location, with inclined flat plate correlation (Motwani et al., 1985)

The suction surface heat transfer coefficient data is relevant despite the fact that ice is not expected to form. The suction side is bathed in recirculating air, and therefore, depending on the amount of liquid water and water vapour in the cloud, will have a surface temperature somewhere between the local dry bulb and wet bulb static temperatures. It may be assumed that the surface temperature on the pressure surface is near 0 °C due to the ice formation. The suction surface-to-pressure surface heat transfer may therefore be significant - of the same order of magnitude as typical convective and evaporative heat fluxes if a 2 °C temperature difference exists over the blade, assuming one-dimensional conduction. If

an FEA model were to be implemented, this heat flux could be predicted more accurately, improving the fidelity of the thermodynamic accretion model. It may also aid shedding prediction, since the through-blade heat flux acts to warm the bond between the ice and pressure surface.

3.3 Summary

Having introduced the proposed structure for the new ice crystal icing code, ICICLE, and discussed the test cases that it will be applied to, it now remains to explore the modelling in detail. In chapter 4, particle shape and size treatment, trajectory and phase change models are explored. Particle-surface interaction is discussed in chapter 5, followed by a description of the new thermodynamic accretion model (EMM-C) in chapter 6.

4 Particle-Fluid Interaction

In the following sub-sections, modelling of particle size and shape parameters will be discussed, followed by selection of empirical correlations for drag coefficient and Nusselt number. These will be used to develop Lagrangian tracking and phase change models. Finally, a sensitivity analysis and assessment of two-way coupling is presented. Modelling will be framed in the context of both atmospheric ice particles and particles generated in the icing wind tunnels used in the project.

4.1 Particle Size Distribution Modelling

Ice particles, both in the atmosphere and icing wind tunnels, can vary in diameter by two to three orders of magnitude, from microns to millimetres. For non-spherical particles, the size is described by the equivalent diameter, D_{eq}, which is the diameter of a sphere with same volume as the particle. It is therefore desirable to statistically represent the particle cloud with a size distribution, which may then be randomly sampled to obtain an individual particle's equivalent diameter. The median mass diameter statistic in the distribution is then referenced to equivalent diameters, i.e. MMD is represented by MMD_{eq}.

Accurate representation of the particle size distribution is important for multiple elements of the model. Particle trajectory and impact location, melt percentage, probability of sticking, bouncing or shattering and capacity to erode accretions are obvious examples.

The most common type of distribution used is the Weibull distribution, termed the Rosin-Rammler distribution when applied to particulates (Rosin and Rammler, 1933). It is regularly used to describe distributions generated by liquid sprays and comminution processes (grinding, crushing or cutting). It is necessary to estimate the error incurred by using this distribution to represent both particles generated in an icing wind tunnel (e.g. by grinding an ice block) and atmospheric particles.

First, size data for atmospheric particles are taken from 'flight 13' and 'flight 16', conducted by the HAIC/HIWC consortia in 2014 (Leroy et al., 2017). Here, the uncertainty in the measured equivalent

diameter of each particle is reported as 5%. Flights 13 and 16 were conducted four days apart in two separate oceanic convective weather systems. Fig. 4-1 (a) shows the measured size distributions for flights 13 and 16, overlaid with their respective approximated Rosin-Rammler distributions. Particle diameter, D_{eq}, is plotted against the mass fraction of particles with a diameter less than D_{eq}. The parameters of the fitted distributions and the mean error for each flight are given in Table 4-1. It may be seen that the Rosin-Rammler distribution is capable of closely representing two quite dissimilar distributions. Further flight test data in both similar and dissimilar convective systems are still required to assess if this is robustly applicable. It is also instructive to consider how the PSD changes between the engine inlet and inlet to the IP or HP compressor. This provides a boundary condition for simulations considering only the core compression system. Safran S.A. used a Rosin-Rammler PSD with $MMD_{eq} = 400$ µm as the inlet icing cloud for a study of crystal ingestion (Aouizerate et al., 2018). In their study, the fan and single stage LP booster of a medium bypass ratio turbofan was modelled. A particle breakup and evaporation model first proposed by ONERA (Villedieu et al., 2014) was used to output the expected PSD at the fan face, downstream of the fan and downstream of the IGV. These data and fitted Rosin-Rammler distributions are shown in Fig. 4-1 (b). The accuracy of the fitted distributions is somewhat hampered by the limited number of bins in the dataset.

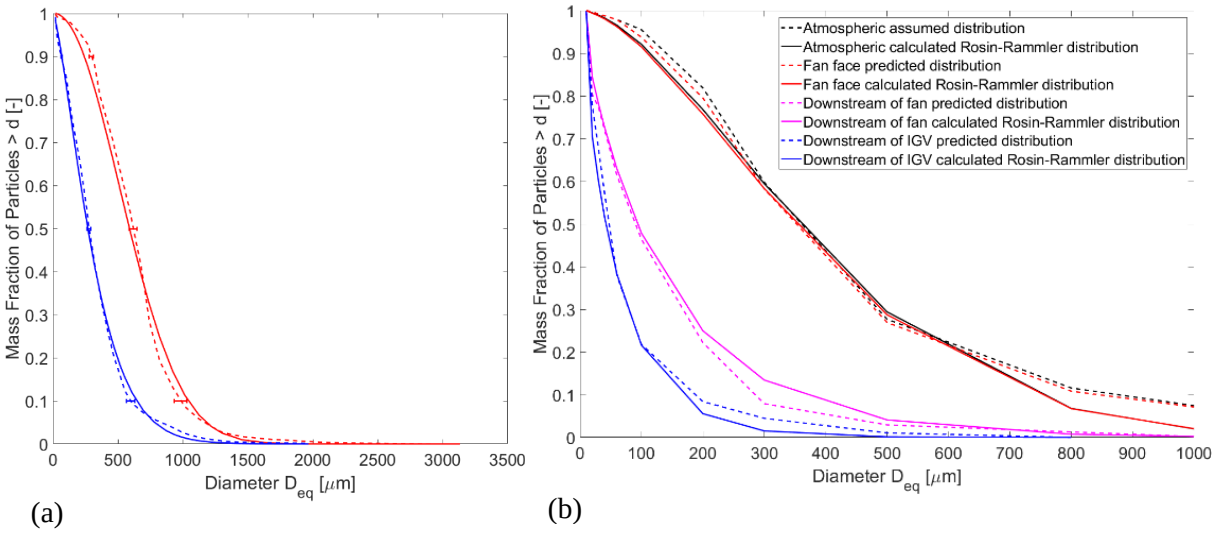

Fig. 4-1 Measured atmospheric PSDs (Leroy et al., 2017) and fitted Rosin-Rammler distributions; (b) predicted PSDs from the Safran ingestion and breakup model (Aouizerate et al., 2018) and fitted Rosin-Rammler distributions

Second, the applicability of Rosin-Rammler distributions to ice crystal clouds generated in icing wind tunnels is assessed. Experiments conducted on the cone and stator test articles used the ice grinder system at the NRC's Research Altitude Test Facility (RATFac). Variation of PSD was a key objective of the campaign. Fig. 4-2 shows measured distributions for three distinct PSDs, which were nominally termed 'small', 'baseline' and 'large'. The PSDs were measured using a Particle Image Velocimetry (PIV) system configured for shadowgraphy. Around 10,000 particles were sampled for each distribution, giving a mean uncertainty in the 10th, 50th and 90th percentiles of diameter of 0.73%, 1.51% and 2.90% respectively (shown as errorbars on Fig. 4-2). The parameters of the fitted distributions are also given in Table 4-1.

In Fig. 4-2, the error in mass fraction is substantial for the smallest particles in the distribution (below the 10th percentile). This is not necessarily significant, since it is demonstrated experimentally in chapter 5 that the rate of erosion (and hence rate of accretion growth) is most sensitive to the largest particles (represented by the $D_{v,max}$ statistic), even if particles of this size represent a very small mass fraction. For a fixed $D_{v,max}$, sensitivity to the smallest particles ($D_{v,10}$) is low. It is therefore more important to accurately model the right hand tail of the distribution.

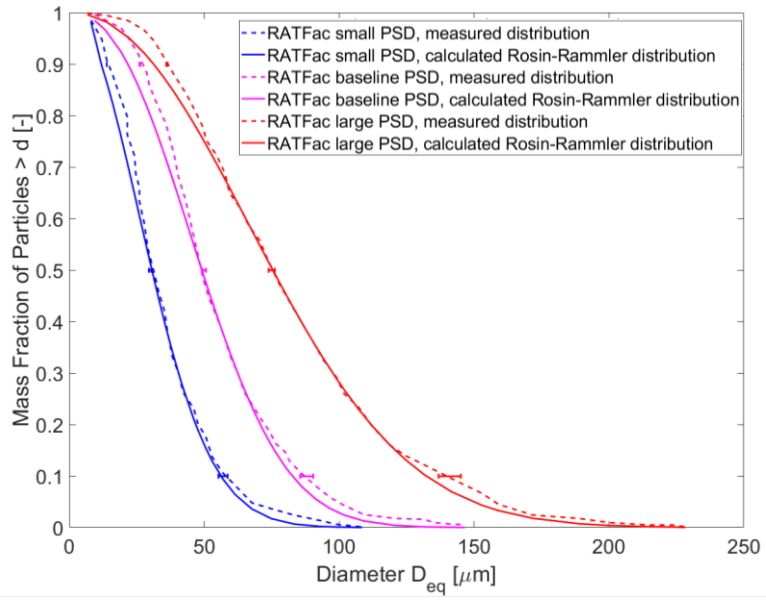

Fig. 4-2 Measured PSDs from the RATFac icing wind tunnel for the 'small', 'baseline' and 'large' configurations and fitted Rosin-Rammler distributions. Errorbars are plotted at the 10th, 50th and 90th percentiles.

Table 4-1 Parameters for Rosin-Rammler fits to HIWC/HAIC flight tests, Aouizerate et al. ingestion study and RATFac PSDs

Case	D_{min} $[\mu m]$	D_{max} $[\mu m]$	$\bar{D}$ $[\mu m]$	n	N_{bins}	*Mean error [%]*
Leroy et al., flight 13	13.6	3130	701	2.11	42	1.4
Leroy et al., flight 16	13.9	1970	351	1.37	42	1.3
Aouizerate et al., downstream of fan	10	3000	140	0.91	11	1.5
Aouizerate et al., downstream of IGV	10	800	62.7	0.92	9	2.3
RATFac 'small' PSD	7.80	109	36.9	1.99	32	2.6
RATFac 'baseline' PSD	9.40	186	57.6	2.31	39	2.5
RATFac 'large' PSD	13.5	233	89.6	2.14	39	1.3

4.2 Particle Shape Modelling

Atmospheric ice particles are inherently non-spherical. Icing wind tunnels that employ freezeout of water droplets may generate spherical particles; tunnels that use grinding processes do not. Therefore, treatment of particle shape requires equal consideration to particle size. The influence of shape in the current work is principally limited to trajectory and heat transfer. However, it has other effects: for example, it also determines how particles change orientation (e.g. tumbling, rolling).

4.2.1 Atmospheric Particle Shapes

Fig. 4-3 shows shadowgraphy images of particles, captured at various timepoints during flight 13 of the HAIC/HIWC flight trials in Darwin, Australia (Leroy et al., 2017). Columnar shapes are prevalent, along with a smaller proportion of more rounded particles. The capped columns (dumbbell shape) in particular present a significant future modelling challenge. To allow the development of a model, in the present work these are approximated as straight columns.

For two-dimensional images of irregular particles, aspect ratio is typically used to quantify shape, defined as the maximum dimension divided by the minimum dimension. In the dataset shown in Fig. 4-3, a mean aspect ratio of 0.45 is reported.

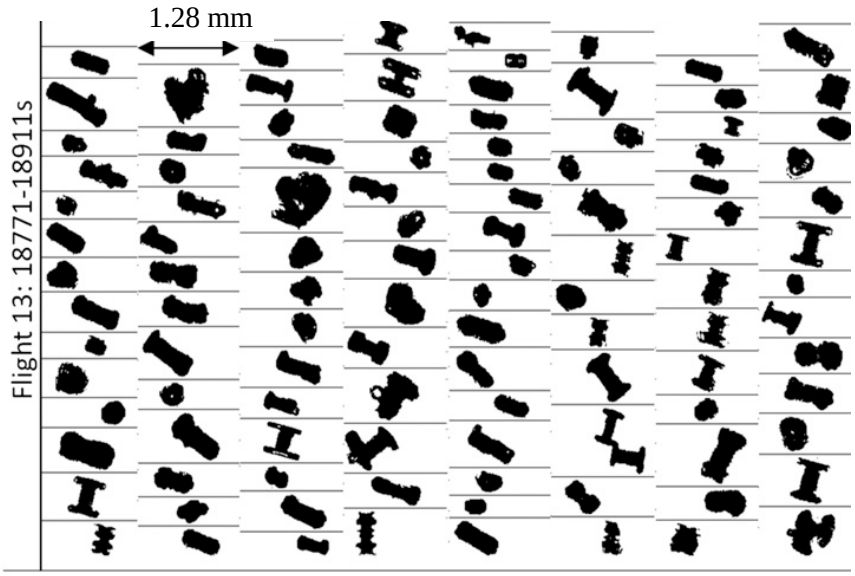

Fig. 4-3 Shadowgraph images of particles taken during HIWC/HAIC flight 13 (Leroy et al., 2017)

4.2.2 Research Altitude Test Facility (RATFac) Particle Shapes

Particles generated in the RATFac grinder system are typically non-spherical. Fig. 4-4 shows crystals captured in an oil film on a glass slide during early characterisation studies (Knezevici et al., 2011). It appears that faceted shapes – plates and shards – are common. Studies of particle shape were also performed in RATFac using a Particle Image Velocimetry (PIV) system configured for shadowgraphy (Fuleki et al., 2015). It was reported that particles of 40 µm D_{v50} had a mean aspect ratio of 0.7.

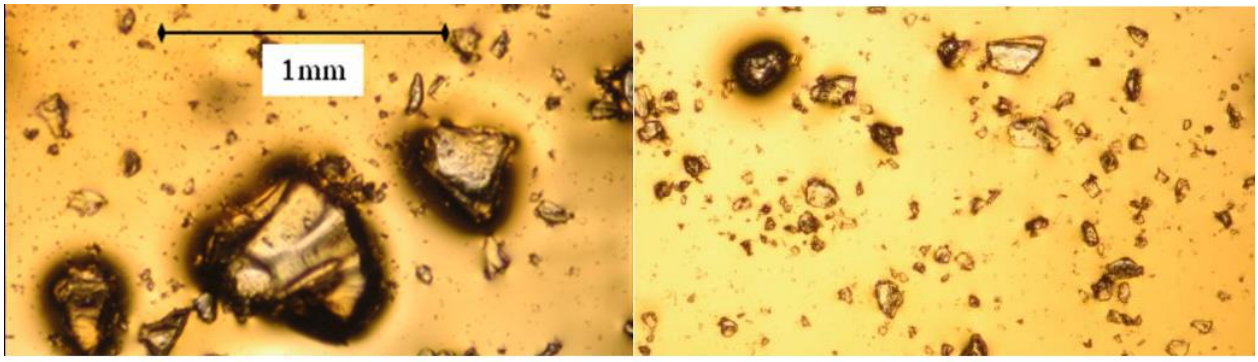

Fig. 4-4 Ice particles from the RATFac grinder captured on an oil slide (Knezevici et al., 2011)

4.2.3 Approximation as Spheroids

Common ice particle shapes comprise plates, discs and columns; it is possible to approximate all as spheroids to a varying degree of accuracy. The attraction of this approach is that a single set of equations defines the particle shape and geometric parameters, and for a given equivalent diameter, D_{eq}, the shape is then defined solely by aspect ratio, E. To generate a range of particle shapes, a suitable distribution of aspect ratios may be randomly sampled. Fig. 4-5 shows the geometry of oblate and prolate spheroids.

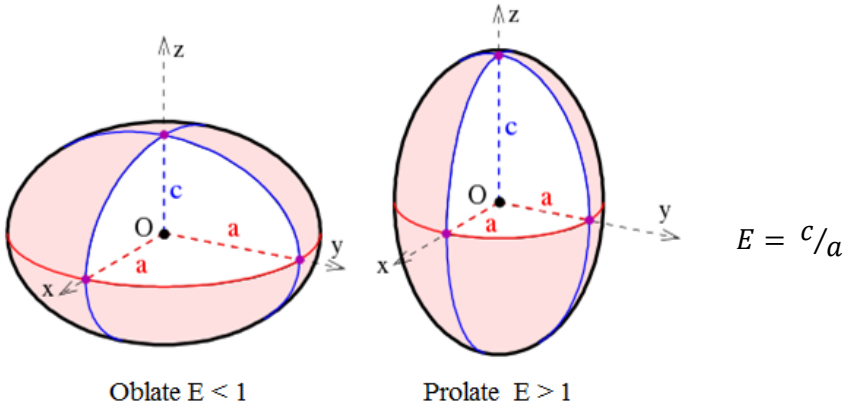

Fig. 4-5 Geometry of oblate and prolate spheroids of aspect ratio E

Aspect ratio, E, is given as $E = {}^{c}/_{a}$ where c and a are the length from centre to pole and equatorial radius respectively. The volume and surface area are given by

$$V_p = V_{eq} = \frac{\pi}{6} {D_{eq}}^3 = \frac{4}{3}\pi a^2 c = \frac{4}{3}\pi a^3 E \tag{4-1}$$

$$A_{oblate} = 2\pi a^2 \left(1 + \frac{c^2}{2ea^2} \ln\left(\frac{1 + e_{oblate}}{1 - e_{oblate}}\right)\right) \tag{4-2}$$

$$A_{prolate} = 2\pi a^2 \left(1 + \frac{c}{ea} \sin^{-1}(e_{prolate})\right) \tag{4-3}$$

where

$$e_{oblate} = \sqrt{1 - {}^{c^2}/_{a^2}} \quad ; \quad e_{prolate} = \sqrt{1 - {}^{a^2}/_{c^2}} \tag{4-4}$$

More simply,

$$e = \sqrt{1 - \min(E^2, {}^1/_{E^2})} \tag{4-5}$$

In chapter 2 sphericity, given by $\varphi = \frac{\pi {D_{eq}}^2}{A_p}$, and crosswise sphericity, $\varphi_\perp = \frac{\pi/_4 {D_{eq}}^2}{A_{p,\perp}}$, were introduced. Substituting equations (4-1) to (4-3) into these relations provides

$$\varphi_{oblate} = \frac{4E^{\frac{2}{3}}}{2 + {E^2}/_e \ln\left(\frac{1+e}{1-e}\right)} \quad ; \quad \varphi_{\perp,oblate} = {E^2}/_3 \tag{4-6}$$

$$\varphi_{prolate} = \frac{2E^{2/3}}{1 + \mathrm{E}(\frac{\sin^{-1} e}{e})} \quad ; \quad \varphi_{\perp,prolate} = {E^{-1}}/_3 \tag{4-7}$$

where the crosswise sphericities are calculated assuming broadside travel. The equations for sphericity asymptote to unity as $e \rightarrow 0$.

Given E and D_{eq}, equation (4-1) gives a. All other parameters then follow. Within ICICLE, a Rosin-Rammler distribution or mono-disperse particle size distribution may be specified. The distribution is then randomly sampled to obtain D_{eq} for each particle. For aspect ratio, a constant, linear distribution, or normal distribution may be specified, which again is randomly sampled per particle.

4.3 Lagrangian Particle Tracking

A force balance is conducted on each particle to determine its trajectory in the next timestep (equation 4-8). The particle acceleration is held constant over the timestep, so equations of motion are used to calculate velocity and position in three dimensions (equations 4-9 and 4-10 respectively).

$$\sum \vec{F}_{x,i} = m_p \frac{d\vec{U}_{p,x}}{dt} \tag{4-8}$$

$$\vec{U}_{p,x,t+1} = \vec{U}_{p,x,t} + \vec{a}_{p,x,t} t_t \tag{4-9}$$

$$\vec{s}_{p,x,t} = \vec{U}_{p,x,t} t_t + {}^1/_2 \, \vec{a}_{p,x,t} {t_t}^2 \tag{4-10}$$

where $\vec{F}_{x,i}$ is the i[th] force term in the $\vec{x}$ direction, and $\vec{a}$ $\vec{U}$, $\vec{s}$ are the acceleration, velocity and displacement in the same direction. For simplicity, the explicit Euler method of time integration is used throughout ICICLE.

A spatially adaptive timestep is used to limit particle travel:

$$t_t = K_t \left({}^{d_{min}}/_{U_t} \right) \tag{4-11}$$

where U_t is the local velocity magnitude, d_{min} is the smallest grid cell dimension in the domain, and K_t is a user-defined constant. The lower the value of K_t, the higher the trajectory accuracy (at a penalty of computational cost). A sensitivity analysis to K_t is given in chapter 7.

4.4 Lagrangian Force Balance

It is stated in chapter 2 that the particle forces considered are gravity and drag.

4.4.1 Gravity

The net gravitational force on the particle is the sum of the weight and buoyancy forces:

$$-\vec{F}_{z,g} = -m_p \vec{a}_{p,z,t} = \rho_p V_p g - \rho_f V_f g \tag{4-12}$$

where g is acceleration due to gravity, 9.81 m/s^2, and V_f, the volume of displaced fluid, is equal to the particle volume V_p. By convention, z is taken as vertically upwards. Therefore:

$$-m_p \vec{a}_{p,z,t} = -\rho_p V_p \vec{a}_{p,z,t} = g V_p (\rho_p - \rho_f) \quad ; \quad \vec{a}_{p,z,t} = -g \, \frac{(\rho_p - \rho_f)}{\rho_p} \tag{4-13}$$

Since $\rho_p \gg \rho_f$, it assumed that $\vec{a}_{p,z,t} = -g$.

The relative importance of the gravitational force to the viscous force may be assessed using the Galilei number (Uhlmann and Doychev, 2014):

$$Ga = \frac{U_g D}{\nu} = \frac{U_g D}{\nu} \tag{4-14}$$

where U_g is the settling velocity. This may be derived from balancing drag and net gravitational force:

$$\rho_f {U_g}^2 D^2 = (\rho_p - \rho_f) D^3 g \tag{4-15}$$

where the D is the characteristic dimension.

Therefore:

$$U_g = \sqrt{\left(\rho_p / \rho_f - 1\right) D\, g} \tag{4-16}$$

Setting $D = D_{eq} = 20\ \mu m$, $Ga = 0.2$, indicating that viscous forces dominate over gravitational forces. Furthermore, inertial forces are expected to dominate over viscous forces since the particle Reynolds number $Re_p \gg 1$ at typical ice crystal icing conditions.

4.4.2 Drag

For a particle travelling at velocity $\vec{U}_{p,x}$ in a fluid of local velocity $\vec{U}_{f,x}$, the drag force is given by

$$\vec{F}_{d,x} = -\frac{1}{2}\rho_f C_D\, A_{p,\perp} \left|\vec{U}_{p,x} - \vec{U}_{f,x}\right| (\vec{U}_{p,x} - \vec{U}_{f,x}) \tag{4-17}$$

Using the definition of crosswise sphericity to substitute for the projected particle area, $A_{p,\perp}$

$$\vec{F}_{d,x} = -\frac{\pi}{8}\rho_f C_D\, \frac{{D_{eq}}^2}{\varphi_\perp} \left|\vec{U}_{p,x} - \vec{U}_{f,x}\right| (\vec{U}_{p,x} - \vec{U}_{f,x}) \tag{4-18}$$

In chapter 2, the following drag correlation was selected (Holzer and Sommerfeld, 2008):

$$C_D = \frac{8}{Re_p}\frac{1}{\sqrt{\varphi_\perp}} + \frac{16}{Re_p}\frac{1}{\sqrt{\varphi}} + \frac{3}{\sqrt{Re_p}}\frac{1}{\varphi^{0.75}} + 0.42\left(10^{0.4(-log_{10}(\varphi))^{0.2}}\right)\frac{1}{\varphi_\perp} \tag{4-19}$$

4.5 Heat Transfer & Phase Change Theory

Fig. 4-6 shows a schematic of the heat and mass transfer processes for an ice particle moving through a fluid. For now, one-way coupling is assumed – i.e. mass, momentum and energy of the continuous

phase is unaltered by the discrete phase. The necessity for two-way coupling is assessed in Section 4.7.

A notional ice particle of arbitrary shape is approximated as a spheroid of the same volume, equivalent diameter, D_{eq}, and initial aspect ratio E_0. The particle has uniform internal temperature T_p. Initially fully glaciated, the particle temperature increases until it reaches the melting temperature T_f. During the fully glaciated phase, aspect ratio remains held at E_0 but D_{eq} can change due to sublimation or deposition. During the melting phase, a concentric water layer surrounds an ice core, with volumes $V_{p,i}$ and $V_{p,w}$ respectively. The particle temperature is fixed at T_f in both the ice and water layers. The latent heat of fusion required for melting is balanced by evaporative and convective heat fluxes. During melting, the particle aspect ratio monotonically approaches unity (Villedieu et al., 2014), on the assumption that when the particle is fully melted it is a spherical droplet. Once fully melted, the temperature is allowed to rise once again, and aspect ratio is held at unity.

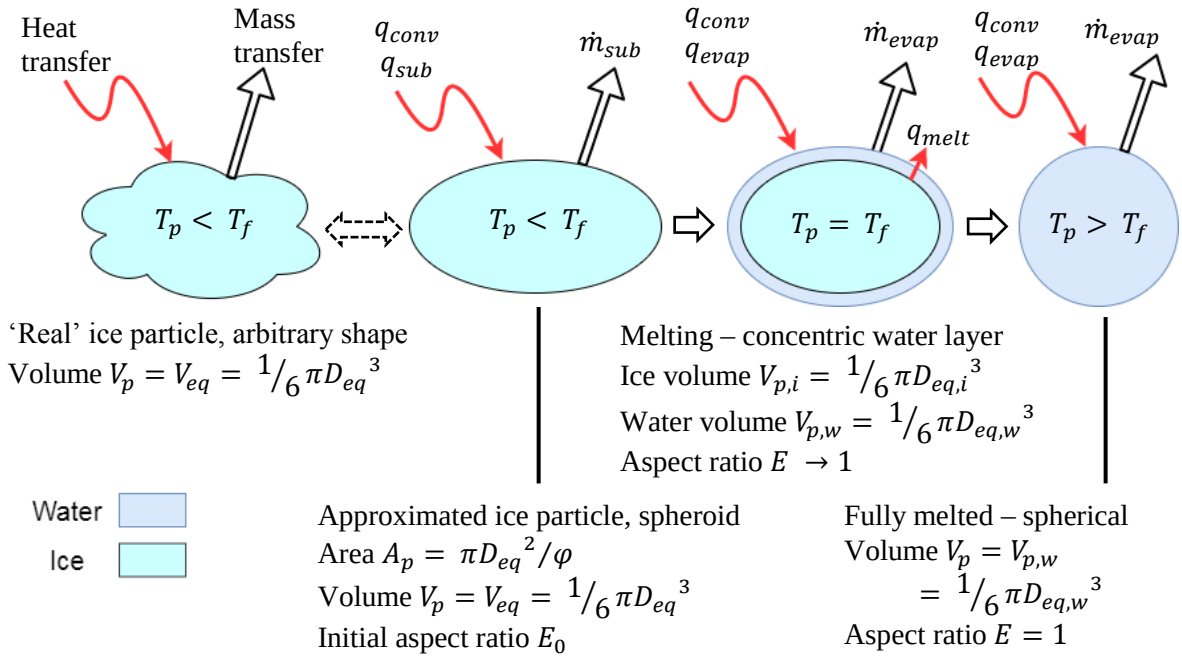

Fig. 4-6 Schematic of the melting process of an ice particle of arbitrary shape

Calculation of the heat fluxes due to convection and evaporation or sublimation requires the heat transfer and mass transfer coefficients to be calculated respectively, or in their non-dimensional forms, Nusselt number and Sherwood number. This is detailed in the following sections.

4.5.1 Nusselt Number Correlation

In chapter 2, the following correlation was selected for the average Nusselt number on a non-spherical particle (Villedieu et al., 2014):

$$\overline{Nu} = 2\sqrt{\varphi} + 0.55\, Pr^{1/3}\varphi^{1/4}\sqrt{Re_p} \tag{4-20}$$

This is validated against literature data up to particle Reynolds numbers of ~ 200. For extremely large particles of 1000 μm equivalent diameter, this limits slip velocity to below ~8 m/s. For the more commonly used particle sizes of ~ 10 – 60 μm, slip velocities can increase to ~ 130 m/s without exceeding the bounds of applicability. Since flow velocities typically chosen in an icing wind tunnel are around 80 – 160 m/s, this restriction is not expected to be limiting. It is also unlikely to be limiting in the freestream environment of an IP compressor – where flow velocities are typically in the range 100 – 200 m/s. Exceptions to this could be particles that have recently been impacted by a rotor blade, or particles that have remained exceptionally large (> 60 μm).

Equation (4-20) is also valid for aspect ratios within the range $0.2 < E < 2$. These limits will be applied to particles injected into the domain.

4.5.2 Sherwood Number Correlation

The mass transfer coefficient or Sherwood number is not generally known a-priori, so a heat-mass transfer analogy is used. A Chilton-Colburn analogy factor for laminar flow is assumed, since the use of equation (4-20) requires sub-critical flow. The analogy factor is given by

$$\frac{Sh}{Nu} = f\left(\frac{Sc}{Pr}\right) = \left(\frac{Sc}{Pr}\right)^{1/3} \tag{4-21}$$

where Sc is the Schmidt number. Substituting for Nu in equation (4-20) produces the correlation for Sherwood number:

$$\overline{Sh} = 2\sqrt{\varphi} + 0.55\, Sc^{1/3}\varphi^{1/4}\sqrt{Re_p} \tag{4-22}$$

and is applied within the same limits of applicability as equation (4-20).

4.5.3 Phase Change Prerequisites

The convective heat flux is given by:

$$Q_{conv} = A_p \, \overline{H} \, (T_f - T_p) \tag{4-23}$$

where H is the average heat transfer coefficient, and T_f is the local flow temperature. Substituting particle area A_p using sphericity, and noting that $\overline{H} = \overline{Nu} \, k_f \big/ D_{eq}$

$$Q_{conv} = \frac{\pi {D_{eq}}^2}{\varphi} \frac{\overline{Nu} \, k_f}{D_{eq}} \left(T_f - T_p\right) = \frac{\pi D_{eq}}{\varphi} \, \overline{Nu} \, k_f \left(T_f - T_p\right) \tag{4-24}$$

where k_f is the local thermal conductivity in the fluid. The flow temperature local to the particle is taken as

$$T_f = T_s \left(1 + r_f \frac{\gamma_f - 1}{2} {M_{rel}}^2\right) \tag{4-25}$$

where the recovery factor, $r_f \cong Pr^{1/3}$ (Chung, 1973), T_s is the local static temperature and M_{rel} is the particle Mach number based on slip velocity. This equation yields $T_f = T_s$ when $M_{rel} = 0$ (i.e. no slip) and $T_f = T_r$ when $M_{rel} = M_\infty$ (stationary particles), where T_r is the recovery temperature.

The heat flux due to evaporation is given by

$$\begin{aligned} Q_{evap} = L_v \dot{m}_{evap} = L_v A_p H_m \rho_f \left(\omega_p - \omega_\infty\right) &= L_v \, \frac{\pi {D_{eq}}^2}{\varphi} \overline{Sh} \, \frac{\rho_f D_{v,a}}{D_{eq}} \left(\omega_p - \omega_\infty\right) \\ &= L_v \, \frac{\pi D_{eq}}{\varphi} \overline{Sh} \, \rho_f D_{v,a} \left(\omega_p - \omega_\infty\right) \end{aligned} \tag{4-26}$$

where $\dot{m}_{evap}$ is the evaporating massflow (kg/s), H_m is the mass transfer coefficient, L_v is the latent heat of vaporisation, and $D_{v,a}$ is the vapour diffusivity in air. The driving mass difference is given by the term $\left(\omega_\infty - \omega_p\right)$ where ω_∞ and ω_p are the vapour mass fractions in the local freestream and at the particle surface respectively. The heat flux during sublimation, q_{sub}, is obtained by replacing L_v with $L_s = L_v + L_f$ where L_f is the latent heat of fusion. The vapour diffusivity is given by

$$D_{v,a} = D_0 \left(\frac{P_{ref}}{P_e}\right)\left(\frac{T_e}{T_{ref}}\right)^{1.81} \tag{4-27}$$

where D_0 = 22.6 x10^{-6} m/s^2, P_{ref} = 101.3 kPa, T_{ref} = 273.15 K, and P and T are the local static pressure and temperature respectively (Hauk et al., 2016).

Using Dalton's law of partial pressures,

$$\omega = \frac{\dot{m}_{vap}}{\dot{m}_{dry\ air}} = \frac{M_w}{M_a}\frac{\dot{n}_{vap}}{\dot{n}_{dry\ air}} = \frac{M_w}{M_a}\frac{P_{vap}}{P_{dry\ air}} = \frac{M_w}{M_a}\frac{P_{vap}}{P - P_{vap}} \tag{4-28}$$

where $\dot{n}_{vap}$ and $\dot{n}_{dry\ air}$ are the molar fluxes of water vapour and dry air respectively, M_w and M_a are the molar masses of water and dry air respectively and P is the local static pressure. P_{vap} is the partial pressure of vapour, given by

$$P_{vap} = RH\ P_{vap,sat} \tag{4-29}$$

where RH is the local relative humidity ($RH = 1$ at the particle surface and $RH \leq 1$ in the freestream), and $P_{vap,sat}$ is the local vapour pressure at saturation. This is calculated from the correlation given in Appendix E-2 (Hyland and Wexler, 1983).

4.5.4 Phase Change Model

In the first stage, the continuity and energy equations are given respectively by

$$\frac{dm_p}{dt} = -\dot{m}_{sub} \quad ; \quad m_{p,i} = m_p \quad ; \quad m_{p,w} = 0 \tag{4-30}$$

$$m_p c_{p,i} \frac{dT_p}{dt} = Q_{conv} - \dot{m}_{sub} L_s \tag{4-31}$$

and aspect ratio is held constant at $E = E_0$. The particle mass is given by $m_p = \rho_i \frac{\pi {D_{eq}}^3}{6}$, where ρ_i is the density of ice, taken as 920 kg/m^3.

In the second stage, the particle is in the process of melting and $T_p = T_f$. The continuity and energy equations are given respectively by

$$Q_{conv} = \dot{m}_{evap} L_v + \dot{m}_{melt} L_f \tag{4-32}$$

$$\frac{dm_p}{dt} = -\dot{m}_{evap} \;\; ; \;\; \frac{dm_{p,i}}{dt} = -\dot{m}_{melt} \;\; ; \;\; m_{p,w} = m_p - m_{p,i} \tag{4-33}$$

The ice and water masses are related to their equivalent diameters by

$$m_{p,i} = {}^{\pi}/_{6}\, \rho_i {D_{eq,i}}^3 \qquad ; \qquad m_{p,w} = {}^{\pi}/_{6}\, \rho_w {D_{eq,w}}^3 \tag{4-34}$$

where ρ_w is the density of pure water, taken as 1000 kg/m^3. The particle melt ratio is given by

$$MR = \frac{m_{p,w}}{m_p} \tag{4-35}$$

The particle shape is assumed to approach spherical as the melt ratio approaches unity (Hauk et al., 2016). The following model is used to calculate the aspect ratio at any point in the melting process:

$$E^2 = (1 - MR){E_0}^2 + MR \tag{4-36}$$

In the third stage, the continuity and energy equations are given respectively by

$$m_p c_{p,w} \frac{dT_p}{dt} = Q_{conv} - \dot{m}_{evap} L_v \tag{4-37}$$

$$\frac{dm_p}{dt} = -\dot{m}_{evap} \;\; ; \;\; m_{p,w} = m_p \;\; ; \;\; m_{p,i} = 0 \tag{4-38}$$

and aspect ratio is held constant at $E = 1$. The particle mass is given by $m_p = \rho_w \frac{\pi {D_{eq}}^3}{6}$.

4.5.5 Validation of Phase Change Model

Validation of the phase change model is possible using the data recorded during the RATFac test campaigns. For each test condition, the relative humidity (and hence total wet bulb temperature) was adjusted until the bulk melt ratio (= LWC/TWC) approximately matched a target value.

Simulations of the RATFac tunnel were run in ICICLE using the baseline aerodynamic conditions given in chapter 3. 10,000 particles were simulated using the baseline particle size distribution (34 μm D_{v50}) and a constant aspect ratio of 0.70.

Table 4-2 shows five test conditions of varying relative humidity, their respective measured melt ratios and an average melt ratio predicted by ICICLE at the same axial location.

Table 4-2 Measured and predicted melt ratio at LWC measurement plane for four test conditions

Condition reference	RH_0 [-]	TWB_0 [°C]	*Melt ratio: experiment* [-]	*Melt ratio: ICICLE* [-]	*Difference (absolute)* [-]
TR728	0.05	-6.37	0.010	0.00	-0.010
TR730	0.15	-3.33	0.022	0.00	-0.022
TR737	0.45	2.64	0.10	0.070	-0.030
TR740	0.65	5.16	0.17	0.14	-0.030

It has been discussed previously that the probe responsible for reading LWC, the Science Engineering Associates (SEA) multiwire, gives a spurious LWC reading when in fully glaciated conditions, attributed to ice particles bouncing off the heated wires. All of the measured melt ratios in Table 4-2 have already been corrected for the false response; however for conditions TR728 and TR730, there remains a small measured melt ratio at significantly negative total wet bulb temperatures (where melting is assumed to be inhibited). The measured values of 0.010 and 0.022 are within the scatter of the false response data (as presented in chapter 5), so are not further considered.

For cases 737 and 740, the model underpredicts the melt ratio at the probe plane by around 3%. This means the model will *overpredict* the total melt time. On the assumption that the aerodynamic conditions are well known and well controlled, then particle size and shape modelling is more likely to be the cause of the discrepancy. The size distribution below the 10^{th} percentile is not known; if there is a significant negative skew in the actual PSD, (a higher concentration of smaller particles), then the measured melt ratio will be higher. Further, if the aspect ratio assumed in the model is too high, then the predicted melt ratio will be lowered. Reducing the initial aspect ratio from 0.7 to 0.5 decreases the difference to within 1% for both cases. Modelling the particles as spheroids also introduces errors;

especially if there is a predominance of slivers or shards with exceptionally high surface area-to-volume ratios, or porous conglomerates of small particles.

4.6 Model Sensitivity

The relative sensitivity of a model to each of its inputs may be assessed by comparing perturbations in the model output for a standard perturbation in each of its inputs. This approach is applied here to the drag and phase change models. The inputs considered, their assumed nominal values and a typical uncertainty or error for each are given in Table 4-3. The latter is taken as the measurement uncertainty in the Research Altitude Test Facility (RATFac), or the known error in a fitted correlation. They may equally be substituted for a known uncertainty in the engine environment or in measured atmospheric conditions. Most modelling effort should be put into inputs with both a high sensitivity and a high uncertainty.

Table 4-3 Input parameters and their baseline values used in sensitivity analysis

Parameter	*Models*	*Baseline value*	*Representative uncertainty (absolute)*
D_{eq} $[\mu m]$	Drag & phase change	40	2.2
Aspect ratio, E $[-]$	Drag & phase change	0.70	0.20
Sphericity, φ $[-]$	Drag & phase change	0.977	0.020
Crosswise sphericity, $\varphi_{\perp}$ $[-]$	Drag & phase change	0.788	0.015
Specific humidity, SH $[kg_{vap}/kg_a]$	Phase change	0.0119	0.00020
$P_{vap,sat}$ $[Pa]$	Phase change	1800	18

4.6.1 Sensitivity in Drag Model

If particles are assumed spheroidal, sphericity and crosswise sphericity are not input parameters, rather derived parameters from the aspect ratio, E. If particles were *not* spheroids, sphericity and crosswise sphericity would be explicit input parameters. They are considered here as inputs so that the sensitivity to the error incurred by making the spheroidal assumption may be understood. The monitored output

was chosen to be particle acceleration. Unlike the subsequent calculations of velocity and displacement, it is independent of timestep.

Fig. 4-7 (a) shows the perturbation in acceleration for a positive and negative 5% perturbation in each of the inputs (equivalent diameter, aspect ratio, sphericity and crosswise sphericity). The particle equivalent diameter gives (marginally) the largest combined output perturbation. It is instructive to consider how the perturbation at input propagates to the output. In this case, the input propagates through the Reynolds number, drag correlation, and drag force calculations in turn to the acceleration calculation. Fig. 4-7 (b) shows how each of these calculations is perturbed by each of the input perturbations.

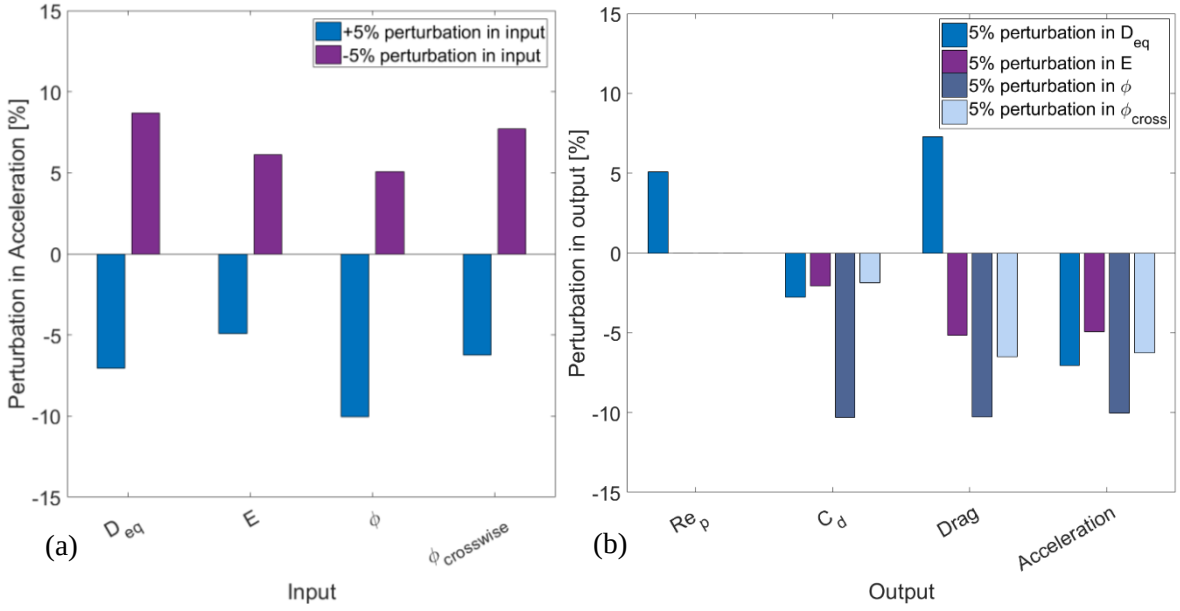

Fig. 4-7 (a) Perturbation in particle acceleration due to 5% perturbations in each of the inputs of the drag model. (b) Perturbations in key derived parameters of the drag model for perturbations in each of the chosen inputs.

The sensitivity of drag coefficient to equivalent diameter is (relatively) small compared to that of drag, which is proportional to $D_{eq}{}^2$. This is in turn overcome in the acceleration equation by the inverse proportionality with particle mass, and hence $D_{eq}{}^3$. It can be seen that drag coefficient is most sensitive to sphericity, with a 5% perturbation in sphericity resulting in a ~10% perturbation in C_d. This perturbation is then maintained through the drag and acceleration calculations. In contrast, drag coefficient is relatively insensitive to crosswise sphericity, but this increases in the drag calculation

due to the $1/\varphi_{\perp}$ term in equation (4-18). The lowest sensitivity in acceleration is due to the spheroid aspect ratio, E, the chosen parameter for defining shape. This is encouraging; however, a particle which is poorly approximated as a spheroid, thus inducing errors in sphericity and crosswise sphericity, will incur the higher sensitivities to these parameters.

4.6.2 Sensitivity in Phase Change Model

For the phase change model, a new output parameter was created, termed the Mass Flux Ratio (MFR). This is defined as

$$MFR = \frac{\dot{m}_{melt}}{\dot{m}_{evap}} \tag{4-39}$$

Particle melt ratio (MR) is a critical parameter as it affects the particle trajectory and surface interaction (sticking, bouncing, splashing). However, it is also residence time dependent and thus not useful outside of a particular wind tunnel at a particular aerodynamic condition. Equation (4-39) may be seen as a similar ratio to MR, with the numerator and denominator being time derivatives of their counterparts in the MR equation. Further, it is independent of both residence time and timestep.

Fig. 4-8 (a) shows the perturbation in the phase change model output (MFR) for a positive and negative 5% perturbation in each of the inputs. The highest sensitivities are clearly to psychrometrics – saturation vapour pressure and specific humidity – and not particle shape or size. The largest single perturbation at output is due to a 5% reduction in specific humidity. This perturbation results in the evaporative mass flux reducing by a factor of 2.2, compared to a reduction of 1.5 times in the melting mass flux. The sensitivity is particularly high on the -5% side since the evaporative mass flux approaches zero, inducing a large percentage change.

Fig. 4-8 (b) shows how the +5% perturbations in equivalent diameter, aspect ratio, sphericity and crosswise sphericity propagate to MFR, through the Reynolds number (Re), Nusselt number (Nu), and Sherwood number (Sh) calculations. Since the equations of Nusselt and Sherwood numbers are equivalent through the Reynolds analogy, the perturbation in equivalent diameter produces near-equal

perturbations in Nu and Sh. Since MFR is proportional to the Nu/Sh, the perturbation in MFR due to equivalent diameter is negligible.

The Nusselt and Sherwood number correlations do not explicitly contain crosswise sphericity, so there is no sensitivity to a perturbation in this parameter alone. Similarly to the drag model, sensitivity to spheroid aspect ratio is low in comparison to sphericity (albeit also low in absolute terms). There is a dependence on $1/\varphi$ in both the convective and evaporative mass flux terms (equations (4-24) and (4-26) respectively). Again, therefore, a particle poorly approximated as a regular shape is liable to the high sensitivity in sphericity.

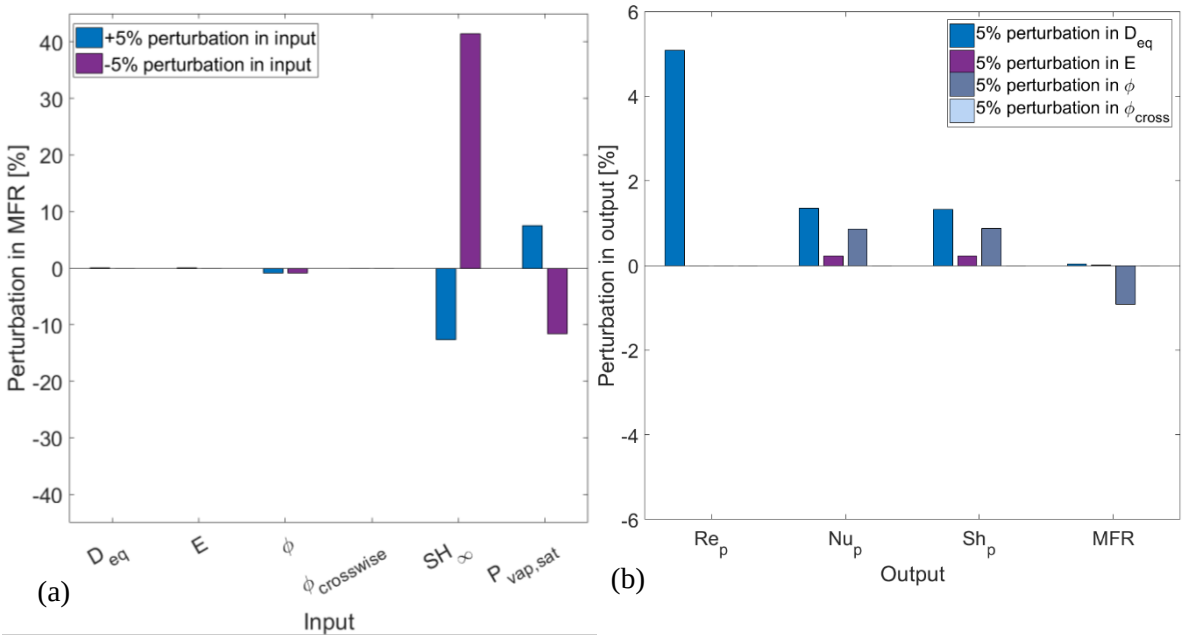

Fig. 4-8 (a) Perturbation in Mass Flux Ratio (MFR) due to 5% perturbations in each of the inputs of the phase change model. (b) Perturbations in key derived parameters of the phase change model for perturbations in each of the chosen inputs.

4.7 Quasi Two-Way Coupling

Thus far, a one-way coupled approach has only been considered. This means that the continuous (fluid) phase may change properties of the discrete (particle) phase, but not vice versa. A general assessment of coupling in a simple axial compressor in ice crystal icing conditions is given in Wright et al., (2010). Mass and momentum coupling are neglected on the basis that the mass loading fraction, $Z = {TWC}/{\rho_a} \ll 1$.

Energy coupling requires more careful consideration. It may be neglected if the following inequality is satisfied (Crowe et al., 2011):

$$\frac{Z}{St_m}\frac{L_{sub}}{C_{p,i}T} \ll 1 \tag{4-40}$$

where the mass transfer Stokes number is given by

$$St_m = \frac{\tau_m U_p}{L} \tag{4-41}$$

where U_p is an average particle velocity, L is a residence length (i.e. tunnel length or compressor length), and the mass transfer relaxation time is given by

$$\tau_m = \frac{\rho_i {D_{eq}}^2}{6\, Sh\, \rho_a D_{v,a}(\omega_p - \omega_\infty)} \tag{4-42}$$

Equation (4-40) therefore states that energy coupling is important in cases of high mass loading, low mass transfer Stokes numbers (thus a low time constant over which mass transfer occurs) and high ratio of latent heat to sensible warming heat. For the validation tests conducted in RATFac, $TWC = 8$ g/m^3, $L \cong 1$ m, $U_p \cong 100$ m/s and $D_{eq} = 40$ μm. Sherwood number is taken as 4.5, and $(\omega_p - \omega_\infty)$ as 0.01. Equation (4-40) may then be evaluated as 0.0048, thus implying that energy coupling is unimportant.

In Wright et al., (2010), equation (4-40) is evaluated for a multistage compressor as a more marginal value of 0.1. In-service data from Rolls-Royce Trent 500 engines (amongst other types) show that the compressor delivery temperature (referred to as T30) can reduce during an ice crystal encounter (and may suffer a spike reduction if there is an ice shed). The reduction in T30 has been used as an indication of when the aircraft entered the ice crystal cloud, although this may be obscured by a transient reduction at top of descent (Jones, 2015b). Use of T30 as an ice crystal detection parameter has been proposed by General Electric Aviation (Califf and Knezevici, 2014). It is therefore apparent that in the 'real' engine environment, energy coupling cannot be neglected.

In AGARD advisory report AR-332 ("*Recommended Practices for the Assessment of the Effects of Atmospheric Water Ingestion on the Performance and Operability of Gas Turbine Engines"*), it is stated that an increase in humidity can also appreciably affect engine performance due to changing fluid properties (AGARD, 1995). It is stated that the parameters with the largest effects are the increasing gas constant, R_f, and the isentropic exponent, γ_f. The latter decreases from its dry air value of 1.4 towards the gaseous water value of 1.333. Both these changes cause the specific heat at constant pressure, C_p, to increase. It is therefore preferable to use enthalpy, rather than temperature, when solving energy coupling. For the conditions used in the RATFac validation experiments, C_p is estimated to be 2% higher than its dry-air value (neglecting evaporation and sublimation) in the case of one-way mass coupling (AGARD, 1995). It remains to investigate how this changes on implementation of two-way coupling.

4.7.1 Two-Way Coupling: Energy

A simple approach is used to calculate the transfer of enthalpy from the airflow to particles. The heat flux transferred from air to particles in the coupled case is given by

$$Q_{air} = \dot{m}_a\left(h_{f,exit} - h_{f,exit,dry}\right) = -Q_p \tag{4-43}$$

$$= -\frac{SF}{\Delta t_{exp}} \sum_{p=1}^{p=N_p} \left[m_{p,i} C_{p,i}\left(T_{i,exit} - T_{i,inlet}\right) + L_f m_{p,w}\right.$$

$$\left. + m_{p,w} C_{p,w}\left(T_{w,exit} - T_f\right) + L_{v,s}\left(m_{p,exit} - m_{p,inlet}\right)\right]$$

where $\dot{m}_a$ is the mass flow rate of air, $h_{f,exit}$ is the enthalpy at the domain exit, $m_{p,w}$ is the proportion of the particle mass that is water, N_p is the total number of numerical particles and Δt_{exp} is the exposure time to the ice cloud.

Equation (4-43) reads that the heat extracted from the air is equal to the sum of the heat transferred to each particle per unit time. This in turn comprises (i) sensible warming of the ice particle at inlet temperature $T_{i,inlet}$ to outlet temperature $T_{i,exit}$ (note $T_{i,exit} = T_f$ if melting has begun), (ii) the latent heat of fusion required to melt a mass $m_{p,w}$, (iii) sensible warming of water to its outlet temperature

$T_{w,exit}$ and (iv) particle evaporation or sublimation between inlet and exit. Note $L_{v,s} = L_s$ until the particle starts to melt; thereafter $L_{v,s} = L_v$. A summation is used since all the information required has already been calculated on a particle-by-particle basis in the phase change model.

The scale factor, SF, is the number of real particles represented by a single numerical particle:

$$SF = \frac{N_{p,real}}{N_p} \cong \frac{TWC\ U_\infty A_f \Delta t_{exp} \Big/ \pi/_6 \rho_i {D_{eq}}^3}{N_p} \tag{4-44}$$

where A_f is the cross sectional inlet area of the domain. If the domain is two-dimensional, both $\dot{m}_a$ and SF are defined per unit depth.

4.7.2 Two-Way Coupling: Mass (Humidity)

It was shown in Section 4.6 that the phase change model is highly sensitive to humidity. Therefore, mass coupling of water vapour will also be included and sensitivity to it assessed. Similarly to air temperature, the bulk specific humidity at exit may be calculated by summing the individual contributions from particle sublimation and evaporation. The change in vapour mass fraction is given by

$$\omega_{exit} - \omega_{exit,dry} = \omega_{exit} - \omega_{inlet} = -\frac{SF}{\Delta t_{exp}} \frac{1}{\dot{m}_a} \sum_{p=1}^{p=N_p} (m_{p,exit} - m_{p,inlet}) \tag{4-45}$$

and the specific humidity at exit is given by

$$SH_{exit} = \frac{\omega_{exit}}{1 + \omega_{exit}} \tag{4-46}$$

4.7.3 Implementation

Since the system of equations are coupled, an iterative scheme is used. In the first iteration, it is assumed that $h_{f,exit} = h_{f,exit,dry}$ and $\omega_{exit} = \omega_{exit,dry}$. The particle trajectory and phase change calculations are then performed. Equation (4-43) is then solved in iteration 'i' to give

$$h_{f,exit,i} = h_{f,exit,dry} - \frac{Q_{p,i}}{\dot{m}_a} \tag{4-47}$$

The new vapour mass fraction at exit, $SH_{exit,i}$ is given directly by equation (4-46). The error in enthalpy and humidity to the previous iteration are given by

$$\Delta_h = h_{f,exit,i} - h_{f,exit,i-1} \quad ; \quad \Delta_{SH} = SH_{exit,i} - SH_{exit,i-1} \tag{4-48}$$

The change in enthalpy and humidity between inlet and exit are assumed to take a linear profile across the axial length of the domain, such that the new distributions of enthalpy and specific humidity in the grid are given by

$$h_f(x)_i = h_f(x)_{i-1} + \frac{x}{x_{exit}} \Delta_h R \quad ; \quad SH(x)_i = SH(x)_{i-1} + \frac{x}{x_{exit}} \Delta_{SH} R \tag{4-49}$$

where R is a user-defined relaxation factor. Convergence is assumed when the residuals, defined as $\Delta_h / h_{f,exit,i-1}$ and $\Delta_{SH} / SH_{exit,i-1}$ are less than 10^{-6}.

It is important to note that the flowfield is not re-calculated – so Mach number, pressure and density are unchanged despite the local change in temperature and gas properties. This is clearly acceptable provided changes are small.

4.7.4 Results

The two-way coupling model was applied to the domain and conditions of tests conducted in the Research Altitude Test Facility (RATFac). Aerodynamic and icing conditions were held at their baseline values given in chapter 3. A TWC of 8 g/m^3 was used with mono-disperse particles of 40 μm equivalent diameter. There was assumed to be no test piece in the domain, such that the particles travelled from inlet to outlet without impact. If there were a test piece, the equations would remain unchanged but the particles that stick (not bounce) would be removed from the calculation at the point of impact.

Fig. 4-9 (a) shows the change in exit enthalpy against iteration number. Two cases are plotted: (i) both energy and mass coupling implemented and (ii) only energy coupling implemented. For each case,

three relaxation factors of 0.25, 0.50 and 0.75 are shown. The change in exit enthalpy of ~1200 J/kg is the product of an increase in specific heat capacity of ~ 2.2 J/kg/K (estimated from data in AGARD AR-332) and a reduction in static temperature of ~ 1.8 K. Since the dry static temperature in this case is around 275 K, this shift is significant for the icing energy balance due to its proximity to freezing temperature. Fig. 4-9 (b) shows the change in specific humidity for the same case, again with three relaxation factors. It was stated in Section 4.7 that two-way mass coupling is not expected to be important in this case. The change in specific humidity at exit represents a ~ -4.5% change compared with the one-way coupled case (indicative that the initially high ambient humidity is promoting deposition or condensation on the particles). This can be seen in Fig. 4-9 (a) to have an appreciable effect in the evaporative term of the energy balance, as the change in enthalpy is shifted by ~1% when both mass and energy coupling are implemented. Fig. 4-10 shows the change in each parameter between the coupled and uncoupled cases as a percentage of the uncoupled case. Enthalpy and static temperature are presented for energy coupling only, and energy and mass coupling. The analysis presented here demonstrates that the simplistic non-dimensional assessment of equation (4-40) is left wanting and may be an insufficient test to determine if energy coupling is required.

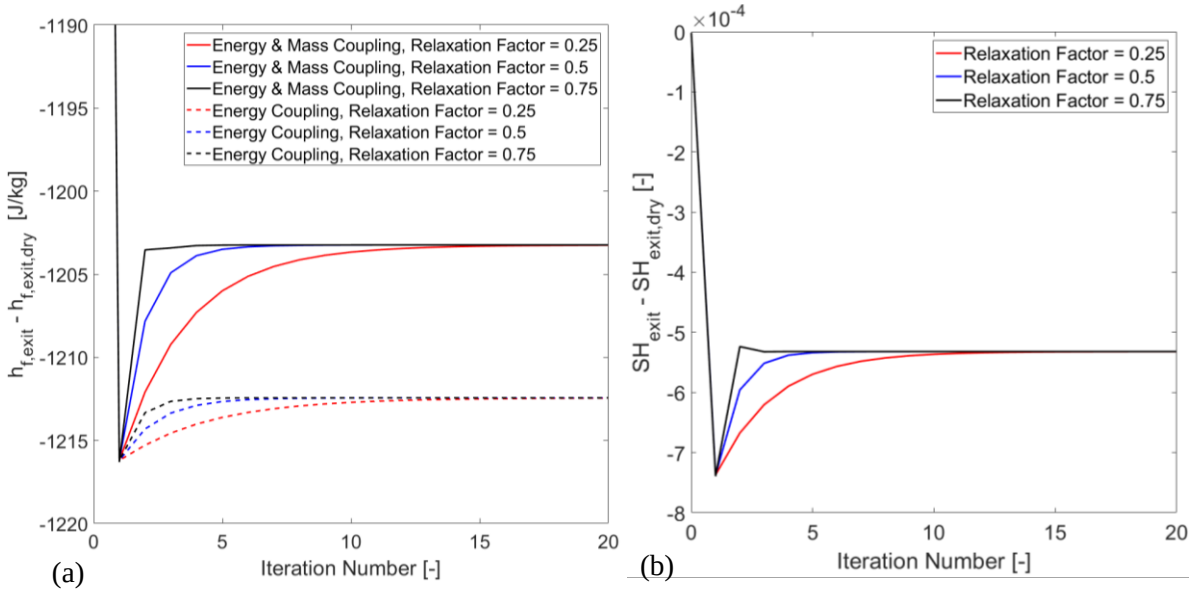

Fig. 4-9 Change in (a) exit enthalpy and (b) specific humidity for two-way coupled mass and energy

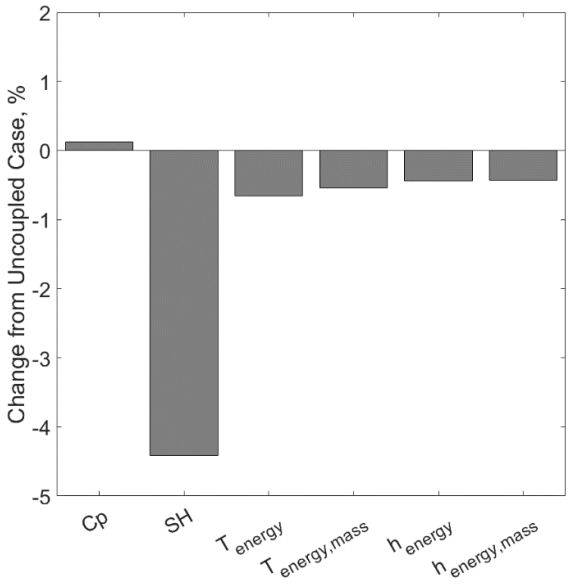

Fig. 4-10 Percentage change in specific heat capacity, specific humidity, static temperature and enthalpy between coupled and uncoupled cases

5 Particle-Surface Interaction

In this chapter, the particle-surface interaction types considered in the model are introduced. These can broadly be split into sticking, bouncing or fragmentation. A new model for sticking probability in 'warm' conditions (surface temperature above freezing) is presented using data from an experimental campaign. A literature model for characterising bouncing and fragmentation is then introduced, followed by results from a second experimental campaign studying heat transfer during particle impacts with warm, clean (deiced) surfaces.

5.1 Particle – Surface Interaction Types

Particle-surface interaction is used as a catch-all term for the mechanical and thermodynamic processes that a particle undergoes when it impinges on a solid (undeflecting) surface. Processes are applied on a particle-by-particle basis and finish either when the particle has stuck to a surface or has been re-emitted into the airflow. The bulk process of ice accretion (i.e. how sticking particles become a homogenous ice layer) is not included here - but is explored in detail in chapter 6. Erosion is also a bulk process; a model is developed in Section 5.2 but is not applied until after the accretion has formed. This is illustrated in Fig. 5-1.

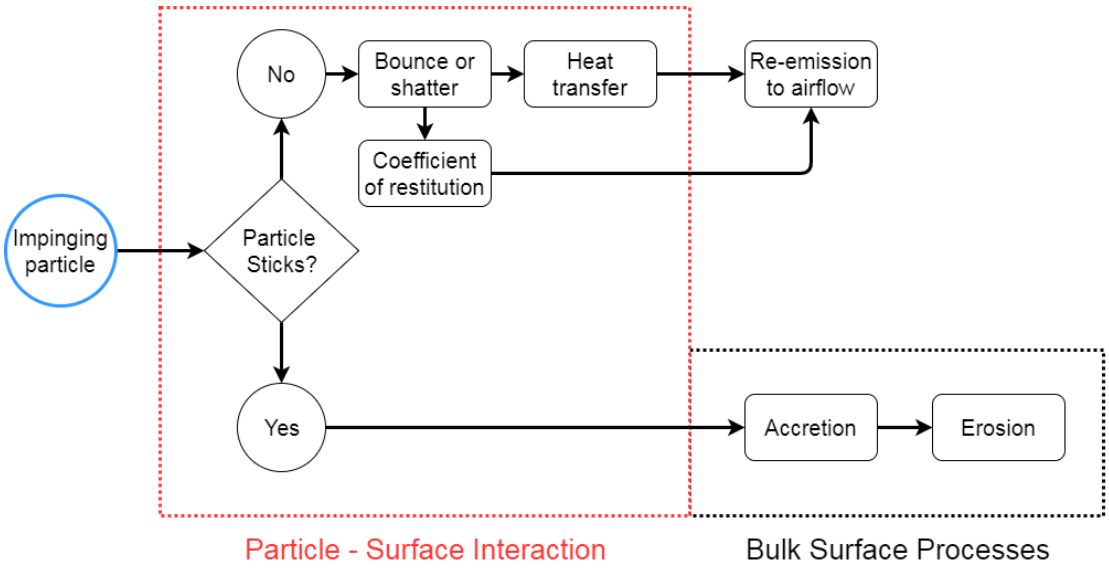

Fig. 5-1 Schematic of processes considered as particle-surface interaction

Note that only sticking or bouncing/shattering are considered. Other mass removal processes such as sliding, rolling, or submersion in runback water are not considered explicitly due to the modelling complexity and the difficulties in experimental validation. They are assumed to be included in the bounce and shatter mass flux.

5.2 Sticking

Sticking probability is a necessary precursor to a thermodynamic accretion model. Consider the case of ice particles impinging on a sub-freezing surface – the vast majority will bounce off.

Two distinct cases must be considered for particle sticking – a surface temperature above freezing ('warm'), and a surface temperature below freezing ('cold'). The former is more akin to the believed mechanism of engine ice crystal icing, whereby partially-melted ice particles are incident on initially warm surfaces. The latter is more akin to supercooled liquid water (SLW) icing – where ice forms due to liquid incident on cold surfaces.

5.2.1 Sticking on Surfaces Below Freezing Temperature ('Cold')

A simple model is used here. An assumption is made that solid ice particles bounce off cold surfaces, and that liquid water fully sticks. This assumption is inherent to all airframe icing codes. The sticking mass is then equal to the impinging liquid mass. The liquid mass is either a fully melted droplet or the meltwater on a particle, shed onto the surface.

$$m_{stuck} = m_{stuck,w} = P_{S,cold,L}\, MR\, m_p \tag{5-1}$$

where the sticking probability of liquid on cold surfaces, $P_{S,cold,L} = 1$, and MR is the particle melt ratio at impact.

5.2.2 Sticking on Surfaces Above Freezing Temperature ('Warm')

It has been shown that air temperatures above freezing can be conducive to ice crystal accretion. This has been observed both in tunnel tests (Currie et al., 2014; Struk and Wright, 2012) and in engine data

analysis (Mason et al., 2006; Veres et al., 2017). However, models for particle sticking in these warm conditions – whether empirical or analytical – remain scarce.

Testing was undertaken at the National Research Council of Canada's (NRC) Research Altitude Test Facility (RATFac). The objectives were to develop sticking probability and erosion models in warm conditions. The results for the cone test article and the models generated were written into a conference paper entitled "*Experimental Studies of Ice Crystal Accretion on an Axisymmetric Body at Engine-Realistic Conditions*" which was presented at the 10th AIAA Atmospheric and Space Environments Conference, part of the AIAA Aviation Forum, in Atlanta, US, in June 2018. The paper is replicated here.

Experimental Studies of Ice Crystal Accretion on an Axisymmetric Body at Engine-Realistic Conditions

Alexander Bucknell[1], Matthew McGilvray[2] and David R. H. Gillespie[3]
University of Oxford, Oxford, OX2 0ES, UK

Geoff Jones[4], Alasdair Reed[5] and Benjamin Collier[6]
Rolls-Royce Plc, Derby, DE24 8BJ, UK

It has been recognised in recent years that high altitude atmospheric ice crystals pose a threat to aircraft engines in flight. Instances of damage, surge and shutdown have been recorded at altitudes significantly greater than those associated with supercooled water icing. It is believed that ice particles can accrete inside the core compressor, although the exact mechanism by which this occurs remains poorly understood. In order to model ice crystal accretion, an estimate of the proportion of the impinging ice and water that sticks to a surface (the 'sticking efficiency') is required. This is believed to be dependent upon a number of parameters including particle melt ratio and diameter, and surface condition (rough or smooth, dry or wetted, warm or cold). This paper presents data from experiments undertaken in the National Research Council of Canada's (NRC) Research Altitude Test Facility (RATFac). An axisymmetric test article, which featured three interchangeable cone 'noses' of varying half-angle, was used over a period of two weeks. A 35° half-angle nose was used for a parametric study of Mach number, Total Water Content (TWC), wet bulb temperature and particle size distribution (PSD). At selected test conditions, 20° and 45° half-angle noses were also tested. An assessment of the response of the Science Engineering Associates WCM-2000 multiwire probe in glaciated condition is presented, as a function of TWC, particle size and Mach number. A shadowgraphy technique was used to measure the ice accretion growth rate on the nose, with isometric camera views for qualitative assessments of spatial uniformity and build/shed events. The results show that sticking efficiency has a strong dependency on particle melt ratio, with maximum values attained when melt is typically between 9-13%. Erosion is shown to be correlated with particle size, Mach number and surface angle. New semi-empirical models are presented for sticking probability and erosion.

I. Nomenclature

Symbols

a = Constant in empirical false response model (-)
α = Angle between axial direction and surface normal (°)
β = Collection efficiency (-)
D = Diameter (µm)
D_{yy} = Diameter for which all particles with D < D_{yy} constitute a volume of yy% of the total volume (µm)
δ = Mass averaged deflection angle (°)
η = Efficiency (sticking, loss, erosion) (-)
$\eta_{s,0}$ = Reference net sticking efficiency (-)
ε = Mass averaged ballistic coefficient (-)
γ = Angle between surface normal and axial (°)
$\dot{h}$ = Thickness growth rate (mm/s)
K = Kinetic energy parameter for erosion model (J/(kg/m^3))
M = Mach number (-)
$\dot{m}$ = Mass flux (kg/s.m^2)
P = Pressure (Pa)
P_S = Sticking probability (-)

[1] PhD Student, Department of Engineering Science, Oxford Thermofluids Institute, AIAA Student Member
[2] Associate Professor, Department of Engineering Science, Oxford Thermofluids Institute.
[3] Associate Professor, Department of Engineering Science, Oxford Thermofluids Institute.
[4] Subject Matter Expert - Icing and Inclement Weather, Engine Environmental Protection Team, System Design.
[5] Technologist, Engine Environmental Protection Team, System Design.
[6] Ice Crystal Tech Focal, Engine Environmental Protection Team, System Design.

r = Radius (m)
ρ = Density (kg/m^3)
T = Temperature (°C)
TWB= Wet bulb temperature (°C)
TWC= Total Water Concentration (g/m^3)
U = Velocity (m/s)

Subscripts
∞ = Freestream
0 = Total
acc= Accretion
cl = Centreline
demand= Setpoint value
i = Test condition reference
imp= Impinging (freestream x collection efficiency)
loc = Local
m = Measured (LWC or TWC)
$multi_j$=LWC value recorded by wire number j on the multiwire probe
w = Water

II. Introduction

Since 1990 there have been at least 240 icing-related events for engines in flight, many of which have occurred at altitudes above 7000 m, approximately the maximum altitude at which water can exist in liquid form. Mason et al [1] analysed the common characteristics of 46 of these events, judged to have occurred due to accretion of ice particles inside the engine compression system.

Development of analytical and empirical models of the ice crystal icing phenomenon is necessary for both future engine design and this-generation engine certification. The research conducted to define these models will also help to specify critical test points for certification campaigns. Work is underway at the University of Oxford to develop a model for ice crystal accretion in a turbofan engine. The modular structure of the code and the approach taken in the component parts are similar to other models in the open literature (notably [2]–[6]). One such component is performing an energy balance on the accretion surface. In turn, this depends upon being able to estimate (i) the proportion of the impinging ice / water that sticks to the surface (the 'sticking efficiency') and (ii) the mass flux removed from the surface by erosion.

Tests conducted by the National Research Council of Canada (NRC), NASA and Boeing on an S-shaped transition duct in 2009 [7] showed that ice accretion could occur at total temperatures above and below 0 °C provided supplemental liquid water was injected. In 2010, NASA and the NRC installed a wedge-shaped test article in the Research Altitude Test Facility (RATFac) cascade rig [8], [9], showing that an adiabatic wet bulb temperature below 0 °C produced strong accretions (when supplemental liquid water was injected), whereas weaker (and more prone to shed) accretions were formed for wet bulb temperatures above 0 °C. Experiments in [7]–[9] served to confirm a hypothesis of Mason et al [1] that liquid water is required for accretion to occur, and also that there is an optimal region of liquid to total water content ratios (melt ratios) in which rapid accretion occurs. In fully glaciated conditions, where total wet bulb temperatures (TWB) are below freezing, particles bounce off unheated surfaces. Conversely, when total wet bulb temperatures are significantly above freezing, an excess of liquid helps to promote particle run-off from surfaces. In addition to in-air melting, Bucknell et al [10] showed that particle impact with warm surfaces (25 - 35 °C) resulted in partial melting, with the heat transferred to the particle dependent upon its diameter and impact type (bouncing or fragmentation).

In 2012, Struk et al [11] used both a wedge aerofoil and a NACA 0012 aerofoil in RATFac to investigate accretion growth rate as a function of flow velocity and wet bulb temperature. At a velocity of approximately 85 m/s, a peak growth rate was found for melt ratios in the region 6 – 12 %. Currie et al [12], [13] used two axisymmetric test articles and one planar test article in RATFac to investigate sticking efficiencies and scaling laws of sea-level testing to altitude conditions. In these tests, a range of melt ratios was achieved through varying total wet bulb temperature, always above freezing. It was assessed that differences in growth rate caused by melting of the accretion at higher wet bulb temperatures was minimal. This was validated through tests conducted at constant melt ratio and TWC, but with varying total wet bulb temperature (achieved using supplemental liquid water injection). It was concluded that a melt ratio range of 10-20% resulted in a plateau of stagnation point sticking efficiencies. However, the results suffer from high uncertainty in the measurement of Liquid Water Content (LWC) and Total Water Content (TWC). Currie et al [13] concluded that erosive effects of oblique impacts were strongly dependent upon surface angle and particle velocity, and weakly dependent on TWC. Studies in RATFac using an intercompressor bleed slot [14] showed that accretion growth rate decreases for increasing particle size – particularly when the size of the largest particles in the distribution (described by the D_{v90}) is

increased. Further experimentation is required to elucidate the key non-dimensional parameters driving erosive processes.

The objectives of this study are therefore to:

1) Perform a parametric study on ice crystal sticking efficiency, centering on known 'critical' conditions. Specifically, total and static wet bulb temperatures ~4°C above and below freezing; Mach numbers between 0.25 and 0.50, particle D_{v50} values between ~ 30 and ~ 70 µm, TWC up to 12 g/m^3 and a range of oblique impact angles;
2) Perform a parametric study on the liquid water false response of the SEA multiwire probe in glaciated conditions, for more accurate calculation of melt ratio;
3) Develop semi-empirical sticking and erosion models, for application in ice accretion models at engine-realistic conditions.

III. Experimental Facility, Test Articles & Test Conditions

A. Test Facility

The test facility used in this study was the Research Altitude Test Facility (RATFac) at the NRC. This facility consists of an altitude chamber divided into two sections, as illustrated in Fig. 1. On the 'cold' side, ice particles of a target Particle Size Distribution (PSD) are generated in a grinder system. These particles are then fed through to the 'warm' side, where they are mixed with any supplemental liquid water and entrained into a flow of target total temperature and relative humidity (the latter controlled via steam injection). The mixture then passes into the bellmouth inlet of the cascade rig. This has a working cross section of 254 mm x 132 mm and has multiple traverse planes for aerodynamic and icing measurements. The total wet bulb temperature (TWB_0) in the 'warm' side of the facility may be varied through adjusting relative humidity, total temperature and/or total pressure. The cascade rig also features a number of heated windows on the top, bottom and side walls, through which video cameras are used to record the accretion growth on the test article. Further details on the facility and instrumentation may be found in [7]–[9].

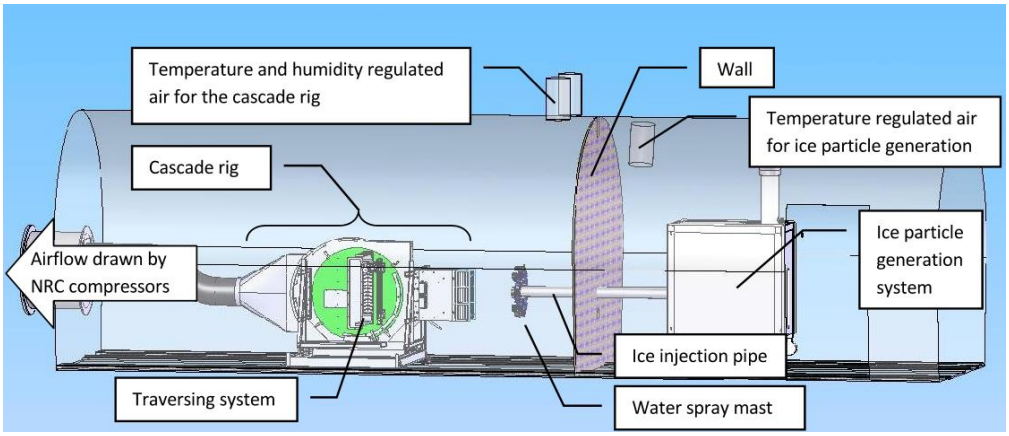

Fig. 1 RATFac cascade rig and ice crystal generation system [14]

B. Test Conditions

A total of 63 test points were completed with the test article installed and an additional 14 cloud calibration tests with the test article absent. The parameters varied and their nominal minimum, baseline and maximum values are shown in Table 1. For the vast majority of tests, the mixed phase cloud was generated using natural particle melt, rather than supplemental liquid water injection. A limited number of runs were conducted with LWC injection in order to generate relatively high values of melt ratio (30-40%), where it was believed that ice crystal sticking was inhibited.

In the results presented, total pressure was held at 34.5 kPa (ISA altitude of approximately 8.2 km / 27,000 ft) and total air temperature at 10 °C. For the parameters in bold Table 1, some form of cloud calibration was performed (LWC and/or TWC traverse measurements) at the minimum, baseline and maximum values whilst all other parameters were held at their baseline value. Additional calibrations were performed at intermediate TWB_0 values of -3.5 °C and -0.5 °C.

Aerodynamic parameters in wet conditions were measured indirectly during the test by taking the measurements obtained directly in dry conditions (P_0, P_S and T_0) and monitoring the delta in these values from

probes designed to operate in icing conditions (for example the downstream-facing Total Air Temperature-Relative Humidity (TAT-RH) probe).

Table 1 Parameters varied, with their ranges and baseline values. For parameters in bold, cloud calibrations were performed at the minimum, baseline and maximum values

Parameter	*Minimum*	*Baseline*	*Maximum*
Mach [-]	0.25	0.40	0.50
TWB_0 [°C]	-6.5	2.5	5.5
TWC [g/m^3]	4.0	8.0	12.0
Ice D_{v50} [µm]	34	40	68
Surface angle, clean [°]	20	35	45

C. Test Articles

The test articles used in this study comprised a number of cone 'noses'. An axisymmetric body was chosen as it easily permits shadowgraphy from multiple angles and avoids the complication of particles bouncing multiple times on the accretion surface (as could occur with concave or other complex geometries). A cone was chosen in particular as discrete surface angles can easily be tested, and accretions do not suffer from gravitational droop as is the case with a hemispherical geometry [13].

The cone noses consisted of 20°, 35° and 45° half angle versions. The 35° half angle nose was instrumented with eight internal thin film heaters, ten K-type thermocouples and 24 thin film heat flux gauges, and was designed to measure steady state heat flux on the icing surface. The heat transfer data is not reported here. All cone noses featured a thin (400 µm) titanium alloy shell as the outer surface, representative of the material used in compressor components. The shells were 3D printed using the Direct Metal Laser Sintering (DMLS) method. The as-printed roughness was approximately 4.5 µm Roughness Average (RA). The noses were wet polished to a nominal RA representative of a gas turbine compressor entry into service condition. The actual surface roughness of all four noses was measured at four azimuthal locations using a Taylor-Hobson Surtronic 3+ profiler, with an accuracy of 2% of the reading.

The cone nose under test was installed in a cylindrical afterbody of 110.0 mm length, which incorporated a 12° half angle conical tail and aerodynamic mounting sting. The total test piece length was 326 mm. The estimated blockage due to the entire test article was 11%, limiting the maximum achievable Mach number to approximately 0.55. The axis of revolution of the cone was designed to be aligned with the tunnel centreline. The angle between the cylindrical afterbody and tunnel floor was found to be -0.1° using a digital protractor with an accuracy of 0.1°. A computer model of the test article, with a 35° half angle nose fitted, is shown in Fig. 2. Images of the test article installed in the cascade rig are shown in Fig. 3 from (a) the side and (b) the front.

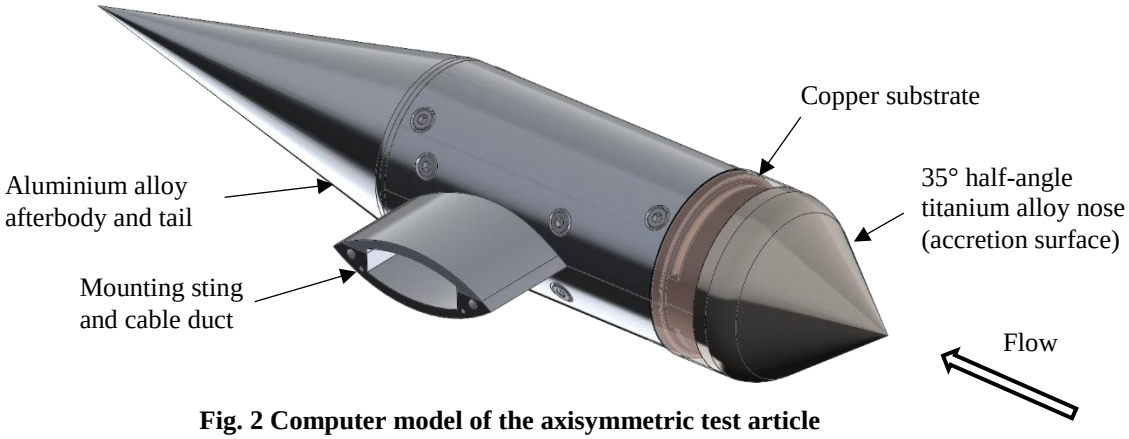

Fig. 2 Computer model of the axisymmetric test article

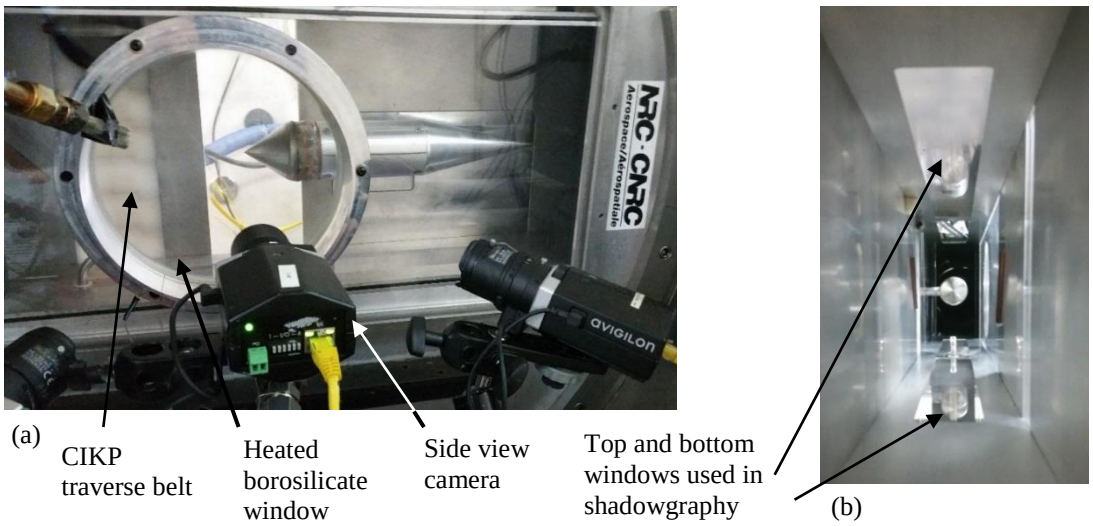

Fig. 3 Test article installed in the RATFac cascade rig, viewed from the (a) side (flow is left to right) and (b) front (flow is into the page)

IV. Icing Cloud Measurement & Calibration

A. Particle Size Distribution (PSD)

Four PSDs were used in the campaign. The nominal values of D_{v10}, D_{v50} and D_{v90} are shown in Table 2.

Table 2 Nominal size statistics for the four PSDs used

Designation	D_{v10} *[µm]*	D_{v50} *[µm]*	D_{v90} *[µm]*
PSD 1 ('small')	18	34	54
PSD 2 ('baseline')	25	40	80
PSD 3 ('large')	28	50	93
PSD 4 ('largest')	35	68	131

In-situ measurement of the actual PSD was achieved for selected runs through a Particle Imaging Velocimetry (PIV) system configured for backlit shadowgraphy. It is located upstream of the cascade rig inlet (i.e. just downstream of the ice injection pipe). This has a resolution of 1.3 microns / pixel and may be operated at particle speeds in excess of 200 m/s. The system is described in detail in [15]. The statistics for the actual PSDs generated during accretion testing were supplied as a 26-bin representation, and may be represented using a Rosin-Rammler distribution. The maximum discrepancy between the measured points of the PSD and the continuous Rosin-Rammler distribution was less than 5%. The uncertainty in the PSD measurement may be found in Section VI.

B. Liquid Water Content (LWC) Measurement

Measurement of Liquid Water Content (LWC) and Total Water Content (TWC) is an area of active research. In previous studies undertaken by Struk et al [11] and Currie et al [13], LWC was measured by the Science Engineering Associates (SEA) WCM-2000 multiwire probe. This probe was designed for use in supercooled liquid water droplet (SLW) conditions, and its ability to measure LWC when in mixed phase conditions is still under investigation. For LWC measurement, the probe contains two robust water-sensing hot wires, of 0.53 mm and 2.1 mm diameter. It is believed that meltwater coating particles is not fully shed onto the elements and thus LWC is underestimated. This is counteracted by a false LWC reading when in fully glaciated conditions (termed the 'false response', referred to here as FR). This has estimated to be in the range 2.5 – 4.5 % of TWC [13], however the dependency of this response on test condition requires further investigation. Fig. 4(a) shows a moving average of the readings from the two LWC-sensing wires, with the window centred on discrete TWB_0 values. The data was taken from tests with a Mach number of 0.4, PSD 1 and 8g/m^3 TWC_{cl}. The figure shows a clear false response of approximately 0.3 g/m^3 LWC (i.e. ~4% of the centerline TWC).

Tests at a selected number of conditions were run in fully glaciated conditions to provide an approximate characterisation. 'Fully glaciated conditions' were defined as having a wet bulb temperature based on total conditions at -2 °C or below (thus a static wet bulb temperature significantly below freezing). PSDs number 1 and 2 were used (D_{v50} values of 34 µm and 40 µm respectively), at a Mach number of 0.25 and 0.4. The nominal centreline TWC was varied between 4 g/m^3 and 8 g/m^3. For all tests, the total air temperature (TAT) was

maintained at 10 °C. Two additional tests with a TAT of 20 °C were used to show that the false response was insensitive to TAT provided the total wet bulb temperature was below freezing. The results are shown in Fig. 4(b). There is a dependency on particle size for the Mach 0.4 tests. For a given nominal TWC, the larger particles generate a higher false response, possibly due to more ballistic trajectories increasing the catch efficiency on the water-sensing wires. The same trend is true with Mach number. For the Mach 0.25 tests, there is a decreasing false response as TWC rises, tentatively attributed to increased particle-particle interaction (bouncing) deflecting particles away from impinging on the wires.

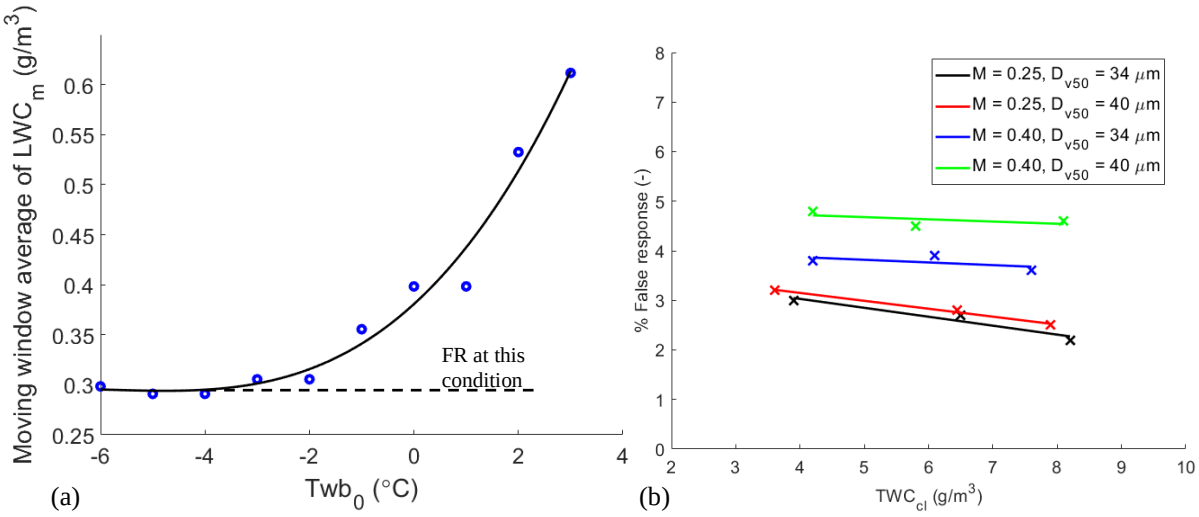

Fig. 4 Characterisation of the SEA multiwire probe false response. (a) A moving window average of LWC readings from the multiwire, with the window centred on discrete TWB_0 values. Conditions: Mach 0.40, TWC = 8g/m^3, PSD 1. (b) False response as a percentage of TWC_{cl}, for PSDs 1 and 2 and M = 0.25, 0.40.

It is unknown how this offset decays as melt ratio increases – clearly in fully liquid conditions it will not exist. At any point in between fully glaciated and fully liquid conditions, there may be false response from the largest, still glaciated particles, a response from meltwater shed onto the wires and a response to the fully melted smallest particles. Isolating the false response signal is then not possible without a second, independent measurement. It is therefore assumed in this study that the false response follows a constant trend across all the melt ratios tested in the campaign. Since the maximum melt ratio tested is below 30 %, the error arising from this assumption may be small, but is likely still significant. Using the data in Fig. 4(b), the following empirical relationship can be given for FR:

$$FR\ (\%) = a + \frac{M - 0.4}{0.017\ D_{v50} + 0.243} TWC_{cl} \tag{1}$$

where values of the constant a are given in Table 3.

Table 3 Determined values of model constant a

Mach [-]	*D_{v50} [μm]*	*Value of a [-]*
0.25	34	3.75
0.25	40	3.79
0.40	34	3.79
0.40	40	4.70

C. Total Water Content (TWC) Measurement

For these studies, TWC at the tunnel centreline (TWC_{cl}) was measured using the NRC Compact Iso-Kinetic Probe (CIKP). A full description and uncertainty analysis of this probe is available in [16] and [17] respectively. For the nominal range of TWCs run in this experiment (4 - 12 g/m^3) the uncertainty in TWC measurement may be taken as +/- 5% of the reading.

D. Calculating Melt Ratio

Given the above considerations, calculation of the corrected melt ratio (MR_{corr}) proceeds as follows:

$$MR_{corr}\ (\%) = \frac{\max\left(LWC_{multi,1}, LWC_{multi,2}\right)}{\beta_{MW} TWC_{CIKP}} - FR \tag{2}$$

where $multi, 1$ and $multi, 2$ refer to the readings from the 0.53 mm and 2.1 mm diameter wires respectively, and FR is given by Equation (1). β_{MW} is the catch efficiency of the wires, which may be less than unity for the smallest particles. Using the values in Struk et al [18], this is taken as ~0.94 for PSD 1, ~0.97 for PSD 2, and unity for PSDs 3 and 4. A correction is also reported in [18] attributed to the water-sensing wires under-measuring LWC in a fully liquid cloud, when compared to the CIKP. Since this term will dominate at high melt ratios (the highest tested here using natural melt believed to be ~ 30%), and since this term has not been calibrated for use in natural melt mixed phase conditions, it is not included. This also means that a reasonable estimate of bias (systematic) uncertainty cannot be applied to the LWC readings. Note also that the expression for FR is only valid for the conditions defined in Fig. 4(b). Given these limitations, the absolute value of MR_{corr} quoted should be viewed with caution.

V. Ice-on-Ice Sticking Efficiency Calculation

In this section, results for ice-on-ice growth are analysed quantitatively by calculation of a sticking efficiency, derived from the ice growth rate. Ice-on-ice sticking was taken from where the tip growth rate was steady (typically within the first 10-20 seconds of the test). This also mitigates against fluctuations in the ice cloud concentration as the feed rate rises to its setpoint. The results shown are from all of the cone noses, with internal heaters always off.

A. Imaging & Analysis

Ice accretion was measured using high definition video recordings of the backlit test piece. Two 5.0 megapixel Avigilon 5.0MP-HD-DN video cameras (2592 x 1944 resolution, 12 fps frame rate) were positioned above the top and starboard windows, providing top and side views. An isometric view, for qualitative assessment of the ice growth and uniformity was provided by a third camera. The side view was not used to quantify ice growth due to the propensity for ice to build up on the window on the camera side, despite heat being applied. The top view remained almost free of build up for all conditions.

For each test condition, video from the top view was exported to an in-house accretion analysis code. The outer edge of the clean test article is firstly defined, followed by a mask defining the region of interest. The mask consists of measurement lines (typically ~1000) normal to the local surface, which are sufficiently long to encompass the maximum extent of the accretion. For each frame and measurement line, a normalised vector of greyscale value is created. The largest step change in greyscale value along this vector (corresponding to the edge of the accretion) is found using a root mean square difference method. A moving average filter is used to 'remove' small agglomerations of ice sliding down either window. The ice thickness and surface angle are then generated for each location and for each timestep.

B. Sticking Efficiency Calculation

The local net sticking efficiency – the proportion of the impinging mass flux that sticks minus the proportion that bounces or is eroded – may be calculated from the local thickness growth rate $\dot{h}$ as follows:

$$\eta_{s,net} = \frac{\dot{m}_{acc}}{\dot{m}_{imp}} = \frac{\dot{m}_{acc}}{\beta\ \dot{m}_{\infty}} = \frac{\dot{h}_{loc}\ \rho_{acc}}{\beta\ \dot{m}_{\infty,loc}} = \frac{\dot{h}_{loc}\rho_{acc}}{\beta\ TWC_{loc}\ U_{\infty}} \tag{3}$$

where $\dot{m}_{\infty,loc}$ is the local impinging mass flux (mass flow rate per unit area). The particle collection efficiency, β, is mass averaged over all particles in the PSD being injected. If, in theory, all particles were ballistic and travelled axially, the collection efficiency on the inclined cone surface would be given by $\beta = \cos(\gamma)$ where γ is the angle between the axial direction and local surface normal at any timestep. As the trajectories will not be fully ballistic in practice, the equation for collection efficiency can be modified as follows:

$$\beta = \varepsilon \cos(\gamma) \tag{4}$$

where ε is the mass averaged ballistic coefficient (equal to unity for truly ballistic particles). For each of the four PSDs, three Mach numbers and three cone half angles used, values of ε were calculated using Lagrangian particle tracking in the commercial CFD package FLUENT. The PSDs were converted to equivalent Rosin-Rammler distributions. The non-spherical particle drag coefficient of Haider & Levenspiel [19] was selected, using a mean particle aspect ratio found during particle morphology studies in RATFac [15]. Values of a mass averaged deflection angle, δ_{γ}, defined as the difference between the actual particle impact angle and the axial direction, were also calculated. This latter calculation assumes that particles are travelling axially at the cascade rig inlet. The lowest value of the ballistic coefficient ε was 0.90, for the case of the smallest nominal PSD, lowest Mach

number and 45° half angle cone. This corresponded to the highest particle deflection angle of 5.4°. For simplicity, the values of ε and δ_γ are assumed to remain constant over the accretion time.

The TWC local to the accretion site, TWC_{loc}, is found through 2D interpolation of the TWC profile obtained during the cloud calibration at the same test conditions. The growth rate, $\dot{h}_{loc}$, is likely to change over the test time, given that some conditions will reach a steady state accretion profile within this time. It is therefore calculated at all timesteps using the change in accretion height over a fixed time period (typically 5 s). For a given time step, the net sticking efficiency is calculated using the current $\dot{h}_{loc}$ value and an estimated value of the accretion surface angle.

VI. Uncertainty Analysis

A full uncertainty analysis is presented in the Appendix.

VII. Results

In the following section, accretion growth rates and net sticking efficiencies are presented across the range of conditions tested. In this paper, 'net' sticking efficiency refers to the sticking efficiency measured in the test, and is a combination of (i) sticking processes and (ii) material removal processes (erosion, bouncing, splashing etc.). A model for isolating terms (i) and (ii) is proposed in Section VIII.

A. Effect of Melt Ratio

Net sticking efficiency, $\eta_{s,net}$, was observed to be strongly dependent upon melt ratio for all values of Mach number, TWC, surface angle and PSD. The effects were most notable at conditions conducive to minimal erosion – i.e. small particles and low velocities – where very different growth rates were possible over a relatively small range of melt ratios. Single or averaged values of net sticking efficiency are taken from early in the test, where tip growth is approximately linear and the change in accretion surface angle is still small. This would typically be in the window of 10 – 40 s after ice initiation.

Images of accretions that occurred during tests at M=0.25, PSD 1, TWC = 8g/m^3 and melt ratios between 1.3% and 18.6% are shown in Fig. 5. Cases conducted at 4.4% and 6.4% melt ratio (accretions (b) and (c)) both approached a steady state near the end of the test and exhibited conical accretions with smooth sides, both characteristic of erosion by a stream of largely solid particles. Both accretions were firmly adhered to the test piece and did not shed during the test. The cases at 11.7% and 18.6% melt ratio (accretions (d) and (e)) were less well adhered with accretion (d) rotating by 90° under gravity after around 180 s, and finally shedding when the ice flow was halted at around 300 s. Accretions created under relatively high liquid water content conditions are characteristically non-aerodynamic in profile, as demonstrated in (d).

At the highest melt ratio of 18.6% (accretion (e)), ice was only able to grow stably on the tip, with water continually running back over the remainder of the surface. The tip accretion of less than 5 mm formed and then shed within a minute of test initiation. A secondary accretion followed with steady growth at a rate of 0.04 mm/s higher than the original accretion. The second accretion (shown in Fig. 5(e)) grew to a thickness in excess of 10 mm before shedding again. The higher growth rate and growth time of the second accretion may be explained by the surface cooling effect of the first. This surface cooling, primarily due to melting of the metal-accretion interface, is demonstrated in the thermocouple trace in Fig. 6. Note that in this test, the total dry and wet bulb temperatures were 10 °C and 5.5°C respectively. The thermocouple was positioned 3 mm aft of the tip and 400 µm below the titanium surface.

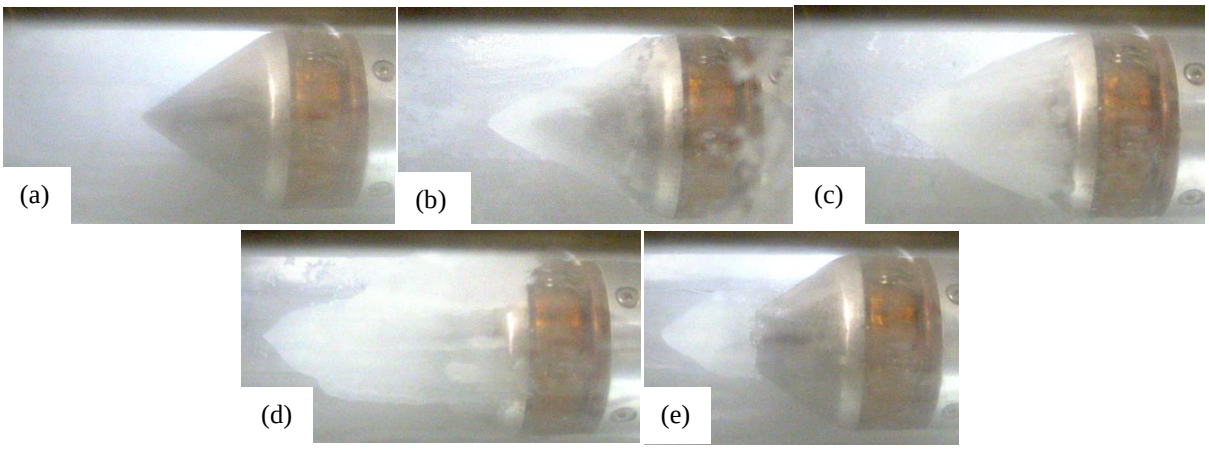

Fig. 5 Accretions after a fixed test time for melt ratios of (a) 1.3%, (b) 4.4%, (c) 6.4%, (d) 11.7%, (e) 18.6%.

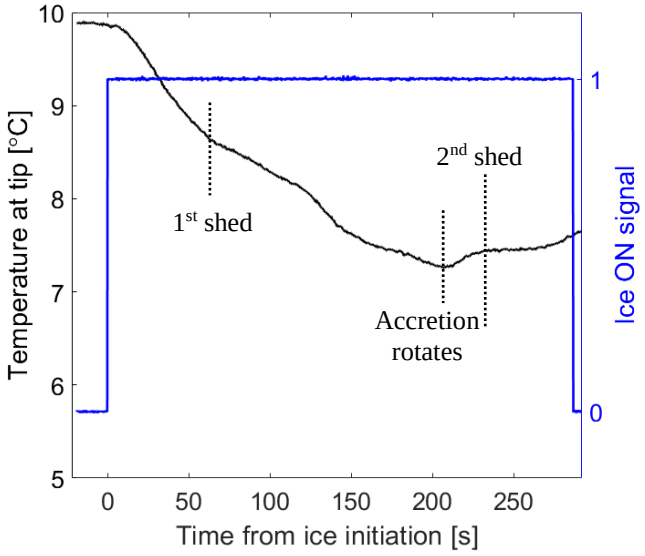

Fig. 6 Temperature trace from tip thermocouple for accretion (e), with shed events marked

Two additional tests were run where 0.8 g/m^3 then 1.6 g/m^3 of supplemental liquid water were injected. The total wet bulb temperature was maintained at 5.5 °C and the centerline TWC at 8 g/m^3. The overall melt ratios were estimated to be 31% and 39% respectively. The tip growth rate dropped to 0.04 mm/s in the first case and then to zero in the second case.

Fig. 7 shows how the 'plateau effect' observed here may be quantified. Tests were grouped by the same 'erosive condition' (i.e. same or similar PSD, Mach number and surface geometry). For each group, sticking efficiency normalised onto a scale of 0 to 1 (termed the sticking probability, P_s) is plotted against melt ratio. Uncertainty bars are provided on the tests conducted at M = 0.25 for the 35° angle cone. The uncertainties on other cases are of a similar magnitude.

The striking feature is that regardless of the erosive condition, the peak normalised sticking efficiency is in a well-defined region of MR, taken as 9 – 13%. The narrow width of the plateau also indicates that changing Mach number has only a small effect on the amount of overall meltwater at the surface (the sum of incoming meltwater and accretion surface melt). The latter term will differ as Mach number varies for two reasons; firstly since the particles' residence time is inversely proportional to Mach number, a higher total wet bulb temperature is required at Mach 0.4 than at Mach 0.25 to obtain the same particle melt ratio. It is worth repeating the conclusion in Currie et al [12] that the effect of total wet bulb temperature on accretion growth rate (beyond its effect on particle melting) is minimal, at least at the range tested here. This conclusion gives confidence that the measured growth rates would be reproduced at other positive wet bulb temperatures if the melt ratio was matched.

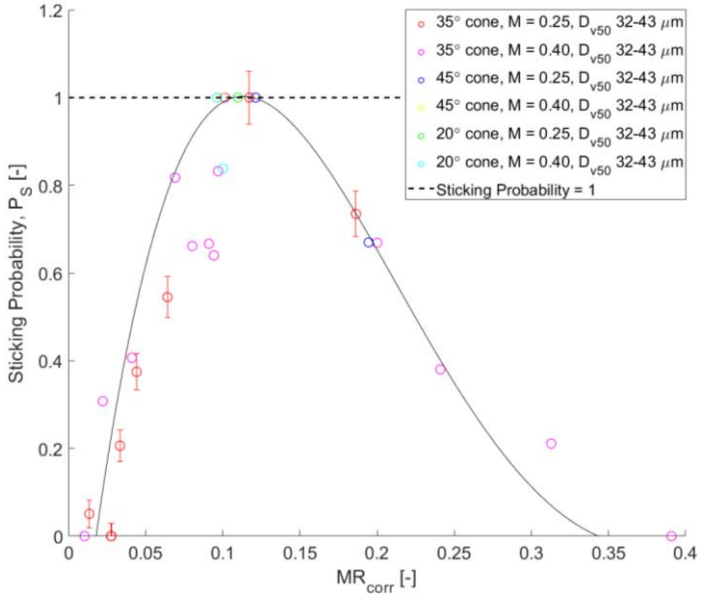

Fig. 7 Sticking probability against melt ratio for all three cones, M = 0.25 and 0.4, PSDs 1 and 2

There are additional thermodynamic effects of raising Mach number on surface melt. For example, increased particle kinetic energy (proportional to ~ M^2) , increased Nusselt and Sherwood numbers (proportional to ~ Re$^{0.8}$ for a turbulent boundary layer over a cone [20]). Again, these effects must be small and form part of a Messinger-

style surface heat transfer balance, which can only proceed *after* an initial estimate of sticking mass flux is made [3], [4]. This initial estimate may be provided by the new model given in Equation 5. At low melt ratios (between 2% and 34%), this takes the equation of the best fit line shown in Fig. 7, which gives a sticking probability, P_s, of 1 at some point in the plateau region. At melt ratios below 2% and above 34%, a constant value of $P_s = 0$ is used. This is valid for partially melted particles in an airstream with positive total wet bulb temperature. However, findings in [12] show that there is minimal difference in ice growth rate when using LWC injection instead of natural melt (at positive total wet bulb temperatures), implying that the model may also be used in these conditions.

$$P_s = \begin{cases} 183\,MR^5 - 494\,MR^4 + 478\,MR^3 - 196\,MR^2 + 30.2\,MR - 0.526 & 0.02 \leq MR \leq 0.34 \\ 0 & 0 \leq MR < 0.02 \text{ and } 0.34 < MR \leq 1.00 \end{cases} \quad (5)$$

B. Effect of TWC

The accretion growth rate was observed to be directly proportional to TWC within the uncertainty of the measurement, for the same Mach number, PSD and melt ratio. Hence sticking efficiency was approximately constant across tested TWC range of 4.0 – 12.0 g/m^3. Particle-particle interactions were therefore assumed to have a negligible effect on accretion growth within this range.

C. Effect of Mach number

Given that the thermodynamic effects of changing Mach number have been discussed in Section VII-A, the following section demonstrates the effect of Mach number on erosion. Fig. 8(a) shows net sticking efficiency at the tip against melt ratio for the tests on the 35° half angle cone using the smallest PSD. The results are normalised against a reference value, $\eta_{s,0}$, taken as the net sticking efficiency at the tip for a test at M = 0.25 and PSD 1. The peak of the plateau region (~9-13% MR) for the Mach 0.40 case is approximately 60% of that of the Mach 0.25 case. Fig. 8(b) shows net sticking efficiency on the 45° half angle cone plotted against Mach number up to M = 0.50. No accretion was observed at the tip or wall for the Mach 0.5 case, even for the smallest PSD.

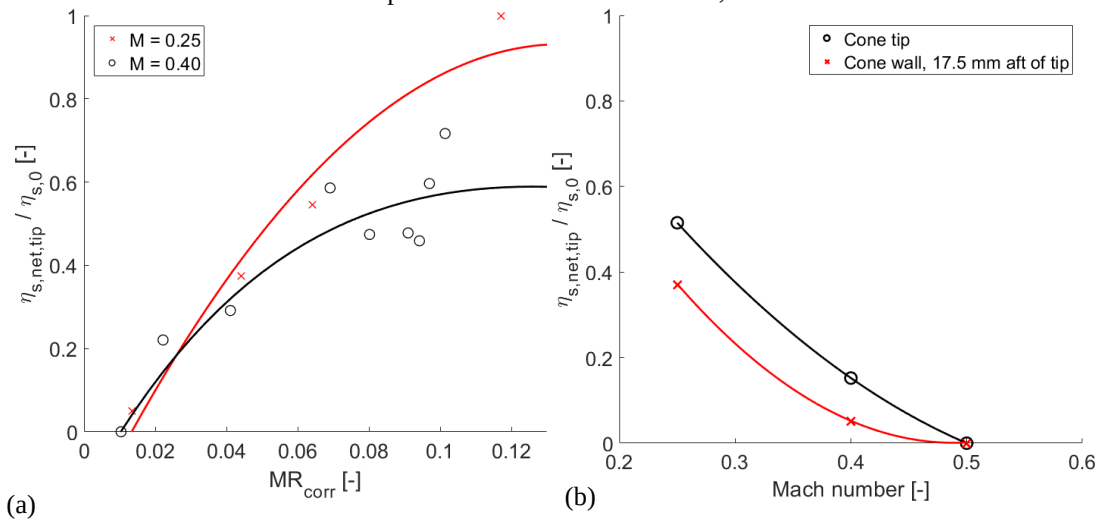

Fig. 8 (a) Normalised net sticking efficiency against melt ratio for M = 0.20 and M = 0.40, PSD 1. (b) Net sticking efficiency against M for the 45° half-angle cone

D. Effect of surface angle

In the initial ice-on-ice sticking phase (i.e. before the surface angle of the accretion has deviated significantly from that of the test piece), data from the three different half-angle cones may be directly compared. This is shown in Fig. 9(a) where net sticking efficiency is taken from the cone wall, at a common measurement point 17.5 mm aft of the tip. All data is again normalised against $\eta_{s,0}$. In all tests, melt ratio was within the plateau region of 9-13%. Fig. 9(a) shows that the wall ice-on-ice sticking efficiency decreases with cone half angle, as would be expected for ductile erosion (mass removal primarily caused by tangential (glancing) impacts [21]). In the engine environment therefore, rapid accretion would be expected at vane leading edges and aggressively shaped endwalls (for example intercompressor ducting). Fig. 9(a) also shows that increasing D_{v50} by a factor of ~ 1.2 and reducing velocity by ~ 1.6 (i.e. moving from the black line to the red line) results in a lower net sticking efficiency (i.e. increased erosion). This then indicates that erosion has a stronger dependency on PSD than on velocity.

Fig. 9(b) shows data from a test (M = 0.25, PSD 2) on the 45° half angle cone, taken over the full test time. This particular case is useful in demonstrating the effect of the accretion surface angle decreasing (relative to the axial direction). The clean geometry is shown in Fig. 10(a). The accretion after test completion is shown Fig. 10(b). The average total wet bulb temperature in this test was 2.78 °C, resulting in relatively wet conditions

(estimated melt ratio of 12.5%, at the right hand end of the plateau region). As a result, runback and sliding are prominent so there is negligible accretion on the curved radius at the rear of the cone. Fig. 9(b) shows that the accretion surface angle local to the 17.5 mm measurement point decreases by approximately 30° over the test time, with the rear portion of the accretion having a near cylindrical shape. The net sticking efficiency on the wall at the same position correspondingly decreases, approaching a minimum of ~10% of the reference case towards the end of the test. This indicates that at this condition, a surface angle of ~15° is the minimum at which sticking efficiency remains appreciably above zero. The net sticking efficiency at the tip reduces at a lower rate, with a total reduction over the test time of 8% of the reference case.

The accretion in Fig. 10(b) may be compared to that in Fig. 10(c), which was run at the same nominal TWC and PSD, but at M = 0.40 and at a reduced melt ratio of 9.3%. In this case, overall growth was sufficiently small that surface angle did not deviate significantly from that of the substrate. Sticking initiated both at the tip and at the rear radius. The latter is attributed to flow acceleration around the radius, which at this condition causes a reduction in static temperature of ~9°C relative to the bulk freestream, and in wall recovery temperature of ~4°C (taking r = 0.89 [20]). Taking into account the change in relative humidity (based on static conditions), there is a local reduction in static wet bulb temperature from around freezing to -4.6°C. This results in a region highly conducive to re-freezing for the partially melted particles and freestream LWC. The accretion on the radius acts to inhibit runback and sliding, resulting in an even accretion thickness on the walls and a reduction in surface angle of less than 5° over the duration of the test. As a result, thickness growth rate was approximately constant over the test time for both the tip and the wall.

The formation of a cylindrical afterbody was also observed in tests where growth occurred over the entire surface – for example on the 20° half-angle cone shown pre- and post-test in Fig. 11 (a) and (b) respectively.

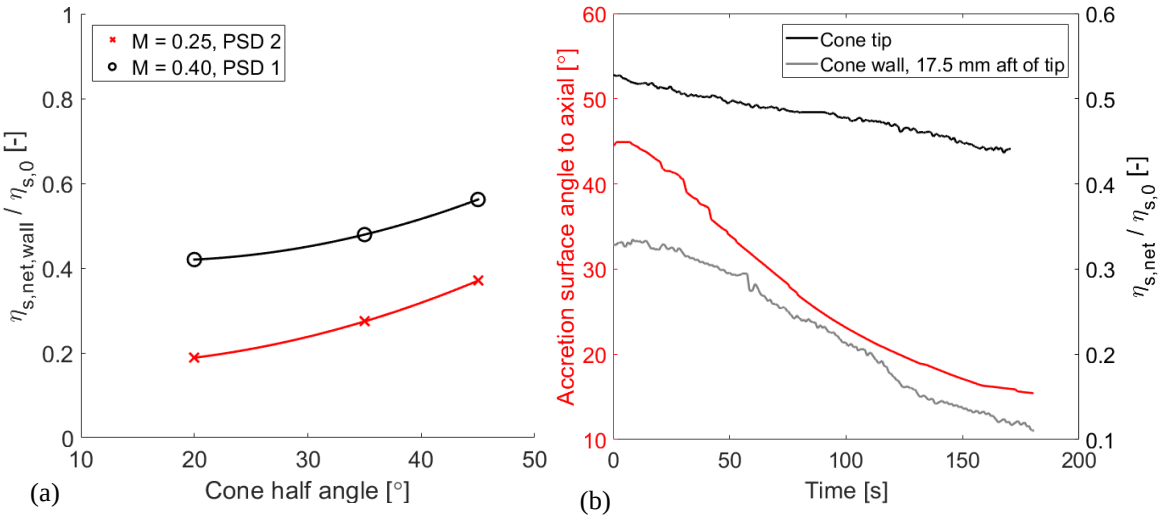

Fig. 9 (a) Net sticking efficiency on the cone wall against (clean) half-angle. (b) Net sticking efficiency and wall surface angle against time for a test on the 45° cone, M=0.25, PSD 2

Fig. 10 (a) Clean 45° half-angle test piece. (b) Accretion corresponding to Fig 9(b) at test completion, M = 0.25, MR = 12.5%, PSD 2. (c) Accretion at test completion for a run at M = 0.40, MR = 9.3%, PSD 2.

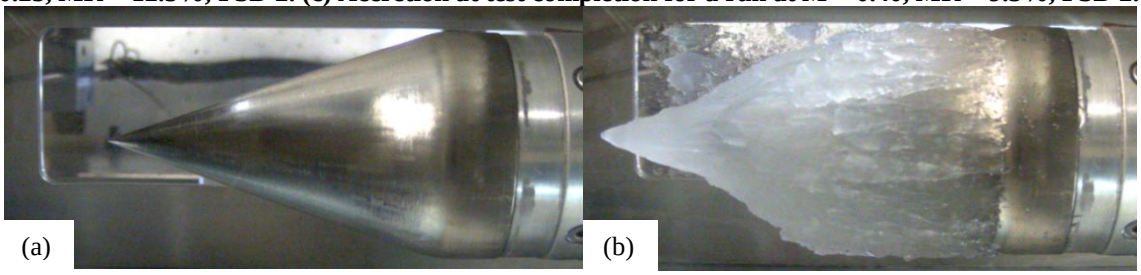

Fig. 11 (a) Clean 20 half-angle test piece. (b) At test completion; M = 0.25, MR = 11.0%, PSD 1.

E. Effect of Particle Size Distribution (PSD)

Fig. 12 shows net sticking efficiency at the tip against particle D_{v50}, for all the cones at M = 0.40 and for the 20° half-angle cone at M = 0.25. All tests were run at TWC = 8 g/m^3 and all test points were within the plateau of sticking probability, at 9 – 13 % melt ratio. The normalised sticking efficiency decreases by at least 60% in all cases when the D_{v50} is raised from ~ 34 µm to ~ 40 µm. For all cases, normalised sticking efficiency is less than 0.02 for D_{v50} greater than 50 µm. For the M = 0.25 case the reduction is more severe, from a peak value of 1.03 to zero within a change of 16 µm D_{v50}.

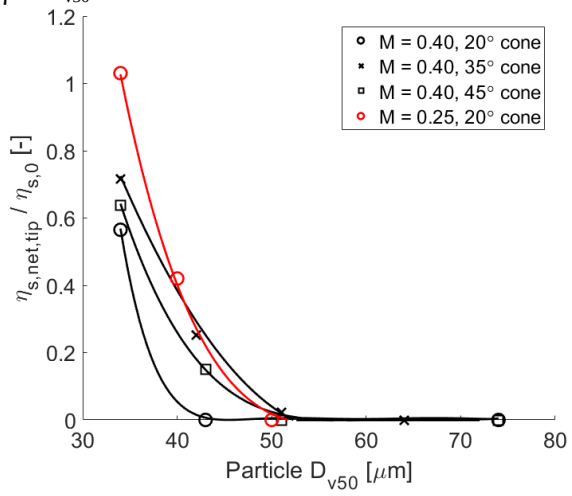

Fig. 12 Net sticking efficiency at the tip against D_{v50}, for cases where MR = 9 - 13 %

It is important to note that in all these cases, D_{v90} is also increasing. It has been proposed in [14] that D_{v90} is more important than D_{v50} in predicting erosion and has a greater effect on sticking efficiency for the same increase in magnitude. To investigate this, a 'transient PSD' run was performed. In this run, ice was injected continuously over ~ 240 s. After every 60 s, the speed of the grinder was reduced (at a fixed injection air velocity). This technique allowed D_{v50} to be held approximately constant, whilst D_{v90}, and the maximum recorded particle size, $D_{v,max}$ were increased. The accretion was built rapidly within the first 60 s (using the smallest PSD), followed by decreasing growth rates as the D_{v90} was raised. Within each 60 s window, the growth rate was approximately constant. Growth data from the first 15 s of each new grinder setting was not included to avoid incorporating transients in the grinder speed. The test was run at M = 0.40. Table 4 shows the measured PSD at each of the four settings and the corresponding normalised net sticking efficiencies.

Table 4 Particle size statistics and corresponding accretion growth rates at the tip for a continuous run with transient grinder speed

Grinder speed [RPM]	D_{v10} *[µm]*	D_{v50} *[µm]*	D_{v90} *[µm]*	$D_{v,max}$ *[µm]*	$\eta_{s,net}$ / $\eta_{s,0}$ *[-]*
4100	17.7	34.6	61.3	94.8	0.758
3600	17.8	35.1	71.6	108.6	0.645
2300	17.7	36.7	77.8	125.8	0.456
1460	16.6	35.1	75.4	176.3	0.0757

Table 4 shows that the D_{v10} and D_{v50} change relatively little over the four conditions, with a maximum difference of 7% and 6% respectively. The first three rows show a steady increase of D_{v90} and $D_{v,max}$. For these rows, there is a good linear fit between net sticking efficiency and D_{v90}^3. This is unsurprising since the onset of erosion will occur when the kinetic energy of the incoming particles (proportional to the cube of the particle diameter) is sufficient to overcome the surface energy of the accreted ice. Between rows 3 and 4, where D_{v10}, D_{v50} and D_{v90} are all held constant within 6%, but $D_{v,max}$ increases by 40%, normalised sticking efficiency falls by ~ 85%. This shows again that a very small number of very high mass particles can have a very strong influence on the total mass of accreted ice. Over longer timescales within the engine environment, Table 4 shows that a significant shift in the right hand tail of the size distribution (which would only manifest itself as a marginal increase in mean diameter) could result in either no accretion or a significant blockage. This re-iterates the importance of accurately modelling preconditioning effects in the low pressure compressor system. In modelling work, since the value of $D_{v,max}$ is not usually known confidently or a priori, the relationship between net sticking efficiency and D^3 will be used.

VIII. Semi-Empirical Erosion Model

A semi-empirical model for erosion may now be defined based on the experimental observations made. In the first analysis, it is assumed that the mass removal is the sum of an erosive term and a constant. These terms are extracted from the experimental data using Equation 6.

$$\eta_{loss} = \eta_{ero} + H = 1 - \frac{\eta_{s,net}}{P_S} \tag{6}$$

This equation essentially reads that the net sticking efficiency is defined as the product of the sticking probability and the mass removal efficiency, η_{loss}. For each datapoint, $\eta_{s,net}$ is known and the value of P_S is calculated for using its melt ratio and Fig. 7. The constant H is a tunable parameter and may account for non-erosive mass loss (e.g. bouncing and sliding).

Based on the experimental observations above, it is assumed that η_{ero} takes the following form:

$$\eta_{ero} = f(U^2, sin^2(\gamma), \overline{D^3}) \tag{7}$$

A quasi- kinetic energy parameter, defined as $K = \overline{D^3}U^2$ is introduced at this stage. $\overline{D^3}$ is calculated by cubing the particle diameter for each bin in the distribution and then taking a mass average. Overall this was found to correlate better with the data than basing it on the cube of the 50th or 90th percentile statistic.

In [2] and [4] the erosion models presented also take into consideration that the lower the accretion surface temperature, the harder the accretion will be and the less erosion will occur. In other words, at higher temperatures a lower strain rate is required to cause the onset of erosion. This term is therefore included for completeness. Equation 7 is then modified to read:

$$\eta_{ero} = f(U^2, sin^2(\gamma), \overline{D^3}, \left({T_w}/{T_f}\right)) \tag{8}$$

Using [4] the dependency of erosion on wall temperature may be expressed by

$$f\left({T_w}/{T_f}\right) = e^{\left(-G\,{Q_s}/{R}\left({1}/{T_w} - {1}/{T_f}\right)\right)} \tag{9}$$

where G is a model constant, T_w is the ice surface temperature (taken as approximately equal to the measured total wet bulb temperature, $T_{wb0,m}$), T_f is the melting temperature, Q_S, the ice activation energy, is 4.82E4 J/K.mol and R, the perfect gas constant, is 8.314 J/K.mol [4].

A final parameter, K_0, is introduced, defined as the kinetic energy at the known reference net sticking efficiency, $\eta_{s,0}$. At M = 0.25 and PSD 1, K_0 ~ 5E-10 J.m^3/kg. The corresponding erosive efficiency is given by $\eta_{ero,0} = 1 - \frac{\eta_{s,0}}{P_S} - H$.

The mass removal model is now fully defined, as given in Equations 10 and 11.

$$\eta_{loss} = \min(1, \eta_{ero} + H) \tag{10}$$

$$\eta_{ero} = A\left(1 + \log_{10}\left({K}/{K_0}\right)\right)(1 + B\,sin^2\gamma)\,(e^{\left(-C\,{Q_s}/{R}\left({1}/{T_w} - {1}/{T_f}\right)\right)}) \tag{11}$$

The model is plotted in Fig. 13 against experimental results. A line of unity slope is also plotted for reference. The model constants and their physical significance are given in Table 5. The results plotted include data from the 20°, 35° and 45° cones, Mach numbers of 0.25, 0.40 and 0.50, all PSDs and melt ratios in the range ~ 8 – 18% (total wet bulb temperatures in the nominal range 1.0 – 5.5 °C). Data is plotted for both the tip and the cone walls. In the case of the walls, net sticking efficiency (and hence mass removal efficiency) has been measured both near the start of the test (where the accretion angle ≈ the cone angle), and also near the end of the test where long, low half-angle accretions have built up. The range of accretion surface angles (γ) at which experimental results are shown is therefore 0 - 74°.

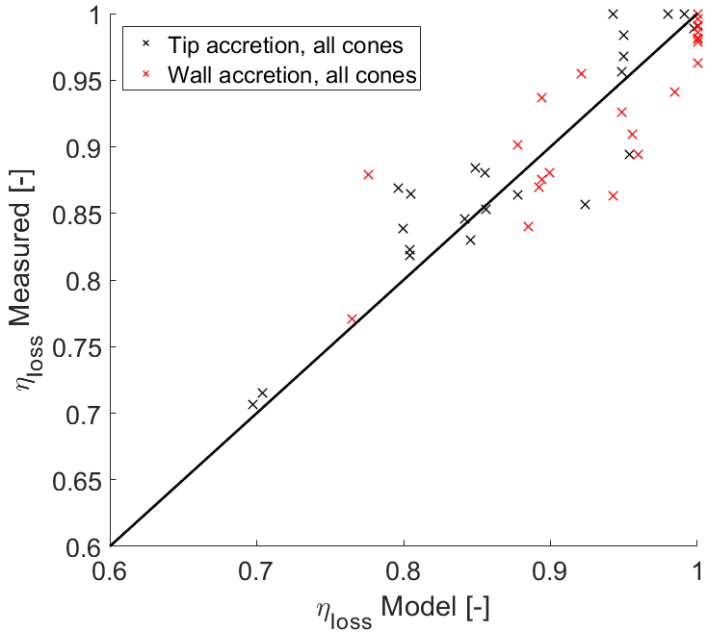

Fig. 13 Measured mass removal efficiency against the model predictions of Equations 15, 16

Table 5 Summary of parameters in the mass removal model

Parameter	*Significance / effect*	*Value*
A [-]	Magnitude of erosion term relative to constant *H*	0.2
B [-]	Influence of wall angle on erosion	1.0
C [-]	Influence of accretion surface temperature on erosion	0.3
H [-]	Constant for other mass loss mechanisms	0.46

IX. Conclusions

An axisymmetric conical test article was used for a parametric study of net sticking efficiency as a function of Mach number, Total Water Content (TWC), melt ratio, surface angle and particle size distribution (PSD). A shadowgraphy technique was used to measure the ice accretion growth rate on the nose, with isometric camera views for qualitative assessments of spatial uniformity and build/shed events. Net sticking efficiency was defined as the net (measured) sticking mass flux as a fraction of the impinging mass flux. The new semi-empirical models for sticking probability and erosion presented here are simply component parts of a complete ice crystal accretion model – specifically, parts responsible for surface continuity – and should be coupled with a thermodynamic Messinger-style model to form a complete icing code. A new ice crystal icing code is being developed alongside this study, however the models presented are also suited for substitution into existing ice crystal codes.

The following conclusions can be made:

1. Net sticking efficiency is highly dependent on melt ratio, for tests at the same nominal 'erosive condition' (i.e. same PSD and Mach number). In purely glaciated conditions, or where melt ratio exceeds ~34%, no sticking is expected. A peak net sticking efficiency is expected in the plateau region, of 9-13% melt ratio. The narrow width of this plateau is indicative that the secondary thermodynamic effects of changing Mach number are small compared with the melt ratio effect. A new model for sticking probability, as a function of melt ratio is presented.
2. There is a strong mechanical effect of increasing Mach number, due to an increasing rate of erosion. For tests at approximately the same melt ratio, the rate of erosion was observed to be dependent upon the square of velocity. At all tests at M = 0.50, there was no sticking at the tip or the straight section of cone wall. In general, areas of high flow velocity within the engine (for example downstream of windmilling rotor stages during descent) are likely to be less susceptible to large accretions. This effect may be negated in areas of flow acceleration; at M = 0.40 and M = 0.50, a small amount of accretion was observed on the curved transition from cone wall to cylindrical afterbody, attributed to a local reduction in static wet bulb temperature.
3. Net sticking efficiency was observed to decrease when the angle between the surface normal and axial direction increases. Peak sticking efficiencies are therefore expected for impacts at tips and leading edges. This may be attributed to a ductile form of erosion, which is maximum for glancing (tangential)

impacts. The rate of particle sliding and water runback may also be increased at shallow impact angles. This effect was observed for both the clean metal and ice-on-ice sticking.

4. Net sticking efficiency was observed to be strongly dependent on Particle Size Distribution (PSD). Peak values were observed for the smallest D_{v50} tested of ~ 34 µm. Generally no or insignificant sticking was observed when D_{v50} exceeded 50 µm. Erosion was approximately correlated with particle diameter cubed, when mass averaged over the distribution. A run with transient grinder speeds showed that erosion is highly sensitive to the maximum particle size, i.e. the level of positive skew in the distribution.
5. Based on the findings in 2 – 4, a new semi-empirical model for erosion was produced, which was dependent upon particle kinetic energy and impact angle. A term was added to model the effect of decreasing wet bulb temperature (at matched melt ratio) reducing the rate of erosion due to harder accretions [4].
6. The Science Engineering Associates WCM-2000 multiwire probe is shown to have a false response in its LWC measurement due to ice crystals (always below 5%), which is an increasing function with Mach number and particle D_{v50}. At M=0.25, the false response decreases as TWC increases, tentatively attributed to increased particle-particle interaction reducing direct impacts with the water sensing wires.

X. Appendix – Uncertainty Analysis

The following uncertainty analysis uses the method of Moffat [22] where the absolute uncertainty in a measured or derived variable is given as the root-sum-square (RSS) of the individual contributing sources.

A. Measured Parameters

Table A1 shows bias and precision uncertainties in directly measured parameters for an example run. The bias uncertainties quoted were either provided by RATFac, taken from the instrument manufacturers' specifications or taken from [15] in the case of the PSD. The aerodynamic parameters are sampled during a steady-state condition with ice off, where 300 samples are taken over a period of 30 s. Ice flow is then initiated and the test run. During this time, the TWC, LWC and PSD measurements are taken, where at least 150 samples are taken for the TWC and LWC and of the order of 10,000 particles are sampled for the PSD calculation. For the reasons stated in Section IV, the uncertainty in the LWC measurement is not quantified here.

Table A1 Bias and precision uncertainties for measured parameters in an example test

		Uncertainty to 95% confidence		
Parameter	*Mean for run*	*Bias (B)*	*Precision (S)*	*Absolute (U)*
T_0 [°C]	10.8	1.0	0.018	1.0
P_0 [kPa]	34.7	0.030	0.0024	0.030
P_S [kPa]	33.3	0.030	0.0039	0.030
M [-]	0.245	0.0030	0.00023	0.030
TWC CIKP [g/m^3]	8.04	0.40	0.081	0.41
RH [%]	46.2	0.68	0.064	0.68
D_{v10} [µm]	14.4	0.72	0.11	0.73
D_{v50} [µm]	29.7	1.49	0.28	1.51
D_{v90} [µm]	52.9	2.65	1.19	2.90

Run-to-run repeatability of the measured ice growth rate is shown in Table A2. Three runs at the baseline condition were performed approximately 3 days apart. The parameters with the highest deviation between runs was observed to be the D_{v10}, D_{v50} and D_{v90} which have a strong influence on the ice growth rate due to erosion effects [14]. The variation over 9 runs at the 'small' PSD (at the same baseline altitude and relative humidity) is also shown in Table A2.

Table A2 Run-to-run repeatability in tip growth rate and PSD. The tip growth rate is normalised against the M=0.25, PSD 1 reference case

Parameter	*Mean*	*Standard deviation*	*Number of runs*
Normalised tip growth rate [-]	0.806	0.0082	3
D_{v10} [µm]	16.4	1.04	9
D_{v50} [µm]	33.5	2.24	9
D_{v90} [µm]	62.0	6.07	9

B. Derived Parameters

For a variable P derived from measured parameters x, y, z, the uncertainty is given by Equation A1 [20].

$$U_p = \sqrt{\left(\frac{\partial P}{\partial x}\,U_x\right)^2 + \left(\frac{\partial P}{\partial y}\,U_y\right)^2 + \left(\frac{\partial P}{\partial z}\,U_z\right)^2} \tag{A1}$$

Struk & Lynch [23] give a methodology for calculating the bias uncertainty in the ice growth measurement. This is based on a general case of a camera viewing a body at an oblique angle β, when the body is at an angle of attack α. For the setup here, α = β = 0.0 +/- 0.2°, measured with a Mitutoyo 950 digital protractor. The ice thickness in mm, h, is related to the detected ice thickness in pixels, P, α and β by equation A2.

$$h = \frac{P}{S\,\cos(\alpha + \beta)} \quad ; \quad S = \frac{np}{L} \tag{A2}$$

where S is a conversion factor in pixels per mm. This is calculated using L, a known length scale in the image and the corresponding number of pixels np. L is taken as the outside diameter of the cylindrical afterbody, which had an uncertainty of +/- 0.2 mm.

The uncertainty in the thickness in mm at any timestep t is then given by Equation A3. Note that $B_\alpha = B_\beta$.

$$U_h(t) = B_h(t) = \sqrt{\left(\frac{\partial h}{\partial P}\,B_P\right)^2 + \left(\frac{\partial h}{\partial S}\,B_S\right)^2 + 2\left(\frac{\partial h}{\partial \alpha}\,B_\alpha\right)^2}$$

$$= \sqrt{\left(\frac{B_P}{S\cos(\alpha+\beta)}\right)^2 + \left(\left(\frac{-P(t)}{S^2\cos(\alpha+\beta)}\right)\left(\sqrt{\left(\frac{-np}{L^2}B_L\right)^2 + \left(\frac{1}{L}B_{np}\right)^2}\right)\right)^2 + 2\left(\frac{P(t)}{S}\sec(\alpha+\beta)\tan(\alpha+\beta)\,B_\alpha\right)^2} \tag{A3}$$

At the baseline test condition, the uncertainty in ice thickness increases from +/-0.089 mm at the test start to +/- 0.17 mm at the test end.

Taking thickness growth rate, $\dot{h}$, as the gradient in ice thickness h against time, calculated over a time period δ (typically taken as 5 s), the uncertainty in growth rate is given by:

$$U_{\dot{h}}(t) = B_{\dot{h}}(t) = \sqrt{\left(\frac{1}{\delta}B_h(t)\right)^2 + \left(\frac{1}{\delta}B_h(t+\delta)\right)^2 + \left(\frac{-h(t+\delta)+h(t)}{\delta^2}B_\delta\right)^2} \tag{A4}$$

The final stage is to calculate the uncertainty in net sticking efficiency (given by Equation 3). Evaluating Equation A1 with respect to $\dot{h}$, γ, TWC and U_∞:

$$U_{\eta_{s,net}} = \sqrt{\left(\frac{K\,\sec(\gamma)}{TWC\,U_\infty}B_{\dot{h}}(t)\right)^2 + \left(\frac{K\dot{h}\,\tan(\gamma)\sec(\gamma)}{TWC\,U_\infty}B_\gamma(t)\right)^2 + \left(\frac{-K\dot{h}\,\sec(\gamma)}{TWC^2U_\infty}U_{TWC}\right)^2 + \left(\frac{-K\dot{h}\,\sec(\gamma)}{TWC{U_\infty}^2}U_{U_\infty}\right)^2} \tag{A5}$$

where $K = \rho_{acc}/\varepsilon$.

The value of B_P, B_L, B_{np}, B_α, B_δ, U_{U_∞} and U_{TWC} are given in Table A3. The local surface angle, γ, is calculated using the difference in ice thickness in pixels across a short axial distance, summed with the half-angle of the clean geometry. $B_\gamma(t)$ is therefore taken as twice B_P.

Table A3 Terms in equations A3-5 for calculating uncertainty in net sticking efficiency to 95% confidence

Term	*Uncertainty in…*	*Value*
B_P [pixels]	Ice accretion edge detection	1
B_L [mm]	Diameter of afterbody for length scale	0.2
B_{np} [pixels]	Number of pixels corresponding to known length	2
B_α [°]	Angle of camera / angle of attack	0.2
B_δ [s]	Time at which growth rate calculated. Taken as 1 camera frame	0.083
U_{U_∞} [m/s]	Velocity	1.01
U_{TWC} [g/m^3]	TWC	See Table A1

XI. Acknowledgements

The authors would like to acknowledge the following people. Firstly EPSRC for support via the CDT in Gas Turbine Aerodynamics studentship; Rolls-Royce Plc for funding the research; and Martin Neuteboom, Dan Fuleki

and the staff at NRC RATFac for their support and guidance throughout the project and experimental campaign. Also to Dr. Peter Struk of NASA Glenn for many useful discussions prior to and during the campaign. Finally to Trevor Godfrey, Greg King and Hassan Ifti at the Oxford Thermofluids Institute, University of Oxford, for assistance in manufacturing the test article.

XII. References

[1] J. G. Mason, J. W. Strapp, and P. Chow, 'The Ice Particle Threat to Engines in Flight', presented at the 44th AIAA Aerospace Sciences Meeting and Exhibit, Reno, Nevada, 2006.

[2] W. B. Wright, P. C. E. Jorgenson, and J. P. Veres, 'Mixed Phase Modeling in GlennICE with Application to Engine Icing', presented at the AIAA Atmospheric and Space Environments Conference, Toronto, Ontario Canada, 2010.

[3] P. Villedieu, P. Trontin, and R. Chauvin, 'Glaciated and mixed-phase ice accretion modeling using ONERA 2D icing suite', presented at the 6th AIAA Atmospheric and Space Environments Conference, Atlanta, GA, 2014.

[4] P. Trontin, G. Blanchard, and P. Villedieu, 'A Comprehensive Numerical Model for Mixed Phase and Glaciated Icing Conditions', presented at the 8th AIAA Atmospheric and Space Environments Conference, Washington, D.C., USA, 2016.

[5] S. Nilamdeen and W. Habashi, 'Multiphase Approach Toward Simulating Ice Crystal Ingestion in Jet Engines', *AIAA J. Propuls. Power*, vol. 27, no. 5, Sep. 2011.

[6] E. J. Grift, E. Norde, E. Van der Weide, and H. Hoeijmakers, 'Computational Method for Ice Crystal Trajectories in a Turbofan Compressor', no. SAE Technical Paper 2015-01-2139, 2015.

[7] J. G. Mason, P. Chow, and D. M. Fuleki, 'Understanding Ice Crystal Accretion and Shedding Phenomenon in Jet Engines Using a Rig Test', *J. Eng. Gas Turbines Power*, vol. 133, no. 4, Apr. 2011.

[8] D. C. Knezevici, D. Fuleki, and J. MacLeod, 'Development and Commissioning of a Linear Compressor Cascade Rig for Ice Crystal Research', *SAE Tech Pap Ser SAE-2011-38-0079*, Jun. 2011.

[9] P. M. Struk *et al.*, 'Fundamental Ice Crystal Accretion Physics Studies', presented at the International Conference on Aircraft and Engine Icing and Ground Deicing, Chicago, Illinois, 2011.

[10] A. Bucknell, M. McGilvray, D. R. H. Gillespie, G. Jones, A. Reed, and D. R. Buttsworth, 'Heat Transfer in the Core Compressor Under Ice Crystal Icing Conditions', presented at the ASME Turbo Expo 2017, Charlotte, NC, USA, 2017.

[11] P. M. Struk, T. Bartkus, and Tsao J., 'Ice Accretion Measurements on an Airfoil and Wedge in Mixed-Phase Conditions', *SAE Tech. Pap. 2015-01-2116*, 2015.

[12] T. C. Currie, D. M. Fuleki, D. C. Knezevici, and J. D. MacLeod, 'Altitude Scaling of Ice Crystal Accretion', presented at the 5th AIAA Atmospheric and Space Environments Conference, San Diego, California, U.S.A, 2013.

[13] T. Currie, D. Fuleki, and A. Mahallati, 'Experimental Studies of Mixed-Phase and Sticking Efficiency for Ice Crystal Accretion in Jet and Engines', presented at the 6th AIAA Atmospheric and Space Environments Conference, Atlanta, GA, 2014.

[14] D. C. Knezevici, D. M. Fuleki, T. C. Currie, and J. D. MacLeod, 'Particle Size Effects on Ice Crystal Accretion', presented at the 4th AIAA Atmospheric and Space Environments Conference, New Orleans, Louisiana, USA, 2012.

[15] D. Fuleki, J. L. Chalmers, and B. Galeote, 'Technique for Ice Crystal Particle Size Measurements and Results for the National Research Council of Canada Altitude Ice Crystal Test System', *SAE Tech. Pap. 2015-01-2125*, 2015.

[16] C. Davison, C. Landreville, and M. Benner, 'Development and Validation of Compact Isokinetic Total Water Content Probe for Wind Tunnel Characterization', presented at the 8th AIAA Atmospheric and Space Environments Conference, Washington, D.C., USA, 2016.

[17] C. Davison, J. W. Strapp, L. E. Lilie, T. P. Ratvasky, and C. Dumont, 'Isokinetic TWC Evaporator Probe: Calculations and Systemic Error Analysis', presented at the 8th AIAA Atmospheric and Space Environments Conference, Washington, D.C., USA, 2016.

[18] P. M. Struk *et al.*, 'An Initial Study of the Fundamentals of Ice Crystal Icing Physics in the NASA Propulsion Systems Laboratory', presented at the 9th AIAA Atmospheric and Space Environments Conference, Denver, Colorado, 2017.

[19] A. Haider and O. Levenspiel, 'Drag Coefficient and Terminal Velocity of Spherical and Nonspherical Particles', *Powder Technol.*, vol. 58, pp. 63–70, 1989.

[20] L. F. Crabtree, R. L. Dommett, and J. G. Woodley, 'Estimation of Heat Transfer to Flat Plates, Cones and Blunt Bodies', R.A.E. Farnborough, 3637, Jul. 1965.

[21] G. P. Tilly, 'A Two Stage Mechanism of Ductile Erosion', *Wear*, vol. 23, pp. 87–96, 1973.

[22] R. Moffat J., 'Describing the Uncertainties in Experimental Results', *Exp. Therm. Fluid Sci.*, vol. 1, no. 1, pp. 3–17, 1988.

[23] P. M. Struk and C. J. Lynch, 'Ice Growth Measurements from Image Data to Support Ice-Crystal and Mixed-Phase Accretion Testing', presented at the 4th AIAA Atmospheric and Space Environments, New Orleans, Louisiana, USA, 2012.

5.4 Bounce and Shatter

5.4.1 ONERA bounce-shatter model

A new bounce-shatter model for ice crystals was developed by the Office Nationale d'Etudes et de Recherches Aérospatiales (ONERA) (Trontin et al., 2016; Villedieu et al., 2014). The model uses a non-dimensional parameter defined as the ratio of normal kinetic energy to surface energy. This parameter was has been observed experimentally to define the change of regime from bounce to shatter for both ice particles (Vidaurre and Hallett, 2008) and hail (Guégan et al., 2012). It is given as

$$\mathcal{L} = \frac{\rho_p \pi \frac{1}{6} {D_{eq}}^3 \frac{1}{2} {U_{p,n}}^2}{\pi e_\sigma {D_{eq}}^2} = \frac{1}{12} \frac{\rho_p D_{eq} {U_{p,n}}^2}{e_\sigma} \tag{5-2}$$

where $U_{p,n}$ is the particle velocity normal to the wall and e_σ is the surface energy per unit area. The ratio may be seen as equivalent to a Weber number for solid particles. At some critical value of this parameter, the energy released by crack propagation exceeds the total surface energy of the particle. The particle is treated as a solid sphere and therefore equation (5-2) is likely to overpredict the shattering threshold – for example shards or porous particles will shatter more readily – and does not capture the effect of particle orientation at the point of impact.

The surface energy is given as (Villedieu et al., 2014)

$$e_\sigma(T) = e_{\sigma,0} \exp\left(Q_s \left(\frac{1}{RT} - \frac{1}{RT_{ref}}\right)\right) \tag{5-3}$$

where Q_s is the crack activation energy, given as $Q_s = 4.82\, x10^4$ J/K. mol and $e_{\sigma,0} = e_\sigma(T_{ref})$ where $e_{\sigma,0} = 0.12$ J/m^2 and $T_{ref} = 253$ K.

Three distinct regimes are defined: (i) a quasi-elastic bounce, (ii) a non-elastic bounce with internal fracturing and (iii) fragmentation. The boundary between (i) and (ii) is given as $\mathcal{L}_1 \cong 0.5$ and between cases (ii) and (iii) as $\mathcal{L}_2 \cong 90$. The bouncing regime (cases (i) and (ii)) is considered first. The semi-empirical models used in both the bounce and shatter regimes were developed from experimental investigations of ice particle impact (Hauk et al., 2014; Higa et al., 1998) and hail impact (Guégan et al., 2012; Pan and Render, 1996; Render and Pan, 1995).

5.4.2 Bouncing Regime

In the bouncing regime, the particle ice density and sphericity are left unchanged pre- and post-impact. In the current model, meltwater is assumed to shed onto the surface. The new particle mass and diameter are given by

$$m_p{}' = m_{p,i} \quad ; \quad D_{eq}{}' = D_{eq,i} \tag{5-4}$$

where dash superscripts denote post-impact properties. The particle velocity normal and tangential to the surface are given by

$$U_{p,t}{}' = \epsilon_t U_{p,t} \quad ; \quad U_{p,n}{}' = -\epsilon_n U_{p,n} \tag{5-5}$$

where the tangential and normal coefficients of restitution, ϵ_t and ϵ_n, are given in the ONERA model as

$$\epsilon_t = 1 \quad ; \quad \epsilon_n = 1 \text{ for } \mathcal{L} < \mathcal{L}_1 \quad ; \quad \epsilon_n = \left(\frac{\mathcal{L}_1}{\mathcal{L}}\right)^{1/3} \text{ for } \mathcal{L}_1 < \mathcal{L} < \mathcal{L}_2 \tag{5-6}$$

5.4.3 Shattering Regime

In the shattering regime, there is significant absorption of normal kinetic energy due to fragmentation. This results in shallow exit angles regardless of the inlet angle (Guégan et al., 2011). For impacts where $L \gg L_2$, as may be expected on airframes or engines, fragments may number in the hundreds (Guégan et al., 2011; Vidaurre and Hallett, 2008), which may be prohibitive for characterising the fragment size distribution. As a result, literature models or data for secondary particle diameter is limited. From a modelling perspective, computational cost may also be prohibitive if hundreds of new particles are created per impact.

In the ONERA model, a single numerical particle is released following impact, which represents all of the shattered fragments. The diameter of the new numerical particle is given by

$$D_{eq}{}' = \alpha D_{eq,max}{}' = \alpha D_{eq} \left(\frac{L_2}{L}\right)^{2/11} \tag{5-7}$$

where α is chosen randomly from a uniform distribution between 0 and 1, and $D_{eq,max}{}'$ is the theoretical diameter of the largest fragment. A simple extension is proposed in the current work where multiple

fragments are released, albeit with the same initial velocity. Particle meltwater is again assumed to shed onto the surface. The total mass of all the fragments therefore sums to the ice core mass pre-impact, similarly to the bouncing regime. It is assumed that if there are N_s fragments, then $(N_s - 1)$ have diameter equal to ${D_{eq,max}}'$, and the remaining fragment has a diameter necessary to maintain the original mass. The number of fragments is therefore given by

$$N_s = ceiling\left(\frac{D_{eq}}{{D_{eq,max}}'}\right) \tag{5-8}$$

The diameter of the last fragment is given by

$${D_{eq,N_s}}' = \frac{6}{\pi}\frac{1}{\rho_i}\sqrt[3]{m_{p,i} - (N_s - 1)\frac{\pi}{6}\rho_i {D_{eq,max}}'^3} \tag{5-9}$$

since the total mass post-impact must equal the ice core mass pre-impact:

$${m_p}' = \sum_{s=1}^{N_s} {m_{p,s}}' = m_{p,i} \tag{5-10}$$

where $m_{p,i}$ is the ice core mass pre-impact, and ${m_{p,s}}'$ is the mass of fragment s. Further work is required to generate a more realistic model of post-impact particle size distribution.

ONERA present an empirical model for the change in tangential velocity during the shattering process. It has been shown that the energy released on shattering may lead to the average tangential velocity of the fragment cloud exceeding the pre—impact tangential velocity (Guégan et al., 2011). In the ONERA model, the change is accounted for using an additional coefficient of restitution, ϵ_{nt}. Since the energy release is related to the severity of fragmentation, it can be related to $\mathcal{L}$. The overall tangential velocity post-impact is given by

$${U_{p,t}}' = \epsilon_{tt} U_{p,t} + \epsilon_{nt} U_{p,n} \tag{5-11}$$

where $\epsilon_{tt} = 1$ and

$$\epsilon_{nt} = 0.4\left(1 - \sqrt{\frac{L_2}{L}}\right) \tag{5-12}$$

The overall tangential coefficient of restitution is then given by $\epsilon_t = {{U_{p,t}}'}/{U_{p,t}}$.

The normal velocity post-impact is given by

$$U_{p,n}{}' = -\epsilon_n U_{p,n} \tag{5-13}$$

where

$$\epsilon_n = \left(\frac{\mathcal{L}_1}{\mathcal{L}}\right)^{1/3} \tag{5-14}$$

At this point it is instructive to consider which regimes are pertinent to engine ice crystal icing. Fig. 5-2 plots lines of $\mathcal{L} = \mathcal{L}_1$ and $\mathcal{L} = \mathcal{L}_2$ for equivalent diameter against normal velocity. Normal velocities above the $\mathcal{L} = \mathcal{L}_1$ line but below the $\mathcal{L} = \mathcal{L}_2$ will result in non-elastic rebounds with internal fracturing; normal velocities above the $\mathcal{L} = \mathcal{L}_2$ line will result in fragmentation. It was highlighted in chapter 2 that the particle equivalent diameter at the inlet to the IPC is expected to be of the order of 10s of microns. Given that velocity magnitudes in the early IPC may typically be in the range 80 – 160 m/s at a top of descent condition, high-slip impacts with static surfaces ($Stk \gg 1$) or impacts with rotors may result in $\mathcal{L} > \mathcal{L}_2$, i.e. particle breakup. Impacts with low slip (i.e. $Stk \sim 1$) are more likely to cause inelastic rebound, $\mathcal{L}_1 < \mathcal{L} < \mathcal{L}_2$. The latter case was found in the ice crystal ingestion simulations of Pratt and Whitney (Feulner et al., 2015). Breakup in the fan and IGV reduced the median mass diameter (MMD) from 150 µm to 28 µm at a cruise condition. However, beyond this the MMD decreased only marginally from 28 µm to 25 µm in four stages of LP booster.

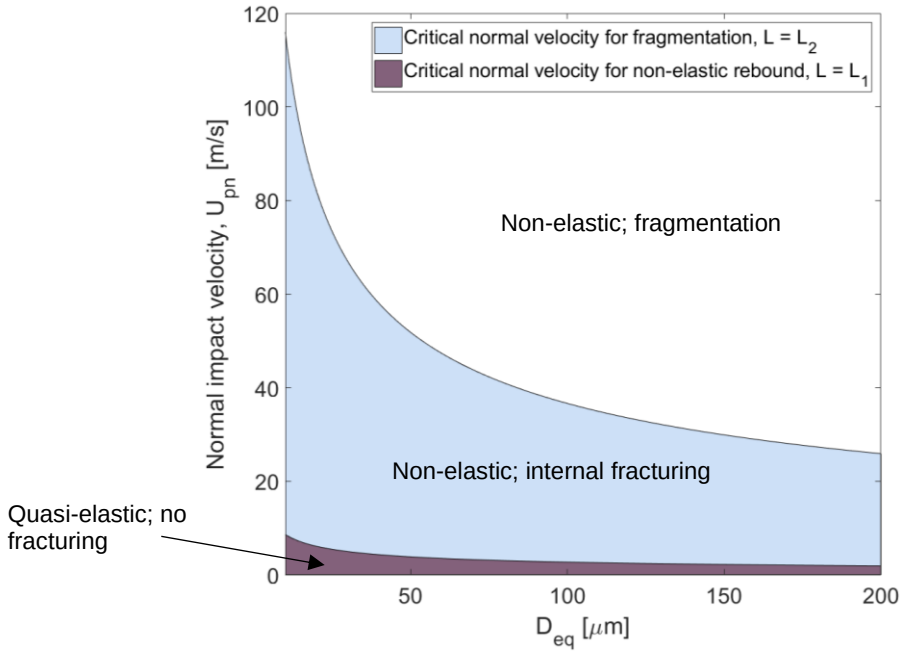

Fig. 5-2 Normal impact velocity against equivalent diameter for lines of $\mathcal{L} = \mathcal{L}_1$ and $\mathcal{L} = \mathcal{L}_2$

Fig. 5-3 shows the normal and tangential coefficients of restitution plotted against $\mathcal{L}/\mathcal{L}_2$. A value of $\mathcal{L}/\mathcal{L}_2 = 1$ signifies the onset of particle fragmentation. At a fixed normal impact velocity of 80 m/s, the corresponding particle equivalent diameter is also given. Particles of < 20 μm will not fragment but will still lose up to ~ 85% of their wall-normal momentum.

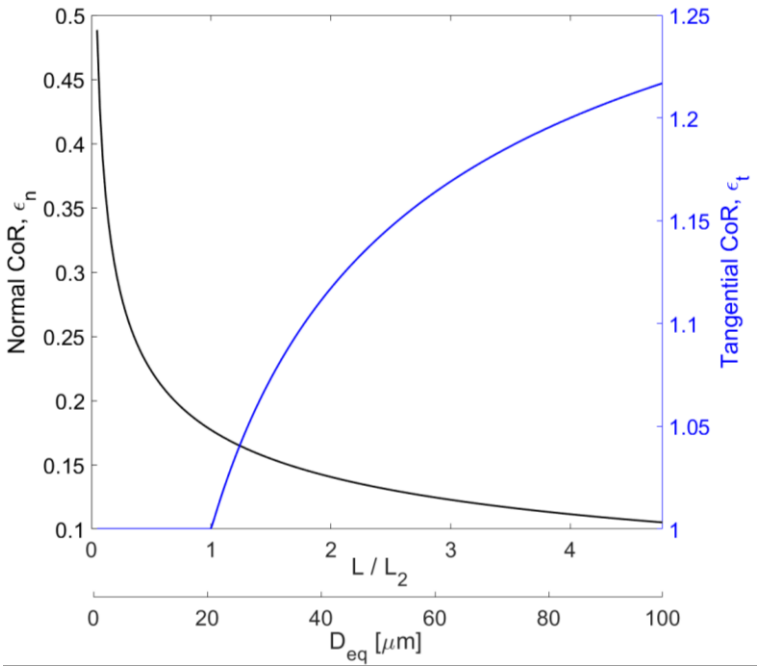

Fig. 5-3 Normal and tangential coefficients of restitution against $\mathcal{L}/\mathcal{L}_2$

5.4.4 Heat Transfer during Impact

It has been shown in previous experimental studies (Currie et al., 2014; Struk and Wright, 2012) that for ice crystal to stick to a surface, a proportion of the impinging cloud must be liquid (whether by particle melt or by injecting supplemental liquid water).

On the assumption that particles may melt through (i) heat transfer with the air and (ii) heat transfer with surfaces, a model for (ii) needs to be defined in order to accurately predict the overall melt ratio. Such a model can be confined to a specific scenario – that of bouncing or fragmenting impacts with a clean (de-iced) surface. This may happen in the engine if particles are incident on heated vanes / struts (e.g. the Engine Section Stator (ESS) when anti-ice heat is switched on); or during the initial transient when the engine first enters the cloud. The restriction of 'clean' surfaces assumes that the heat transfer incurred during impacts with iced surfaces is negligible since both surface and particle will have a temperature at or near the freezing temperature.

If the ‘bulk’ heat transfer from the surface to the particle cloud can be predicted, the average change in particle melt ratio may also be calculated. If a Finite Element Model (FEA) is available, the thermal response of the substrate can thus be determined. Current ice crystal icing models (Villedieu et al., 2014; Wright et al., 2010) neglect this heat transfer due to a lack of literature data at engine-representative conditions.

Experimentation was therefore required to generate a useable dataset. A test campaign was conducted at the National Research Council of Canada’s Altitude Icing Wind Tunnel (AIWT) to parametrically characterise heat transfer from a flat plate in glaciated conditions. The findings were written into a paper entitled “*Heat Transfer in the Core Compressor Under Ice Crystal Icing Conditions”* which was presented at the 2017 ASME TurboExpo, in Charlotte, NC, USA. It was later published under the same title in the ASME Journal of Engineering for Gas Turbines and Power (paper GTP-140-071501). The paper is replicated here. Full citations may be found in chapter 1.

Heat Transfer in the Core Compressor Under Ice Crystal Icing Conditions

Alexander Bucknell
Department of Engineering Science,
University of Oxford,
Oxford OX2 0ES, UK
e-mail: alexander.bucknell@eng.ox.ac.uk

Matthew McGilvray
Department of Engineering Science,
University of Oxford,
Oxford OX2 0ES, UK

David R. H. Gillespie
Department of Engineering Science,
University of Oxford,
Oxford OX2 0ES, UK

Geoff Jones
Rolls-Royce Plc,
Derby DE24 8BJ, UK

Alasdair Reed
Rolls-Royce Plc,
Derby DE24 8BJ, UK

David R. Buttsworth
School of Mechanical and Electrical Engineering,
University of Southern Queensland,
Toowoomba QLD 4350, Australia

It has been recognized in recent years that high altitude atmospheric ice crystals pose a threat to aircraft engines. Instances of damage, surge, and shutdown have been recorded at altitudes significantly greater than those associated with supercooled water icing. It is believed that solid ice particles can accrete inside the core compressor, although the exact mechanism by which this occurs remains poorly understood. Development of analytical and empirical models of the ice crystal icing phenomenon is necessary for both future engine design and this-generation engine certification. A comprehensive model will require the integration of a number of aerodynamic, thermodynamic, and mechanical components. This paper studies one such component, specifically the thermodynamic and mechanical processes experienced by ice particles impinging on a warm surface. Results are presented from an experimental campaign using a heated and instrumented flat plate. The plate was installed in the Altitude Icing Wind Tunnel (AIWT) at the National Research Council of Canada (NRC). This facility is capable of replicating ice crystal conditions at altitudes up to 9 km and Mach numbers up to 0.55. The heated plate is designed to measure the heat flux from a surface at temperatures representative of the early core compressor, under varying convective and icing heat loads. Heat transfer enhancement was observed to rise approximately linearly with both total water content (TWC) and particle diameter over the ranges tested. A Stokes number greater than unity proved to be a useful parameter in determining whether heat transfer enhancement would occur. A particle energy parameter was used to estimate the likelihood of fragmentation. Results showed that when particles were both ballistic and likely to fragment, heat transfer enhancement was independent of both Mach and Reynolds numbers over the ranges tested. [DOI: 10.1115/1.4038460]

Introduction

Over 240 icing-related engine events have been recorded since 1990. Mason et al. [1] analyzed 46 of these events, many of which occurred at altitudes above 7000 m, the recognized upper limit at which water can exist in liquid form.

Figure 1 shows the fan and compressor of a generalized two shaft turbofan engine, with the low pressure compressor stators and intercompressor duct highlighted as areas of potential ice crystal accretion. Mason et al. theorized that partially melted ice particles may stick and refreeze on these surfaces, thus the heat transfer rate between particles and the surface is of great interest.

Fundamental experimental studies have been performed in recent years to further physical understanding and thus enable modeling capability. A key observation is that ice crystal accretion cannot initiate without liquid water present at the accretion location. A study was conducted by the National Research Council of Canada (NRC), Boeing and NASA Glenn Icing Research Branch in 2009 [2] using an S-shaped intercompressor duct with integral titanium strut. The study concluded that the likelihood of accretion is maximized over a specific range of liquid-to-total water content ratios ("melt ratios"). At ratios below this range, particles are more likely to bounce, whereas at high ratios the low ice quantity and water runback also inhibit accretion. Surface thermocouples were able to indicate the onset of accretion, however, could not detect shedding and reforming events. A wedge-shaped simplified aerofoil was used by NASA/NRC in the research altitude test facility in 2010 [3] to measure accretion growth rates for a range of aerodynamic and icing conditions and also to measure heat transfer in dry conditions.

Further research at research altitude test facility by Currie et al. [4] using simple axisymmetric geometries led to a proposed optimal melt ratio band of 10–17%. The data from this study are shown in Fig. 2. These findings imply that during previous engine events in ice crystal conditions, a proportion of liquid water within this critical band was present at the point of accretion. Currie et al. [5] previously reported on experiments to develop altitude scaling rules for mixed phase accretion. As part of these studies, they determined that the accretion growth rate and the steady-state volume were insensitive to how the desired melt ratio was generated—whether by natural melt of ice particles or by injection of supplemental liquid water.

However, what remains unclear in the engine environment is what proportion of the liquid water at the point of accretion is generated by particle-air heat transfer and what proportion by particle-surface heat transfer. Of these, particle-surface heat transfer is significantly more difficult to predict analytically as it depends strongly on the dynamics of the particle-surface impact.

Roisman and Tropea [6] conducted experiments on single particle impacts, using spherical ice particles. These were used to develop analytical and semi-empirical models for particle impact with dry, wet, and heated surfaces. However, the models are unable to capture particle–particle interactions and neglect the effect of bulk particle melting on the convective heat transfer from the surface.

Therefore, at present, there is an absence of data in the open literature on surface heat transfer enhancement in bulk mixed phase or glaciated conditions. These data are critical for understanding and modeling accretion physics in real-world conditions.

The research questions for this paper, therefore, comprise the following:

Contributed by the Combustion and Fuels Committee of ASME for publication in the Journal of Engineering for Gas Turbines and Power. Manuscript received July 22, 2017; final manuscript received September 13, 2017; published online April 10, 2018. Editor: David Wisler.

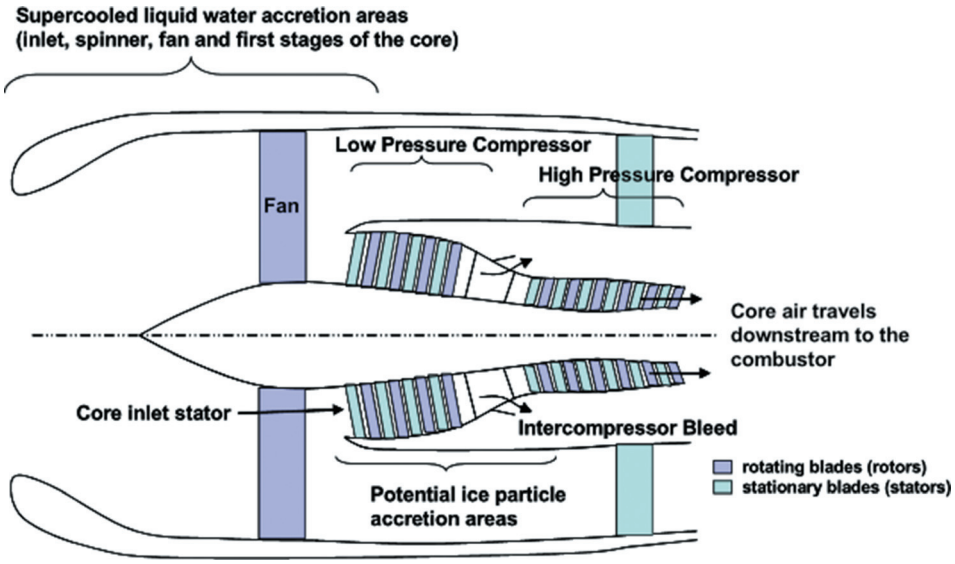

Fig. 1 Schematic of two shaft turbofan, with potential ice accretion sites highlighted [1]

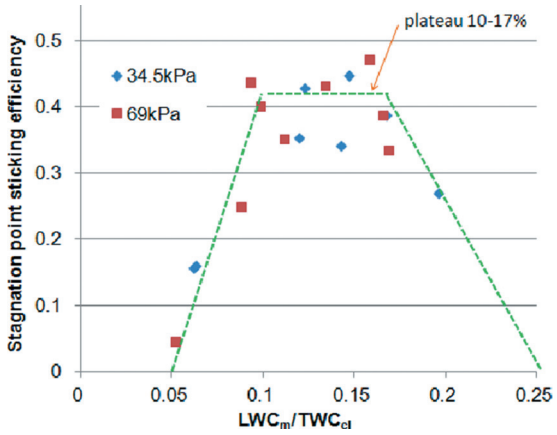

Fig. 2 Ice crystal sticking efficiency versus melt ratio, with a plateau at 10–17% [4]

(1) To what extent does a surface, heated to temperatures representative of the core compressor, contribute to particle melting?
(2) What is the surface heat transfer enhancement over a range of icing and aerodynamic parameters?
(3) Is it possible to use data on particle breakup dynamics to explain the heat transfer behavior observed?

Methodology

Approach. In order to determine the heat transfer enhancement in icing conditions, it is necessary to be able to validate the measured convective heat flux in dry conditions. A flat plate design at variable angle of attack was, therefore, chosen as this is well covered in the open literature. A flat surface also avoids the complication of individual particles bouncing multiple times as may occur on a curved surface when ice is introduced.

To take steady-state heat transfer measurements, the plate (substrate) was designed to be maintained at an elevated design point temperature and be approximately isothermal through high thermal mass. Two nominal substrate temperatures of 25 °C and 35 °C were specified. These temperatures may be found in the core compressor under both cruise and descent idle operating conditions.

Table 1 Experimentally tested parameter ranges

Parameter	Range
M	0.1–0.5
P_{dyn} (kPa)	5–13
MMD (μm)	20–80
AoA (deg)	10–30
TWC (g/m^3)	0.0–3.0
T_{sub} (°C)	25, 35

They also allow a sufficient driving temperature difference with the air and ice, such that the mixed phase heat flux is significant and measurable. Dual layer thin film heat flux gauges (TFGs) were specified to measure surface heat flux.

Parameter ranges of interest to the ice crystal icing phenomenon, and specific to surface heat transfer, were defined as shown in Table 1.

Facility. The facility used in this study was the Altitude Icing Wind Tunnel (AIWT) at the National Research Council, Canada. This is a closed loop altitude facility that uses liquid nitrogen to freeze water particles generated by air blast atomization. The operating envelope and facility characterization may be found in Ref. [7]. A schematic of the facility is shown in Fig. 3. The test section is 520 mm × 330 mm. There is a spatial variation in ice concentration across the tunnel area (i.e., the highest ice concentration may be found along the tunnel centerline). This profile was calibrated prior to the campaign and used in the data postprocessing routines. The aerodynamic and icing calibrations are available in Ref. [8].

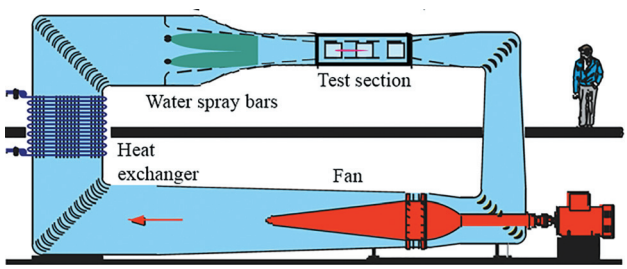

Fig. 3 Schematic of the Altitude Icing Wind Tunnel [7]

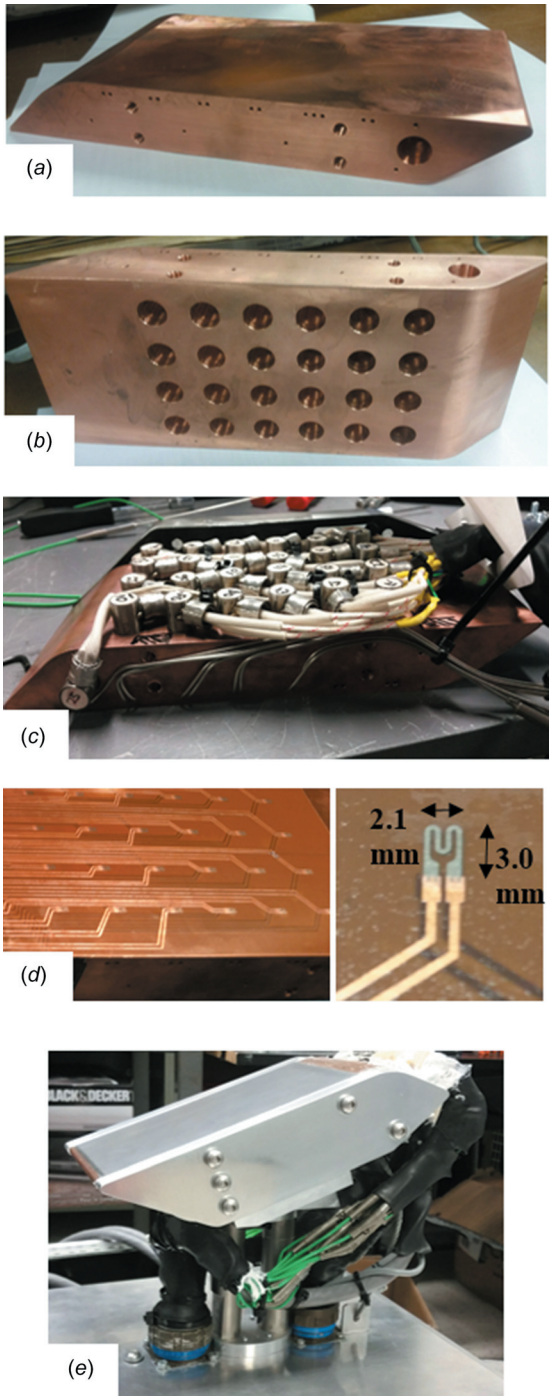

Fig. 4 Test article during stages of assembly. The substrate leading edge is on the right in (*a*) and (*b*); flow is left to right in (*e*): (*a*) Copper flat plate substrate, (*b*) underside of copper substrate, (*c*) installation of thermocouples in the sidewalls and heater cartridges in the underside, (*d*) installation of Kapton layer with integrated thin film heat flux gauges on top surface, and (*e*) addition of Ti90-Al6-V4 layer, and mounting hardware.

Test Piece. The test piece is shown in Fig. 4. It consists of a copper flat plate substrate (Fig. 4(*a*)), of approximate dimensions 240 mm × 100 mm × 32 mm with a 3-mm radius leading edge. The target heat transfer surface is a 150 mm × 100 mm portion immediately downstream of the leading edge. The plate is heated from the underside (shown in Fig. 4(*b*)) using Omega high density heater cartridges, each delivering up to 100 kW/m^2. There are 24 heater cartridges (25.4 mm in length) installed in the underside, and two heater cartridges (50.8 mm in length) installed in the leading edge portion (shown in Fig. 4(*c*)). Above the copper top surface are two additional layers. These comprise a polyimide (Kapton) layer onto which 24 dual layer thin film heat flux gauges are mounted (Fig. 4(*d*)). A simple skin depth calculation was used to specify that the top of the heaters should be no less than 8 mm from the TFG layer to significantly reduce noise on the TFG signals due to AC mains interference.

The TFGs are of a design commonly used at Oxford University and offer high speed temperature measurements with a bandwidth of over 100 kHz. Each consists of a thin (∼40 nm) layer of platinum, sputtered onto each side of a 50-μm-thick polyimide substrate, with 500-μm-wide copper tracks running back to the trailing edge. A constant current of 10 mA is applied to each gauge (which have a resistance of approximately 50 ohms) and the voltage is recorded. Using the method of Collins et al. [9], the temperature T is calculated from the instantaneous voltage V by the following equation:

$$T - T_1 = \frac{(V - V_1)(1 + \alpha(T_1 - T_0))}{\alpha V_1} \tag{1}$$

where T_1 and V_1 are the temperature and voltage, respectively, of a pretest isothermal condition.

The temperature coefficient of resistance, α, was found by calibration, whereby the test piece was immersed in a temperature controlled water bath. The length and type of connecting leads was kept constant between the calibration and the experiment. The resistance of each gauge, R, was measured using a digital multimeter at 18 isothermal conditions in the range 0–80 °C. A linear regression fit was applied to Eq. 2 to find α. R_0 is the gauge resistance at T_0 (0 °C)

$$R - R_0 = \alpha R_0 (T - T_0) \tag{2}$$

The final, top layer of the test piece is a 400-μm thick sheet of Ti90-Al6-V4 foil. This is representative of the material used in gas turbine compressor blades, and thus, provides a representative coefficient of friction when in icing conditions. The complete test piece with mounting hardware is shown in Fig. 4(*e*). A schematic of the test piece (not to scale) is shown in Fig. 5.

Temperature Control. The test piece is designed for both steady-state and high frequency heat transfer measurements. To reference results easily to operating conditions, the test piece is designed to be isothermal both temporally and spatially. This is achieved using embedded heaters controlled using a proportional-integral-derivative negative feedback loop system. For each heater, a K-type thermocouple embedded in the copper substrate between the top of the heater and icing surface provided the error signal for the controller. To achieve spatial temperature uniformity, the substrate was designed to have a Biot number below ∼0.1 for all test cases (∼0.039 at the baseline flow condition). The spatial and temporal uniformity of the substrate temperature is shown in Fig. 6, for a dry run and a run at the maximum ice concentration of 3.0 g/m^3. The average temperature difference between the two runs is ∼0.6 K. In both runs, the plate is isothermal both spatially and temporally within 0.4 K (i.e., within the uncertainty of the thermocouples used).

The heat flux from the plate is expected to vary spatially, both due to falling heat transfer coefficients in the streamwise direction and also due to the higher ice concentration at the center of the plate compared with the outer edges. Therefore, the true wall temperature will also vary spatially between tests at different conditions. It is calculated analytically post-test from the measured heat flux.

The test piece and heater control system designs were validated at the ice crystal wind tunnel at the University of Southern Queensland, Australia. This campaign was also used to develop a

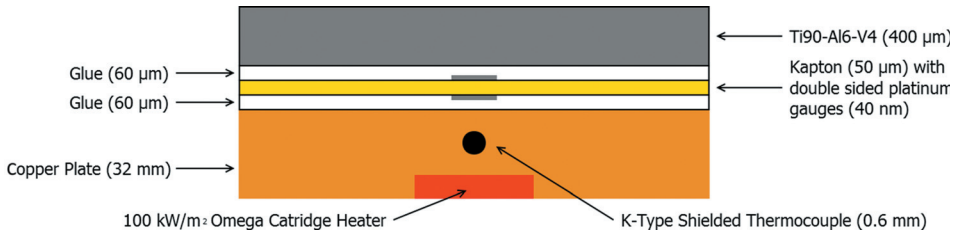

Fig. 5 Schematic of test article (not to scale)

new design of thin film heat transfer amplifier. These boost high frequency, low amplitude temperature fluctuations to avoid quantization errors when sampling. Details of their design are available in Ref. [10]. The new design of heat transfer amplifier combined the signal conditioning circuitry with a variable sample rate data acquisition system in the same unit. This proved to reduce signal noise by a factor of 6 compared with the previous systems, when used in the same environment.

Heat Transfer Modes. The heat transfer balance in a steady-state condition is given by Eq. (3), with heat sources to the plate on the left-hand side and heat sinks on the right-hand side

$$q_h A_h + q_{kin} A_{surf} = (q_{conv} + q_{melt} + q_{sens,ice} + q_{sens,water} + q_{evap}) A_{surf} + Q_{losses} + q_{radiation} A_{plate} \quad (3)$$

The term $q_{sens,ice}$ is the heat required to raise the temperature of the incoming particles to the melting temperature, and $q_{sens,water}$ the heat required to raise the temperature of any meltwater to the wall temperature of the plate. However, evaluating these terms requires prior knowledge of the amount of melting that has occurred (if any). As this is unknown, it is most useful to use a combined mixed phase heat flux term, $q_{mixedphase}$. There is an additional heat source, q_{kin}, due to the kinetic energy of the incoming particles. If all the incoming energy is transferred (i.e., no bouncing), then it may be expressed as in the below equation:

$$q_{kin} = \frac{1}{2}\frac{\dot{m}_{ice}}{A} v_n^2 = \frac{1}{2}\frac{TWC}{1000} v_\infty^3 \sin^2\alpha \quad (4)$$

At the highest flow speed, this term is the same order of magnitude as that of the convective heat flux. However, particle imaging using a particle image velocimetry (PIV) system indicated bouncing and shattering occurred at all flow speeds, so the actual magnitude of this term may be significantly lower. As it is difficult to quantify this, it is therefore also included in the $q_{mixedphase}$ term. This is given by the following equation:

$$q_{mixed\,phase} = q_{conv} + q_{melt} + q_{sens,ice} + q_{sens,water} - q_{kin} \quad (5)$$

The AIWT is a closed loop tunnel, and so evaporation of recirculating ice crystals causes the air to approach saturation conditions. Relative humidity (RH) data from the tunnel (shown in Fig. 7) indicate that the tunnel reaches 85–90% humidity after the first run of the day. In subsequent runs (where data are captured), humidity initially drops to 80–85% as the tunnel is allowed to settle on the target condition in dry flow. When spray is initiated, the humidity rises again, typically remaining above 90% for the 100 s test duration. The lowest measured humidity during an icing run was 89%. Therefore, the $q_{evap/sub}$ term in Eq. (3) was considered negligible.

For the highest wall temperature, the radiative heat flux (assuming that the surroundings were uniformly at the air total temperature) was two orders of magnitude lower than the dry convective heat flux, so $q_{radiation}$ was also neglected. The heat balance of Eq. (3), therefore, may be simplified as given in the below equation:

$$q_{mixed\,phase} A_{surf} = q_{TFG} A_{surf} \quad (6)$$

Particle Glaciation. A prerequisite of the tests was that particles should be fully frozen out at the point of impact. This first allows the replication of conditions early in the core compressor, and also allows in-air melting and evaporation to be neglected, provided the total air temperature was always below freezing and approximately equal to the particle temperature. Pretest

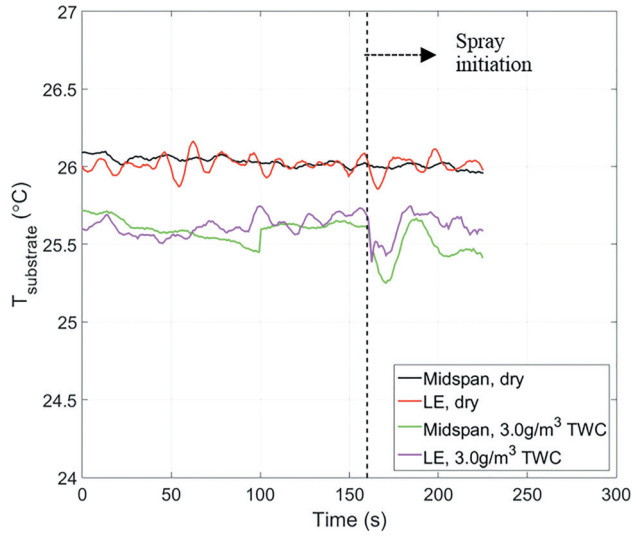

Fig. 6 Spatial and temporal uniformity of substrate temperature (measured 2.5 mm below the copper top surface) for dry and maximum ice concentration runs

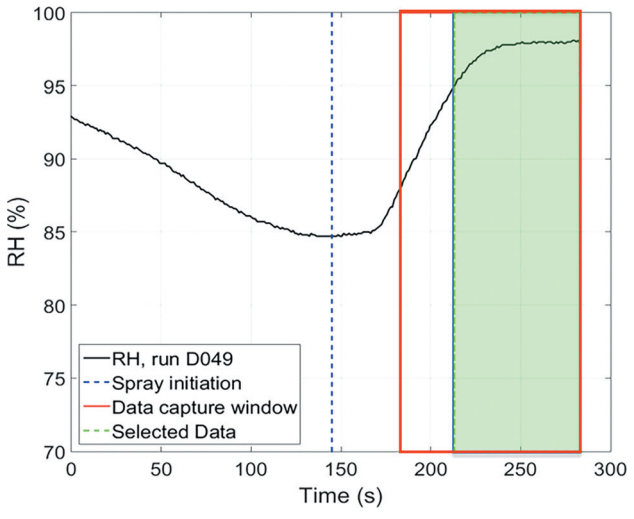

Fig. 7 RH (%) profile pre- and during run, with the data capture window highlighted

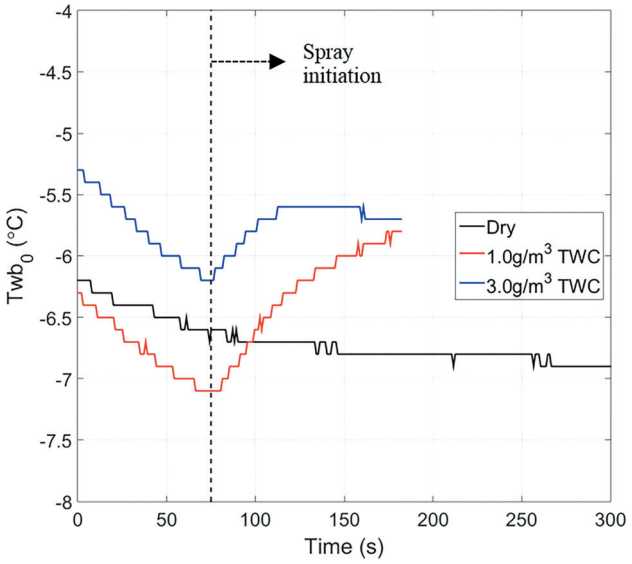

Fig. 8 Total wet bulb temperature profile pre- and during run

calibrations showed that full glaciation could be achieved at the baseline condition of Mach 0.4 and the highest total water content (TWC) of 3.0 g/m^3 for particles with median mass diameter (MMD) of 60 μm or less. To ensure that particles remained frozen between the point of glaciation and the test piece, the total wet bulb temperature was maintained below −5 °C for all tests. This was achieved by maintaining the total dry bulb temperature at −5 °C. With a typical relative humidity of ∼90%, the total wet bulb temperature was, therefore, slightly below this, as shown in Fig. 8.

Experimental Method and Processing. A test matrix was defined using the parameter ranges outlined in Table 1. For each condition, the test point was run in dry conditions followed by a run using the target TWC. Data were gathered for all tests under steady-state conditions (100 s run time). A flow chart of the experimental process and postprocessing tasks is shown in Fig. 9.

For each test, $q_{\text{mixedphase}}$ was converted to Stanton number as shown in the flow chart. Stanton number may be described as the ratio of the total heat flux transferred into a fluid to the mass velocity weighted thermal capacity of the fluid, as shown in the below equation:

$$\text{St}_{\text{exp}} = \frac{h}{\rho v C_{\text{p}}} = \frac{\text{Nu}}{\text{RePr}} \tag{10}$$

Between dry and icing runs, the fluid composition changes. In icing runs, excess nitrogen (used in the liquid water freezeout) and water vapor also exist at the test piece surface. The relative mass flows of these components were used to define a mass fraction average of specific heat capacity and density. An overall thermal conductivity for the mixture was calculated using the method of Lindsay and Bromley [11].

The heat transfer enhancement was calculated by dividing the experimental Stanton number by its theoretical value in dry conditions (Eq. (11)), according to the empirical Nusselt number correlation of Motwani et al. [12] (Eq. (12))

$$\text{St}_{\text{enh}} = \frac{\text{St}_{\text{exp}}}{\text{St}_{\text{dry,corr}}} = \frac{\text{St}_{\text{exp}}\,\text{RePr}}{\text{Nu}_{\text{dry,corr}}} \tag{11}$$

where

$$\text{Nu}_{\text{dry,corr}} = \begin{cases} 0.056\left(1 - \dfrac{\alpha}{44.2}\right)\text{Re}^{0.77} & (\text{for } \alpha = 0 - 15\,\text{deg}) \\ 0.084\text{Re}^{0.68} & (\text{for } \alpha = 30 - 45\,\text{deg}) \end{cases} \tag{12}$$

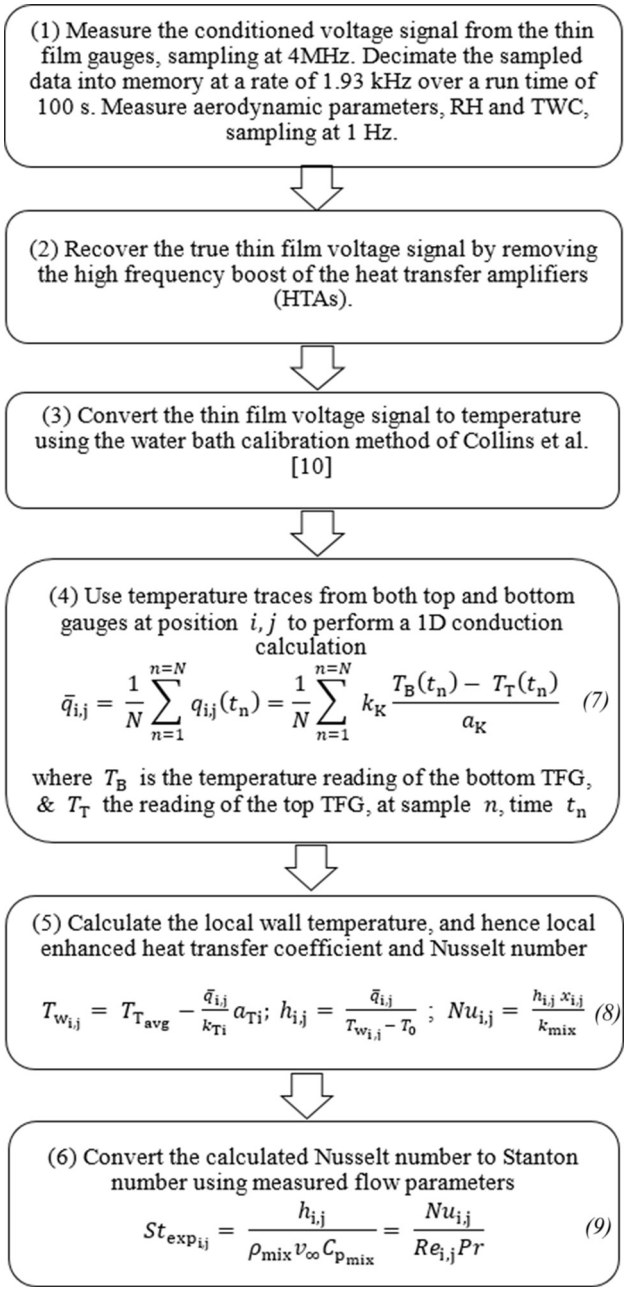

Fig. 9 Flowchart of experimental procedure and postprocessing

This is valid for the Reynolds number range tested experimentally of 2×10^4 to 3×10^5. A Bezier curve fit was used to interpolate between the correlations for angles of attack between 15 deg and 30 deg. Figure 10 shows $Nu_{\text{dry,corr}}$ plotted against local Reynolds number for angles of attack between 0 deg and 45 deg. A theoretical flat plate, turbulent flow Nusselt number correlation is also plotted. This is for the case of a very high aspect ratio plate at 0 deg angle of attack.

Uncertainty Analysis. An uncertainty analysis was conducted using the Taylor Series Method described in Coleman and Steele [13]. A baseline test condition was selected, as shown in Table 2.

Numerical Setup

Numerical discrete phase simulations using Lagrangian particle tracking were used to qualitatively relate the observed heat transfer behavior with particle trajectories in the test section. A

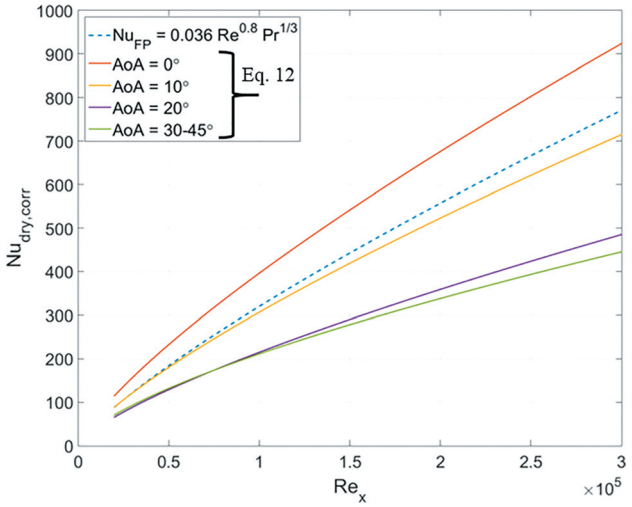

Fig. 10 Nusselt number against local Reynolds number according to Eq. (12), with a theoretical flat plate solution

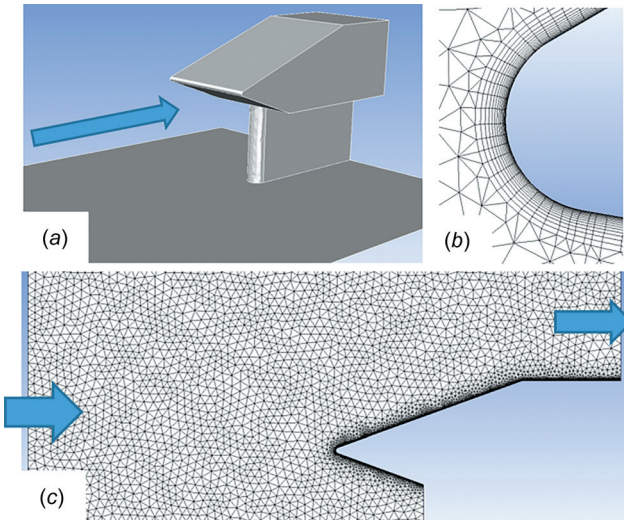

Fig. 11 Computational domain: (*a*) simplified solid model used in computation, (*b*) mesh refinement at the leading edge, and (*c*) two-dimensional slice of computational domain at midspan

flowfield solution was generated using computational fluids dynamic package ANSYS FLUENT for the baseline aerodynamic case and a simplified three-dimensional geometry, at angles of attack of 10 deg and 20 deg. The 20 deg geometry, generated in SOLIDWORKS, and the mesh, generated in meshing package ICEM, are shown in Fig. 11. A sensitivity analysis to turbulence model was conducted. The particle collection efficiency on the impact surface was selected as the parameter under test. It is important to note that the effect of turbulent dispersion on particle trajectory was expected to be minimal; ballistic particles will pass through eddies with little deviation, whereas smaller particles are more likely to be deflected due to the potential field of the test article. The models tested comprised of k–ε with standard wall functions applied, the standard k–ω model and the k–ω shear stress transport (SST) model, as shown in Fig. 12. In all cases, one-way aerodynamic coupling was assumed in the discrete phase model.

The maximum discrepancy in particle collection efficiency between models is below 2%. Using a k–ω formulation (thus resolving down to the wall) was computationally practical for the domain size. The SST model was selected, thus utilizing the k–ε model in the mainstream to define the bulk particle trajectories. The effect of modeling two-way aerodynamic coupling was also investigated, as shown in Fig. 12. The difference in collection efficiency between one- and two-way coupling was less than 0.5%, and therefore, one-way coupling was chosen for all other tests. Sensitivity to the Lagrangian step length—defining the length of the time-step over which the particle equations of motion are integrated—was halved from the standard length of 1 mm to 0.5 mm. At Mach 0.4, this corresponds to a time-step of approximately 2 ms. The discrepancy in collection efficiency between the two cases was again less than 0.5%, thus the original value of 1 mm was maintained.

A mesh sensitivity analysis was also conducted as shown in Fig. 12. Four computational domains of 1.0 M, 1.9 M, 3.7 M, and 7.2 M cells were generated. The difference in collection efficiency for the 3.7 M and 7.2 M was approximately 0.2%, so the 3.7 M cell mesh was used in all subsequent simulations. The maximum y^+ value on the test piece surface was 4.75.

Inlet Mach number, total pressure, and total temperature were matched to the baseline condition in Table 2. Details of the computational domain and setup for the fluid phase are summarized in Table 3, and for the discrete (particle) phase in Table 4. A

Table 2 Uncertainty analysis of measured and derived parameters for baseline test condition

Parameter	Baseline case value	Uncertainty (absolute)	Uncertainty (%)	Source
Measured parameters				
T (°C)	−13.0	0.200	1.54	[8]
T_{TFG} (°C)	28.9	0.150	0.519	
T_{sub} (°C)	35.0	0.500	1.43	
Altitude (m)	5490	12.6	0.229	[8]
P (Pa)	44,780	67.2	0.150	[8]
M	0.40	6.60×10^{-5}	0.0165	[8]
v (m/s)	129.0	0.142	0.110	[8]
RH (%)	90.0	1.80	2.00	[8]
TWC (g/m^3)	1.00	0.200	20.0	[8]
MMD (μm)	40.0	3.00	7.50	[8]
α (deg)	20.0	0.100	0.500	[14]
Derived parameters				
q_{TFG} (W/m^2)	4069	327	8.04	
h (W/m^2/K)	135.4	10.9	8.24	
Nu	225.7	18.2	10.8	
Re	172,100	589	0.342	
St_{exp}	0.002472	1.51×10^{-4}	11.1	
St_{corr}	0.002736	1.13×10^{-4}	4.13	
St_{enh}	0.903	0.0550	11.5	

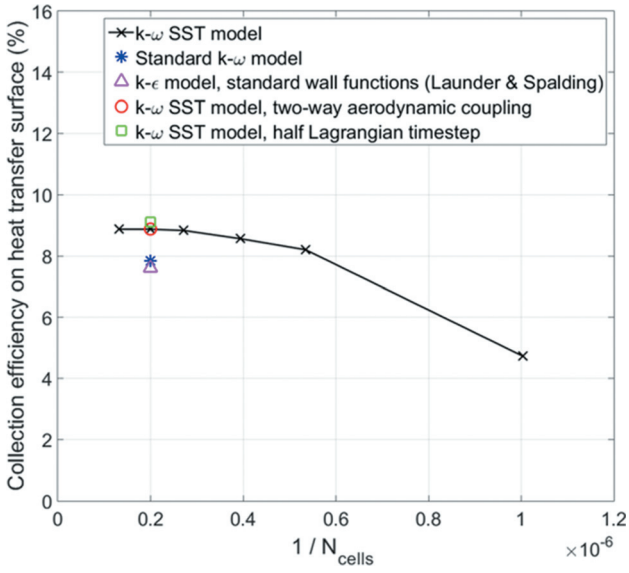

Fig. 12 Sensitivity analysis on particle collection efficiency for varying computational setup

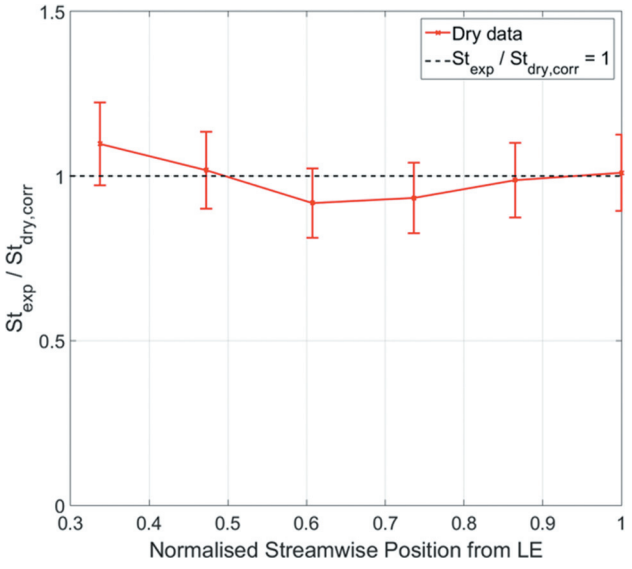

Fig. 13 Validation of measured Stanton number for all streamwise positions

Table 3 Computational domain and boundary conditions

Mesh	Unstructured, 3.7M cells
Boundary layer mesh	15 prism layers
Maximum wall y^+	4.75
Inlet profile	Fully developed turbulent pipe flow
Freestream Tu (%)	0.6 [8]
Turbulence model	k–ω SST
M_∞	0.400
Altitude (m)	5490
T_{01} (K)	268.2

Table 4 Discrete phase modeling parameters

Particle tracking method	Lagrangian
Particle diameters (μm)	10, 20, 40, 60
Particle density (kg/m^3)	940
Body forces	Gravity, drag, pressure gradient, Saffman's lift force
Drag coefficient	Spherical
Wall interaction	Bounce
Lagrangian step length (mm)	1.0
Aerodynamic coupling	one-way
Thermal coupling	None

spherical drag coefficient was applied. The ice particles in the test facility are generated by freezing out water droplets from an air blast atomizer, so this is a reasonable assumption.

Results

Conventions. In the following discussion, the streamwise direction is taken as the flow direction resolved parallel to the test piece surface. Unless otherwise stated, this is 20 deg to the axial direction. In agreement with NRC convention, the left-hand side of the tunnel or test piece when facing downstream is the starboard side and vice versa for port side.

Test Piece Aerothermal Validation

Heat Transfer in Dry Conditions. The dry-flow heat transfer at a range of streamwise positions was first validated against Eq. (12), as shown in Fig. 13. Agreement between the experimental data and correlation is within 10%.

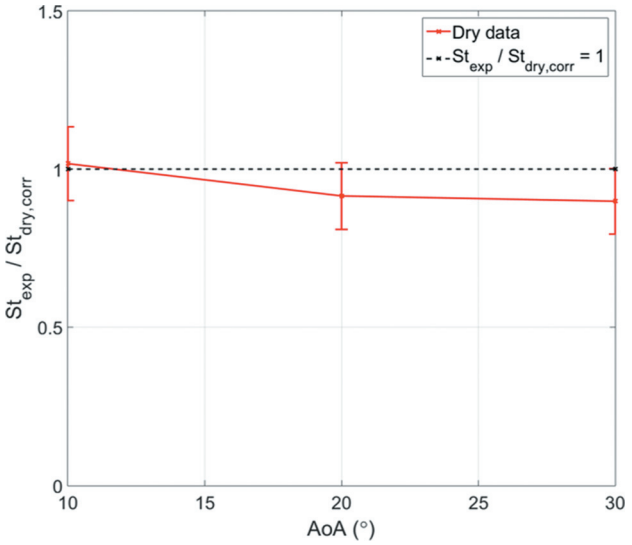

Fig. 14 Validation of measured Stanton number for all angles of attack

Figure 14 shows a comparison of experimental and correlation data for heat transfer at varying plate angles of attack. This was again done in dry conditions at the same baseline condition. Agreement is again within 10%.

The Reynolds number based on streamwise position is in the range 6×10^4 to 3×10^5 for the baseline case defined in Table 2, and thus, is likely to be transitional toward the rear of the plate. Motwani et al. used tripwires to promote a turbulent boundary layer when generating the correlations given in Eq. (12). However, they also found the state of the boundary layer to be dependent upon the angle of attack. The 0.77 exponent on Reynolds number in the first part of Eq. (12) is indicative of a fully turbulent boundary layer. This is attributed to a separation bubble just downstream of the leading edge causing transition. As angle of attack increases, the Nusselt number decreases for a given Reynolds number. This is attributed to the separation bubble decreasing in size as angle rises, as an increasingly favorable pressure

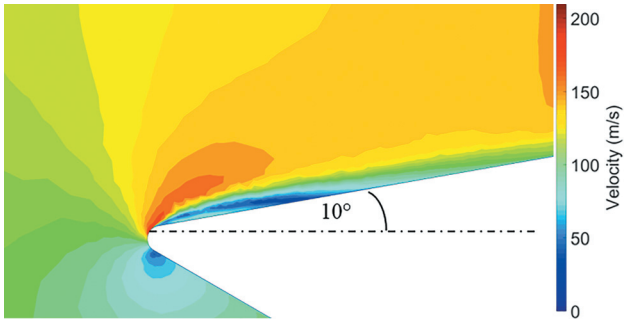

Fig. 15 Velocity contours at midspan for the 10 deg angle of attack case, baseline flow condition. Flow is left to right

gradient is established. The reattachment location, therefore, moves upstream. Increasing angle of attack still further results in relaminarization, as indicated by the 0.68 exponent in the second part of Eq. (12).

Figure 15 shows contours of velocity for the 10 deg angle of attack numerical solution. A separation bubble is clearly visible immediately downstream of the leading edge in agreement with Motwani et al. This separation is eradicated when the angle is raised above 20 deg, compared to above 30 deg for Motwani et al. The discrepancy in Fig. 14 between correlation and experiment at these values could be attributed to this difference.

Spanwise Variation in Total Water Content. The plate was characterized in icing conditions using a series of runs at the baseline aerodynamic condition given in Table 2 and a TWC of 0.5 g/m^3. Figure 16 shows a calibration plot of TWC over the central tunnel area at a nominal injected TWC of 0.5 g/m^3, a particle MMD of 40 μm, and a freestream velocity of 90 m/s [8]. Overlaid as black circles are the positions of the 24 thin film gauges, with the streamwise position mapped to the "vertical" (Z) direction using the plate angle of attack of 20 deg.

For all particle diameters used, heat transfer enhancement readings from the two inner rows of TFGs were always within 5% of each other at a given streamwise position. The outer rows of gauges suffer from a reduction in TWC due to the profile in the tunnel (especially for the port side), sidewall heat loss, and also particle deflection away from the test piece due to its own potential field. Figure 17 shows particle tracks for (*a*) 10 μm and (*b*) 40 μm diameter particles, using the flowfield solution described in Table 3. The particles are injected along a line that is parallel to the most port gauges (also shown on the figure). At a diameter of 10 μm, particles are well entrained in the flow and are deflected around the sidewalls. The only impingements occur on or immediately after the leading edge. In the 40 μm case (the same nominal diameter as used in the calibration data in Fig. 16), particle

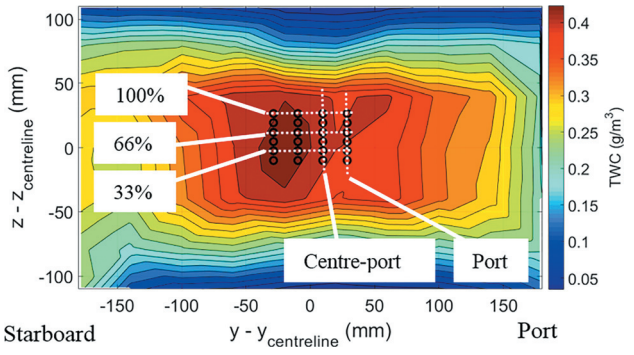

Fig. 16 Profile of total water content over the central tunnel area [7], with the TFG locations overlaid as black circles. 33, 66, and 100% streamwise position gauges are highlighted

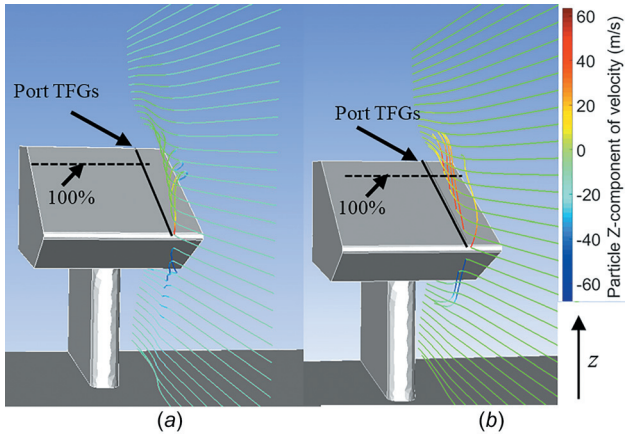

Fig. 17 Particle traces for (*a*) 10 μm particles and (*b*) 40 μm particles, injected in line with the port row of TFGs. Tracks are colored by particle velocity in the *Z* (vertical) direction. Baseline aerodynamic condition; flow is into the page.

deflection increases in the streamwise direction and is significant at the 100% streamwise position. As a result, TWC impinging on the plate is locally reduced. It was, therefore, preferable when comparing between test cases to use an average of the readings of the two central gauges at a given streamwise position. Particle deflection will of course occur for these rows also, albeit with a smaller spanwise component. The effect of this for a range of particle sizes is covered in the Streamwise Variation in Total Water Content for Central Gauges section.

Streamwise Variation in Total Water Content for Central Gauges. Particle studies were conducted using the same setup as described in Table 3, with particles this time injected parallel to the center-port row of gauges (highlighted in Fig. 16). Particle trajectory behavior is approximately symmetrical with the center-starboard location.

Figure 18 shows the streamwise TWC distribution for particles with MMD of 10, 20, and 40 μm. The solid lines denote the distribution if computational fluid dynamics-predicted particle trajectories are only considered, with a uniform TWC profile injected. The distribution was determined by taking the time-averaged particle concentration at a plane immediately upstream of the plate surface. For these studies, the plate surface was assumed to trap all impinging particles, to prevent bouncing particles from passing back through the measurement plane. The dashed lines show the

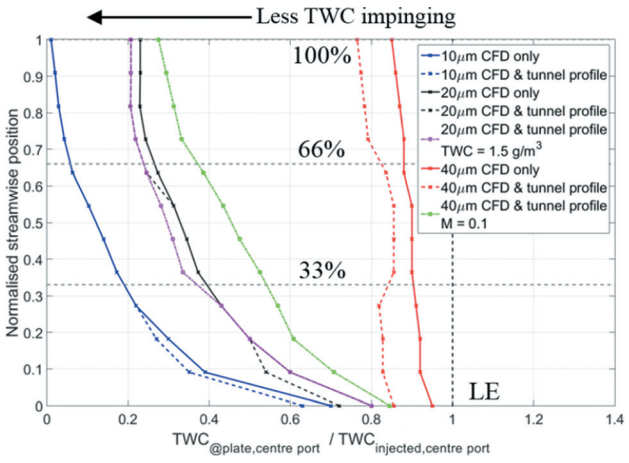

Fig. 18 Total water content impinging on the plate as a fraction of TWC injected, against streamwise location. Baseline aerodynamic condition and TWC = 0.5 g/m^3 unless otherwise stated

Table 5 Particle Stokes number for the test conditions given in Fig. 18

MMD (μm)	Mach	Stokes number (Stk)
10	0.4	0.0761
20	0.4	0.305
40	0.4	1.22
40	0.1	0.334

combined effect of particle trajectories and the nonuniform TWC profile of the tunnel. This is, therefore, the TWC profile that the plate "actually" sees. The data show that at the leading edge, where the potential field effect of the plate is minimal, at least 60% of all particles injected impinge (albeit at increasingly shallow angles as particle diameter decreases). By the 66% streamwise row of gauges, the concentration of 10 and 20 μm particles has fallen to approximately 5% and 20% of the injected TWC, respectively. Conversely, for 40 μm particles, over 80% of particles impinge on the 66% streamwise gauge row. Additionally, there is only a small TWC reduction (~6%) across the length of the plate. Two additional datasets are also plotted, with the aim of investigating how the concentration profiles are expected to change as the conditions are varied from the baseline case (i.e., as points from the test matrix are run). The first of these is the case of an elevated TWC, raised from 0.5 g/m^3 to 1.5 g/m^3. The maximum difference between the cases is 3% of the injected TWC. The second additional line corresponds to a test run at Mach 0.1, which more importantly is the lowest Reynolds number tested experimentally. In this case, the data diverge from the baseline aerodynamic condition (Mach 0.4).

This behavior can be described using the particle Stokes number. Particles with a Stokes number much greater than unity will tend to follow the flow poorly—particularly in regions of high curvature or acceleration—and are termed ballistic. For Stokes numbers of much less than unity, particles tend to follow the flowfield well—i.e., with small or negligible slip velocities. It is given by

$$\mathrm{Stk} = \frac{\tau_p v}{D} \tag{13}$$

where

$$\tau_p = \frac{4}{3}\frac{\rho_p d_p^2}{\mu}\frac{1}{\mathrm{Re}C_d} \tag{14}$$

Stokes numbers were calculated for the three MMDs by using the baseline flow condition to estimate the fluid relaxation time, and the nominal particle diameter to estimate the particle relaxation time. Stokes numbers for the cases shown in Fig. 18 are given in Table 5. As may be expected from the trends in Fig. 18, 10 and 20 μm particles have a Stokes number of less than unity at Mach 0.4, while for 40 μm particles it is less than unity at Mach 0.1 but greater at Mach 0.4.

The 66% streamwise gauge row was selected for use in comparing between test cases. The 33% row may also have been used. The 100% row sees a lower TWC due to the variation in the tunnel profile. It is important to note that in the following results and discussion, the TWC values stated refer to the nominal (injected) values—not the TWC that is present at the plate.

Repeatability Studies. Three tests conducted on three separate days using the baseline case in Table 2 showed measured values of Stanton number repeatable within ~8% for the dry runs and ~11% for the icing runs.

Steady-State Heat Transfer Enhancement Results

Effect of Total Water Content. Figure 19 shows Stanton number enhancement against varying TWC. Aerodynamic conditions

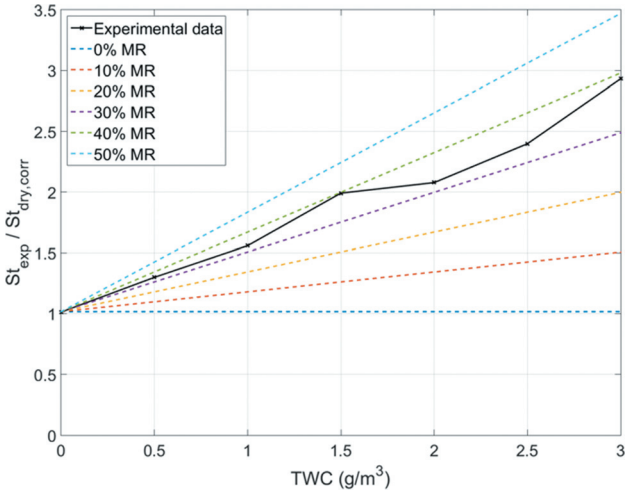

Fig. 19 Stanton number enhancement against total water content, baseline aerodynamic condition

were held constant and TWC was varied between dry conditions (0 g/m^3) and 3.0 g/m^3. Plotted as dashed lines are theoretical values of Stanton number enhancement at a range of melt ratios. On a line of 10% melt ratio, for example, 10% of the incoming mass flow of ice is assumed to be melted by impact with the plate. The experimentally calculated wall temperature is used at each value of TWC to calculate Stanton number. Thus, where the experimental data line intersects the theoretical lines indicates the expected particle melt ratio. The figure indicates that the total heat flux is approximately linear with increasing TWC. Up to 3.0 g/m^3, a particle melt ratio of 30–40% would be expected. It is worth noting that as TWC rises, wall temperature falls (although the copper substrate temperature is approximately constant).

The calculated wall temperature for the same tests is plotted in Fig. 20. The driving temperature difference of the convective heat flux is reduced by approximately 6 °C between the dry case and the heaviest icing case (3.0 g/m^3 TWC). Taking the heat transfer coefficient from the dry case, this approximates to a reduction of 2 kW/m^2 between the two cases. Thus, if the total heat transfer enhancement in Fig. 19 is linear, heat flux to the ice and water must rise nonlinearly to cancel out this reduction. One explanation for this is the development of a surface water film at high TWCs. The effect of this is twofold. First, surface-water conduction increases the overall heat transfer, and second, the impact time of impinging particles is increased as they are "held" in the water layer.

Runs were repeated at a number of selected test points, with the aim of imaging particle impacts. A particle imaging velocimetry method was used, details of which may be found in Fuleki et al. [15]. In the future, the data will be used to build bounce and shatter models. It is used here to qualitatively relate the impact behavior with the heat transfer measured. Two output images are shown in Figs. 21 and 22, with TWCs of 0.5 g/m^3 and 2.0 g/m^3, respectively. Both show a collection of secondary particles postimpact and were captured approximately 3 min after spray was initiated. In both cases, the baseline aerodynamic condition was used. As PIV uses two concurrent images to calculate particle velocity and size distribution, these two images are overlaid. Any given particle from the first image is colored black and the same particle in the second image is colored white. There is clear evidence of particle shattering in Fig. 21, as well as micron-scale spherical particles, indicative of water droplets. The largest secondary particle is approximately 50 μm, and the smallest under 5 μm. Figure 22 shows a shattering and splashing event, with the splash pattern clearly visible in the first (black) image. The images suggest that a water film has developed when TWC = 2 g/m^3 but has not at 0.5 g/m^3.

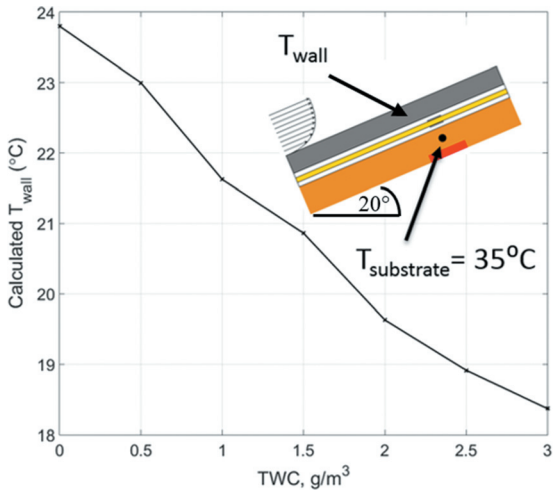

Fig. 20 Wall temperature versus total water content. Schematic of test piece inset

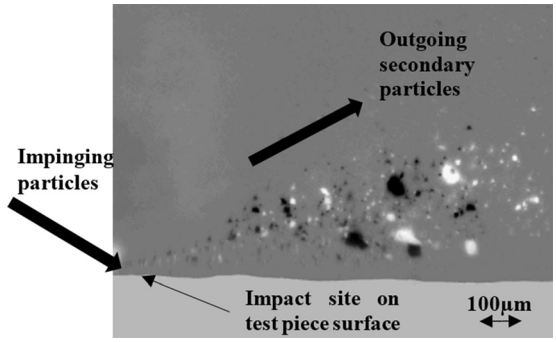

Fig. 21 PIV image, showing a shattering event. MMD = 60 μm, TWC = 0.5 g/m^3

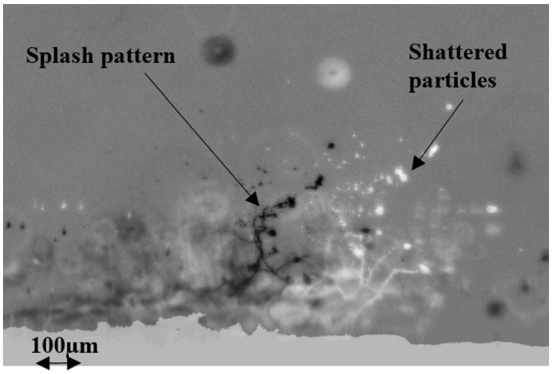

Fig. 22 PIV image, showing a splashing event. MMD = 60 μm, TWC = 2.0 g/m^3

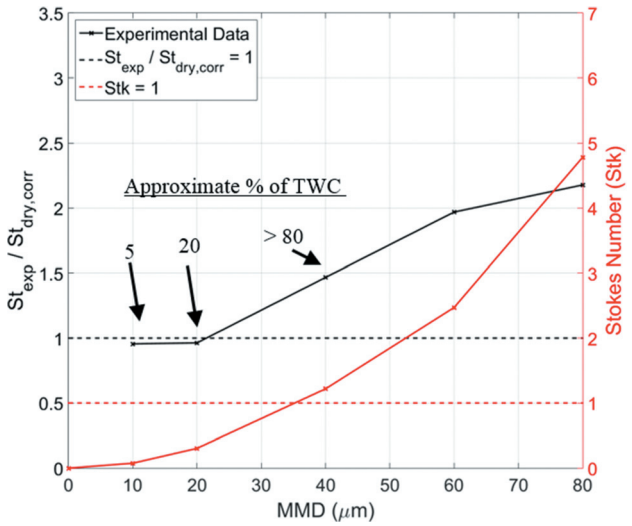

Fig. 23 Stanton number enhancement against particle diameter (MMD), baseline aerodynamic condition

Effect of Particle Diameter. Figure 23 shows data for runs conducted at median mass diameters in the range 10–80 μm. All other conditions were maintained at the baseline values in Table 2. Stanton number enhancement is plotted in black and the particle Stokes number on the right-hand axis.

The data show that there is negligible heat transfer enhancement for particles of 10 and 20 μm MMD, corresponding with Stokes numbers less than unity. Figure 18 shows that by the 66% streamwise row of gauges, where the data in Fig. 23 are taken, the concentration of 10 and 20 μm particles has fallen to approximately 5% and 20% of the injected TWC, respectively. This corresponds to a TWC of 0.05 g/m^3 and 0.2 g/m^3, respectively. These levels are sufficiently low that negligible heat transfer enhancement is measured, which is supported by the data shown in Fig. 19.

Conversely, for particles with MMDs of 40 μm and above, the Stokes number exceeds unity and so particles are more ballistic in nature, and thus, likely to impinge on the inclined heat transfer surface. It should be noted that at 80 μm MMD, full freezeout of the particles could not be assured, so this data point may be an underestimate of the true heat transfer enhancement.

Total water content, air velocity, and air density were held constant throughout the tests, so the mass flow rate of ice impinging on the plate is constant. The pressure in the air blast atomizer was varied to obtain many small particles or fewer large particles. If particles are assumed ballistic for any MMD above 40 μm, then the increasing Stanton number enhancement for larger particles implies that impact dynamics are an important driver in heat transfer. Roisman [6] gave a theoretical particle impact time as

$$t_{\max} \approx \frac{d_{p_0}\sqrt{\rho}}{2\sqrt{\sigma_Y}} \tag{15}$$

It was demonstrated using data from Tippman et al. [16] that impact time was approximately proportional to particle diameter for particles between 25.4 and 50.8 mm, impinging at constant velocity. If this effect is replicated for the smaller particles used in this experiment, then this may explain the linear trend in Fig. 23.

Roisman et al. also developed a semi-empirical quantity to describe the likelihood of particle fragmentation, as a function of impact velocity resolved normal to the surface and initial diameter. This is given by the following equation:

$$\gamma = v_{n_0} d_{p_0}^{2/3} \tag{16}$$

Fragmentation was assessed to be likely if γ exceeded ~0.04 for a dry wall and ~0.10 for a wall with a water film. The nominal normal impact velocities for the MMD range are shown in Table 6. The nominal Mach number was held at 0.4 for all tests. Using Eq. (16), the corresponding values of γ were calculated, as well as particle Stokes number.

The data show that fragmentation is expected for all particles that impinge heavily on the plate (40 μm and above). The impact dynamics for these tests is, therefore, likely to be similar, indicating that the increasing impact time could be a principle driver of the increasing heat transfer.

Table 6 Values of Stokes number and γ for the range of experimentally tested particle diameters

M	v_{n0} (m/s)	d_{p0} (μm)	γ (m$^{5/3}$/s)	Stk
0.4	44.2	10	0.026	0.076
0.4	44.2	20	0.032	0.30
0.4	44.2	40	0.052	1.22
0.4	44.2	60	0.068	2.74
0.4	44.2	80	0.081	4.78

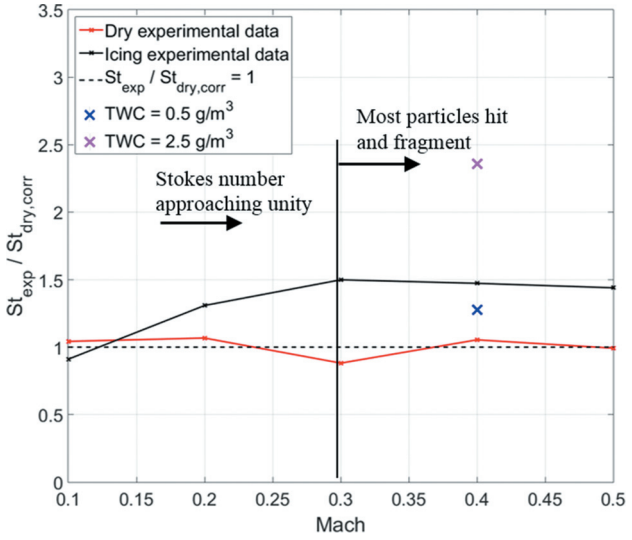

Fig. 24 Stanton number enhancement against Mach number, TWC = 1.0 g/m^3

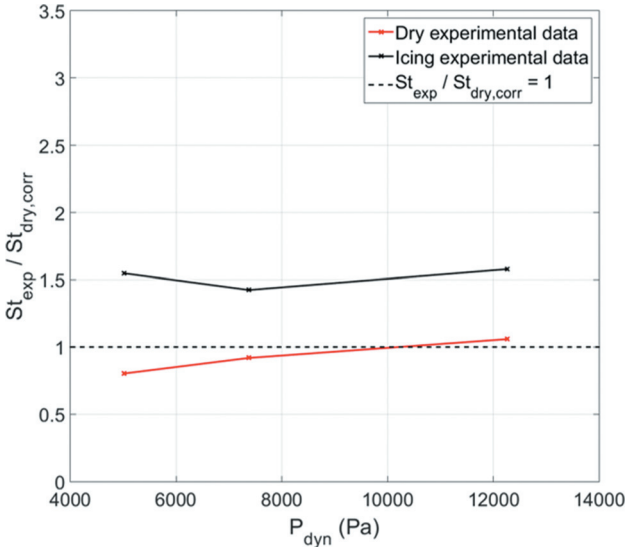

Fig. 25 Stanton number enhancement against dynamic pressure, TWC = 1.0 g/m^3

Table 7 Values of Stokes number and γ for the range of experimentally tested Mach numbers

M	v_{n0} (m/s)	d_{p0} (μm)	γ (m$^{5/3}$/s)	Stk
0.1	11.2	40	0.013	0.31
0.2	22.4	40	0.026	0.61
0.3	33.4	40	0.039	0.92
0.4	44.2	40	0.052	1.22
0.5	54.8	40	0.064	1.51

Effect of Mach Number. Mach number was varied between 0.1 and 0.5 by varying freestream velocity at constant altitude and total temperature. Reynolds number is, therefore, also increasing in these tests. Stanton number enhancement at a constant TWC of 1.0 g/m^3 is shown in Fig. 24. The data show that the enhancement factor of approximately 1.7 at Mach 0.4, also observed during other baseline condition runs, appears to be a plateau, within experimental uncertainty. The rise in heat transfer enhancement between Mach 0.1 and Mach 0.3 is attributable to the particle Stokes number increasing toward unity, resulting in gradually increasing particle impingement rate. Figure 18 shows that at Mach 0.1, less than 40% of the injected TWC is expected to impinge on the 66% streamwise row of gauges, where the data in Fig. 25 are taken.

The nominal MMD (40 μm) and TWC (1.0 g/m^3) are constant, and so again any variation in heat transfer between cases is likely driven by impact dynamics. Values of γ were again calculated, as shown in Table 7. For tests at Mach 0.1 and 0.2, γ is below the threshold value of 0.04; it is approximately equal to it at Mach 0.3 and above it for Mach 0.4 and Mach 0.5. It is important to note that increasing impact velocity will decrease impact time for fragmenting particles, as the yield strength σ_y is strain rate dependent. Tippmann et al. [16] studied the effect of impact velocity on yield strength, compared to a static case. Over the range of velocities studied here, yield strength may be expected to vary by approximately 30% [16]; however, when the square root is applied on the denominator of Eq. (15), impact time may be considered approximately constant. Therefore, heat transfer enhancement was observed to be approximately constant for fragmenting ballistic particles at constant TWC and impact time. However, the data are not independent of Reynolds number. This is addressed in the Effect of Dynamic Pressure section.

Effect of Dynamic Pressure. Runs were conducted at varying dynamic pressures in order to observe the effect of varying Reynolds number at constant Mach number. Dynamic pressure was varied between 5 and 13 kPa (0.7–1.8 psi) by varying altitude at constant velocity and total temperature. Figure 25 shows Stanton number enhancement for three tests at dynamic pressures of 5015, 7376, and 12,270 Pa. The baseline test case of Mach 0.4 at an altitude of 5.5 km corresponds to the 5015 Pa case. The heat transfer in dry conditions is well matched to the correlation of Motwani et al., implying that the effect on Reynolds number is well captured. In icing conditions, it is difficult to determine a trend in Stanton number enhancement, as it appears to be approximately constant within the uncertainty of the experiment.

Calculating the ratio of experimental Nusselt number to correlation Nusselt number ($Nu_{exp}/Nu_{dry,corr}$), the values are 1.54 and 1.58 for the lowest and highest dynamic pressures, respectively, which in turn produce the approximately constant Stanton number enhancement shown in Fig. 25.

This can partially be attributed to Stokes number exceeding unity and γ exceeding 0.04 for all three testpoints; hence, ballistic fragmenting particles are expected for all cases. However, it also implies an independency to Reynolds number, over the range tested. Given the heat transfer enhancement plateau in section (iii), where Reynolds and Mach numbers were both varied, the result of Reynolds number independency furthermore implies Mach number independency. It is important to note, however, that both of these conclusions are valid only for fully glaciated particles.

Effect of Angle of Attack. The angle of attack (AoA) of the flat plate was varied between 10 deg and 30 deg, using the baseline aerodynamic and icing conditions given in Table 2. Stanton

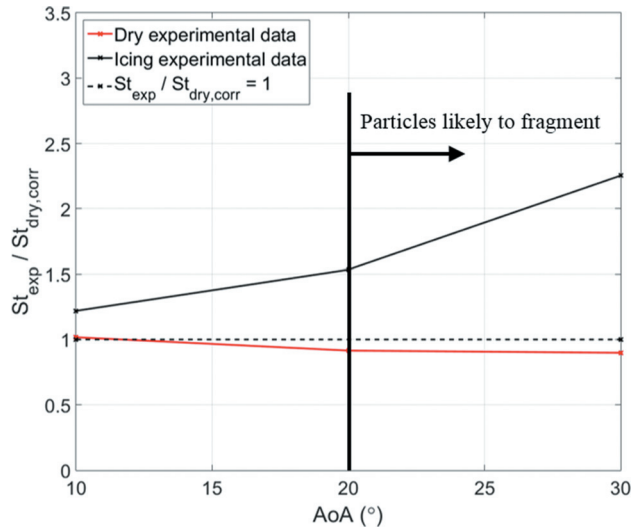

Fig. 26 Stanton number enhancement against angle of attack, TWC = 1.0 g/m^3

Table 8 Values of γ for the range of experimentally tested angles of attack

M	α (deg)	v_{n0} (m/s)	d_{p0} (μm)	γ (m$^{5/3}$/s)
0.4	10	22.4	40	0.026
0.4	20	44.2	40	0.052
0.4	30	64.6	40	0.076

number enhancement is shown in Fig. 26. The data show a nonlinear increase of heat transfer enhancement as angle increases. These tests can be viewed as varying γ (as normal impact velocity increases with angle) at constant Stokes number. The analysis of Roisman et al. is performed once again, as shown in Table 8. At 10 deg angle of attack, fragmentation is unlikely. Additionally, smaller particles in the size distribution will follow the flowfield over the leading edge separation bubble and only impinge on the late heat transfer surface, if at all. At higher angles, fragmentation is likely and the effect of the separation bubble is eradicated.

Conclusions

The development of a model for ice crystal accretion in gas turbine compressors requires, as one constituent part, an understanding of the thermodynamic and mechanical processes occurring when a bulk flow of ice particles impinges on a warm surface. A heated and instrumented flat plate was used to measure heat transfer enhancement over a range of aerodynamic and icing conditions. Thin film heat transfer gauges were successfully used for the first time in glaciated and mixed phase environments. Total water content, particle diameter, Mach number, angle of attack, and dynamic pressure were systematically varied. The following conclusions may be drawn:

(1) Over the range of 0.5–3.0 g/m^3 TWC, heat transfer enhancement was approximately linear, resulting in a theoretical particle melt ratio of 30–40% for a substrate temperature of 35 °C. Evidence of splashing events was observed. In a real engine environment, the meltwater and subsequent evaporative cooling would result in favorable conditions for accretion.
(2) At a baseline condition of 1.0 g/m^3 TWC, heat transfer from the test piece was observed to be approximately double compared with dry conditions. This rises to an enhancement of approximately three times at 3.0 g/m^3. Due to centrifuging effects within an engine, local TWCs could be over ten times this value [17].
(3) Heat transfer enhancement was also observed to be approximately linear with particle diameter at constant TWC. This was tentatively attributed to the increasing particle impact time.
(4) For fully glaciated particles, heat transfer enhancement was observed to be dependent on impact dynamics. This was observed in tests where particle diameter, Mach number, and angle of attack were varied. A Stokes number of above unity resulted in high impingement rates and heat transfer enhancement. An empirical quantity (γ) defined by Roisman et al. was used to predict the likelihood of fragmentation. At conditions where particles were both ballistic and likely to fragment, heat transfer enhancement was independent of Reynolds number and Mach number, within the uncertainty of the experiment.
(5) When angle of attack was increased from 10 deg to 30 deg, heat transfer enhancement increased nonlinearly in accordance with the rising normal impact velocity. In an engine environment, this has implications both for large particles with high tangential slip velocities and also for variable geometry stages.

These conclusions will support development of a model for the ice crystal accretion phenomena, as well as providing simple predictive rules for use in preliminary engine design.

Acknowledgment

The authors would like to gratefully acknowledge the following people. Dr. David Orchard, Catherine Clark, Gislain Chevrette, and Stuart Stevenson at the NRC AIWT for their support and guidance throughout the experimental campaign. Also to Dr. Khalid Saleh and Ramiz Ibraheem for providing insight and access to the ice crystal tunnel at the University of Southern Queensland, where the test article was developed. Also to Professor Martin Oldfield and Dr. Paul Beard of the Osney Thermofluids Laboratory for driving forward the development of the new TFG signal conditioning units, and to Trevor Godfrey, Gerald Walker, Brian Bunce, James Carter, Peter Forsyth, and Sebastien Wylie for manufacturing the test article.

Funding Data

- Rolls-Royce Plc.
- EPSRC.

Nomenclature

a = thickness, m
A = area, m^2
c = sound speed, m/s
C_d = drag coefficient
C_p = specific heat capacity at constant pressure (J/kg K)
d_p = particle diameter (μm)
D = characteristic dimension (m)
h = heat transfer coefficient (W/m^2 K)
k = thermal conductivity (W/m K)
$\dot{m}$ = mass flow rate (kg/s)
n = sample number at time t
N = total number of samples
P = pressure (Pa)
q = heat flux (W/m^2)
Q = heat flow rate (W)
R = specific gas constant (J/kg K)
t = time (s)
T = temperature (K)
v = velocity (m/s)
x = streamwise position (m)
y = spanwise position (m)
z = vertical position (m)
α = angle of attack (deg)

μ = dynamic viscosity (Pa·s)
ρ = density (kg/m^3)
σ_Y = yield strength (Pa)
τ_p = particle relaxation time (s)

Subscripts

0 = total conditions
01 = total conditions at inlet
∞ = freestream conditions
conv = convective
corr = correlation
dyn = dynamic (pressure)
enh = enhancement (heat transfer)
exp = experimentally measured
evap = evaporation
h = heater
i = ice
i, j = local streamwise, spanwise position
kin = kinetic
K = Kapton
p = particle
sub = substrate
surf = surface
sens = sensible heating
Ti = titanium
w = water
wall = top surface of titanium layer (icing surface)
wb = wet bulb (temperature)

Abbreviations

AC = alternating current
AIWT = Altitude Icing Wind Tunnel (NRC)
AoA = angle of attack (deg)
MMD = median mass diameter (μm)
NRC = National Research Council of Canada
PIV = particle image velocimetry
RH = relative humidity (%)
SST = shear stress transport
TFG = thin film heat flux gauge
TWC = total water content (g/m^3)

Groups

Bi = Biot number = ha/k
M = Mach number = v/c
Nu = Nusselt number = hx/k
Pr = Prandtl number = $\mu C_p/k$
Re = Reynolds number = $\rho vx/\mu$
St = Stanton number = $h/\rho v C_p$
Stk = Stokes number = $\tau_p v/D$
γ = particle energy quantity = $v d_p^{2/3}$, m$^{5/3}$/s

References

[1] Mason, J. G., Strapp, J. W., and Chow, P., 2006, "The Ice Particle Threat to Engines in Flight," AIAA Paper No. 2006-206.
[2] Mason, J. G., Chow, P., and Fuleki, D. M., 2011, "Understanding Ice Crystal Accretion and Shedding Phenomenon in Jet Engines Using a Rig Test," ASME J. Eng. Gas Turbines Power, **133**(4), p. 041201.
[3] Struk, P. M., Broeren, A. P., Tsao, J., Vargas, M., Wright, W. B., Currie, T., Knezevici, D., and Fuleki, D., 2011, "Fundamental Ice Crystal Accretion Physics Studies," SAE Paper No. 2011-38-0018.
[4] Currie, T., Fuleki, D., and Mahalllati, A., 2014, "Experimental Studies of Mixed-Phase and Sticking Efficiency for Ice Crystal Accretion in Jet and Engines," AIAA Paper No. 2014-3049.
[5] Currie, T. C., Fuleki, D. M., Knezevici, D. C., and MacLeod, J. D., 2013, "Altitude Scaling of Ice Crystal Accretion," AIAA Paper No. 2013-2677.
[6] Roisman, I., and Tropea, C., 2015, "Impact of a Crushing Ice Particle Onto a Dry Solid Wall," Proc. R. Soc. A, **471**(2183), p. 20150525.
[7] Myron, O. M., Hyde, F. H., and Penna, P. J., 2001, "In-Flight Icing Simulation Capabilities of NRC's Altitude Icing Wind Tunnel," AIAA Paper No. 2001-0094.
[8] National Research Council Canada, 2014, "NRC Altitude Icing Wind Tunnel Calibration Reports, Appendix B," National Research Council Canada, Ottawa, ON, Canada, Report No. LTR-AL-2014-0118.
[9] Collins, M., Chana, K., and Povey, T., 2015, "New Technique for the Fabrication of Miniature Thin Film Heat Flux Gauges," Meas. Sci. Technol., **26**, p. 025303.
[10] Anthony, R. J., Oldfield, M. L. G., Jones, T. V., and LaGraff, J. E., 1999, "Development of High-Density Arrays of Thin Film Heat Transfer Gauges," ASME/JSME Thermal Engineering Joint Conference, San Diego, CA, Mar. 14–19, Paper No. AJTE99-6159.
[11] Lindsay, A. L., and Bromley, L. A., 1950, "Thermal Conductivity of Gas Mixtures," Ind. Eng. Chem., **42**(8), pp. 1508–1511.
[12] Motwani, D. G., Gaitonde, U. N., and Sukhatme, S. P., 1985, "Heat Transfer From Rectangular Plates Inclined at Different Angles of Attack and Yaw to an Air Stream," ASME J. Heat Transfer, **107**(2), pp. 307–312.
[13] Coleman, H. W., and Steele, W. G., 2009, *Experimentation, Validation, and Uncertainty Analysis for Engineers*, 3rd ed., Wiley, Hoboken, NJ.
[14] Mitutoyo USA, 2017, "Digital Protractor Series 950-Pro 360 Pro 3600," Mitutoyo America Corporation, Aurora, IL, accessed Nov. 23, 2017, http://ecatalog.mitutoyo.com/Digital-Protractor-Series-950-Pro-360-Pro-3600-C1438.aspx
[15] Fuleki, D., Chalmers, J. L., and Galeote, B., 2015, "Technique for Ice Crystal Particle Size Measurements and Results for the National Research Council of Canada Altitude Ice Crystal Test System," SAE Paper No. 2015-01-2125.
[16] Tippmann, J. D., Kim, H., and Rhymer, J. D., 2013, "Experimentally Validated Strain Rate Dependent Material Model for Spherical Ice Impact Simulation," Int. J. Impact Eng., **57**, pp. 43–54.
[17] Feulner, M., Liao, S., Rose, B., and Liu, X., 2015, "Ice Crystal Ingestion in a Turbofan Engine," SAE Paper No. 2015-01-2146.

Statement of Authorship for joint/multi-authored papers for PGR thesis

To appear at the end of each thesis chapter submitted as an article/paper

The statement shall describe the candidate's and co-authors' independent research contributions in the thesis publications. For each publication there should exist a complete statement that is to be filled out and signed by the candidate and supervisor **(only required where there isn't already a statement of contribution within the paper itself).**

Title of Paper	Experimental Studies of Ice Crystal Accretion on an Axisymmetric Body at Engine-Realistic Conditions
Publication Status	x Published (conference proceedings) □ Accepted for Publication □Submitted for Publication □Unpublished and unsubmitted work written in a manuscript style
Publication Details	Bucknell A., McGilvray M., Gillespie D.H., Jones G., Reed A. and Collier, B. "*Experimental Studies of Ice Crystal Accretion on an Axisymmetric Body at Engine-Realistic Conditions*", 2018 Atmospheric and Space Environments Conference, AIAA AVIATION Forum, June 25th-29th 2018, Atlanta, GA, USA. Paper 2018-4223

Student Confirmation

Student Name:	Alexander Bucknell		
Contribution to the Paper	Designed test articles and test matrix, ran the testing schedule (testing performed by trained operators at the test facility used). Performed the data reduction and postprocessing, and wrote the manuscript.		
Signature 		Date	4/10/2018

Supervisor Confirmation

By signing the Statement of Authorship, you are certifying that the candidate made a substantial contribution to the publication, and that the description described above is accurate.

Supervisor name and title: Prof. M. McGilvray		
Supervisor comments Alex performed the contributions in his statement		
Signature 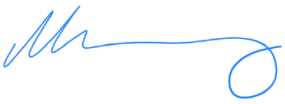	Date	4/10/2018

This completed form should be included in the thesis, at the end of the relevant chapter.

Statement of Authorship for joint/multi-authored papers for PGR thesis

To appear at the end of each thesis chapter submitted as an article/paper

The statement shall describe the candidate's and co-authors' independent research contributions in the thesis publications. For each publication there should exist a complete statement that is to be filled out and signed by the candidate and supervisor **(only required where there isn't already a statement of contribution within the paper itself).**

Title of Paper	Heat Transfer in the Core Compressor Under Ice Crystal Icing Conditions
Publication Status	x Published □ Accepted for Publication □Submitted for Publication □Unpublished and unsubmitted work written in a manuscript style
Publication Details	Bucknell A, McGilvray M, Gillespie DH, Jones G, Reed A, Buttsworth DR. *Heat Transfer in the Core Compressor Under Ice Crystal Icing Conditions.* ASME J. Eng. Gas Turbines Power. 2018; 140 (7)

Student Confirmation

Student Name:	Alexander Bucknell		
Contribution to the Paper	Designed test article and test matrix, ran the testing schedule (testing performed by trained operators at the test facility used. Performed the data reduction and postprocessing, and wrote the manuscript.		
Signature 		Date	4/10/2018

Supervisor Confirmation

By signing the Statement of Authorship, you are certifying that the candidate made a substantial contribution to the publication, and that the description described above is accurate. Supervisor name and title: Prof. M. McGilvray		
Supervisor comments Alex performed the contributions in his statement.		
Signature 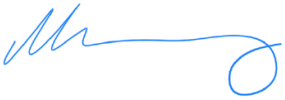	Date	4/10/2018

This completed form should be included in the thesis, at the end of the relevant chapter.

6 Thermodynamic Accretion Model

In this chapter, a new thermodynamic ice accretion model is introduced. The Extended Messinger Model (Myers, 2001) is adapted from supercooled water icing conditions to ice crystal icing conditions. Two distinct cases are considered – that of a substrate initially above 0 °C ('warm substrate'), and that of a substrate initially below 0 °C ('cold substrate'). Continuity, heat and energy equations are solved for each case, to output ice and water layer thicknesses as a function of time. Several simplifying assumptions are introduced and justified. Finally, example results are given for accretion on a single panel under a range of aerodynamic and icing conditions.

6.1 The Extended Messinger Model

The Extended Messinger Model (EMM) (Myers, 2001) was written to improve ice accretion predictions on aircraft wings when flying in supercooled liquid water (SLW) droplet conditions. In these conditions, water droplets may exist at temperatures as low as -40 °C, forming ice after impact with the sub-freezing wing.

The EMM aimed to improve upon the model of Messinger (Messinger, 1953), the first formalised thermodynamic accretion model for wing icing. This model still forms the basis of the most highly developed icing codes today (for example those of NASA and ONERA (Wright et al., 1997)). It has also been used in the first generation of ice crystal icing codes (Trontin et al., 2016; Villedieu et al., 2014). It is a steady approach that assumes that the component surface (substrate) immediately adopts its steady-state temperature. Temperature gradients normal and parallel to the wall are neglected. The freezing fraction (the proportion of the water in the control volume that freezes) is constant for all time.

In contrast, the EMM permits a linear temperature gradient normal to the substrate, and thus heat flux from the substrate through water and/or ice layers. This approach is therefore quasi-steady: time enters the problem through the changing accretion height - which due to the spatial temperature gradient produces a time-dependent accretion surface temperature. Moreover, this approach then allows a prediction of the time at which a water layer will form on top of the accretion.

The underlying equations in the EMM are perfectly adaptable to ice crystals. The primary differences are:

1. In ice crystal icing, the underlying component (substrate) may be either above or below freezing temperature. At the point in the engine of ice build-up (typically within the LP booster or IP compressor), total air temperatures are around or a little above 0 °C, facilitating the partial melt required for accretion. The original EMM only assumes a substrate below freezing.
2. The impinging particulates may be mixed phase (a mixture of glaciated crystals, partially melted crystals and fully liquid droplets). The original EMM only considers a purely liquid cloud. In the ice crystal case, the unknown freezing or melting of the mixed phase flux at the surface necessitates the addition of an equation or a simplifying assumption.

Fig. 6-1 shows the assumed form of the liquid water droplet icing problem. An ice layer forms first as the droplets impact and freeze on the substrate. The ice layer has thickness $B(t)$ and temperature profile $T(z,t)$. Energy is released, proportional to the latent heat of fusion, as the ice layer grows. This is summed with the other heat fluxes at the surface (evaporation, convection etc.). The sign and magnitude of this summation will determine whether the exposed surface will reach 0 °C, allowing a water film to form on top. In the EMM, the water film thickness is given by $h(t)$ and temperature profile by $\theta(z,t)$. The nomenclature used here will be retained when adapted to ice crystal icing.

The problem is framed in one dimension, where the accretion grows uniformly over a single surface. Simple adaptations will be presented for use in two dimensions, including runback water.

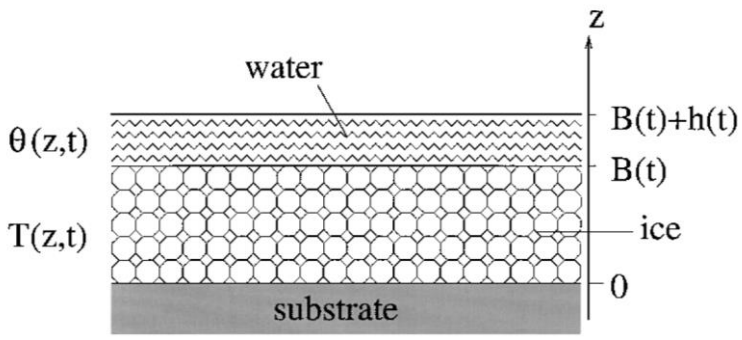

Fig. 6-1 Assumed form of supercooled water icing problem in original EMM (Myers, 2001)

The four equations describing the problem comprise continuity (equation 6-1), one dimensional heat equations in the ice and water layers (equations 6-2 and 6-3) and an energy balance (equation 6-4) at the ice-water interface. The latter states that the imbalance between the rate of heat conduction in the ice layer and water layer determines the heat of fusion available at the interface, and hence the freezing rate.

$$\rho_w \frac{dh}{dt} + \rho_i \frac{dB}{dt} = \dot{m}_{stuck} + \dot{m}_{run,in} - \dot{m}_{evap} \tag{6-1}$$

$$\frac{\partial^2 \theta}{\partial z^2} = \frac{C_{p,w}\,\rho_w}{k_w} \frac{\partial \theta}{\partial t} \tag{6-2}$$

$$\frac{\partial^2 T}{\partial z^2} = \frac{C_{p,i}\,\rho_i}{k_i} \frac{\partial T}{\partial t} \tag{6-3}$$

$$\rho_w L_f \frac{dh}{dt} = -k_w \frac{\partial \theta}{\partial z} + k_i \frac{\partial T}{\partial z} \tag{6-4}$$

6.2 Model Assumptions

The primary assumptions in the EMM are:

(A1) Lateral conduction may be ignored – i.e. there are negligible wall-parallel temperature gradients. Enthalpy may be transferred laterally in two- or three-dimensional problems only through runback water.

(A2) The time derivative of the ice and water temperatures may be neglected, i.e. the heat equations may be simplified to

$$\frac{\partial^2 \theta}{\partial z^2} = \frac{\partial^2 T}{\partial z^2} = 0 \tag{6-5}$$

The problem is then quasi-steady one-dimensional conduction. Time enters the problem only through the changing accretion thickness (via the continuity equation). Physically this assumption implies that advective transport due to the growth of the accretion has a significantly longer timescale than the thermal diffusivity (α). This assumption is invariably used in aircraft icing codes (Gent et al., 2000)

and has been used in the first generation of ice crystal icing codes (Villedieu et al., 2014). The validity of this assumption may be assured if the Péclet number is significantly below unity, defined as

$$Pe = \frac{advective\ transport\ rate}{thermal\ diffusivity\ in\ ice} = \frac{UL}{\alpha_i} = \frac{\dot{h}\ L\ \rho_i C_{p,i}}{k_i} \tag{6-6}$$

where U is a velocity, taken as $\dot{h}$, the ice growth rate. A typical ice growth rate on the cone test piece in the RATFac validation tests is $\dot{h} = 0.1$ mm/s. L is a characteristic dimension, taken as the length of the panel onto which ice is accreting – a typical value would be $L = 0.5$ cm. Substituting these values into equation (6-6) results in $Pe \cong 0.4$. This shows that the validity of the assumption in ice crystal icing conditions is marginal – compared to supercooled liquid water icing where growth rates are typically significantly lower (Myers, 2001). The error introduced therefore may be significant for cases of peak growth rate (~0.25 mm/s) where $Pe \cong 1$. Adaptation of the method to unsteady heat conduction is outside of the scope of the current work, but has been attempted recently by Chauvin et al., (2018), with application to supercooled water icing.

(A3) There is perfect thermal contact between the accretion and substrate. The substrate may have a fixed or time dependent temperature

$$T(z = 0, t) = T_{subs}(t) \tag{6-7}$$

Whilst the assumption of perfect thermal contact simplifies the modelling significantly, it will likely lead to an overestimation of the conductive heat flux in the layer adjacent to the substrate. Due to the complexity of modelling a 'realistic' thermal contact (dependent upon ice type, local surface roughness etc.) the error arising from this assumption cannot easily be quantified. Recent work on ice adhesion on rough surfaces (e.g. Dawood et al., 2018) may lead to future improvements.

The assumption also leads to a secondary implication: that the first layer grown on the substrate must adopt the substrate's surface temperature 'instantaneously' – or at least within the first timestep. The validity of this may be assessed by calculating the time required for a layer of impinging particles to warm to the substrate temperature, if perfect thermal contact is assumed. Using a typical impinging mass flux of $\dot{m}_{imp} = 0.1$ kg/s.m^2, a substrate temperature of $T_{subs} = 283$ K, a particle temperature

of $T_f = 273.15$ K and the a panel length of $L = 0.5$ cm, the time required for the particle temperature to reach 99% of the substrate temperature is ~0.05 s. Since a typical model timestep is 1 s, the assumption is justified – albeit within the realm of perfect thermal contact.

(A4) The temperature at the ice-water interface is equal to the freezing temperature

$$T(z = h, t) = T_f \tag{6-8}$$

(A5) Energy sources and sinks at the exposed surface comprise convection, evaporation or sublimation, kinetic energy transfer from impinging droplets, latent heat of fusion, aerodynamic heating, sensible warming of impinging droplets and sensible warming of incoming runback water. Radiation is neglected; conduction within the substrate is neglected or included via a temperature boundary condition.

(A6) In order to allow an analytical solution, a piecewise linear approach is used to approximate saturation vapour pressure as a function of temperature. Typically an empirically-fitted polynomial would be used in preference. The error incurred though this approach is assessed in Appendix E-3.

(A7) At the start of the calculation, the substrate is clean or has an existing accretion of known height. In the ensuing derivations, the assumption of an initially clean substrate will be used throughout.

$$h(t = 0) = B(t = 0) = 0 \tag{6-9}$$

6.3 EMM-C Model Proposition

In this section, the approach and equations for adapting the EMM to ice crystal icing are presented. The new model is hereon referred to as EMM-Crystals, or EMM-C.

In the following derivation, calculations are performed in one dimension for a single surface panel. Where there is a surface water film, the ‘gross’ water height is calculated first (neglecting runback water). After the thermodynamic analysis has been performed, the new water height is known and runback water out of the domain may then be calculated. It is assumed to run axially downstream, as shown in Fig. 6-2.

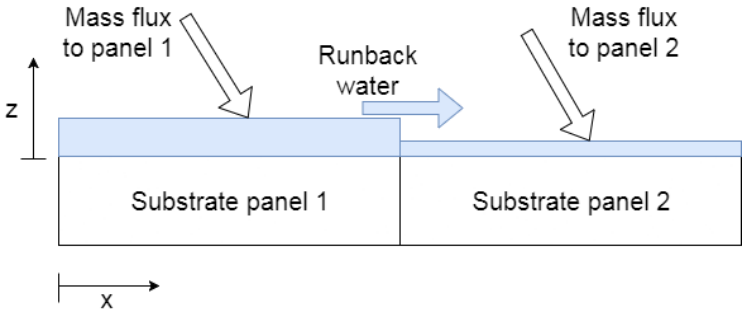

Fig. 6-2 Schematic of runback water between axially adjacent panels

Timestepping is in pseudo-time, with thicknesses and temperature profiles updated after every timestep. Timestep length is constant and is typically 1 s, for an accretion grown over several minutes. Within each timestep, panels are marched through in an axial direction. For example, calculations on a stator vane start at the leading edge, march axially down the pressure surface, then return to the leading edge and march down the suction surface. Axial marching is also performed for the panels defining the endwalls.

Two separate solution routes must be considered depending on whether the clean substrate is above or below freezing, as shown in Fig. 6-3. This determines whether the first impinging particles will melt, forming a water layer, or freeze, forming an ice layer. The assumed situations for either scenario are shown in Fig. 6-4.

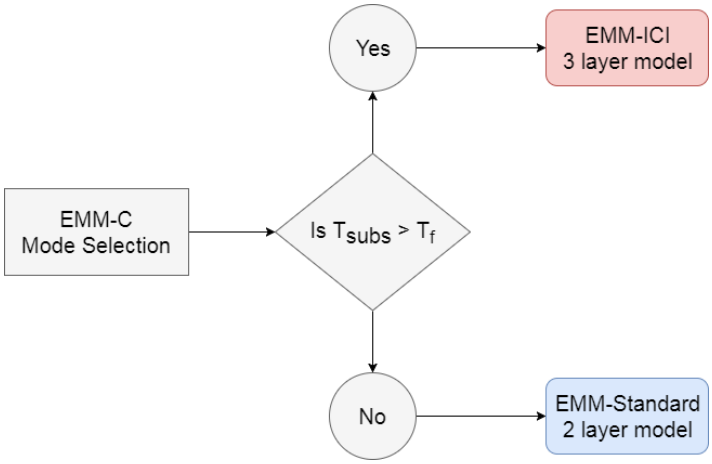

Fig. 6-3 Model selection within EMM-C based on initial substrate temperature

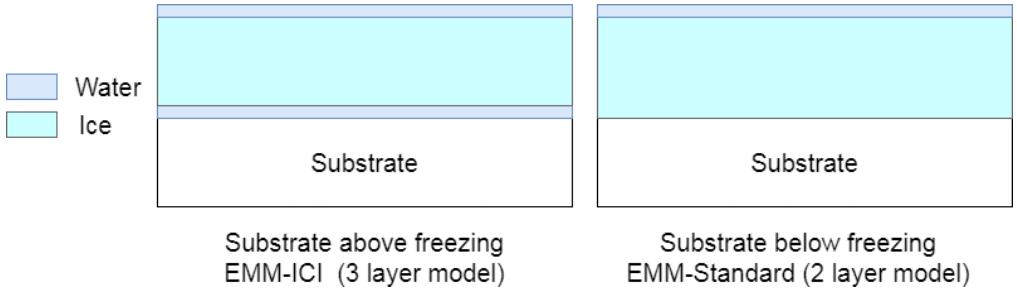

Fig. 6-4 Assumed form of the ice crystal icing problem for a substrate above freezing (left) and below freezing (right).

The case of a substrate below freezing (EMM-Standard) is largely similar to the classical EMM model, albeit with some additional considerations to account for glaciated or mixed phase conditions. The calculations for this case are given in Appendix D.

The case of a substrate above freezing (a 'warm substrate', EMM-ICI) is now considered. The proposed three layer model is entirely novel and thus worthy of description in detail.

6.4 EMM-ICI Model

The case of a clean substrate initially above freezing may be divided into two distinct stages. In stage 1, the impinging mixed phase flux of partially melted ice particles fully melts on impact, producing a water film. The assumed geometry and fluxes of heat and mass are shown in Fig. 6-5.

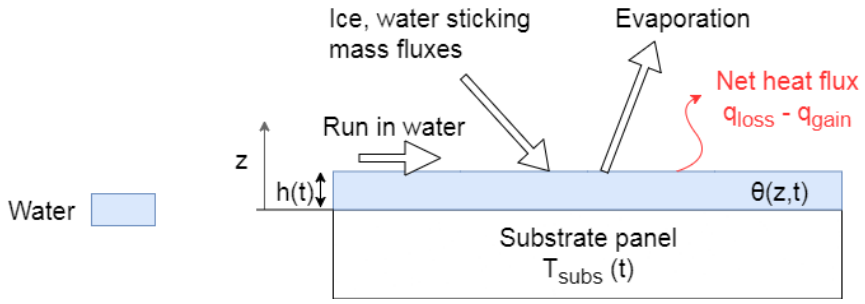

Fig. 6-5 Schematic of stage 1 (water film) with fluxes of heat and mass

Since in this stage all of the impinging mass flux is assumed to melt, the water layer height is solved directly from the continuity equation (6-1), with $dB/dt = 0$:

$$h = \frac{1}{\rho_w}\left(\dot{m}_{stick,i} + \dot{m}_{stick,w} + \dot{m}_{run,in} - \dot{m}_{evap}\right) t \tag{6-10}$$

The temperature profile through the water layer at a given timestep may now be solved. Starting from the quasi-steady assumption, the one-dimensional heat equation for the water layer is

$$\frac{\partial^2 \theta}{\partial z^2} = 0 \tag{6-11}$$

Integrating twice and applying boundary condition (6-7), the temperature in the water layer is given by

$$\partial\theta/_{\partial z} = K_1 \;\; ; \quad \theta = K_1 z + T_{subs} \tag{6-12}$$

where K_1 is a constant of integration. The net heat flux through the exposed water surface may be used as a boundary condition, applied at $z = h$:

$$\begin{aligned} -k_w \frac{\partial \theta}{\partial z} &= q_{loss} - q_{gain} \\ &= \left(q_{conv} + q_{evap} + q_{sens,imp} + q_{sens,run}\right) - \left(q_{kin} + q_{freeze}\right) \end{aligned} \tag{6-13}$$

where

$$q_{conv} = H\,(\theta_h - T_r) \tag{6-14}$$

$$q_{evap} = L_v\,\dot{m}_{evap} = L_v(E_e\theta_h + E_A) \tag{6-15}$$

$$q_{freeze} = -L_f \dot{m}_{stick,i} \tag{6-16}$$

$$q_{sens,imp} = \dot{m}_{stick,i} C_{p,i}\left(T_f - T_{p,i}\right) + \dot{m}_{stick,i} C_{p,w}\left(\theta_h - T_f\right) + \dot{m}_{stick,w} C_{p,w}(\theta_h - T_{p,w}) \tag{6-17}$$

$$q_{sens,run} = \dot{m}_{run,w} C_{p,w}(\theta_h - T_{run}) \tag{6-18}$$

$$q_{kin} = {}^1/_2\left(\dot{m}_{stick,i} + \dot{m}_{stick,w}\right)\overline{U_p}^2 \tag{6-19}$$

where θ_h is the temperature of the water at the exposed surface, i.e. $\theta_h = \theta(z = h, t)$. The runback water temperature, T_{run}, is typically taken to be the freezing temperature T_f. $\overline{U_p}$ is the average velocity of particles (water and ice) impinging on the panel in question, and H is the heat transfer coefficient, assumed to adopt a single value for each panel.

Estimation of the evaporating or sublimating mass flux uses a heat-mass transfer analogy procedure since the mass transfer coefficient is generally not known a-priori (Gent et al., 2000). The evaporative mass flux is therefore expressed in terms of the local heat transfer coefficient. The calculation also requires the local saturation vapour pressure to be evaluated, such that the freestream vapour mass fraction may be found. Saturation vapour pressure is typically calculated from an empirical formula such as that of Hyland and Wexler (1983). In the Extended Messinger Model (Myers, 2001) saturation vapour pressure is approximated as a linear function over the range $257 \leq T\ (\mathrm{K}) \leq T_f$, given by

$$P_{vap,sat} \cong -6.803\, x10^3 + e_0 T \tag{6-20}$$

The maximum error introduced by this equation over the range specified is reported as 8%. Using a linear function in the EMM allows for analytical solutions to be derived directly, avoiding the need for a numerical solution procedure and reducing computational cost. This approach is maintained in the current work, however it is modified to a piecewise linear approximation over an extended range of applicability. This is necessitated by the adaptation of the model to ice crystal icing, where temperatures may be significantly *above* freezing as well as below. A 19-segment piecewise linear fit is used instead, applicable over the range $245 \leq T\ (K) \leq 320$. The new piecewise fit, and a full derivation of the evaporative heat flux (equation (6-15)) are given in Appendix E.

Substituting equations (6-14) through (6-19) into equation (6-13) leads to

$$\frac{\partial \theta}{\partial z} = \frac{1}{k_w}\left(q_{gain} - q_{loss}\right) = \frac{1}{k_w}\left(q_2 - q_1 \theta_h\right) \quad , \quad z = h \tag{6-21}$$

where

$$q_1 = H + L_v E_e + \dot{m}_{stick,i} C_{p,w} + \dot{m}_{stick,w} C_{p,w} + \dot{m}_{run,w} C_{p,w} \tag{6-22}$$

$$\begin{aligned} q_2 = {}& {}^1\!/_2 \left(\dot{m}_{stick,i} + \dot{m}_{stick,w}\right)\overline{U_p}^2 - \left(L_v E_A - L_f \dot{m}_{stick,i} - H T_r \right. \\ & + \dot{m}_{stick,i} C_{p,i}\left(T_f - T_{p,i}\right) - \dot{m}_{stick,i} C_{p,w} T_f - \dot{m}_{stick,w} C_{p,w} T_{p,w} \\ & \left. - \dot{m}_{run,w} C_{p,w} T_{run}\right) \end{aligned} \tag{6-23}$$

Substituting equations (6-21) through (6-23) into equation (6-12) produces

$$\theta = \frac{1}{k_w}(q_2 - q_1\theta_h)\, z + T_{subs} \tag{6-24}$$

Evaluating this expression at $z = h$ and rearranging for θ_h yields

$$\theta_h = \frac{{}^{h}/_{k_w}\, q_2 + T_{subs}}{1 + {}^{h}/_{k_w}\, q_1} \tag{6-25}$$

Substituting equation (6-25) into equation (6-24) yields the final equation for the water temperature profile

$$\theta = \frac{1}{k_w}\left(q_2 - q_1\left(\frac{{}^{h}/_{k_w}\, q_2 + T_{subs}}{1 + {}^{h}/_{k_w}\, q_1}\right)\right) z + T_{subs} = \frac{q_2 - q_1 T_{subs}}{k_w + h q_1} z + T_{subs} \tag{6-26}$$

The calculation continues until either (i) the temperature of the exposed water surface falls to freezing, i.e. $\theta(h,t) = T_f$, or (ii) the surface temperature remains above freezing for the entire calculation time (running wet conditions). If scenario (i) occurs, the calculation moves to the second stage.

In the second stage, an ice layer is assumed to form over the initial water film. A surface water film may also form on top of the ice layer, producing a three layer system. This is illustrated in Fig. 6-6.

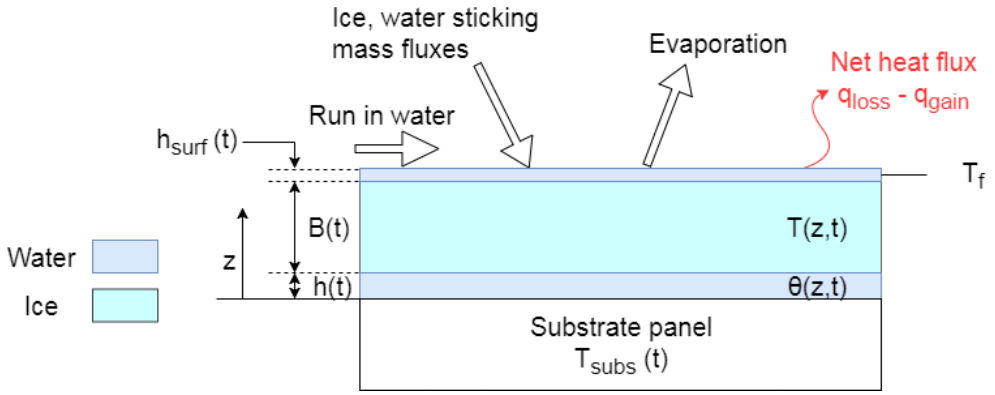

Fig. 6-6 Schematic of stage 2 (three layer model) with fluxes of heat and mass

The internal water layer is a necessary outcome of assumption (A3); if the substrate temperature remains above freezing, the layer directly above it must be water. If the substrate temperature falls below freezing during the calculation, then the internal water layer will shrink. The internal water layer is assumed to be trapped, and may not flow axially between panels.

An additional assumption is added at this point:

(A8) The surface water film is sufficiently thin that wall-normal temperature gradients may be neglected. Since the temperature at the water-ice interface must be at the freezing temperature T_f, it is therefore taken that the whole film is at this temperature. The validity of this assumption is assessed in Appendix F.

First, consider the internal water layer and ice layer. The heat and energy equations are given by

$$\frac{\partial^2 \theta}{\partial z^2} = \frac{\partial^2 T}{\partial z^2} = 0 \tag{6-27}$$

$$\rho_w L_f \frac{dh}{dt} = -k_w \frac{\partial \theta}{\partial z} + k_i \frac{\partial T}{\partial z} \tag{6-28}$$

The heat equations may be integrated simply:

$$\frac{\partial \theta}{\partial z} = \frac{T_f - T_{subs}}{h} \quad ; \quad \theta = \frac{T_f - T_{subs}}{h} z + T_{subs} \quad ; \quad \frac{\partial T}{\partial z} = 0 \quad ; \quad T = T_f \tag{6-29}$$

Substituting (6-29) into (6-28):

$$\frac{dh}{dt} = \frac{1}{\rho_w L_f} \left(-k_w \frac{T_f - T_{subs}}{h} \right) \tag{6-30}$$

This may then be solved over the timestep by separation of variables, providing that T_{subs} is held constant over the step.

It is instructive at this point to separate the two contributions to ice layer growth – from (i) the freezing or melting at the interface with the internal water layer and (ii) freezing or melting at the top surface.

$$\frac{dB}{dt} = \frac{dB_{int}}{dt} + \frac{dB_{surf}}{dt} \tag{6-31}$$

where

$$\frac{dB_{int}}{dt} = -\frac{\rho_w}{\rho_i} \frac{dh}{dt} \tag{6-32}$$

An additional equation for continuity of water at the top surface is now added:

$$\rho_w \frac{dh_{surf}}{dt} = \dot{m}_{stuck,w} + \dot{m}_{run,in} - \dot{m}_{evap} - \dot{m}_f \tag{6-33}$$

where $\dot{m}_f$ is the mass flux freezing at the top surface. The corresponding equation for surface ice growth is

$$\frac{dB_{surf}}{dt} = \dot{m}_{stuck,i} + \dot{m}_f \tag{6-34}$$

It then remains to find $\dot{m}_f$. Similarly to the water-only first stage, the net surface heat flux may be used as a boundary condition, except applying assumption (A8) requires the net flux to be zero.

$$q_{loss} - q_{gain} = q_{net} = \left(q_{conv} + q_{evap} + q_{sens,imp} + q_{sens,run}\right) - \left(q_{kin} + q_{freeze}\right) = 0$$

$$z = h + B + h_{surf} \tag{6-35}$$

where the terms are as defined previously (using a surface temperature of T_f) and q_{freeze} is the freezing latent heat release, $q_{freeze} = L_f \dot{m}_f$. Equation (6-35) may be solved directly for q_{freeze} and hence $\dot{m}_f$.

6.5 Temperature Response of Substrate

For the case of a substrate initially above freezing temperature, the substrate response determines (i) the time at which ice first forms – or whether running wet conditions are maintained; and (ii) growth or shrinking of the internal water layer as ice grows above. Aside from accurately modelling accretion growth rates, the latter is also important for modelling the adhesive strength of the ice-substrate interface, and thus the propensity to shed.

In a complete system, the substrate would be accurately modelled (geometry and material) and a Finite Element Analysis (FEA) would be used to allow two-way thermal coupling between it and the accretion. The temperature profile at various surface locations could then be extracted and compared to existing thermocouple data to tune the model and coupling. Since this is outside of the scope of the

current work, another approach is required. Three simple options are available and may be chosen depending upon the geometry and data available:

1. The 'thin shell' model. There is no transient response of the substrate; the substrate adopts the total wet bulb temperature, TWB_0, from the start of the simulation and holds it for all time. This is based on empirical evidence from the NASA/NRC fundamental ice crystal icing studies in 2010 (Struk and Wright, 2012). A wedge test article with a thin Ti90-Al6-V4 alloy icing surface and embedded surface thermocouples was tested in RATFac. The steady state thermocouple readings, generally reached within the first 10 s of exposure, were found to be a reasonable match for the TWB_0 at a particular test condition.
2. The 'infinite thermal capacity' model. It is assumed that the substrate has thermally soaked to equilibrium in dry flow (no icing cloud) and is isothermally at the dry recovery temperature, $T_{r,dry}$. The substrate is assumed to have infinite thermal capacity and therefore does not change temperature when exposed to the icing cloud.
3. The 'experimental boundary condition' model. A transient substrate temperature response is imposed, using experimental measurements for the same geometry and test conditions.

6.6 Surface Water Film Modelling

ICICLE currently does not have an embedded surface water film model. A model, based on lubrication theory, was integrated into the first iteration of the ONERA ice crystal model (Villedieu et al., 2014), but was abandoned in a later version (Trontin et al., 2016) as it was found that the predicted growth rate was overly sensitive to film thickness. In ICICLE, therefore, film growth is treated in a simplistic manner.

Two models are available:

1. The 'thick film model': water runback is inhibited, so the film thickness grows without limit. This is essentially a one-dimensional version of EMM-C.
2. The 'thin film model': water runback is enabled. In this case, the film thickness at the end of the timestep is fixed at a user-defined value, and any excess water above this thickness is

allowed to run back to the next panel. If the film thickness is below the user-defined value, then its value is left unchanged. Based on empirical evidence in Wang, (2008), the default film thickness is taken as:

$$h_{film} \approx 2\, k_{RA} \tag{6-36}$$

where k_{RA} is the arithmetic roughness average. When the substrate is not iced (i.e. a single water film), the RA may be measured directly or estimated given the substrate material and manufacturing processes applied. When the substrate is iced, the local surface roughness will likely be significantly higher, and vary with melt ratio, velocity, erosion rate, surface position etc. Surface roughness for supercooled water droplet icing has been characterised in several studies (McClain et al., 2018; Shin, 1996), but not for ice crystal icing to date. Between the two icing types, the particle deposition mechanics differ significantly, not least because the former involves purely liquid particles and the latter a mixture of solid and liquid particles. Therefore in the present work there is no attempt made to estimate the iced surface roughness.

When partially melted particles stick to the surface, all of their water is transferred to the film (i.e. no splashing). When partially melted particles bounce off a surface, their water is also transferred (shed) into the film. The water mass flux remaining on the surface is therefore given by

$$\dot{m}_{w,stuck} = \dot{m}_{w,stuck\ particles} + \dot{m}_{w,bounced\ particles} \tag{6-37}$$

6.7 Model Results

The following results are intended to be indicative of the operation of the EMM-C model. The simple test case here is ice growing on a single panel at a stagnation point, for a fixed exposure time of 20 s. The surface roughness of the panel is taken as $k_{RA} = 1$ μm. The height of any surface water film that forms, $h_{w,surf}$, is therefore taken as 2 μm. To aid clarity of the data, the surface water film is not plotted in the ensuing results.

Erosion is not considered in the calculation and a sticking probability of unity is assumed, regardless of condition. The ice and water thicknesses are therefore determined solely by the continuity and energy equations.

The baseline aerodynamic and icing conditions used in the simulations are given in Table 4. Differing values of melt ratio, relative humidity, Mach number were also tested. The effect of implementing the three different substrate thermal response models is also assessed.

Table 4 Parameters used in initial simulations with EMM-C

Parameter	*Baseline value*
M [-]	0.4
T_0 [K]	283
P_0 [kPa]	34.5
TWC [g/m^3]	8.0
RH_0 [-]	0.45
Average melt ratio, MR[-]	0.2
Initial substrate temperature [K]	283

At the baseline conditions given, $Twb_0 = 275.5$ K, and the dry recovery temperature is taken as $T_r = 282$ K. It is assumed that the impinging particles are in the process of melting and thus have uniform temperature T_f. Unless otherwise stated, the experimental boundary condition substrate model is used.

6.7.1 Effect of Substrate Thermal Model

Fig. 6-7 shows the predicted internal water layer thickness, h, and ice thickness B for the thin shell, infinite thermal capacity and experimental boundary condition models. Data for the latter are taken from thermocouple measurements from the cone test article at the same test conditions. The case of an isothermal 'cold' substrate (at 263 K) is also considered.

The predicted internal water layer height for the thin shell model after 10 s is approximately 280 μm, for the infinite thermal capacity model it is 569 μm, and 440 μm for the experimental boundary condition model. In all cases, a water film forms first, but the surface temperature reaches freezing within 1 s. The 'cold' substrate case correctly predicts no internal water layer.

The predicted temperature at the exposed accretion surface is plotted in Fig. 6-8 for the first three seconds of exposure, for the experimental boundary condition substrate model and the isothermal cold substrate model. For the former case, the surface of the water layer cools to freezing temperature within the first ~0.6 s; in the latter case a water film may form over the ice layer after ~ 2 s.

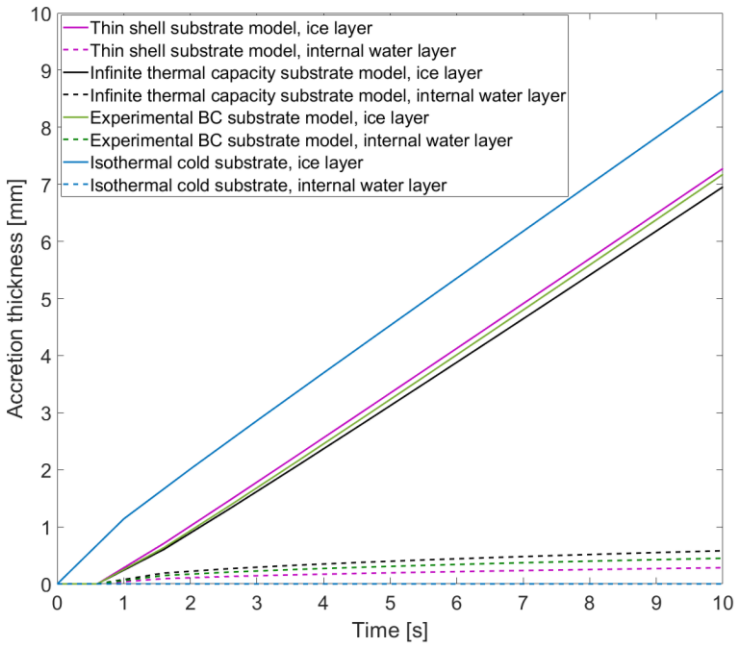

Fig. 6-7 Predicted thickness of ice and internal water layers for the thin shell, infinite thermal capacity and experiment boundary condition substrate models, as well as an isothermal 'cold' substrate case.

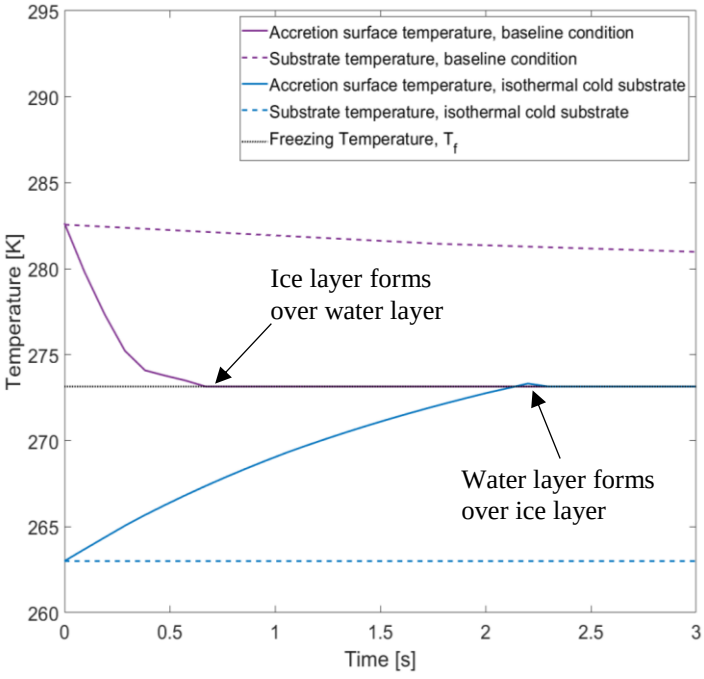

Fig. 6-8 Predicted temperature of the accretion surface over time for the baseline condition (with experimental boundary condition substrate model) and for a case of an isothermal 'cold' substrate at 263 K.

Fig. 6-9 shows the constituent heat flux terms in the EMM-C model over the first five seconds of exposure, for the baseline conditions and the experimental boundary condition substrate model. Heat fluxes at the exposed water surface comprise convection (q_{conv}), sensible warming of runback water ($q_{sens,run}$), sensible warming of impinging particles ($q_{sens,imp}$), evaporation (q_{evap}), kinetic heating (q_{kin}) and freezing (q_{freeze}). These terms are summed to attain the next heat flux at the surface, $q_{surf,net}$, which is given by equation (6-35). Finally, the heat flux in the internal water layer, $q_{cond,w}$, is calculated. This is the heat conducted from the substrate to the water-ice interface, balanced by the rate of melting at the interface.

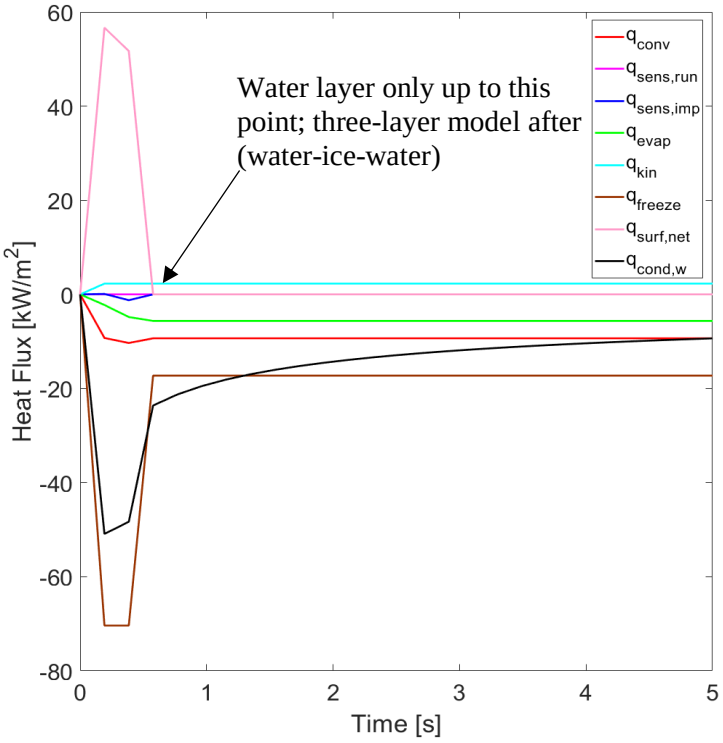

Fig. 6-9 Constituent heat fluxes in EMM-C for the baseline case and experimental boundary condition substrate model

There is a positive peak in q_{net} during the water-only stage (the first ~0.6s). This signifies net heat transfer *away* from the exposed surface, driven by the heat flux required to melt the impinging ice particles. There is a constant heat source to the surface due to kinetic energy transfer of $q_{kin} = 2.3\ kW/m^2$. The remaining heat flux terms vary as the water surface temperature decreases towards the freezing temperature, T_f. The convective and evaporative heat flux terms are negative, signifying heat and mass transfer *to* the water surface respectively. The sensible warming of run-in water (q_{run})

is zero for all time since it is assumed that there can be no run-in water for a panel at a stagnation point (tip or leading edge).

Once the exposed surface reaches freezing temperature, assumption (A8) requires that $q_{surf,net} = 0$ and the surface heat flux terms adopt their steady values. The steady freezing heat flux, q_{freeze}, at the exposed surface remains negative, showing that there is sufficient heat to the surface to continue melting impinging ice. The heat conducted in the internal water layer, $q_{cond,w}$, does not reach a steady value over the exposure time. It is given by

$$q_{cond,w} = -k_w \frac{T_f - T_{subs}}{h} = L_f \frac{dh}{dt}$$

As the internal water layer grows, and h increases, the value of $q_{cond,w}$ decreases, hence decreasing the heat flux available to melt the interface. The rate of increase of h therefore decreases over time.

6.7.2 Effect of Perturbing Test Condition

Fig. 6-10 shows the accretion thicknesses for the cases of a melt ratio (MR) of 0 (full glaciated cloud) and a melt ratio of unity (fully melted cloud), as well as the baseline (MR = 0.2) case. It is assumed the differing melt ratios are achieved artificially (e.g. by injection of water, and the thermodynamic conditions are unchanged from the baseline case). As a result, the internal water layer thickness changes negligibly between the baseline and the MR = 0 cases. Sticking efficiency is assumed to be unity regardless of melt ratio.

For the MR = 1 case, the initial q_{freeze} term falls to zero since no ice requires melting. The surface energy balance predicts that there is sufficient heat to the surface that ice does not form within the exposure time (i.e. running wet conditions). Changing external condition, e.g. lowering relative humidity and/or lowering dry total air temperature beyond a critical point would result in enough heat being removed from the surface that ice *would* form within the exposure time. For example, this may be achieved by lowering the relative humidity to $RH_0 = 0.2$ whilst keeping other conditions the same, increasing evaporative cooling.

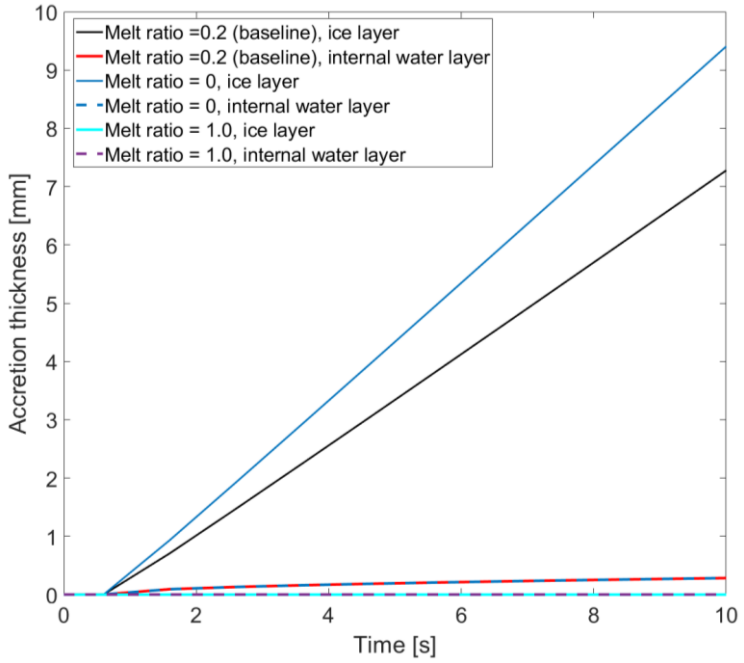

Fig. 6-10 Predicted ice and water accretion thicknesses for varying melt ratio. The baseline case (MR = 0.2) and cases of MR = 0 and MR = 1 are plotted.

Fig. 6-11 shows predicted accretion thickness for cases where Mach number and relative humidity were each perturbed in turn. Data are given for the case of a reduced Mach number of 0.25 (with the baseline relative humidity), and the case of an increased relative humidity of 0.65 (with the baseline Mach number). The accretion thicknesses for the baseline condition are once again plotted. In the case of the Mach 0.25 case, the TWC is increased to hold the mass fluxes of ice and water constant.

The primary effect of the reduced Mach number is a reduction in heat flux *to* the accretion surface. This is due in part to the slower-moving particles reducing the kinetic energy transfer, q_{kin}, but primarily due to the reduction in convective and evaporative heat flux to the surface due to the reduction in heat transfer coefficient. These effects result in a reduced melting mass flux and reduced water runback mass flux. The ice thickness after 10 s is therefore ~0.7 mm greater than the baseline case. This illustrates that a significant difference in accretion thickness may be obtained solely by differing thermodynamic conditions, and demonstrates that icing codes cannot rely alone on a continuity-based model (sticking probability, erosion) to produce realistic overall ice profiles.

When the relative humidity is increased from it baseline value of 0.45 to 0.65, the total wet bulb temperature rises to 5.5 °C. The substrate therefore remains warmer for longer, resulting in a thickened

internal water layer. For simplicity, it is assumed that the elevated wet bulb temperature does not increase the rate of particle melting, so the average melt ratio is held constant. The evaporative heat flux to the surface increases, due to the increased freestream vapour pressure. This is balanced by an increase in the melting mass flux at the surface, thus generating a higher runback mass flux. The ice thickness is therefore less than half its value in the baseline case.

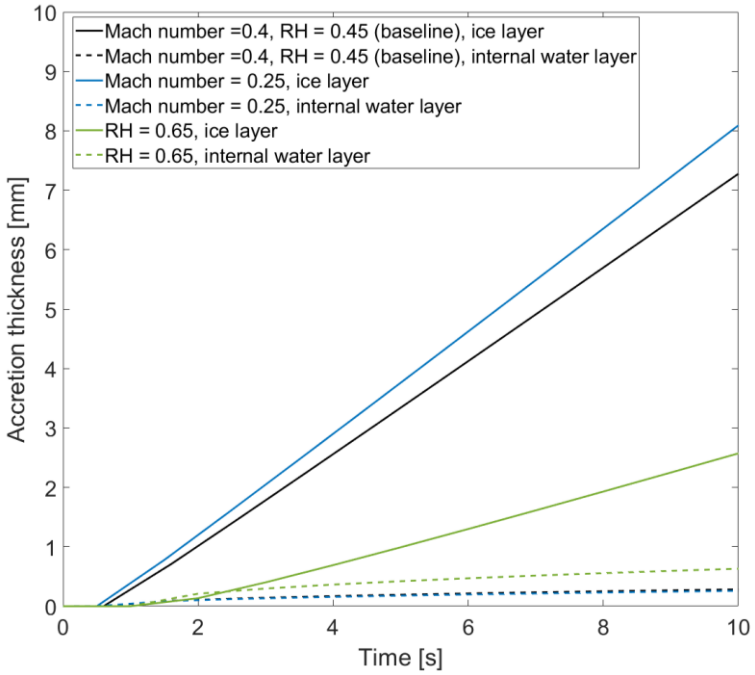

Fig. 6-11 Predicted accretion thicknesses for perturbed Mach number and relative humidity. Data are plotted for the baseline case (M = 0.4, RH = 0.45), for a case with M = 0.25 and for a case with RH = 0.65.

6.8 Summary

A new thermodynamic model for ice accretion under ice crystal icing conditions has been proposed, and applied to a simple test case. The inherent assumptions in the model have been described, and where possible justified.

It now remains to integrate the model into ICICLE to validate its performance against experimental test cases.

7 Code Development & Results

In this chapter, ICICLE is applied to the validation test cases (the cone and stator test articles). Sensitivity to key numerical parameters including particle count, timestep and grid size is assessed. Predictions for the cone test article are then compared to experimental results, including a study of the effect of two-way coupling of mass and energy, and geometry update. Note that these results are merely confirmation that the code can operate as a whole, since the results from the cone tests are already embedded in the code in the form of the sticking and erosion models. Finally, validation test cases are performed using results from the stator test article. The effect of updating the flowfield during the accretion time is also investigated.

7.1 Collection Efficiency Calculation & Sensitivities

Fig. 7-1 shows the arrangement of panels on the cone surface. A panel is made up of a group of contiguous 'wall points' (the points that define the geometric domain). The placement and size of panels must be chosen carefully; smaller panels increase spatial resolution but at an increased computational cost. Ice crystal accretion surface roughness can vary significantly depending on test condition. It is not expected that this will ever be able to be directly solved; so panel size is chosen to best predict local bulk growth rates.

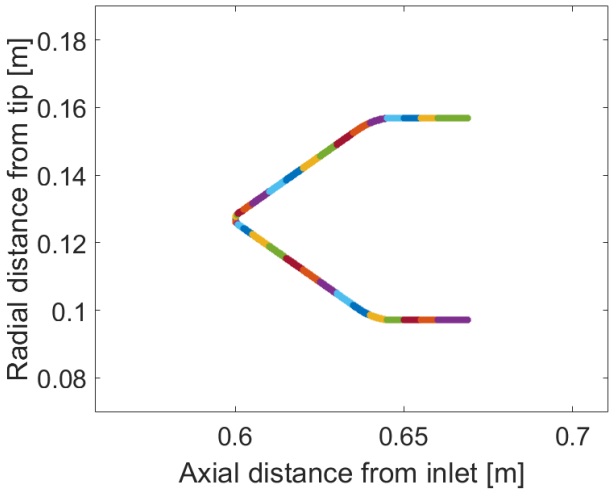

Fig. 7-1 Cone test article as a 2D slice inside ICICLE. Panels are denoted by the coloured segments. Flow is left to right.

The number of particles tracked must be sufficient to afford statistical convergence. The number of 'real' (physical) particles represented by a single numerical particle is given by the scale factor, SF. This is calculated as

$$SF = \frac{Real\ particles}{Numerical\ particles} \cong \frac{TWC\ U_\infty \Delta t_{layer} A_{injection} \Big/ \left(\frac{\pi}{6}\ {D_{eq}}^3 \rho_p\right)}{N_{particles}} \tag{7-1}$$

where $N_{particles}$ is the number of numerical particles and $A_{injection}$ is the inlet area over which particles are injected in the simulation. A high value of SF means that each numerical particle represents more physical particles. Since the numerical particle cloud is a statistical representation of the physical cloud, the accuracy of the representation decreases as SF increases.

The parameters that will be investigated in this chapter and their baseline values are given in Table 7-1. All other conditions are fixed at their baseline values as given in chapter 3. The baseline value of melt ratio is within the plateau region of sticking probability (i.e. where rapid accretion occurs). A range is given since, in the RATFac experiments, melt ratio is targeted rather than controlled directly. A target value is attained by controlling temperature, pressure and relative humidity and so is subject to the uncertainty in each of these parameters.

Table 7-1 Summary of baseline values for the parameters varied experimentally

Parameter	*Baseline*
Mach [-]	0.40
Melt ratio [-]	0.09-0.13
Ice D_{v50} [μm]	34
Cone half angle [°]	35

Fig. 7-2 (a) shows particle trajectories for the cone test article at the baseline conditions. Fig. 7-2 (b) shows the same condition, windowed on the lower half of the cone surface. 10,000 particles are tracked; every 20th is plotted. At this condition, the mean sticking probability is ~ 0.95. The majority of particles are therefore more likely to stick on impact. However, individual particle sizes range from 138 μm down to 2 μm, resulting in melt ratios in the range 0.02 to 1.00. At these extremes of melt ratio, sticking probability on individual particles falls to zero, and so bouncing occurs.

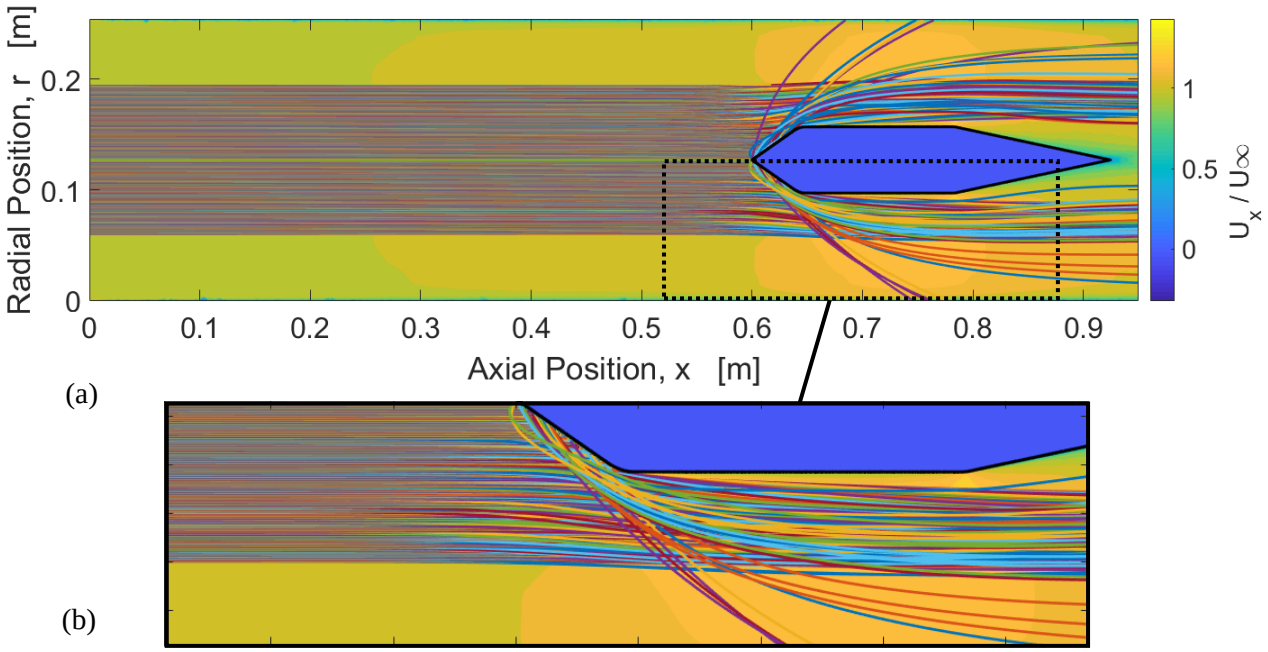

Fig. 7-2 Particle trajectories for the cone test article, overlaid onto a contour of normalised axial velocity. 500 trajectories are plotted, for the condition of M = 0.4, D_{v50} = 34 µm, TWC = 8 g/m^3. Flow is left to right.

The number of impinging particles is used to estimate an average collection efficiency for the panel:

$$\beta_{avg,panel} = \frac{N_{p,imp} / A_{panel}}{N_{p,injection} / A_{injection}} \tag{7-2}$$

where $N_{p,imp}$ and $N_{p,injection}$ are the number of particles impinging on the panel, and the number of particles injected respectively.

Statistical convergence of particle trajectories may be assessed by calculating collection efficiency using equation (7-2). Calculations were performed at baseline conditions on the 35° half-angle cone. Fig. 7-3 (a) shows the average collection efficiencies over the inclined cone wall for a range of scale factor, SF. Results are shown for both Mach 0.25 and 0.4 cases. Note that if trajectories are ballistic, the local collection efficiency is given by $\beta = \sin(35) = 0.574$. Convergence may be seen for the lower values of SF. For the Mach 0.4 case, the corresponding number of numerical particles is also shown; 10,000 particles would be suitable. At lower particle counts (< 1000), the smallest panels incur sufficiently low impact counts that local collection efficiency can spuriously deviate from the ballistic value.

A sensitivity analysis to Lagrangian timestep was also performed. It was introduced in Chapter 4 that the local timestep is given by

$$t_t = K_t \left({}^{d_{min}}/_{U_t} \right) \tag{7-3}$$

where K_t is a user-defined constant. A shorter timestep increases the accuracy of both the trajectory and the assignment of impact location. For the latter, a shorter travel distance when the particle is approaching a wall results in a more accurate estimate of the wall point the particle is near when impact is detected. A longer timestep can lead to the particle trajectory stopping short, 'entering' the test piece, or the impact location being assigned to the wrong panel. Fig. 7-3 (b) shows the same calculation of average collection efficiency for a range of K_t. The value of K_t was set at unity for the remainder of the simulations.

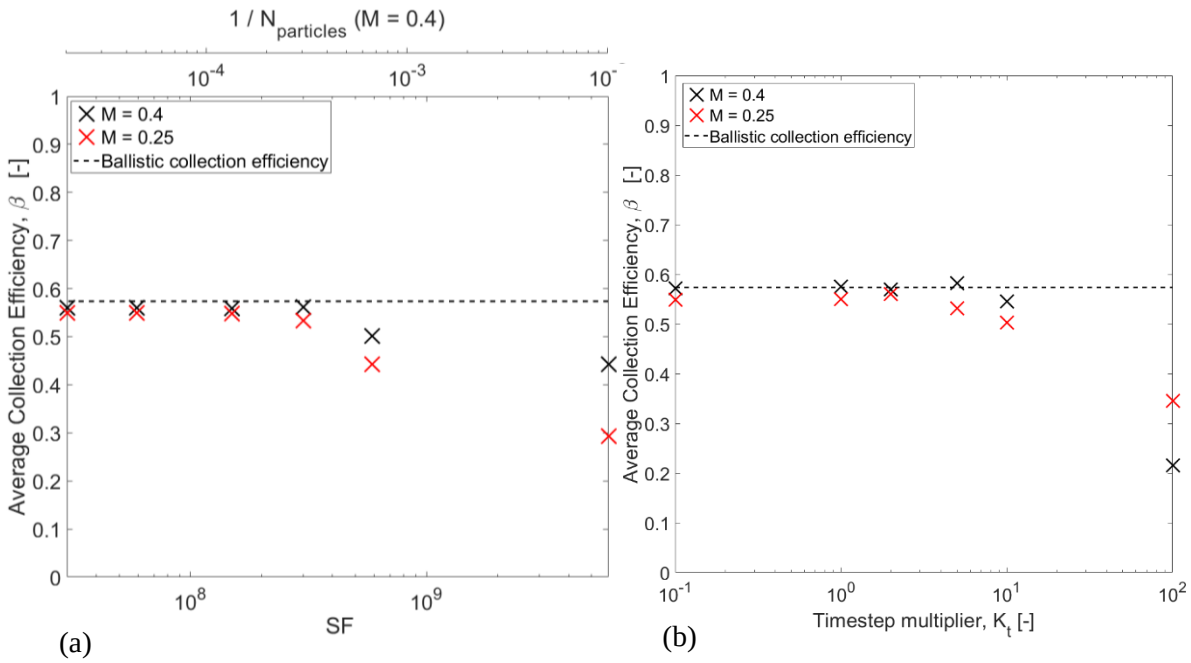

Fig. 7-3 Sensitivity in collection efficiency to (a) particle scale factor and (b) timestep multiplier, K_t

A sensitivity analysis was also performed to the flowfield grid, using grids with 120k, 240k, 320k, 960k and 1.9M cells, using collection efficiency and Mach number distribution around cone as the parameters under test. The maximum difference in collection efficiency and Mach number were found to be 1% and 0.5% respectively between the 960k and 1.9M cell cases. The 960k cell grid was selected, comprising 1200 nodes in the axial direction and 800 nodes in the radial direction.

7.2 Growth Calculation & Sensitivities

The rate of particle sticking is scaled using SF to get the mass fluxes of ice and water under 'real' conditions, $\dot{m}_{i,panel}$ and $\dot{m}_{w,panel}$. The thermodynamic model (EMM-C) is solved per panel, using $\dot{m}_{i,panel}$, $\dot{m}_{w,panel}$, $\dot{m}_{w,run\ in}$, H_{panel}, $\omega_{e,panel}$, $T_{e,panel}$ and $P_{e,panel}$ as its primary inputs. H_{panel} is the average heat transfer coefficient, and $\omega_{e,panel}$, $T_{e,panel}$ and $P_{e,panel}$ are the local freestream specific humidity, static temperature and static pressure respectively. The local heat transfer coefficient is interpolated from the CFD-derived values given in chapter 3. As there are no upstream bodies, bouncing and surface heat transfer prior to impingement on the test article is not considered.

The model outputs the 'gross growth' (neglecting erosion) of ice ($\Delta B_{gross,panel}$) and water ($\Delta h_{gross,panel}$). An erosive efficiency ($\eta_{ero,}$, between zero and unity) is then calculated individually for each point in the panel, using the model proposed in chapter 5. Individual calculations are performed since points on curved panels will have a range of surface normals, and thus a range of erosive efficiencies. The 'net' ice and water layer growths for each point are then given by equations (7-4) and (7-5), where it is assumed that erosion only changes the ice layer thickness.

$$\Delta B_{net,point} = \Delta B_{gross,panel}\,(1 - \eta_{ero,point}) \tag{7-4}$$

$$\Delta h_{net,point} = \Delta h_{gross,panel} \tag{7-5}$$

The inputs required for the erosion model are the surface normal (γ) for each wall point, and the average diameter, velocity and temperature of particles impinging on the panel. Fig. 7-4 shows the growth process schematically.

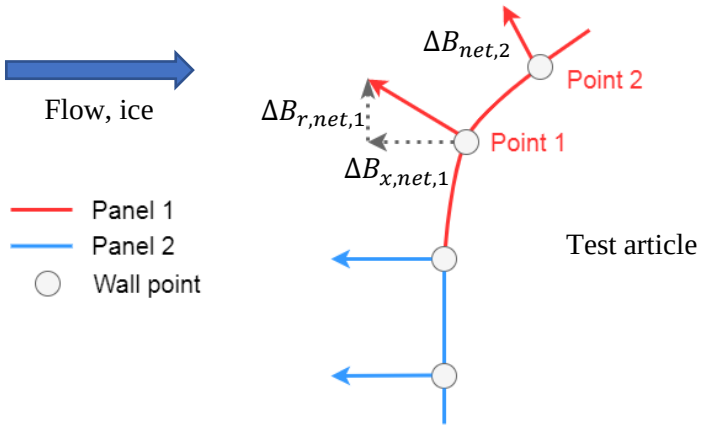

Fig. 7-4 Schematic of ice layer growth for a notional geometry

Since the sticking mass flux is defined on a panel-by-panel basis, the accretion can adopt a stepped profile, with discrete thickness changes and spurious surface normal angles where panels meet. A spurious erosive efficiency may be calculated in the ensuing timestep – resulting in a still larger inter-panel step. This self-exciting behaviour can result in solution instability. Fig. 7-5 shows the change in surface normal, γ, for four wall points at various locations on the cone test article. An instability can be seen for the mid-wall location after around 100 s.

A stepped accretion profile could, under certain circumstances (for example cases of low erosion or high melt ratio), be a real phenomenon. However, it is not desirable at this point in the code development to allow one to form. Solution stability and an accurate prediction of bulk growth rates - such that the overall volume of the predicted ice is close to reality – is more important. Maintaining stability and reducing the numerical error caused by smoothing when encountering these stepped profiles is therefore an area of ongoing work.

Several techniques to smooth the accretion profile were trialled, covering spline-fitting and digital filtering methods. It was desired to improve solution stability without generating a non-physical accretion profile, with a single method that would be applicable to both the cone and stator test articles.

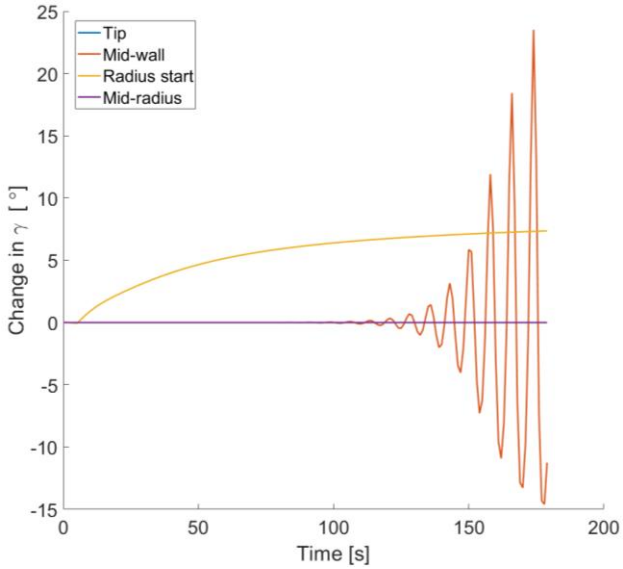

Fig. 7-5 Change in local surface normal angle over accretion time for an unsmoothed (unstable) case

Spline fitting was rejected for the cone case since it was observed that the spline could not replicate both the smooth sidewalls of the accretion and the sharp tip, both of which are physical features. A Savitsky-Golay digital filter was selected, which sequentially performs least-squares polynomial fitting over a small subset of the data. By keeping the window length of the subset sufficiently small, the sharp accretion tip can be maintained whilst also maintaining stability. The method is described in Savitsky and Golay, (1964), implemented in a MATLAB library function.

7.3 Growth Prediction on Baseline Case

Fig. 7-6 shows accretions on the 35° cone at the baseline aerodynamic and icing conditions after (a) 120 s and (b) 180 s of exposure. For all simulations, the thick shell (infinite thermal capacity) substrate model was used.

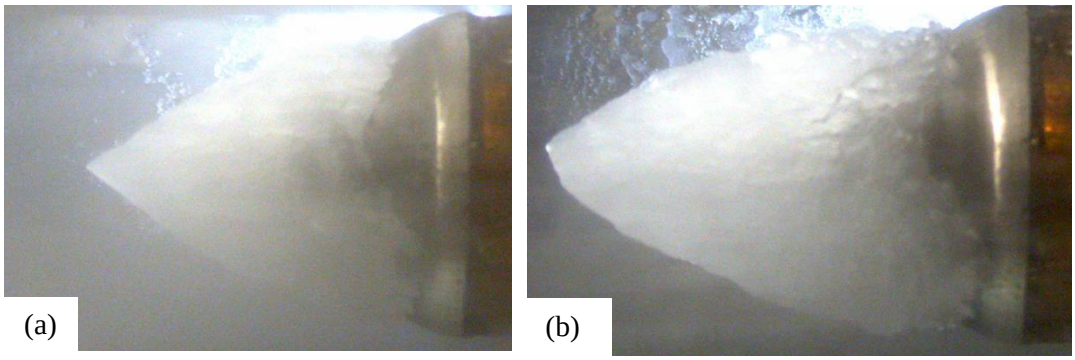

Fig. 7-6 Accretion on the cone at the baseline condition after (a) 120 s and (b) 180 s

Fig. 7-7 shows a comparison of ICICLE-predicted and experimental accretion profiles at the baseline test conditions on the 35 ° half-angle cone. Collection efficiencies were updated after 2 s of simulation time (multi-layer growth). A comparison is shown for discrete exposure times of 120 s and 180 s.

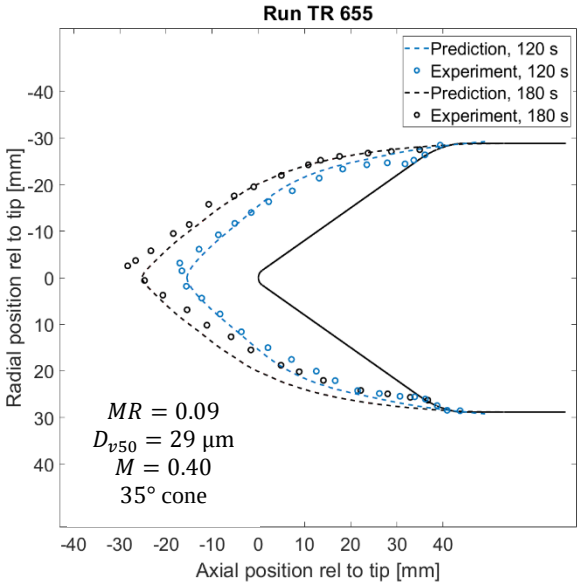

Fig. 7-7 Comparison of ICICLE-predicted and experimental accretion profiles for a test at baseline conditions

For both cases, the agreement on accretion thickness at the tip is within 10%. Agreement on the rest of the accretion is generally good, but notably poorer towards the rear, where the accretion meets the test article. This will be discussed further in the ensuing sections. The result in Fig. 7-7 is now used to investigate the effect of (i) single versus multi-layer simulations, and (ii) two-way mass/energy coupling.

Fig. 7-8 shows a comparison of predicted accretion growths for single layer and multi-layer calculations, for the same case as Fig. 7-7. The predicted accretion thickness at the middle of the cone wall (‘the mid-wall’) is given for simulations with, 1, 18, 36 and 90 layers. This is equivalent to the collection efficiencies and geometry being re-calculated every 180 s, 10 s, 5 s and 2 s respectively. Data are given at exposure times of 90 s and 180 s, as well as the experimentally-measured thickness at the same location and time.

The predicted thicknesses converge as the number of layers increases; for a growth time per layer of less than 5 s, the predicted growth after 180 s is within 5% of the experimental value. In subsequent simulations, a layer time of 2 s was typically used.

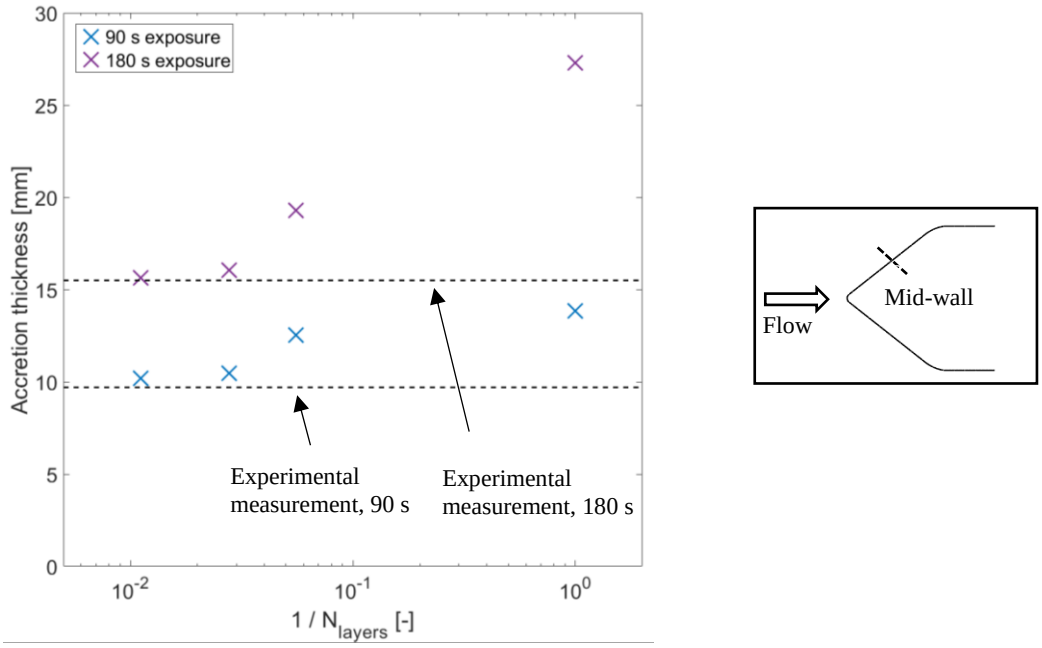

Fig. 7-8 Predicted accretion growth at the cone mid-wall for single layer and multi-layer simulations.

Fig. 7-9 shows a comparison of predicted and experimental accretion profiles, where the predictions have been generated both with and without two-way coupling of mass and energy implemented. For the two-way coupled cases, eight iterations with a relaxation factor of 0.75 were found to be sufficient to achieve convergence of both enthalpy and specific humidity at the exit plane. The axial tip growth in the two-way coupled case is around 2 mm greater than the one-way coupled case after 180 s, more closely matching the experimental measurement.

In the two-way coupled case a reduction of 3% in specific humidity and 0.5% in static temperature was observed compared to the one-way coupled case. This in turn resulted in the average particle melt ratio at impact with the test article being reduced from 0.14 to 0.13, and the sticking probability increasing from 0.98 to 1.00. This accounts for approximately a 0.6 mm increase in axial tip growth in the two-way coupled case. The overall shape is otherwise unchanged, indicating that the effect of two-way coupling on erosion is negligible. Under the current assumptions, the only effect would be the change in evaporative mass flux altering the particle equivalent diameter at the point of impact.

Under the conditions used, the evaporative mass flux from accretion to freestream is negative (condensation, a heat source to the accretion surface). In the two-way coupled case, this mass flux is reduced and thus the heat source also reduces. As a result there is a 4% increase in the tip growth rate; this approximately accounts for another 1.2 mm increase in axial tip growth. The 2 mm difference between the one- and two-way coupled cases can therefore nearly be accounted for through these two mechanisms.

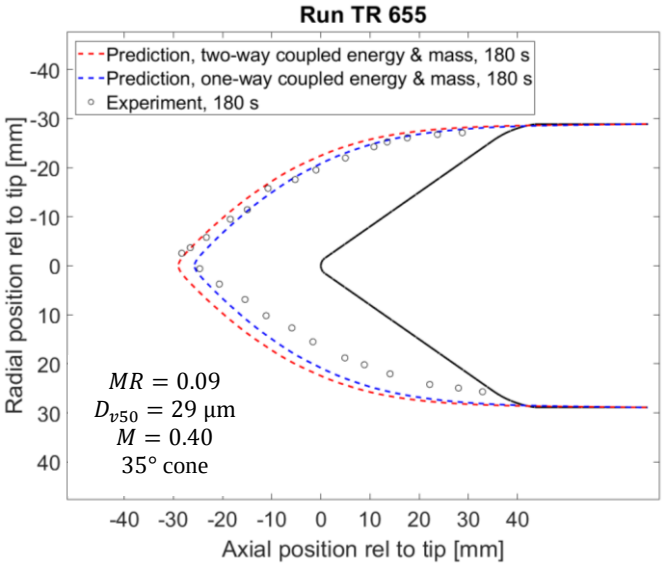

Fig. 7-9 Comparison of ICICLE-predicted and experimental accretion profiles with and without two-way mass and energy coupling implemented.

Growth histories are shown in Fig. 7-10, with data given at the tip, mid-wall (50% streamwise distance) and radius. At the mid-wall, data is plotted for 30 s onwards, due to unreliable data before. Near the start of the test, cloud fluctuations and thin accretions can lead to spurious thickness calculations. Errorbars are plotted for every 20th point of the tip data. An uncertainty analysis is given in chapter 5. There is significant discrepancy within the first 60 s for the predicted and measured thickness at the tip. The predicted growth has a transient reduction through the first ~ 30s, followed by an approximately linear growth for the rest of the exposure time. This is an artefact of the necessity to divide the geometry into panels. The cone tip is modelled as reasonably blunt, with a 1 mm radius. This is representative of the real test-article (the 35° half-angle cone had a 0.7 mm radius after the necessary surface polishing had been completed), but also aids solution stability compared to a perfectly sharp tip. The panel covering the tip therefore has an initially high average catch efficiency

(more normal to the flow). As the accretion grows forward, the tip sharpens, impacts become more oblique, average catch efficiency decreases and thus the predicted growth rate decreases. An approximately steady growth rate is reached within the first 30 s. The effect of panel placement and width is further investigated on the stator test article in Section 7.5.1.

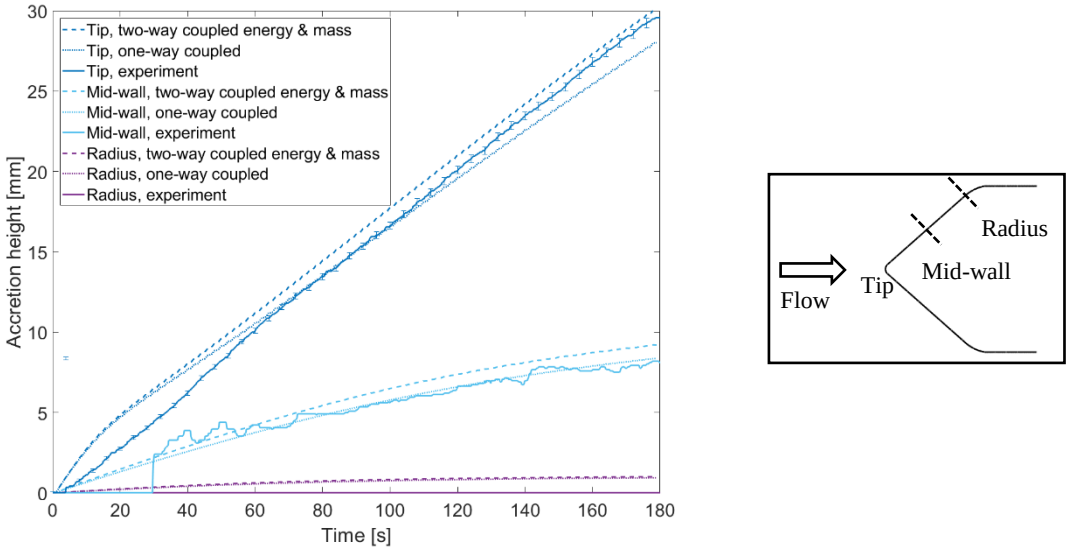

Fig. 7-10 Comparison of ICICLE-predicted and measured accretion growth histories for three locations on the cone surface. Predictions are given with and without two-way coupling of mass and energy implemented.

In general, accretion growth at the tip and mid-wall is well predicted. For the radius, ICICLE predicts accretion, with a steady thickness of ~ 1mm after 180 s. In the experiment, as may be seen in Fig. 7-9, the diameter of the accretion is less than that of the cone – and the radius is clear of accretion. This is believed to be due to the propensity for water flow over the radius to promote particle sliding and reduce sticking probability. Since a physics-based filming model is not yet part of ICICLE, this phenomenon is outside of the predictive capability. This is explored further in the ensuing sub-section, where predictions from ICICLE are compared to experimental measurements for tests with differing melt ratios, erosive conditions and cone half-angles.

7.4 Simulation Results for the Cone Test Article

7.4.1 Tests at Differing Melt Ratio

Fig. 7-11 shows four comparisons of experimentally-measured and predicted accretion profiles on the 35° half-angle cone. In these four cases, relative humidity was varied between 0.05 and 0.65 to obtain

total wet bulb temperatures in the range -6.5 °C to 5.5 °C. This in turn generated measured particle melt ratios of (a) =0.01, (b) =0.04, (c) =0.09 and (d) =0.17. It was introduced in chapter 5 that the 'plateau region' for particle sticking probability occurs for melt ratios in the range 0.09 - 0.13. All other conditions were held at their baseline values to ensure no difference in the rate of erosion. The particle D_{v50} of =29 µm in case (c) is slightly lower than the nominal of =34 µm.

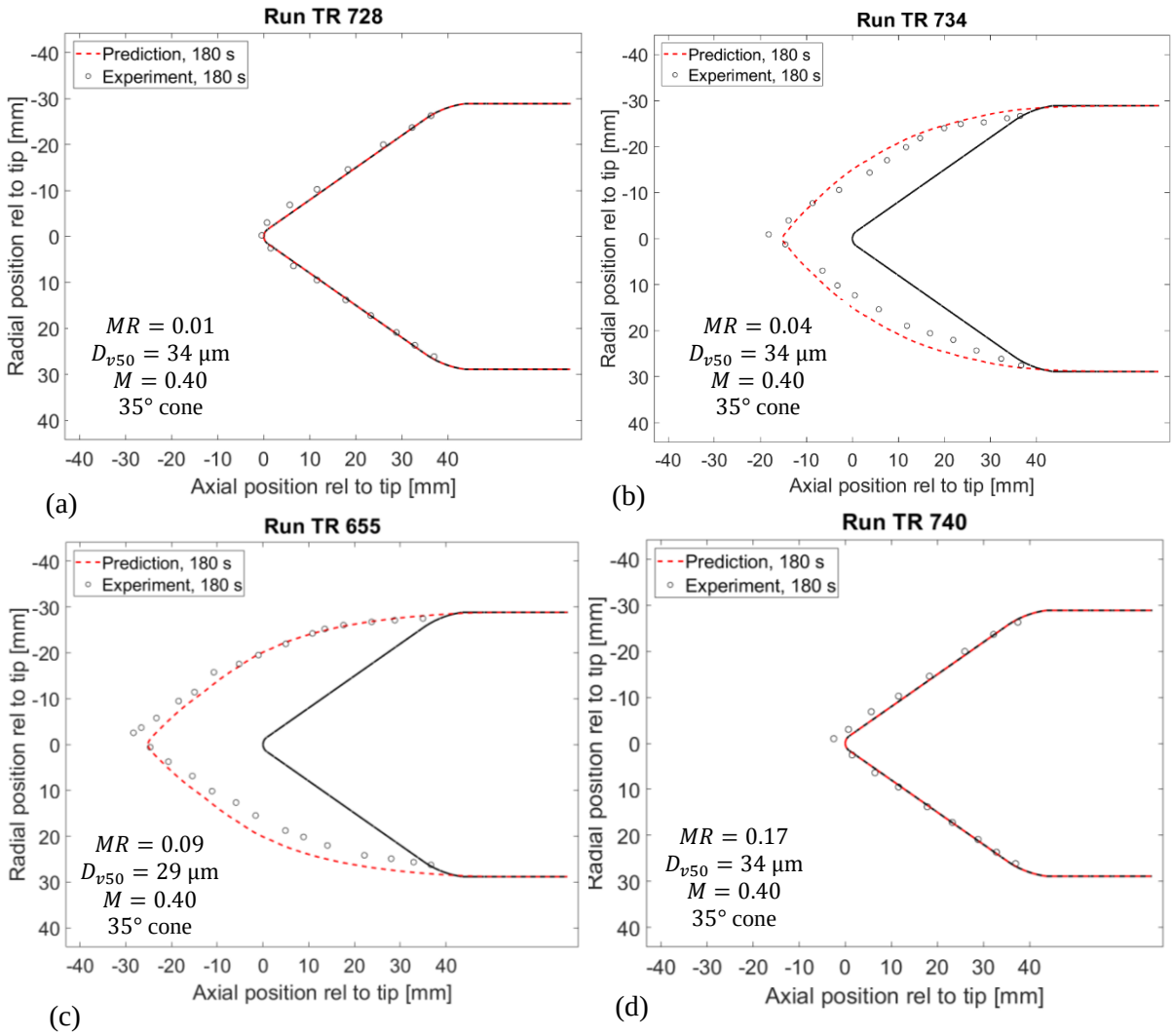

Fig. 7-11 Comparison of experimental and ICICLE-predicted accretion profiles on the 35° half-angle cone after 180 s. The pre-test relative humidities were (a) 0.05; (b) 0.30; (c) 0.45 and (d) 0.65.

It may be seen that in general the accretion profile is well predicted, with agreement on the axial tip growth within 15% for Fig. 7-11 (b) and within 4% for Fig. 7-11 (c). Although the tip agreement is better in (c), the shape of the accretion is more poorly predicted at this wetter test condition. Empirically, at wetter conditions significant run back of water is observed over the rear radius,

promoting particle sliding and inhibiting sticking. This results in an accretion that does not extend across the entire diameter, an effect that cannot be captured without integration of a physics-based water filming model. This therefore forms an area of future development for ICICLE.

Fig. 7-12 shows the accretions of cases TR734 and TR737 after ~200 s of exposure. In the drier case (a), the accretion extended almost to the rear of the cone, and was more firmly bonded to the test article. The accretion in Fig. 7-12 (b) rotated upwards and shed in its entirety around 10 s after the image was recorded, indicative of a water layer between test article and accretion permitting movement.

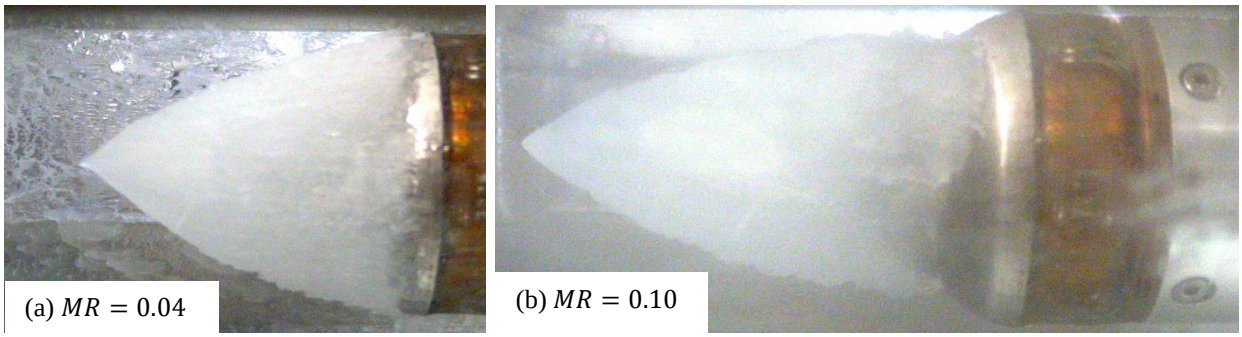

Fig. 7-12 Accretion profiles after ~ 200 s for cases (a) TR 734 and (b) TR737.

7.4.2 Tests at Differing Erosive Conditions

It was introduced in chapter 5 that the rate of mass loss due to erosion is strongly dependent upon particle kinetic energy and impact angle. Erosion was found to be greatest for large particles, high velocities and glancing (tangential) impacts. In the following test cases, the erosive condition is varied whilst maintaining melt ratio within the plateau region of sticking probability.

Fig. 7-13 shows a comparison of ICICLE-predicted and experimental comparisons for four test cases with differing erosive conditions. Cases (a) and (b) are at Mach 0.25, with D_{v50} values of 34 and 51 μm respectively. Approximately the same two particle size distributions are shown in cases (c) and (d), but at a Mach number of 0.4. Case (c) is the baseline condition, with a slightly low value of D_{v50}. The dependency on particle size may clearly be seen in cases (c) and (d); since the erosive efficiency is dependent upon particle kinetic energy, it is dependent upon the cube of D_{v50}.

The accretion in case (c) is only marginally smaller than its Mach 0.25 counterpart, case (a). This may be partially explained by the low D_{v50} value in case (c). There is a factor of 2.6 increase in kinetic energy between the Mach 0.25 and Mach 0.4 cases at a constant particle size of 34 µm. This factor is reduced to 1.6 if the particle size decreases to 29 µm in the Mach 0.4 case. Case (a) is also the wettest with $MR = 0.12$. An increased water content tended to result in rough, non-aerodynamic accretions with irregular profiles and growth rates. Case (c), in drier conditions, has a more steady rate of tip growth. Within the uncertainty of the melt ratio measurement, case (c) may also be off the right-hand edge of the plateau region, resulting in a depressed sticking probability.

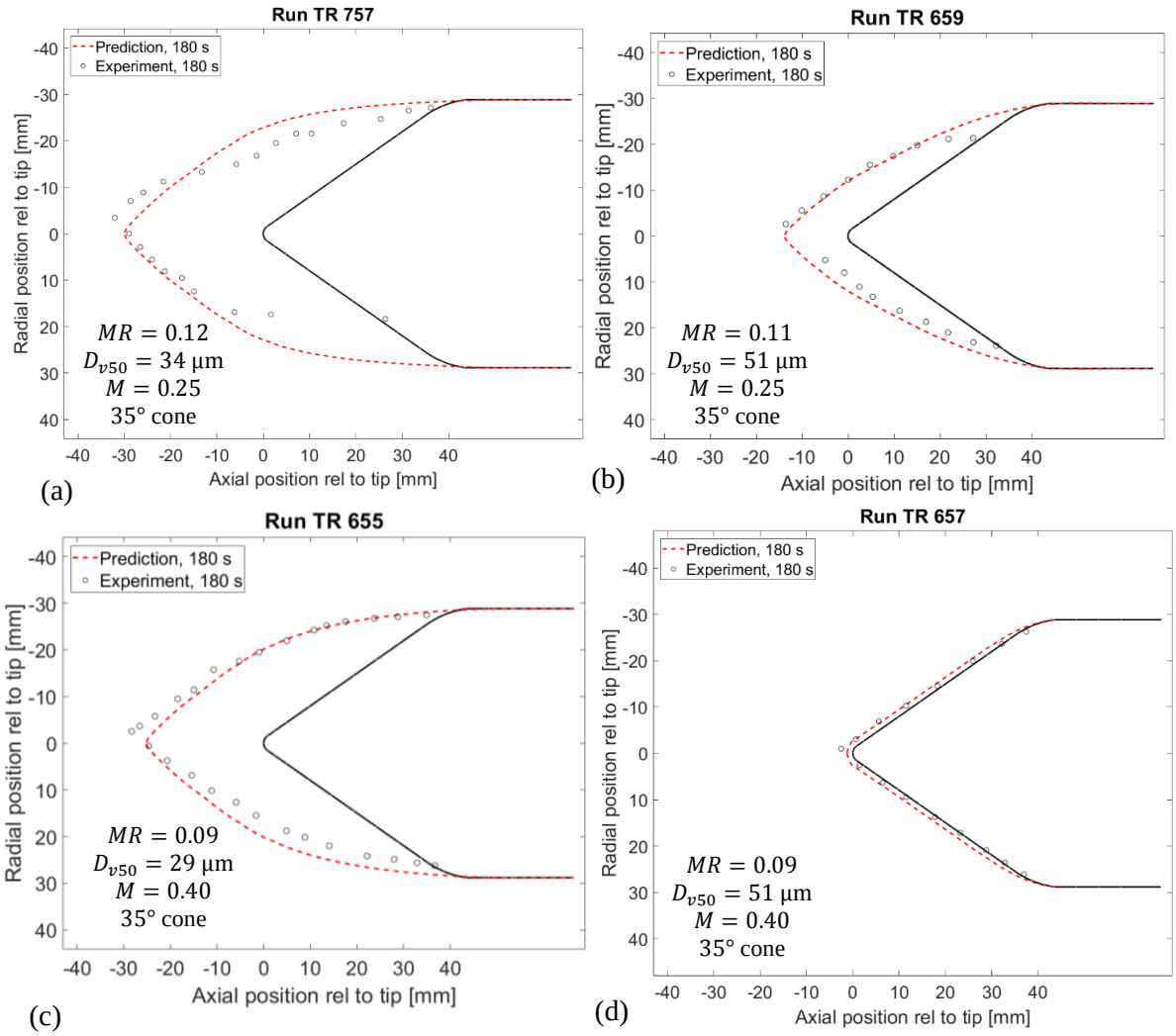

Fig. 7-13 Comparison of experimental and ICICLE-predicted accretion profiles on the 35° half-angle cone after 180 s.

7.4.3 Tests at Differing Cone Half-Angles

Fig. 7-14 shows experimental and predicted accretion profiles for tests conducted at (a) Mach 0.25 and (b) Mach 0.4 on the 45° half-angle cone. For both cases a 43 µm D_{v50} was used.

In case (b), the overall growth is significantly reduced compared to case (a) due to the higher rate of erosion (dependent upon the square of velocity). However, the accretion, although patchy in places, is more conical in shape, and extended back to the radius on the top side of the cone. This may partially be explained by the reduced melt ratio compared to case (a). Additionally, it was observed in multiple other test cases with the 45° cone at Mach 0.4 and 0.5 that accretions could grow stably on the radius. This is attributed to the high flow acceleration around the radius for this geometry. At a freestream Mach number of 0.4, the peak Mach number of 0.69 is a factor of ~1.2 greater than that of the 35 ° cone. Locally, there are reductions in static temperature of ~9 °C, in wall recovery temperature of ~4 °C (assuming a recovery factor of 0.89), and in static wet bulb temperature of ~5 °C relative to the freestream. This results in a region highly conducive to re-freezing for the partially melted particles and freestream LWC.

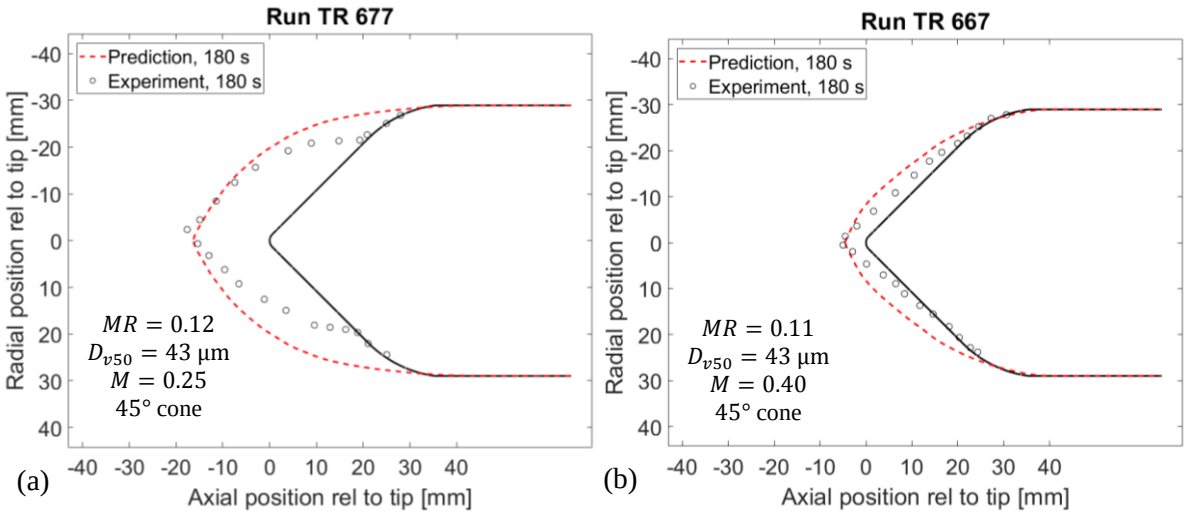

Fig. 7-14 Comparison of ICICLE-predicted and experimental accretions on the 45° half-angle cone

In Fig. 7-15, case TR677 is compared to a case on the 35° cone at similar conditions, albeit with a slightly elevated D_{v50}. Both cases have almost identical melt ratios, and are similar in that the diameter of the accretion is significantly less than that of the cone, with a radius clear of accretion. In both cases,

there was evidence of water runback over the rear radius, seemingly inhibiting particle sticking. In case (a), small lumps (a few millimetres in size) were also seen to detach from the rear of the accretion, slide backwards and shed into the airflow.

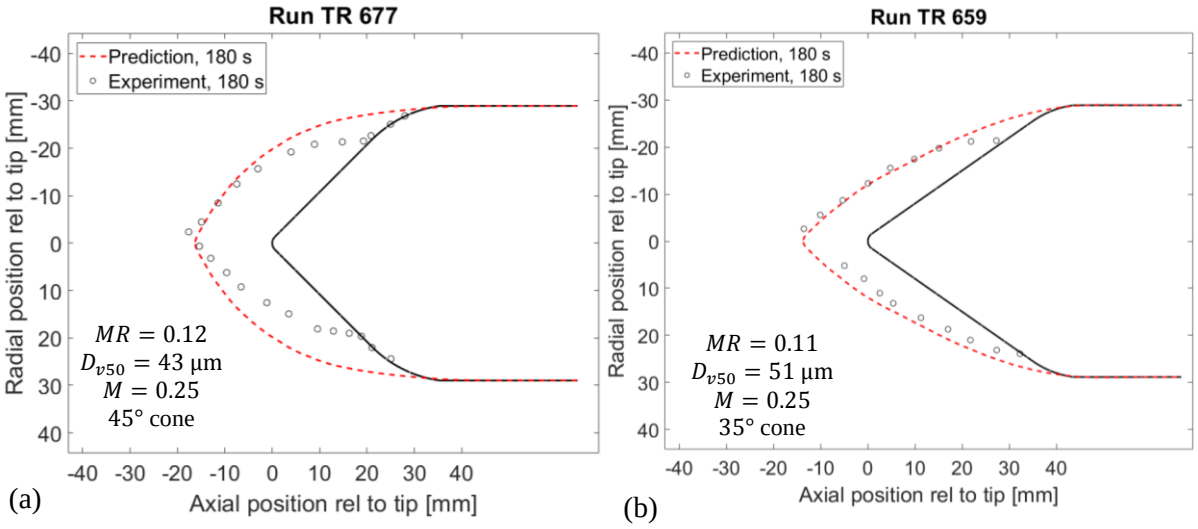

Fig. 7-15 Comparison of experimental and ICICLE-predicted accretion profiles on the 45° and 35° half-angle cones after 180s

Tests using the 20° half-angle cone revealed that sliding and conglomeration could have a significant effect on accretion shape, even in highly erosive conditions. Ice would grow in axially-aligned sharktooth shapes, formed by coalescing rearward-sliding particles. This tended to form rough accretions with axially-aligned striations, as shown in Fig. 7-16.

Fig. 7-16 Accretion on the 20° cone for M = 0.25, D_{v50} = 34 µm and MR = 0.11 after ~ 240 s of exposure

Fig. 7-17 shows experimental and predicted accretion profiles for tests conducted at (a) D_{v50} = 34 µm and (b) D_{v50} = 74 µm, both at M = 0.25. Both cases have a melt ratio of 0.11. In (b), the large particle

size and shallow impact angle leads to a predicted erosive efficiency of unity, i.e. an accretion cannot grow. This matches the experimental observation.

In case (a), there is an abrupt transition from the front of the accretion, which adopts a conical shape with concave walls, to the rear which adopts a rough cylindrical profile. The latter is indicative that tangential (shearing) erosion is preventing growth at highly oblique impact angles (glancing impacts), a feature that the code is able to replicate. The concave profile at the front of the accretion is seemingly unique to the 20° half-angle cases and cannot be predicted with the models currently implemented. Further testing with shallowly-inclined surfaces and investigation of sliding and filming models is required to understand the behaviour further.

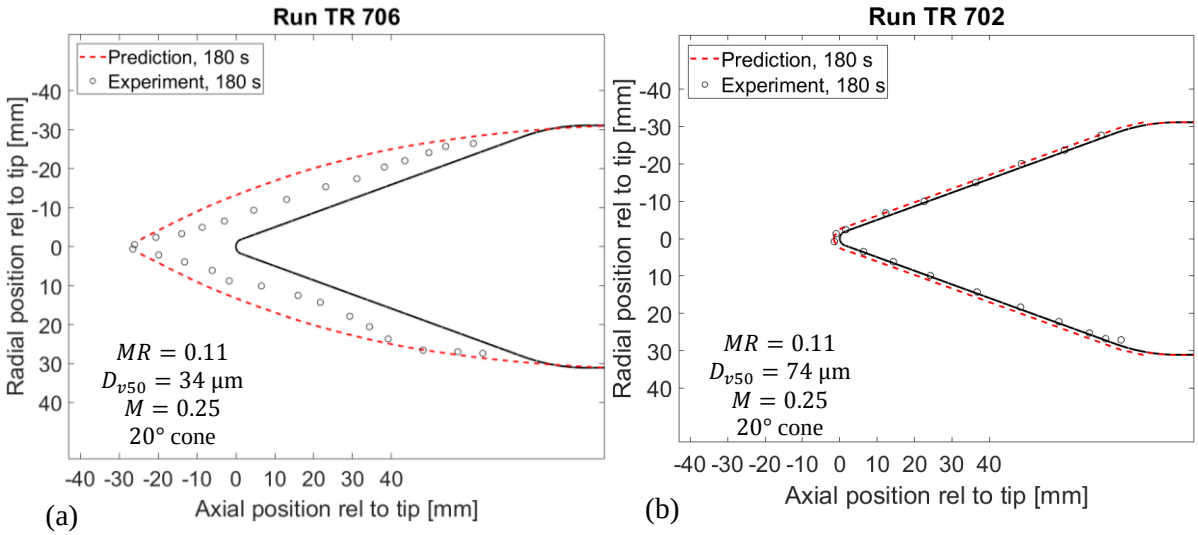

Fig. 7-17 Comparison of experimental and ICICLE-predicted accretion profiles on the 20° half-angle cone after 180 s

7.5 Simulations on Stator Test Article

Having validated that ICICLE can operate as a fully integrated code, and that it can replicate experimental accretions on the cone test article to a good level of accuracy, it remains to apply it to an entirely new test case – the stator. First, particle trajectories and collection efficiencies will be studied. Second, a baseline test case using the same baseline experimental conditions as the cone will introduced, followed by simulations in cases of differing melt ratio and particle size. Finally, the effect of implementing flowfield updating (two-way aerodynamic coupling) will be investigated.

In keeping with the convention used in RATFac, the stator results, similarly to the cone, define the vertically upwards direction as the 'radial' direction. It is recognised that this is not in keeping with the conventional use of 'radial' when applied to turbomachinery (i.e. the spanwise direction).

7.5.1 Particle Trajectories

Fig. 7-18 shows (a) the CFD-predicted flowfield and (b-d) particle trajectories for the stator test article at the baseline test condition. Trajectories are shown for three differing bands of initial particle size. Each band was defined as a nominal value, with particles with a diameter within 2.5 μm from the nominal value being tracked. The nominal values are (b) the minimum injected diameter, $D_{v,min} =$ 2 μm; (c) the 5th percentile diameter, $D_{v05} = 9$ μm; (d) the median diameter, $D_{v50} = 34$ μm; and (e) the maximum diameter, $D_{v,max} = 74$ μm. Trajectories are coloured by melt ratio, with cyan representing fully glaciated particles, and red representing fully melted particles. All particles enter the left-hand domain fully glaciated.

The RANS solution presented in Fig. 7-18 (a) is inherently unable to resolve the large separation from the stator suction surface. The particle trajectories downstream of the stator should therefore be viewed with suspicion, although qualitatively offer insight. Particle trajectories and impingement locations on the leading edge and pressure surface – where icing is expected – are taken to be correct.

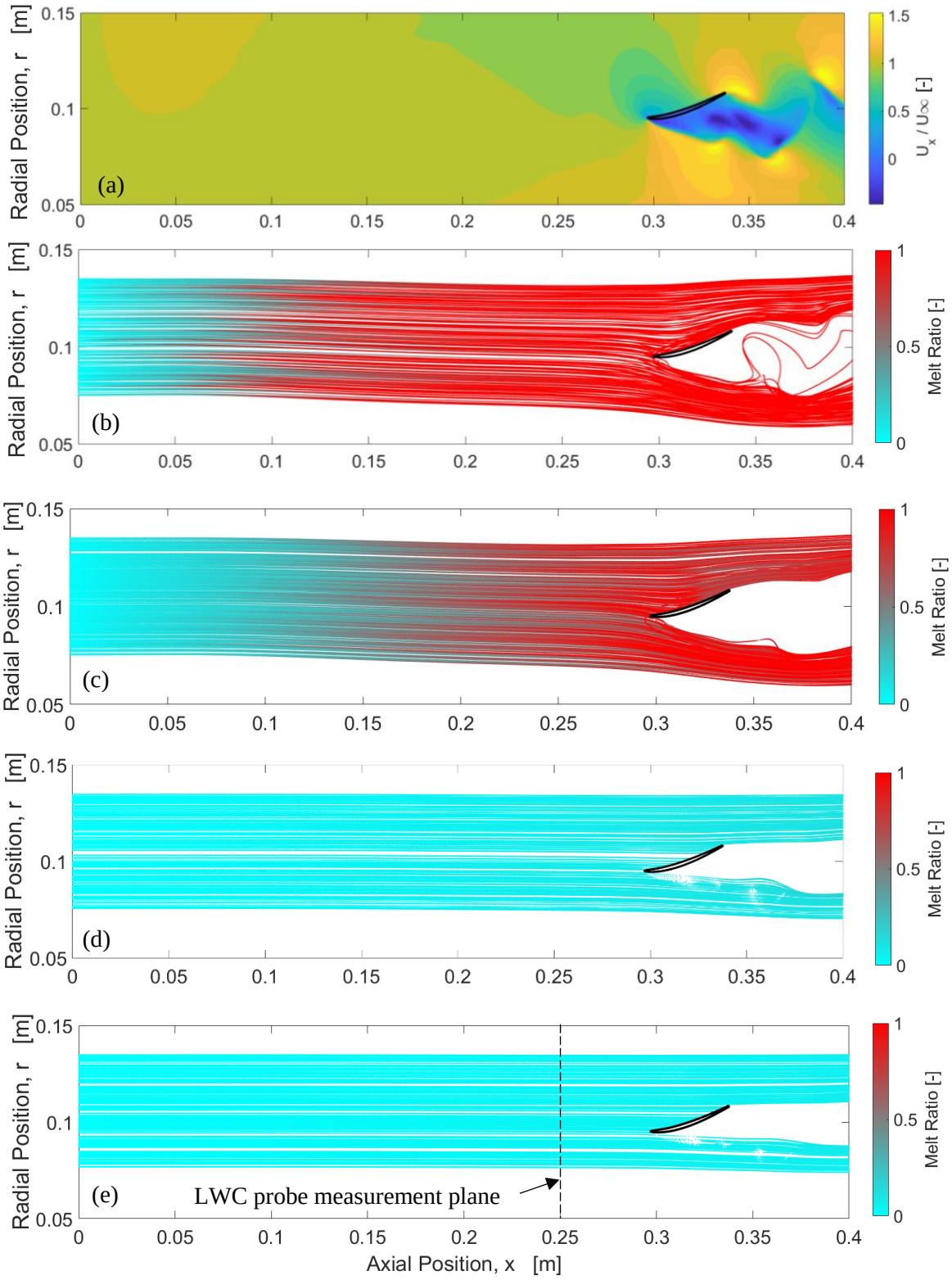

Fig. 7-18 (a) Contour plot of CFD-predicted normalised axial velocity at the baseline test condition; (b-d) particle trajectories at the baseline condition, for particles with diameter within 2.5 µm of (b) $D_{v,min}$ = 2 µm, (c) D_{v05} = 9 µm (d) D_{v50} = 34 µm, and (e) $D_{v,max}$ = 74 µm. Flow is left to right in all plots.

The smallest particles in the distribution fully melt prior to impact with the test article, with an average melt ratio at the exit plane of case (a) of 0.98. This is reduced to 0.78 in (b), 0.16 in (c) and 0.02 in case (d). Both the particle heat-up rate and change in melt ratio over a timestep are inversely proportional to the cube of particle diameter. The bulk LWC measured in the experiment at the probe plane (shown in Fig. 7-18 (c)) is primarily due to a small concentration of high melt ratio particles.

The larger particles that are not incident on the test article and traverse the wake experience significant slip velocities. For example, a particle of 34 μm equivalent diameter that traverses the wake below the stator gains a peak slip velocity of 105 m/s, up from a minimum of 2 m/s upstream of the stator. This results in a proportional rise in Reynolds number, Re_p, and corresponding increase in Nusselt (dependent on $\sqrt{Re_p}$). The air temperature also recovers towards total conditions. The resulting increase in convective heat transfer to the particles results in the rate of melting increasing by a factor of 1.8 compared to the freestream. Wake-enhanced melting has also been predicted in the simulations of Safran (Aouizerate et al., 2018), where the particle melting model of ONERA (Villedieu et al., 2014) was applied to particle trajectories in a fan and LP booster model. A similar effect occurs for bouncing particles, where radial slip incurs a step change in magnitude.

The stator acts to radially re-distribute the particles. Fig. 7-19 shows the particle equivalent diameter against radial position at (a) the inlet and (b) the outlet. The shadow zone of the stator is clearly visible. It is larger for the smallest particles, which are deflected away from the centreline by the stator potential field and also 'kicked' towards the top and bottom walls in the wake region. There is a lensing effect on the lower edge of the shadow zone, indicative of particle entrainment within the accelerating flow just aft of the leading edge. Particle bouncing off the pressure surface can also be seen. Particles of a larger diameter attain a greater radial height by the time they get to the outlet plane, due to more oblique (ballistic) impacts with the stator and reduced propensity to turn back towards the axial direction post-impact.

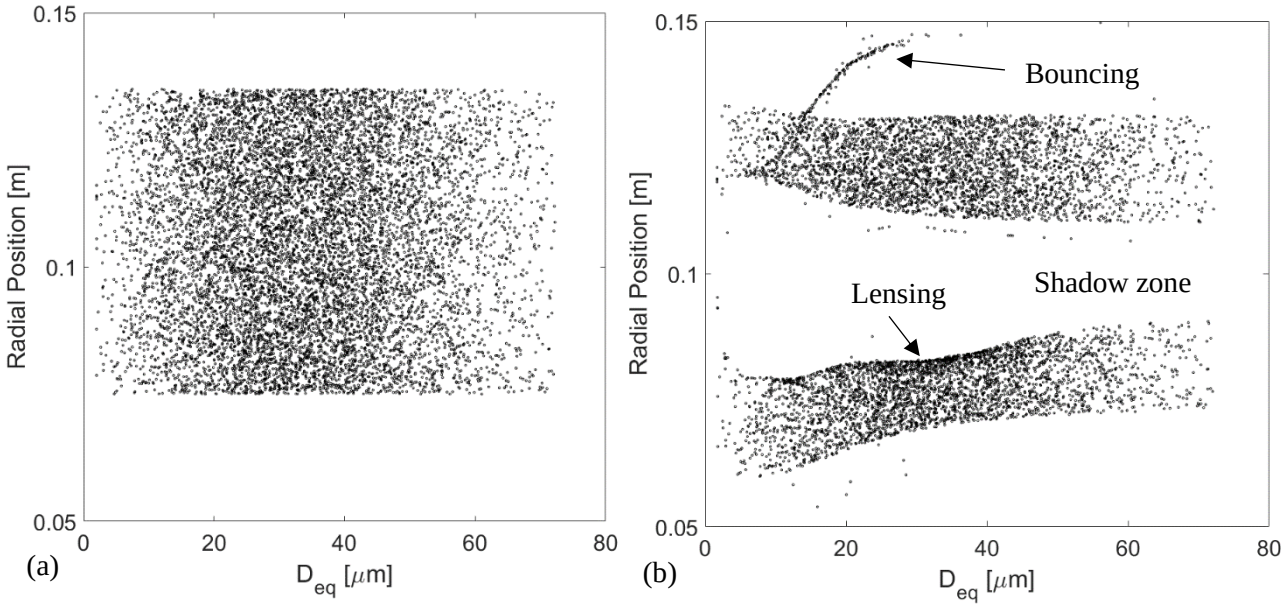

Fig. 7-19 Particle radial position against equivalent diameter at (a) the inlet and (b) the outlet planes.

The isolated stator therefore has a significant effect on downstream particle size distribution, concentration and melt ratio. Similar effects would be expected in a cascade or full annulus of blades, albeit modified as a result of the bulk flow turning.

Placement of panels must be considered as a precursor to predicting accretion growth. This is especially important for the leading edge, where a change in surface normal of ~ 160° is effected over a surface length of < 5 mm. Fig. 7-20 shows the average panel collection efficiency over the stator surface, for three different arrangements. The 'coarse' arrangement has three panels covering the leading edge; the 'fine' has five and the 'finer' has six. The panel covering the stagnation point in the coarse arrangement contains wall points with surface normals between -35° and 44°. As a result the average collection efficiency is unrealistically low – and this average is then assigned to every point in the panel. The fine and finer panel arrangements allow the collection efficiency of ~0.95 at the stagnation point to be correctly captured. The mass flux assigned to this panel is therefore more accurate, resulting in a more accurate accretion profile.

The computational cost of the accretion calculation scales proportionally to the number of panels. However, since the total number of panels, incorporating those on the pressure surface, suction surface

and top and bottom tunnel walls typically number around 100 for this geometry, the increase in run time between the coarse and finer cases is marginal.

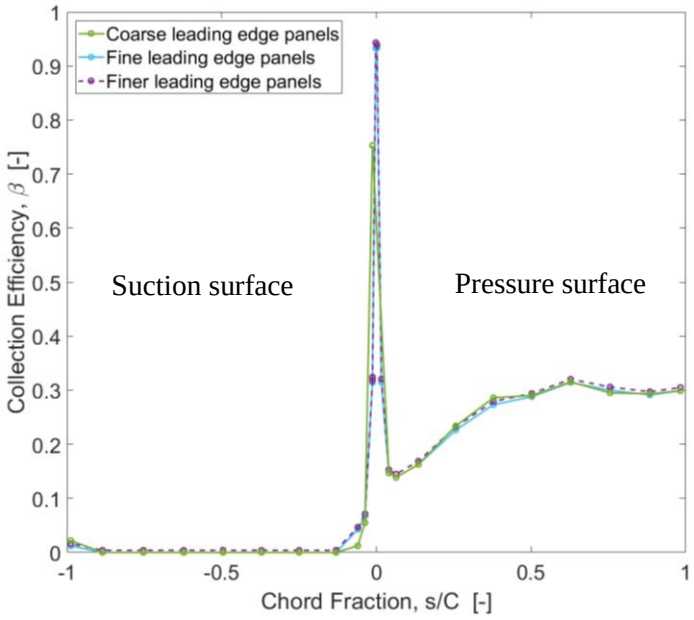

Fig. 7-20 Collection efficiency over the stator test article surface for coarse, fine and finer panel arrangements

7.5.2 Growth Predictions on Baseline Case

Fig. 7-21 shows a comparison of ICICLE-predicted accretion profiles and experimental measurements for a test on the stator at the baseline icing and aerodynamic conditions. Comparisons are shown for discrete exposure times of 60 s, 120 s and 180 s. The thin shell substrate model is used throughout.

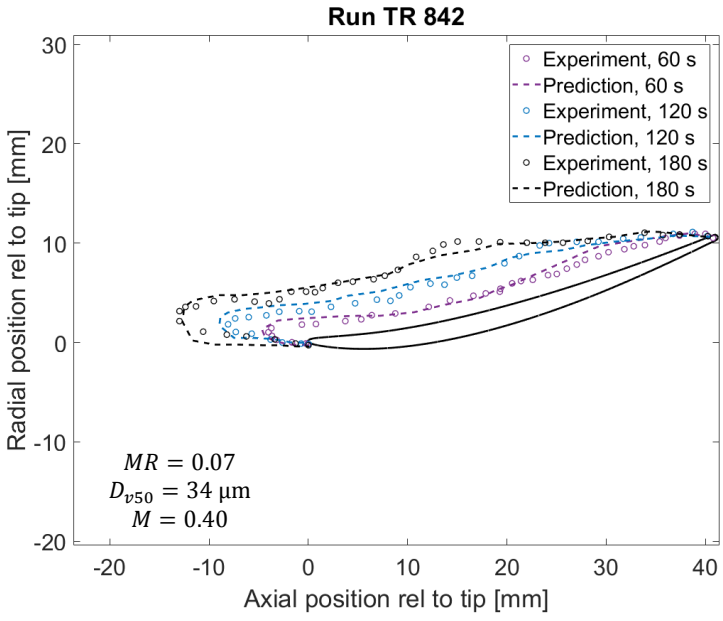

Fig. 7-21 Comparison of ICICLE-predicted and measured accretion profiles

Fig. 7-22 (a) shows the accretion viewed from the top, onto the pressure surface; (b) shows a side view, which is used for growth rate data extraction. It may be seen that the accretion at this condition is reasonably uniform from around 20% to 100% span (tip). This gives confidence that the measured thicknesses at the tip are representative of those at midspan.

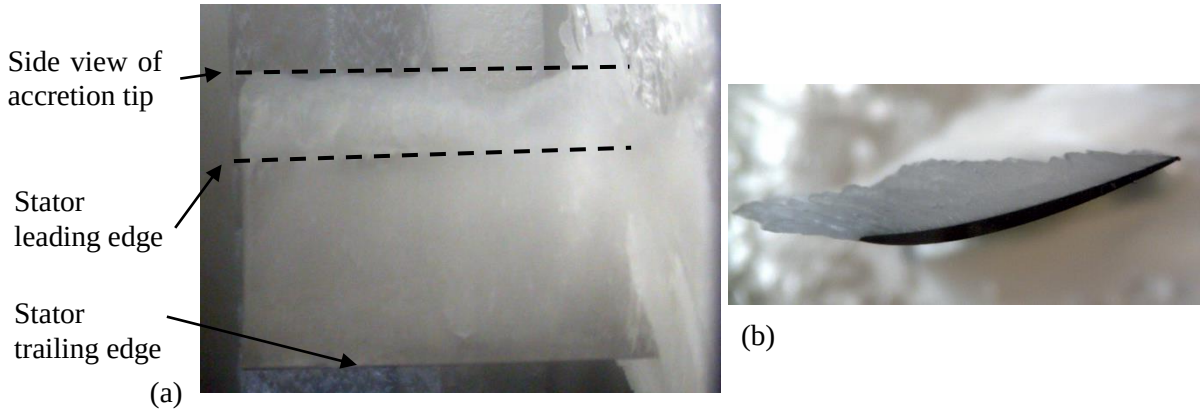

Fig. 7-22 Accretion for the baseline case at ~ 180 s, viewed from (a) the top, onto the pressure surface, and (b) the side

Fig. 7-23 shows ICICLE-predicted and experimentally measured accretion growth histories for the same case. Data is shown at three chordwise positions, with errorbars plotted on every 20th datapoint of the 5% chord position. Gaps in the data – most notably in the 90% chord position – denote a failure of the postprocessing script to detect the edge of the ice accretion at that timestep. This is invariably due to obscuration of the camera window or a fluctuation in the icing cloud washing out the image background. At low accretion thicknesses (< 2 mm) the noise in the edge detection is also significant.

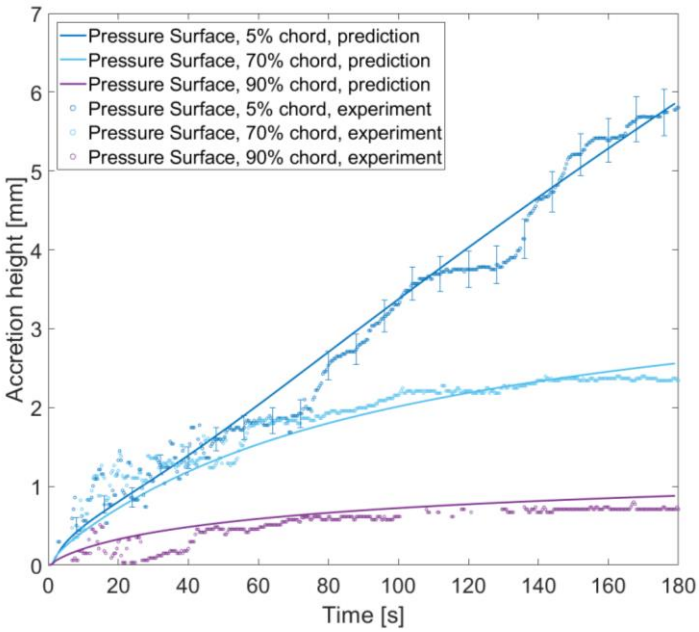

Fig. 7-23 Comparison of measured and predicted accretion thicknesses over the exposure time at three chordwise positions, for the baseline case (run TR 842)

Fig. 7-23 shows that the transient growth behaviour on the pressure surface can be predicted by the code, notably at the 70% chord position. Erosion and collection efficiency ensure that the accretion does not grow once the local surface normal is perpendicular to the axial direction. The growth at the 5% chord position is irregular, with consecutive periods of rapid and slow accretion. The ice appears to grow in a columnar structure, with the column axis aligned at an angle just above the axial direction. Bridging between 'columns' can lead to a perceived short-term increase in growth rate. This irregular behaviour results in a maximum error between prediction and measurement of around 20%.

7.5.3 Comparison of Accretion Profiles at Differing Melt Ratio

Fig. 7-24 shows four comparisons of experimentally-measured and predicted accretion profiles for varying melt ratio. Similarly to the cone, humidity was varied between 0.05 and 0.65 to attain total wet bulb temperatures in the range -6.5 °C to 5.5 °C. This in turn generated measured particle melt ratios of (a) 0.01, (b) 0.04, (c) 0.10 and (d) 0.18. All other conditions were held at their baseline values to ensure no difference in the rate of erosion.

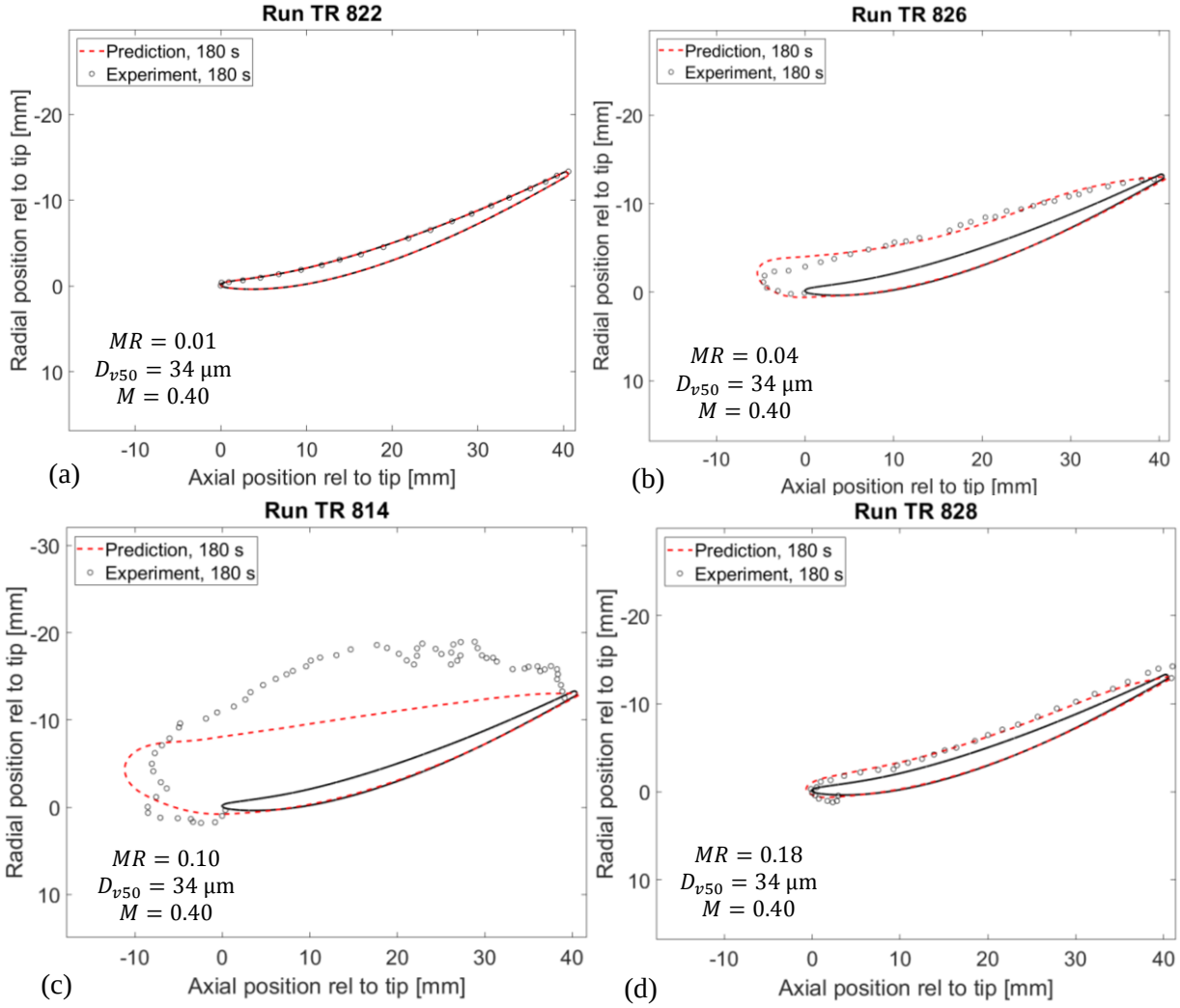

Fig. 7-24 Comparison of experimental and ICICLE-predicted accretion profiles on the stator test article after 180 s.

In cases (a), (b) and (d) the predictions give reasonable agreement with the experimental measurements, with a maximum error of ~ 30% at the leading edge of case (b). In case (d), the wet conditions are conducive to a slushy accretion that slides readily – resulting in ice overhanging the trailing edge. This cannot currently be predicted within ICICLE. The accretion also shed in its entirety just after the 180 s mark.

In case (c), the comparison between prediction and experiment is clearly poorer. This condition is in the plateau region of particle sticking, so a large accretion would be expected. The primary issue is that growth that exceeds the projected area of the test article (for example growth vertically above the trailing edge) will be predicted to occur slowly. This is due to the profile edge being approximately

aligned with the axial direction, maximising erosive efficiency and minimising collection efficiency. This issue is likely to be reduced at low Mach numbers, where the erosive efficiency is reduced, and furthermore may be reduced through the use of an updated flowfield as discussed in Section 7.6.

The case is also complicated by the fact that the accretion rotates forwards after around 120 s, also increasing the collection efficiency on the top surface. The surface in contact with the aerofoil prior to rotation is shown by the black dashed line in Fig. 7-25. Future simulations could include artificially rotating the predicted accretion profile by the same angle to investigate if ensuing growth may be predicted. This rotation may also be able to be predicted if aerodynamic forces on the accretion at discrete timesteps are calculated.

Fig. 7-25 Run TR814 after the cloud was switched off, after ~ 180 s of exposure. The contact surface between accretion and aerofoil before rotation is shown by the black dashed line.

The new thermodynamic accretion model (EMM-C) also produces an estimate for the thickness of any internal water layer between the solid accretion and the test article. Table 7-2 shows that height of these water layers after 180 s for three cases with accretion. This agrees qualitatively with the observation that case (d) is more translucent (indicative of a water layer on the test article surface) and also slides and sheds more readily. The information in Table 7-2 could therefore potentially be used to develop or test future shedding models.

Table 7-2 Internal water layer height for three cases of varying relative humidity

Case	*Melt ratio*	*Water height,* h_{int} $[mm]$
TR 826	0.04	0.60
TR 814	0.10	1.1
TR 828	0.18	1.5

7.5.4 Comparison of Accretion Profiles at Elevated Particle Size

Tests at an elevated particle size tended to lead to rough, unstable accretions, prone to shedding or cracking. Accretions were more likely to form at the tip and/or root of the stator, with the midspan typically remaining clear.

Fig. 7-26 shows a comparison of a predicted accretion profile and measured profiles for a case with an elevated D_{v50} of 43 µm. Experimental profiles are plotted for both the tip and midspan. Fig. 7-27 shows images of the accretion at ~ 180s from (a) the side, viewing the tip, and (b) the top, viewing of the pressure surface. As may be expected, the 2D code matches the midspan prediction. Use of 3D CFD at the tip may, at least in a qualitative sense, give some insight as to why it is a favourable location for accretion. There is also a small (~ 1 mm thick) semi-cylindrical accretion at the leading edge, which is not predicted by ICICLE. This may be indicative that the panels defining the leading edge are too coarsely defined; further simulations are required to identify the numerical setup at which this can be predicted. This is, however, of minor concern: accretions of large mass clearly have the capability to cause most damage and so require most modelling effort.

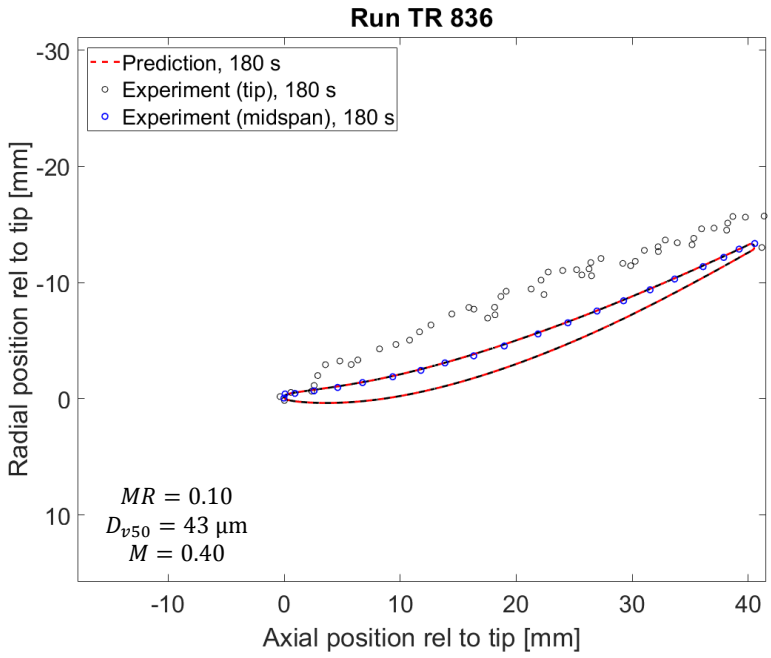

Fig. 7-26 Comparison of ICICLE-predicted and experimental accretion profiles for a case with elevated particle size. The experimental profile at midspan and at the tip are plotted.

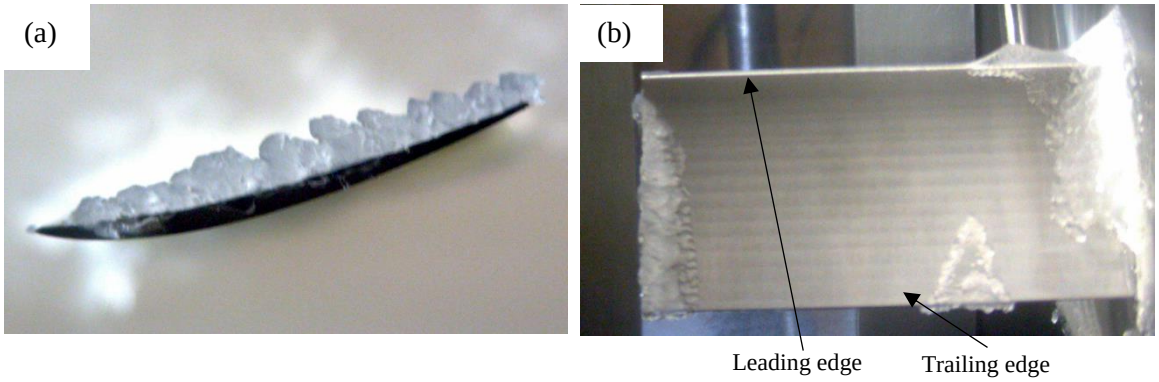

Fig. 7-27 Images of case TR836 at ~ 180s of exposure, viewed from (a) the side (tip) and (b) top (pressure surface)

7.6 Flowfield Update Simulations

It has been previously discussed that 'large' accretions – that grow to a similar dimension to the test article – can have a significant effect on the external flowfield. This in turn alters particle trajectories, collection efficiency, and melt ratio at impact, as well as local conditions used in the accretion calculation such as temperature, pressure and Mach number.

A case at the lowest erosive condition (Mach number of 0.25 and particles of 34 μm D_{v50}) was used to test the effect of flowfield update. The experimental accretion profile was extracted at exposure times of 33 s and 66 s, smoothed, re-meshed and the flowfield re-calculated in ANSYS Fluent. More details of the method may be found in Connolly, (2018). The flowfield was then re-imported into ICICLE, trajectories re-calculated and the accretion grown over the ensuing time period.

Fig. 7-28 shows a contour plot of velocity magnitude normalised by freestream velocity for the simulation at 33 s of exposure. The multi-coloured segments denote the new arrangement of panels. There is significant (~ 5 mm) accumulation on the pressure surface, and the accretion overhangs the leading edge. This results in separation immediately downstream, and a larger wake region than the clean aerofoil case.

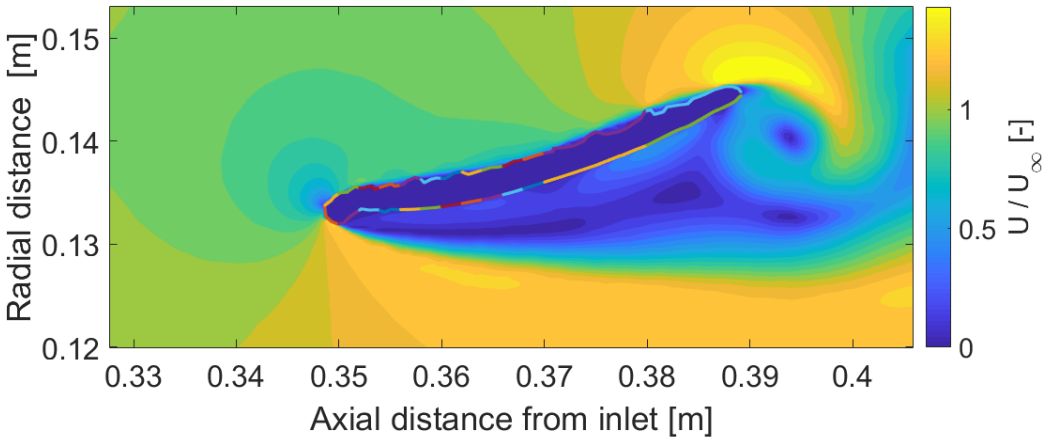

Fig. 7-28 Contours of normalised velocity magnitude for the simulation of the 33 s accretion profile

Fig. 7-29 shows the collection efficiency calculated by ICICLE over the stator surface for the no-update, and 33 s and 66 s flowfield update cases. In general, the peak widens as time progresses, in keeping with the nose of the accretion becoming increasingly blunt. The peak also decreases in magnitude between the clean and 66 s case, indicative that as the accretion becomes increasingly bluff, particles are diverted away from impacting on the leading edge by the potential field.

The low rate of erosion results in a rough, uneven accretion surface; this is generally smoothed out at a higher erosive condition. These undulations in the surface are reflected in the surface angles within each panel. This in turn affects the calculated average collection efficiency for each panel. A panel that has highly oblique, or even out-of-wind portions, yields a low collection efficiency. This is shown in the somewhat spiky distribution of collection efficiencies on the pressure surface for the 33 s and 66 s update cases. This is clearly a real phenomenon, but the accuracy of the average collection efficiency assigned to each panel will increase as the spatial resolution of the panels also increases.

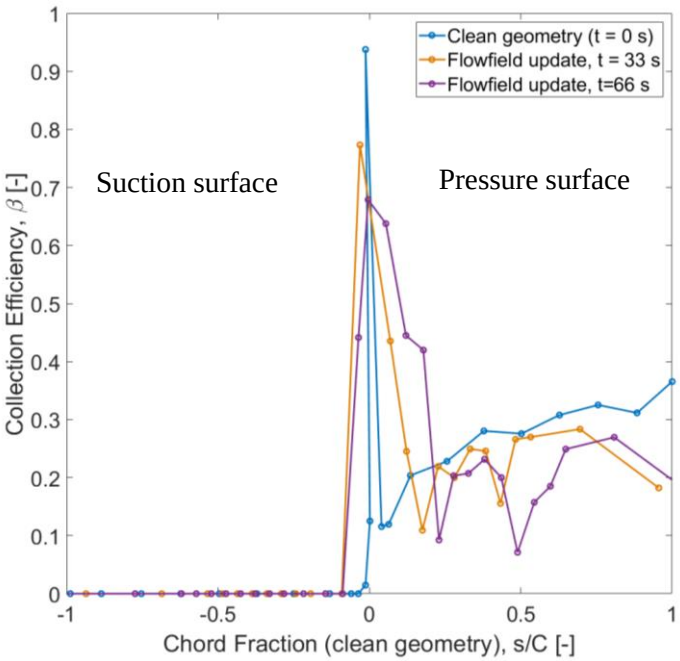

Fig. 7-29 Collection efficiency over stator surface for the clean geometry, and flowfield update simulations after 66s and 110 s

Fig. 7-30 shows a comparison of experimental and ICICLE-predicted accretion profiles with and without flowfield update. In (a), the accretion profile at 85 s is compared, against a case with no flowfield update, and against a case where the flowfield was updated after 33 s. In (b), the accretion profile at 118 s is compared, against a case with no flowfield update and against a case with flowfield updates at 33 s and 66 s. The accretion profile at 66 s is outlined in black.

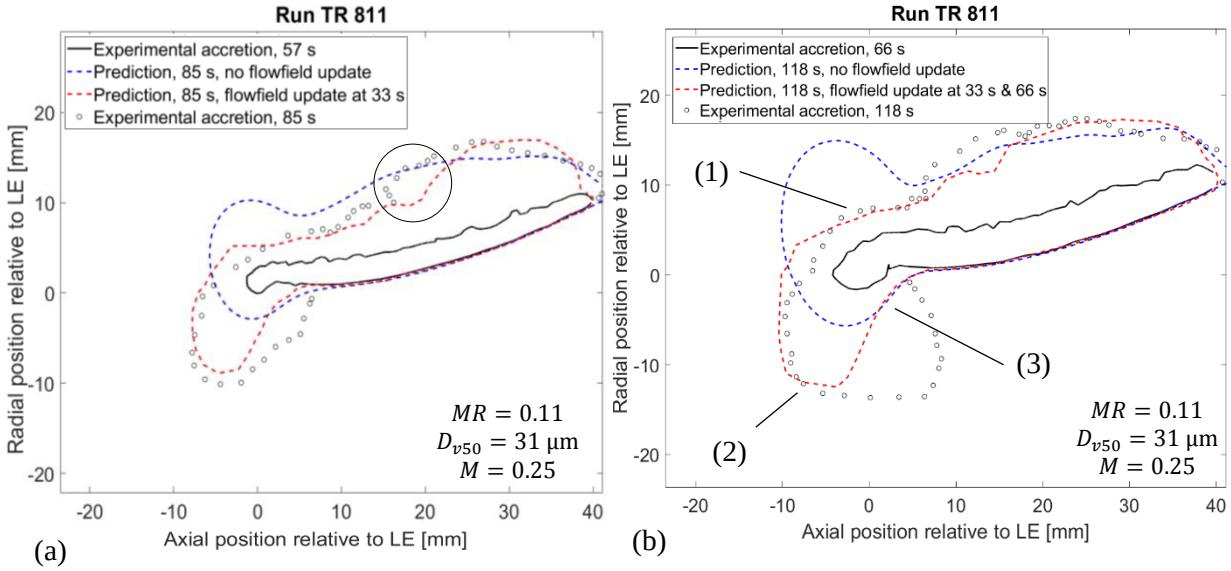

Fig. 7-30 Comparison of ICICLE-predicted and experimental accretion profiles at (a) 85 s and (b) 118 s, with and without flowfield update implemented.

For this low erosion case, the erosive efficiency is sufficiently small that the predicted pressure surface accretion can grow above the vertical extent of the blade. As a result, the growth prediction on the pressure surface has relatively good agreement with the no flowfield update cases - within 20 %, for locations between the 10 % chord position and trailing edge. In the flowfield update case in (a), this agreement is worse rather than better – at ~ 35 % error at the circled location. This coincides with the low value of collection efficiency at around ~ 50% chord in Fig. 7-29. However, both simulation and experiment predict a discontinuity, albeit in slightly different locations. It is at least encouraging that this feature may be predicted, and the differing location may be a function of the panel coarseness or local over-smoothing to maintain stability. Further simulations with reduced smoothing are required to ascertain this.

The gain in accuracy in the updated flowfield cases is most evident in the leading edge region, where a substantial improvement is observed of the prediction of the overhanging accumulation. The error in accretion thickness at the position labelled (1) is reduced by 90 %. A similar gain is attained at (2). However, the improvement is not maintained around position (3). As this position is out of the wind, ICICLE predicts minimal particle impact (only those small enough to be entrained in the downstream recirculation region), and thus negligible growth normal to the surface. The experimental profile, however, continues to expand under the suction surface. The primary reason for this is that the aerodynamic force on the bluff overhang pushes it rearwards, until it partially detaches at ~ 100 s. An entire shed of the pressure surface accretion then occurs at around 120 s and a shed of the leading edge accretion at around 180 s. Calculation of aerodynamic forces on the accretion as it grows would therefore again benefit the prediction of geometry, and hence flowfield.

7.7 Model Sensitivity

In chapter 4, a sensitivity analysis was presented for the trajectory and phase change models. In this chapter, sensitivity to computational inputs such as timestep, grid size, particle count and panel count are discussed. It remains to investigate the sensitivity of the accretion and erosion models to key global inputs.

Appendix G gives a sensitivity analysis to key flowfield inputs, or parameters derived from the flowfield, including total temperature and pressure, Mach number, specific humidity and heat transfer coefficient. Sensitivity was found to be highest to total temperature, with a 5% perturbation giving a ~ 2% change in ice growth rate. Sensitivity to total pressure and heat transfer coefficient was found to be lowest; in the latter case this is encouraging since the uncertainty can be substantial, especially for calculations on iced surfaces.

8 Conclusions & Further Work

8.1 Conclusions

This work undertaken for this thesis allowed the creation of a new comprehensive ice crystal icing model (ICICLE), which offers a step change in modelling capability compared to the first generation of ice crystal models in the open literature. The model was designed to be applicable at a range of operating and atmospheric conditions typical of those experienced during fleet ice crystal icing events.

The problem is expansive in scope, requiring modelling of flowfield, particulates, phase change, mechanical interactions and accretion. Using a Stokes number and non-dimensional particle relaxation time analysis, it was determined that particle motion was sufficiently inertia-driven that particle motion could be described using only drag and gravity as body forces. It was assessed that the Rosin-Rammler particle size distribution could be used to statistically represent particles in the atmosphere, in the ice crystal wind tunnels used during the project, and after breakup in the early stages of the engine. Assessment of common particle shapes – plates, discs and columns – led to the assessment that the commonly-used assumption of spherical particles is not applicable, but that particles may be approximated as prolate or oblate spheroids. The approach has the benefit that all shape parameters – sphericity, crosswise sphericity, surface area and volume – are described by a single set of equations, that depend only upon equivalent diameter and aspect ratio. A recent literature model for the drag coefficient of non-spherical particles in the sub-critical regime was used to build a Lagrangian particle tracking model.

A literature model for Nusselt number, applicable to spheroids with aspect ratios between 0.2 and 2, was used predict the rate of phase change for a particle mid-flight. This model was validated against measured particle melt ratios in the Research Altitude Test Facility (RATFac). The absolute error (typically ~ 0.03) was always within the uncertainty of the liquid-water sensing probe. A simple model was introduced to account for two-way coupling of mass and energy between the flowfield and continuous phase. This was necessitated by fleet observations that the compressor delivery temperature

is typically depressed during an ice crystal icing encounter. At the baseline test condition, a ~0.5 % reduction in enthalpy and a ~ 4% reduction in humidity were calculated when two-way coupling was implemented. This element of the model represents a significant forward step for modelling engine icing, since it is neglected in the codes available in the open literature.

It was assessed that modelling of particle-surface interactions required further experimentation in three key areas: sticking, erosion and heat transfer. To this end, two experimental campaigns were performed in the ice crystal wind tunnels at the National Research Council of Canada (NRC). The first used an inclined flat plate to measure heat transfer from a substrate under ice crystal cloud conditions, installed in the Altitude Icing Wind Tunnel. This test article demonstrated for the first time that thin film heat flux gauges could be successfully used to attain high spatial and temporal resolution heat flux data in mixed phase conditions. Heat transfer from the substrate to the icing cloud was measured parametrically, varying Mach number, Total Water Content (TWC), particle size and impact angle. A method for calculating the particle phase change post-impact was presented. This effect is important to capture since the likelihood of the particle sticking to a downstream surface is strongly dependent upon its melt ratio. This element is neglected from existing first-generation ice crystal icing models in the literature.

The second experimental campaign at the NRC, this time in the RATFac ice crystal wind tunnel, aimed to generate new models for particle sticking and erosion. Previous studies did not attempt to decouple the two and were applicable to a narrow range of conditions. An axisymmetric conical test article was used, and melt ratio, Mach number, particle size, TWC and impact angle were varied parametrically in ranges typical of ice crystal icing in the IP compressor. A model for shear erosion dependent on particle size, velocity and impact angle was developed and validated using approximately 70 experimental test points. The mean error from the correlation to the datapoints is 4%. The erosion model is the first to model the effect of the entire PSD – rather than just the median mass diameter. It was discovered that the rate of erosion is strongly dependent upon the level of positive skew in the PSD – described by the largest measured particle, $D_{v,max}$. This effect has been suspected by other authors but not shown experimentally or quantified.

By normalising all test points by their erosive efficiency, it was shown that particle sticking probability can be expressed solely as a function of melt ratio. A new correlation, applicable to melt ratios between zero and unity, was developed. The false response of the liquid-water sensing probe was also measured parametrically, and an empirical correction factor correlation derived. The sticking model is therefore defined for a significantly expanded range of conditions than other models in the literature, and to a greater degree of accuracy.

A new thermodynamic accretion model was proposed, applicable to ice crystal icing where the underlying substrate can be either above or below freezing temperature. This is a substantial contribution to modelling engine icing, as it is believed that ice crystal accretion occurs in locations that are initially warm (above freezing), but may transiently cool. The model was developed from the Extended Messinger Model (EMM) of Myers (2001). This model has only previously been applied to airframe icing, where the substrate is always assumed to be below freezing. Adaptations were proposed to allow an impinging mixture of ice particles, partially melted ice and water droplets. For the case of a substrate above freezing, an entirely novel three-layer accretion model was proposed. Similarly to the EMM, the new model may be solved analytically, enabling fast computation. Additional consideration was given to calculation of the evaporative heat flux and treatment of the thermal response of the underlying substrate. Finally, results from the model were presented for a simple case of ice growing at a stagnation point under engine-realistic aerodynamic and icing conditions.

ICICLE was then applied to two tests cases and a sensitivity analysis performed. Imposed numerical parameters, including particle tracking timestep, grid size, particle count and number of accretion layers were varied to find values that were a compromise of solution accuracy and computational cost. The code was first applied to the cone test article for Mach numbers of 0.25 and 0.40, total wet bulb temperatures of -6.5 to 5.5 °C, and particle sizes between 34 and 74 μm D_{v50}. The code was also tested on two other cones of differing half-angle. The results show that ICICLE is able to predict both the accretion profile at a given exposure time, and the transient growth histories to a good degree of accuracy; the maximum error in growth at the tip is within 20%. This level of agreement is considered acceptable for even the most heavily developed icing codes (Gent, 2000). The error at the cone

sidewalls tended to be small for conical-shaped accretions, but could be significant (> 20%) for more rounded accretions, typically caused by wetter icing conditions. This is discussed further in Section 8.2.

Finally, a prismatic stator test article was tested in RATFac to provide independent validation for the ICICLE code. This test article was designed to generate accretion profiles on an engine-realistic geometry. The stator was tested at the same range of aerodynamic and icing conditions as the cone. Simulations were run in ICICLE on the stator geometry. The number of panels required to attain convergence in the collection efficiency distribution was first assessed, followed by a study of the performance of the code for a test case at the baseline aerodynamic and icing conditions. For three chordwise locations on the stator pressure surface, experimental and predicted growth histories were compared, and again found to agree within 20%. ICICLE was then applied to test cases with differing melt ratio and particle size. In the majority of cases the accretion profile was well predicted, with the notable exception of wet, slushy cases where the experimental accretion was invariably larger than the prediction. This is also further discussed in the next section. It was shown that for the case of large accretions, a substantial reduction in error (up to 90%) could be attained by updating the flowfield at discrete time intervals, in order to capture the effect of changing particle trajectories and flow properties. Further work is required to assess how often the flowfield should be updated to achieve a good compromise between accuracy and computational cost.

The generally good agreement is a significant advance for the ice crystal icing community, as previously codes have only been validated against simple geometries (hemispheres, cones, cylinders). Previous attempts to predict ice growth in the engine environment have been restricted to qualitative assessments of likely impact locations, rather than a quantitative study of growth rates. The code and results presented represent a major step forward to achieving this goal.

Finally, sensitivity analyses have been performed to key inputs in ICICLE – particle size and shape, aerodynamic parameters and flow properties, and thermodynamic parameters such as heat transfer coefficient. It was found that ICICLE is most sensitive to particle sphericity – as it appears in the drag and Nusselt number correlations – and total temperature. The latter is typically well known, at least

experimentally, whereas uncertainty in the former may be significant, especially when the approximation of a particular particle as a spheroid is poor.

8.2 Further Work

Being such a multi-faceted problem, there are many avenues of further work that could be pursued. Some have already been identified in the current work as necessary to advancing the model capability.

First, the code would benefit from a water filming model. There is evidence that in wet cases, runback and sliding strongly determine whether ice will form or not. It is also an assumption of the EMM-C model that any water film that forms on top of the accretion is sufficiently thin that wall-normal temperature gradients may be neglected. This assumption may only be validated after integration of a filming model. Previous work (for example Villedieu et al. (2014)) may aid the development. In a similar vein, improved microscopic particle-surface interaction models – such as splashing and sliding – may benefit the sticking model, which is currently defined based on macroscopic experimental data.

Second, the trajectory, fragmentation and phase change models all assume solid (non-porous) particles. This may be limiting for atmospheric particles, especially those grown over a significant time period in a sustained weather system. Further modelling, and possibly experimentation, is required to assess how sensitive models are to this discrepancy. A cloud chamber could be used to generate suitable particles for testing.

A limitation in the erosion model has also been introduced – that it does not contain a term dependent upon melt ratio. Empirical evidence suggests that erosion is higher for a lower melt ratio cloud, since solid ice particles are more erosive than water droplets. Decoupling this from sticking probability, which also depends upon melt ratio, is likely challenging. Additionally, the erosion model has only been validated down to a D_{v50} of 34 μm. The bounce-shatter model introduced in chapter 5 suggests that catastrophic fragmentation may occur at the impact velocities that would be encountered in the engine environment. Locally, therefore, particle sizes may be significantly smaller than 34 μm. It would be beneficial to assess if the erosion model still holds at these extremely low particle kinetic

energy conditions. This could be achieved relatively simply with experimentation on existing test articles.

There are also more major developments that would occur over a longer timescale and involve significant experimental and/or modelling effort. First, the development thus far has entirely neglected ice shedding. This is justified on the basis that if the ice is assumed not to shed, then the predicted ice mass is a conservative case. Empirically, shedding is prevalent at wetter conditions (melt ratios greater than ~ 0.15), but partial sheds may occur in colder, drier cases. As observed in chapter 7, a partial shed or rotation of the accretion can also lead to an augmented growth rate, where the accretion is significantly enlarged before it finally sheds. The new EMM-C model make a first step towards this capability, in its ability to predict the presence and thickness of an internal water film between the substrate and accretion. This should be coupled with calculation of the aerodynamic forces on the accretion, as well as empirical data, to assess the likelihood of a shed. An integrated FEA model would also be beneficial for improving the accuracy of the substrate thermal response, and thus the performance of the EMM-C model. This will also feed into the shedding prediction.

Second, there is work to be completed to apply the model to a turbomachinery case. In the first instance, it should be assessed if extension to three dimensions is required. Blade aspect ratios in the IP compressor are sufficiently low (at least compared to an aircraft wing) that 3D flows will have a strong influence on particle trajectories and the thermodynamics of accretion. The desired fidelity of the flowfield will need to be decided, based on the desired run time and the intended purpose of the output (whether to just indicate a condition that is likely susceptible to accretion or to produce quantitative growth rates). Calculation of heat transfer coefficient requires additional consideration, especially for iced surfaces; the steady-flow, flat plate assumptions inherent in the calculation of evaporative mass flux will also not be suitable to turbomachinery. Further heat transfer experimentation may be required to aid development of models.

As previously discussed, there is significant scope to improve the computational efficiency of the code, especially the particle tracking which would benefit from parallelisation. Migration of the code from MATLAB to a pre-compiled language would also afford reductions in run time.

Appendix A Numerical Setup

The following gives the numerical setup for the CFD simulations of the validation test articles.

A-1: Cone Test Article

The numerical domain is the test article installed in the Research Altitude Test Facility (RATFac), which is modelled as a simple cuboidal domain at a scale of 1 – 1. The tunnel working section is 132 mm x 254 mm. A length of ten cone diameters were modelled upstream (0.6 m from inlet to tip). Fig. A-1 shows the domain, with the 35° half-angle installed. Flow is into the left boundary. Corresponding simulations were run for the 20° and 45° half-angle cones using the same numerical setup.

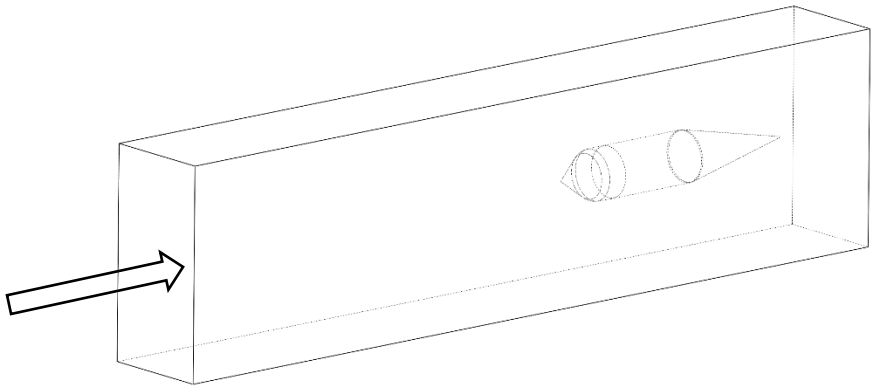

Fig. A-1 CFD domain for cone test piece

A hybrid tetrahedral-prism unstructured mesh was used, comprised of 4.8M cells. 15 prism layers were used on solid boundaries, with an expansion ratio of 1.2, and an initial cell height of 0.084 mm. This resulted in $y+ < 2$ on the test piece conical surface for all conditions.

The solver was ANSYS Fluent v16.2, using density-based RANS. The k-ω SST turbulence model was used. The inlet boundary conditions were a total temperature of 283 K, total pressure of 34.5 kPa and freestream Mach numbers of 0.25 & 0.40, matching the baseline aerodynamic conditions given in chapter 3. The inlet turbulence intensity was set at 7.5%, based on previous measurements in RATFac, with a lengthscale of 0.08 m (Knezevici et al., 2011). For heat transfer studies, the test piece boundary

condition was an applied uniform wall temperature of 300 and 310 K. Surface heat flux data for each case was exported to calculate heat transfer coefficient.

The criteria for convergence were residuals in continuity below 10^{-3}, and below 10^{-6} for x, y, z-velocities, energy, turbulent kinetic energy, and specific turbulent dissipation rate.

A grid sensitivity study was performed for four meshes of 6.3M, 4.8M, 4.2M, and 1.05M cells. Fig A-2(a) shows circumferentially-averaged wall shear stress on the cone surface, from the tip to the front of the cylindrical afterbody. Fig A-2(b) shows a spanwise traverse of the tunnel at mid-height, at a distance of 70 mm upstream of the outlet (i.e. through the cone wake).

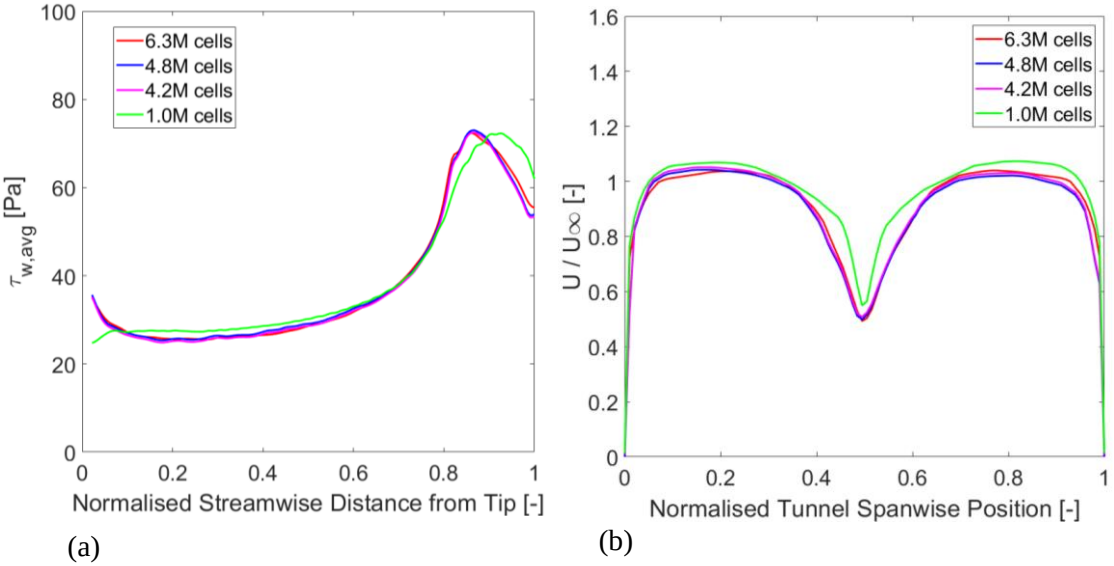

Fig. A-2 (a) Circumferentially averaged wall shear stress on the cone; (b) wake traverse at mid-height

A-2: Prismatic Stator Test Article

The numerical domain is a thin (5mm) 3D slice of the stator test article installed in the Research Altitude Test Facility (RATFac). Using a 3D slice was found to aid convergence compared to a 2D case. Periodic boundary conditions were applied on the side walls of the domain. Approximately 8 chord lengths were modelled upstream (0.35 m from inlet to leading edge).

A hybrid tetrahedral-prism unstructured mesh was used. 22 prism layers were applied at solid boundaries. Grid independence study performed, with a 2.3M cell grid selected (more detail in

Connolly, (2018)). The maximum y+ on the stator surface up to 90% chord was 1.5. Fig. A-3 shows the domain, flow is left to right.

The solver was ANSYS Fluent v16.2, using density-based RANS. The k-ω SST turbulence model was used. Inlet boundary conditions were fixed at a total temperature of 283 K, total pressure of 34.5 kPa, and freestream Mach numbers of 0.25 & 0.40, matching the baseline aerodynamic conditions given in chapter 3. The inlet turbulence intensity was set at 7.5%, based on previous measurements in RATFac, with a lengthscale of 0.08 m (Knezevici et al., 2011). For heat transfer studies, the test piece boundary condition was an applied uniform wall temperature of 300 and 320 K. Surface heat flux data for each case was exported to calculate heat transfer coefficient.

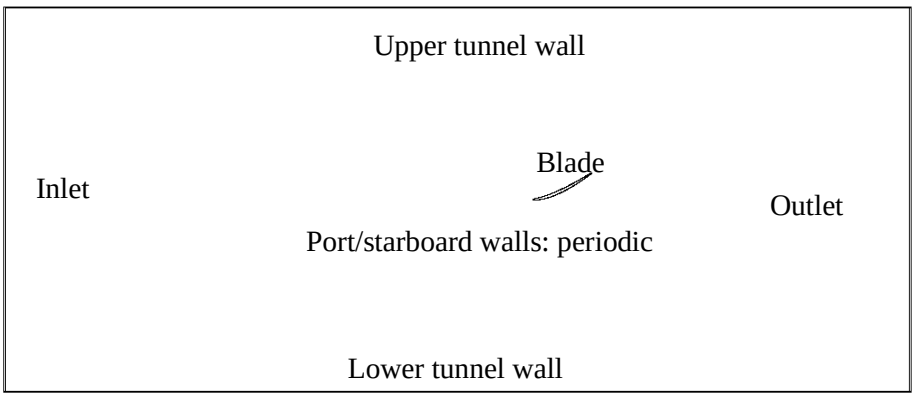

Fig. A-3 Numerical domain for stator, flow is left to right.

Appendix B Validation Cases Test Matrix

Table B-1 gives the aerodynamic and cloud setpoint, as well as details of the geometry. In the 'Notes' column, 'LWC inj' signifies tests where supplemental liquid water was injected (mixed phase regime rather than melting regime); 'Twall' refers to tests where the test article was internally heated to a target wall temperature; 'grinder transient' refers to tests where the ice grinder speed was varied during a run to transiently vary particle size; 'elevated RA' refers to tests on a second 35° cone with an elevated surface roughness; 'AoA' refers to stator tests where the angle of attack relative to the axial direction was varied.

Table B-1 Test Matrix for Validation Test Articles in RATFac

Test Ref	*Aerodynamic Setpoints*				*Cloud Setpoints*					*Test Article*	*Derived*	*Notes*
	T_0 °C	**P_0 kPa**	**M_∞ -**	**RH_0 %**	**TWC_{cl} g/m3**	**IWC_{cl} g/m3**	**D_{v10} µm**	**D_{V50} µm**	**D_{V90} µm**		**TWB_0 °C**	
CAL	10.0	34.5	0.40	40	8.0	8.0	25	40	80	None	1.60	
CAL	10.0	34.5	0.40	40	8.0	7.2	25	40	80	None	1.60	LWC inj
CAL	10.0	34.5	0.40	40	8.0	6.4	25	40	80	None	1.60	LWC inj
CAL	10.0	34.5	0.40	50	8.0	8.0	25	40	80	None	3.19	
CAL	10.0	34.5	0.40	60	8.0	8.0	25	40	80	None	4.80	
CAL	10.0	34.5	0.40	70	8.0	8.0	25	40	80	None	6.20	
CAL	10.0	34.5	0.40	60	8.0	8.0	18	34	54	None	4.80	
CAL	10.0	34.5	0.40	60	8.0	8.0	28	50	93	None	4.80	
CAL	10.0	34.5	0.40	60	8.0	8.0	35	68	131	None	4.80	
CAL	10.0	34.5	0.40	25	8.0	8.0	25	40	80	None	-1.00	
CAL	10.0	34.5	0.40	15	8.0	8.0	25	40	80	None	-3.50	
Cone Test Article												
627	10.0	34.5	0.40	30	8.0	8.0	25	40	80	Cone 35°	-0.50	
629	10.0	34.5	0.50	30	8.0	8.0	25	50	80	Cone 35°	-0.50	
631	20.0	34.5	0.40	30	8.0	8.0	25	40	80	Cone 35°	6.00	
634	20.0	34.5	0.40	7	8.0	8.0	25	40	80	Cone 35°	-0.50	
636	10.0	34.5	0.25	30	8.0	8.0	25	40	80	Cone 35°	-0.50	
638	10.0	34.5	0.25	Off	8.0	8.0	25	40	80	Cone 35°	-6.70	
642	-2.5	34.5	0.25	Off	8.0	8.0	25	40	80	Cone 35°	-12.00	
644	10.0	34.5	0.40	45	4.0	4.0	25	40	80	Cone 35°	2.50	
647	10.0	34.5	0.40	45	4.0	4.0	25	40	80	Cone 35°	2.50	

649	10.0	34.5	0.40	45	6.0	6.0	25	40	80	Cone 35°	2.50	
651	10.0	34.5	0.40	45	10.0	10.0	25	40	80	Cone 35°	2.50	
653	10.0	34.5	0.40	45	8.0	8.0	18	34	54	Cone 35°	2.50	
655	10.0	34.5	0.40	40	8.0	8.0	18	34	54	Cone 35°	1.50	
657	10.0	34.5	0.40	45	8.0	8.0	28	50	93	Cone 35°	2.50	
659	10.0	34.5	0.25	45	8.0	8.0	28	50	93	Cone 35°	2.50	
661	10.0	34.5	0.25	52	8.0	8.0	28	50	93	Cone 35°	3.50	
664	10.0	34.5	0.40	45	4.0	4.0	25	40	80	Cone 45°	2.50	
667	10.0	34.5	0.40	45	8.0	8.0	25	40	80	Cone 45°	2.50	
669	10.0	34.5	0.40	45	12.0	12.0	25	40	80	Cone 45°	2.50	
671	10.0	34.5	0.40	45	8.0	8.0	18	34	54	Cone 45°	2.50	
673	10.0	34.5	0.40	45	8.0	8.0	28	50	93	Cone 45°	2.50	
675	10.0	34.5	0.40	40	8.0	8.0	35	68	131	Cone 45°	2.50	
677	10.0	34.5	0.25	45	8.0	8.0	25	40	80	Cone 45°	2.50	
679	10.0	34.5	0.25	45	8.0	8.0	35	68	131	Cone 45°	2.50	
681	10.0	34.5	0.25	52	8.0	8.0	25	40	80	Cone 45°	4.00	
683	10.0	34.5	0.50	45	8.0	8.0	25	40	80	Cone 45°	2.50	
685	10.0	34.5	0.50	45	8.0	8.0	35	68	131	Cone 45°	2.50	
687	10.0	34.5	0.50	45	8.0	8.0	35	68	131	Cone 45°	4.00	
690	10.0	34.5	0.40	45	8.0	8.0	25	40	80	Cone 20°	2.50	
692	10.0	34.5	0.40	45	4.0	4.0	18	34	54	Cone 20°	2.50	
694	10.0	34.5	0.40	45	8.0	8.0	18	34	54	Cone 20°	2.50	
696	10.0	34.5	0.25	45	12.0	12.0	25	40	80	Cone 20°	2.50	
698	10.0	34.5	0.25	45	8.0	8.0	25	40	80	Cone 20°	2.50	
700	10.0	34.5	0.25	45	4.0	4.0	25	40	80	Cone 20°	2.50	
702	10.0	34.5	0.25	45	8.0	8.0	35	68	131	Cone 20°	2.50	
706	10.0	34.5	0.25	45	8.0	8.0	18	34	54	Cone 20°	2.50	
714	10.0	34.5	0.40	5	8.0	7.2	18	34	54	Cone 35°	-6.50	LWC inj
722	10.0	34.5	0.40	5	8.0	6.4	18	34	54	Cone 35°	-6.50	LWC inj
725	10.0	34.5	0.40	5	8.0	5.6	18	34	54	Cone 35°	-6.50	LWC inj
728	10.0	34.5	0.40	5	8.0	8.0	18	34	54	Cone 35°	-6.50	
730	10.0	34.5	0.40	15	8.0	8.0	18	34	54	Cone 35°	-3.50	

732	10.0	34.5	0.40	30	8.0	8.0	18	34	54	Cone 35°	-0.50	
734	10.0	34.5	0.40	30	8.0	8.0	18	34	54	Cone 35°	-1.00	
737	10.0	34.5	0.40	45	8.0	8.0	18	34	54	Cone 35°	2.50	
740	10.0	34.5	0.40	65	8.0	8.0	18	34	54	Cone 35°	5.50	
745	10.0	34.5	0.25	5	8.0	8.0	18	34	54	Cone 35°	-6.50	
753	10.0	34.5	0.25	15	8.0	8.0	18	34	54	Cone 35°	-3.50	
755	10.0	34.5	0.25	30	8.0	8.0	18	34	54	Cone 35°	-0.50	
757	10.0	34.5	0.25	45	8.0	8.0	18	34	54	Cone 35°	2.50	
759	10.0	34.5	0.25	65	8.0	8.0	18	34	54	Cone 35°	5.50	
767	20.0	34.5	0.40	5	8.0	8.0	18	34	54	Cone 35°	2.50	
769	20.0	34.5	0.40	20	8.0	8.0	18	34	54	Cone 35°	5.50	
786	10.0	34.5	0.40	65	8.0	7.2	18	34	54	Cone 35°	5.50	LWC inj
789	10.0	34.5	0.40	65	8.0	6.4	18	34	54	Cone 35°	5.50	LWC inj
771	10.0	34.5	0.40	45	8.0	8.0	18	34	54	Cone 35°	2.50	
775	10.0	34.5	0.40	45	8.0	8.0	18	34	54	Cone 35°	2.50	Twall
777	10.0	34.5	0.40	45	8.0	8.0	18	34	54	Cone 35°	2.50	
779	10.0	34.5	0.40	45	8.0	8.0	18	34	54	Cone 35°	2.50	
781	10.0	34.5	0.40	45	8.0	8.0	Transient			Cone 35°	2.50	Grinder transient
783	10.0	34.5	0.40	45	8.0	8.0				Cone 35°	2.50	
793	10.0	34.5	0.40	45	8.0	8.0	25	40	80	Cone 35° R	2.50	Elevated RA
795	10.0	34.5	0.40	45	12.0	12.0	25	40	80	Cone 35° R	2.50	Elevated RA
799	10.0	34.5	0.40	45	8.0	8.0	18	34	54	Cone 35° R	2.50	Elevated RA
797	10.0	34.5	0.40	45	8.0	8.0	28	50	93	Cone 35° R	2.50	Elevated RA
802	10.0	34.5	0.40	52	8.0	8.0	25	40	80	Cone 35° R	4.00	Elevated RA

Stator Test Article

Test Ref	*Aerodynamic Setpoints*				*Cloud Setpoints*					*Test Article*	*Derived*	*Notes*
	T_0 °C	**P_0 kPa**	**M_∞ -**	**RH_0 %**	**TWC_{cl} g/m3**	**IWC_{cl} g/m3**	**D_{V10} µm**	**D_{V50} µm**	**D_{V90} µm**		**TWB_0 °C**	
805	10.00	34.5	0.25	45	8.0	8.0	25	40	80	Stator	2.50	
808	10.00	34.5	0.25	45	8.0	8.0	35	68	131	Stator	2.50	
811	10.00	34.5	0.25	45	8.0	8.0	18	34	54	Stator	2.50	
814	10.00	34.5	0.40	45	8.0	8.0	18	34	54	Stator	2.50	
817	10.00	34.5	0.40	45	8.0	8.0	25	40	80	Stator	2.50	
820	10.00	34.5	0.40	45	8.0	8.0	35	68	131	Stator	2.50	
822	10.0	34.5	0.40	5	8.0	8.0	18	34	54	Stator	-6.50	
824	10.0	34.5	0.40	15	8.0	8.0	18	34	54	Stator	-3.50	

826	10.0	34.5	0.40	30	8.0	8.0	18	34	54	Stator	-0.50	
828	10.0	34.5	0.40	65	8.0	8.0	18	34	54	Stator	5.50	
830	20.0	34.5	0.40	5	8.0	8.0	18	34	54	Stator	2.50	
832	20.0	34.5	0.40	20	8.0	8.0	18	34	54	Stator	5.50	
836	10.0	34.5	0.40	45	4.0	4.0	25	40	80	Stator	2.50	
839	10.0	34.5	0.40	22	4.0	4.0	18	34	54	Stator	1.00	
842	10.0	34.5	0.40	22	8.0	8.0	18	34	54	Stator	1.00	
845 / 846	10.0	34.5	0.40	22	4.0	4.0	18	34	54	Stator	1.00	AoA
848	10.0	34.5	0.40	22	8.0	8.0	18	34	54	Stator	1.00	AoA
850	10.0	34.5	0.40	22	4.0	4.0	18	34	54	Stator	1.00	AoA
852	10.0	34.5	0.40	22	8.0	8.0	18	34	54	Stator	1.00	AoA
854	10.0	34.5	0.40	22	4.0	4.0	18	34	54	Stator	1.00	AoA
856	10.0	34.5	0.40	22	8.0	8.0	18	34	54	Stator	1.00	AoA
858	10.0	34.5	0.40	22	4.0	4.0	18	34	54	Stator	1.00	AoA
860	10.0	34.5	0.40	22	8.0	8.0	18	34	54	Stator	1.00	AoA
868	10.0	34.5	0.40	22	8.0	8.0	28	50	93	Stator	1.00	AoA
862	10.0	34.5	0.40	22	8.0	8.0	35	68	131	Stator	1.00	AoA
866	10.0	34.5	0.40	22	8.0	8.0	28	50	93	Stator	1.00	AoA
864	10.0	34.5	0.40	22	8.0	8.0	35	68	131	Stator	1.00	AoA
860	10.0	34.5	0.40	22	8.0	8.0	18	34	54	Stator	1.00	AoA
875	10.0	34.5	0.40	45	8.0	8.0	18	34	54	Stator	1.00	AoA
905	10.0	34.5	0.40	45	8.0	8.0	18	34	54	Stator	1.00	AoA
878	10.0	34.5	0.40	45	8.0	8.0	18	34	54	Stator	1.00	AoA Twall
880	10.0	34.5	0.40	45	8.0	8.0	18	34	54	Stator	1.00	AoA Twall
882	10.0	34.5	0.40	45	8.0	8.0	18	34	54	Stator	1.00	AoA Twall
884	10.0	34.5	0.40	45	8.0	8.0	18	34	54	Stator	1.00	AoA Twall
888	10.0	34.5	0.40	45	8.0	8.0	25	40	80	Stator	1.00	AoA Twall
890	10.0	34.5	0.40	45	8.0	8.0	35	68	131	Stator	1.00	AoA Twall
895	10.0	34.5	0.40	5	8.0	8.0	18	34	54	Stator	-6.50	AoA Twall
897	10.0	34.5	0.40	15	8.0	8.0	18	34	54	Stator	-3.50	AoA Twall
899	10.0	34.5	0.40	30	8.0	8.0	18	34	54	Stator	-0.50	AoA Twall
901	10.0	34.5	0.40	65	8.0	8.0	18	34	54	Stator	2.50	AoA Twall
903	10.0	34.5	0.40	65	8.0	8.0	18	34	54	Stator	5.50	AoA Twall

Appendix C RATFac Cloud Calibrations

In Table B-1, the first 11 runs are given the test reference 'CAL', indicating a cloud calibration run without any test article present. It was desired to determine the spatial uniformity of the distribution of both TWC and LWC. The former determines the overall growth rate; the ratio of the two is the melt ratio which then affects particle sticking.

Area and linear traverse systems were available. The area traverse system was used to calibrate TWC using the NRC Compact Iso-kinetic Probe; and the linear traverse to calibrate LWC using the SEA multiwire probe. The latter started in the tunnel centreline and move horizontally outwards in increments of 0.4" (10.2 mm). Example plots of normalised TWC, LWC and melt ratio are given in Fig. C-1 (a), (b), and (c) respectively.

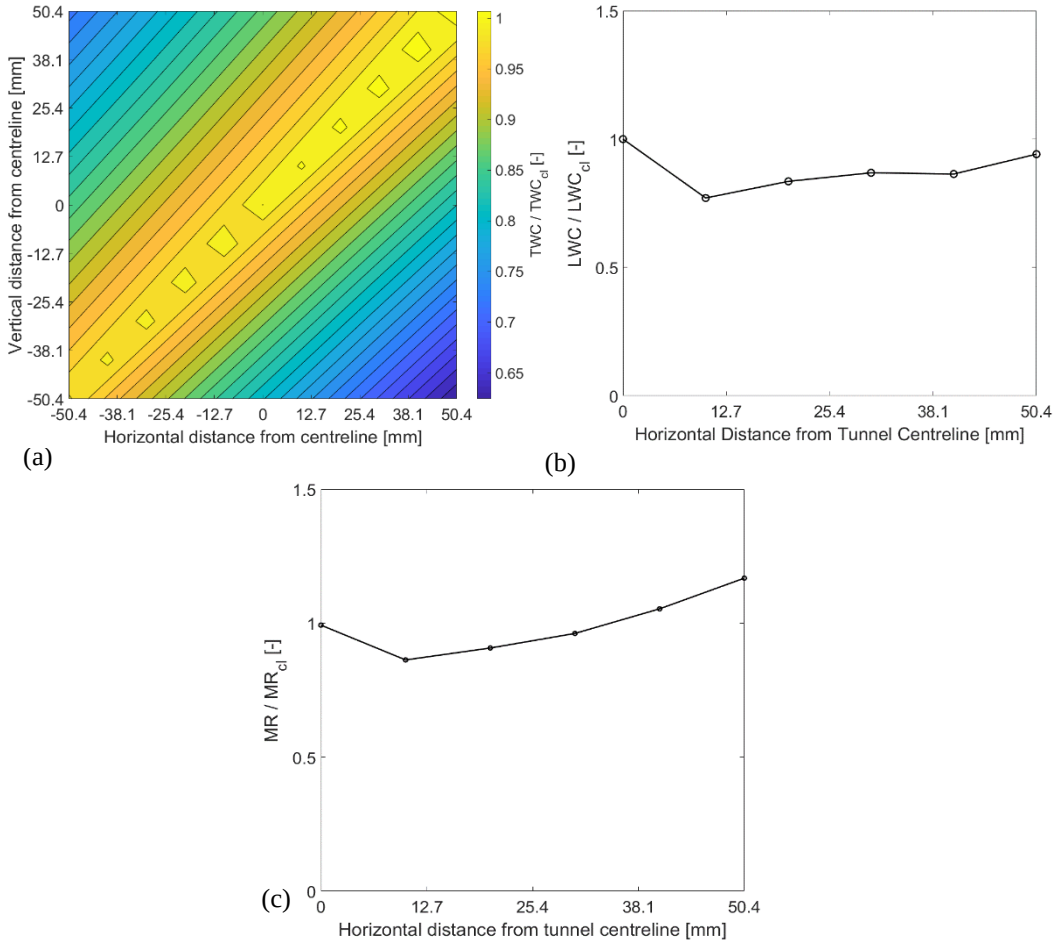

Fig. C-1 Cloud calibrations plots for the baseline test conditions defined in chapter 3, for (a) normalised TWC, (b) normalised LWC and (c) normalised melt ratio. The view of the plots is looking downstream.

Appendix D EMM-C Cold Substrate Model

In the case of a substrate with a surface temperature initially below freezing, then according to assumption (A3) in chapter 6, an ice layer must form first (referred to a stage 1). This is illustrated in Fig D-1. If there is sufficient energy in the system, then a water film may form on top (referred to as stage 2).

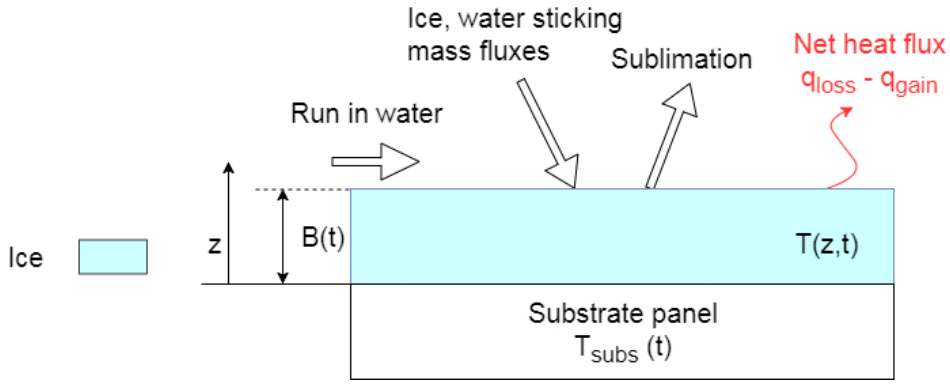

Fig. D-1 Schematic of stage 1 (ice layer) with fluxes of heat and mass

Continuity is given by

$$\rho_i \frac{dB}{dt} = \dot{m}_{stick,i} + \dot{m}_{stick,w} + \dot{m}_{run,in} - \dot{m}_{sub} \tag{D-1}$$

where $\dot{m}_{sub}$ is the sublimating mass flux. The ice layer thickness is then given by

$$B = \frac{1}{\rho_i}\left(\dot{m}_{stick,i} + \dot{m}_{stick,w} + \dot{m}_{run,in} - \dot{m}_{sub}\right) t \tag{D-2}$$

Finding the temperature profile through the ice layer then follows the same procedure as for the single water layer, in the case of a substrate initially above freezing. Equations (6-11) through (6-19) may be used, replacing $\theta(z,t)$ with $T(z,t)$. The surface heat flux boundary conditions changes to

$$-k_i \frac{\partial T}{\partial z} = q_{loss} - q_{gain} = \left(q_{conv} + q_{sub} + q_{sens,imp} + q_{sens,run}\right) - \left(q_{kin} + q_{freeze}\right)$$

$$z = B \tag{D-3}$$

where

$$q_{sub} = L_s\,\dot{m}_{sub} = L_s\,(E_e\theta_h + E_A) \quad ; \quad L_s = L_v + L_f \tag{D-4}$$

$$q_{freeze} = L_f \dot{m}_{stick,w} \tag{D-5}$$

and all other heat flux terms are as defined in chapter 6.

The ice temperature profile is then given by

$$T = \frac{q_2 - q_1 T_{subs}}{k_i + B q_1} z + T_{subs} \tag{D-6}$$

where

$$q_1 = H + L_s E_e + \dot{m}_{stick,i} C_{p,i} + \dot{m}_{stick,w} C_{p,w} + \dot{m}_{run,w} C_{p,w} \tag{D-7}$$

$$q_2 = {}^1/_2\left(\dot{m}_{stick,i} + \dot{m}_{stick,w}\right)\overline{U_p}^2 + L_f \dot{m}_{stick,w} - (L_s E_A - H T_r - \dot{m}_{stick,i} C_{p,i} T_{p,i} - \dot{m}_{stick,w} C_{p,w} T_{p,w} - \dot{m}_{run,w} C_{p,w} T_{run}) \tag{D-8}$$

The calculation continues until either (i) the temperature of the exposed ice surface rises to freezing, i.e. $T(B,t) = T_f$, or (ii) the surface temperature remains below freezing for the entire calculation time ('dry' ice conditions).

If (i) occurs, the calculation moves to the second stage, where a water film is assumed to form over the ice layer. This is illustrated in Fig. D-2.

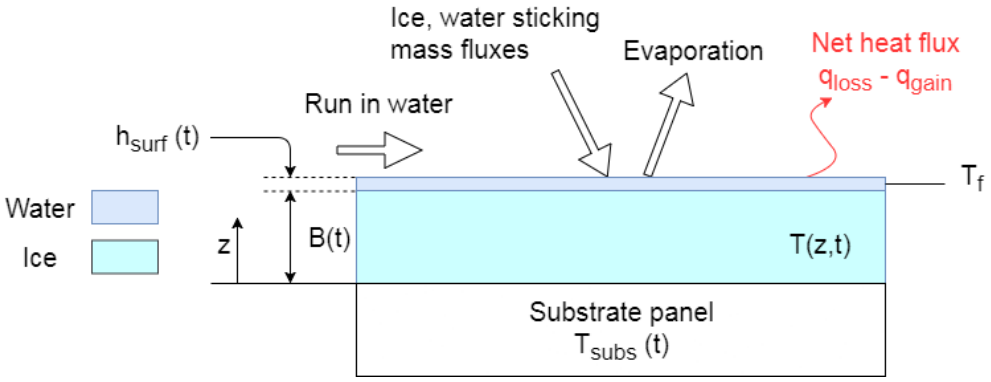

Fig. D-2 Schematic of stage 2 (two layer model) with fluxes of heat and mass

In chapter 6, assumption (A8) was introduced. This states that the top water film is sufficiently thin that wall-normal temperature gradients may be neglected. This assumptions is applied here as well:

$$\theta(z,t) = T_f \tag{D-9}$$

The heat and energy equations are given by

$$\frac{\partial^2 \theta}{\partial z^2} = \frac{\partial^2 T}{\partial z^2} = 0 \tag{D-10}$$

$$\rho_i L_f \frac{dB_{int}}{dt} = -k_w \frac{\partial \theta}{\partial z} + k_i \frac{\partial T}{\partial z} \tag{D-11}$$

where $\frac{dB_{int}}{dt}$ is the rate of ice growth at the interface with the water layer. This is summed with the freezing mass flux due to the surface heat flux balance to gain the overall ice growth rate:

$$\frac{dB}{dt} = \frac{dB_{int}}{dt} + \frac{dB_{surf}}{dt} \tag{D-12}$$

Integrating the heat equations:

$$\frac{\partial T}{\partial z} = \frac{T_f - T_{subs}}{B} \quad ; \quad T = \frac{T_f - T_{subs}}{B} z + T_{subs} \tag{D-13}$$

and

$$\frac{\partial \theta}{\partial z} = 0 \quad ; \quad \theta = T_f \tag{D-14}$$

Substituting (D-13) and (D-14) into (D-11)

$$\frac{dB_{int}}{dt} = \frac{1}{\rho_i L_f}\left(k_i \frac{T_f - T_{subs}}{B}\right) \tag{D-15}$$

The corresponding change in water height is given by

$$\frac{dh_{int}}{dt} = -\frac{\rho_i}{\rho_w}\frac{dB_{int}}{dt} \tag{D-16}$$

Continuity in the water layer at the exposed surface is given by

$$\rho_w \frac{dh_{surf}}{dt} = \dot{m}_{stuck,w} + \dot{m}_{run,in} - \dot{m}_{evap} - \dot{m}_f \quad \text{(D-17)}$$

The corresponding equation for ice growth is given by

$$\frac{dB_{surf}}{dt} = \dot{m}_{stuck,i} + \dot{m}_f \quad \text{(D-18)}$$

The overall change in water layer height is then given by

$$\frac{dh}{dt} = \frac{dh_{int}}{dt} + \frac{dh_{surf}}{dt} \quad \text{(D-19)}$$

If the overall change is negative (i.e. the water film shrinks), and is sufficient to remove any pre-existing water film, then a single ice layer model is presumed. Freezing is assumed to occur throughout the timestep, such that the surface temperature is kept at T_f.

The heat balance boundary condition at the exposed water surface is given by equation (D-20). This may be solved directly for q_f and hence $\dot{m}_f$.

$$q_{loss} - q_{gain} = q_{net} = \left(q_{conv} + q_{evap} + q_{sens,imp} + q_{sens,run}\right) - \left(q_{kin} + q_{freeze}\right) = 0$$

$$z = h + B \quad \text{(D-20)}$$

Appendix E Evaporative Heat & Mass Transfer

E-1 Derivation of Evaporative Heat Flux Equation

The evaporative heat flux from the accretion surface on a given panel is given by

$$q_{evap} = L_v \dot{m}_{evap} = L_v H_m \rho_f \left(\omega_{surf} - \omega_\infty\right) = \frac{L_v}{L} Sh\, \rho_f\, D_{v,a}\left(\omega_{surf} - \omega_\infty\right) \tag{E-1}$$

where H_m is the average mass transfer coefficient over the panel, L is the length of the panel, Sh is the average Sherwood number, $D_{v,a}$ is the diffusivity of vapour in air, and ω_{surf} and ω_∞ are the humidity ratios at the surface and in the freestream respectively. Sublimation heat flux may be calculated by replacing L_v with $L_v + L_f$. The vapour diffusivity is given by

$$D_{v,a} = D_0 \left(\frac{P_{ref}}{P_e}\right)\left(\frac{T_e}{T_{ref}}\right)^{1.81} \tag{E-2}$$

where D_0 = 22.6 x10^{-6} m/s^2, P_{ref} = 101.3 kPa, T_{ref} = 273.15 K, and P_e and T_e are the local static pressure and temperature at the edge of the boundary layer respectively (Hauk et al., 2016).

A Chilton-Colburn heat-mass transfer analogy is used to express Sherwood number in terms of the previously-calculated heat transfer coefficient (or its non-dimensional form, Nusselt number). This is ratio is described by the analogy factor:

$$J = \frac{Nu}{Sh} = f\left(\frac{Pr}{Sc}\right) \tag{E-3}$$

It has been shown by comparison with experiment (Eckert et al., 2001) that for a two-dimensional laminar boundary layer over a turbine blade profile with uniform wall temperature,

$$f\left(\frac{Pr}{Sc}\right) = \left(\frac{Pr}{Sc}\right)^{1/3} \tag{E-4}$$

The uncertainty in the experiment is given as 5%. For a fully turbulent boundary layer over a plane wall at uniform temperature, it is shown in Häring and Weigand (1995) that

$$f\left(\frac{Pr}{Sc}\right) \approx \left(\frac{Pr}{Sc}\right)^{0.653} \tag{E-5}$$

This was shown to agree moderately well with experiments of naphthalene evaporating in air with a turbulent boundary layer. Here, the analogy factor was reported as

$$f\left(\frac{Pr}{Sc}\right) = 0.5 = \left(\frac{Pr}{Sc}\right)^{0.591} \tag{E-6}$$

The uncertainty is given as 10%.

For the remainder of the derivation, the analogy factor will be written as

$$J = \frac{Nu}{Sh} = \left(\frac{Pr}{Sc}\right)^{a} \tag{E-7}$$

Defining the Lewis number as $Le = {Sc}/{Pr}$, equation (E-7) may be re-written as

$$Sh = Nu\left(\frac{Pr}{Sc}\right)^{-a} = Nu\ Le^{a} = \frac{HL}{k_f} Le^{a} \tag{E-8}$$

Substituting (E-8) into (E-1) yields

$$q_{evap} = L_v\ Le^{a}\ \frac{H}{k_f} \rho_f D_{va} \left(\omega_{surf} - \omega_{\infty}\right) \tag{E-9}$$

Rearranging the equation for Lewis number:

$$\frac{\rho_a D_{va}}{k_f} = \frac{1}{Le\ C_{p,a}} \tag{E-10}$$

Substituting (E-10) into (E-9):

$$q_{evap} = \frac{L_v\ H}{C_{p,a}\ Le^{(1-a)}} \left(\omega_{surf} - \omega_{\infty}\right) \tag{E-11}$$

Applying Dalton's law of partial pressures,

$$\omega = \frac{m_{vap}}{m_{dry\ air}} = \frac{M_w}{M_a}\frac{P_{vap}}{P_0 - P_{vap}} \cong \frac{M_w}{M_a}\frac{P_{vap}}{P_0} \tag{E-12}$$

provided that $P_{vap} \ll P_0$ where P_{vap} is the local vapour pressure. The error arising from this assumption is assessed in Section E-3.

Therefore:

$$q_{evap} \cong \frac{L_v H}{P_0\, C_{p,a}\, Le^{(1-a)}}\,\frac{M_w}{M_a}\left(P_{vap,surf} - P_{vap,\infty}\right) \tag{E-13}$$

where at the surface interface, $P_{vap,surf} = P_{vap,sat,surf}$ and in the freestream, $P_{vap,\infty} = RH_\infty\, P_{vap,sat,\infty}$, where RH_∞ is the relative humidity based on total conditions. It then remains to calculate $P_{vap,sat}$, the vapour pressure of water in saturated air.

E-2 Calculation of Saturation Vapour Pressure

Saturation vapour pressure is typically calculated from an empirical formula such as that of Hyland and Wexler (1983). The saturation vapour pressure over ice in the range $174 < T\ (K) \leq T_f$ is given by

$$\ln p_{vap,sat,ice} = \frac{C_1}{T} + C_2 + C_3 T + C_4 T^2 + C_5 T^3 + C_6 T^4 + C_7 \ln T \tag{E-14}$$

and the saturation vapour pressure over water in the range $T_f < T\ (K) \leq 473$ is given by

$$\ln p_{vap,sat,w} = \frac{C_8}{T} + C_9 + C_{10} T + C_{11} T^2 + C_{12} T^3 + C_{13} \ln T \tag{E-15}$$

where the coefficients are given in Table E-1.

Table E-1: Coefficients for Hyland and Wexler saturation vapour pressure model

Coefficient	*Value*	*Coefficient*	*Value*
C_1	−5.6745359 E+03	C_8	−5.8002206 E+03
C_2	6.3925247	C_9	1.3914993
C_3	−9.6778430 E–03	C_{10}	−4.8640239 E−02
C_4	6.2215701 E−07	C_{11}	4.1764768 E−05
C_5	2.0747825 E−09	C_{12}	−1.4452093 E−08
C_6	−9.4840240 E−13	C_{13}	6.5459673
C_7	4.1635019		

In the Extended Messinger Model (Myers, 2001) saturation vapour pressure is approximated as a linear function over the range $257 \leq T\ (K) \leq T_f$, given by

$$P_{vap,sat} \cong\ -6.803\ x10^3 +\ e_0 T \tag{E-16}$$

where $e_0 = 27.03$. Using a linear function in the EMM allows for analytical solutions to be derived directly. The maximum error introduced by this equation over the range specified is reported as 8%. This approach is maintained in the current work, however it is modified to a piecewise linear approximation over an extended range. This is necessitated by the adaptation of the model to ice crystal icing, where temperatures may be significantly above freezing as well as below. A 19-segment piecewise linear fit is used instead, applicable over the range $245 \leq T\ (K) \leq 320$. The application of this fit is described in the ensuing derivation.

According to equation (E-13)

$$q_{evap} = \frac{L_v H}{P_0\ C_{p,a}\ Le^{(1-a)}}\ \frac{M_w}{M_a}\left(P_{vap,surf}\ -\ P_{vap,\infty}\right) \tag{E-17}$$

$$= \frac{L_v H}{P_0\ C_{p,a}\ Le^{(1-a)}}\ \frac{M_w}{M_a}\left(P_{vap,sat,surf}\ -\ RH_\infty P_{vap,sat,\infty}\right)$$

Introducing constant K,

$$K = \frac{H}{P_0\ C_{p,a}\ Le^{(1-a)}}\ \frac{M_w}{M_a} \tag{E-18}$$

$$q_{evap} = L_v K \left(P_{vap,sat,surf} - RH_\infty P_{vap,sat,\infty}\right) = L_v K \, \Delta P_{vap} \tag{E-19}$$

Consider the case shown in Fig. E-1. Vapour pressure curves for a saturated condition (surface) and a freestream condition at 30% relative humidity are shown. The surface is assumed to be at 278 K (red dot) and is evaporating into a freestream at approximately 316 K, 30% relative humidity (blue dot). The difference in vapour pressure between the two dots (ΔP_{vap}), multiplied by the constant K and latent heat of vaporisation L_v, gives the evaporative heat flux q_{evap}.

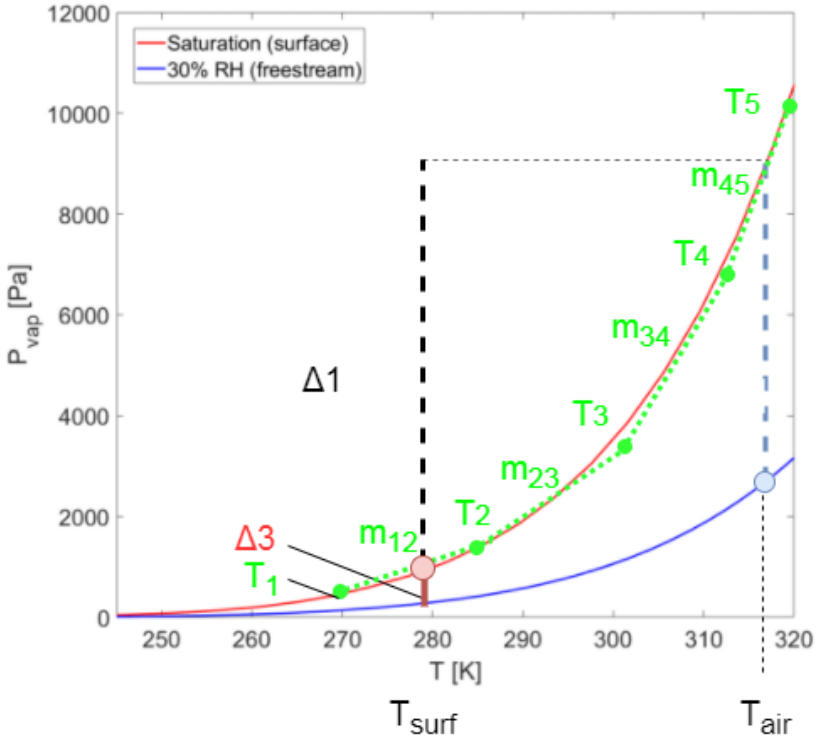

Fig. E-1 Schematic for deriving the driving vapour pressure difference for an arbitrary piecewise linear fit

An arbitrary coarse linear piecewise fit has been overlaid in green, with the start and end temperatures of each segment and the respective gradient also shown e.g. T_2, T_3, m_{23}.

Stating that

$$\begin{aligned} \Delta P_{vap} &= \Delta 1 \, RH_\infty + \Delta 3 \\ &= \left[\left(T_{surf} - T_2\right)m_{12} + \left(T_2 - T_3\right)m_{23} + \left(T_3 - T_4\right)m_{34}\right. \\ &\left. + \left(T_4 - T_{air}\right)m_{45}\right]RH_\infty + (1 - RH_\infty)(m_{12}T_{surf} + C_{12}) \end{aligned} \tag{E-20}$$

where C_{12} is the y-intercept for the line segment with gradient m_{12}.

More generally, for any temperature range where the air temperature exceeds the surface temperature:

$$\Delta P_{vap} = \left[m_{ij}\left(T_{surf} - T_j\right) + m_{jk}\left(T_j - T_k\right) + \cdots + m_{xy}(T_x - T_{air})\right]RH_\infty + (1 - RH_\infty)\left(m_{ij}T_{surf} + C_{ij}\right) \tag{E-21}$$

$$= \left[m_{ij}RH_\infty + (1 - RH_\infty)m_{ij}\right]T_{surf} + \left[m_{jk}\left(T_j - T_k\right)RH_\infty + \cdots + m_{xy}T_xRH_\infty + (1 - RH_\infty)C_{ij} - m_{ij}T_jRH_\infty - m_{xy}RH_\infty T_{air}\right]$$

Therefore, expressing this in the form of equation (6-15),

$$q_{evap} = L_vK\,\Delta P_{vap} = L_v(E_eT_{surf} + E_A) \tag{E-22}$$

where

$$E_e = K\left[m_{ij}RH_\infty + (1 - RH_\infty)m_{ij}\right] = Km_{ij} \tag{E-23}$$

$$E_A = K\left[m_{jk}\left(T_j - T_k\right)RH_\infty + \cdots + m_{xy}T_xRH_\infty + (1 - RH_\infty)C_{ij} - m_{ij}T_jRH_\infty - m_{xy}RH_\infty T_{air}\right] \tag{E-24}$$

The equations for the case where the air temperature is below the surface temperature are given by

$$E_e = Km_{ji} \tag{E-25}$$

$$E_A = K\left[m_{ih}(T_i - T_h) + \cdots + m_{ba}T_b + (1 - RH_\infty)C_{ba} - m_{ji}T_i - m_{ba}RH_\infty T_{air}\right] \tag{E-26}$$

The 19 segments of the piecewise linear fit used in the current work have the lower temperature limits, gradients and y-intercepts given in Table E-2.

Table E-2 Parameters for the 19 segments of the piecewise linear fit used in the current work

Segment	*Lower T bound*	*Gradient, m*	*Intercept, C*
1	245.0	5.698	-1350
2	249.0	8.231	-1982
3	253.1	11.74	-2871
4	257.1	16.56	-4112
5	261.1	23.110	-5821
6	265.2	31.89	-8151
7	269.2	43.62	-11311
8	273.3	50.96	-13315
9	277.3	65.49	-17344
10	281.3	83.42	-22391
11	285.4	105.4	-28663
12	289.4	132.11	-36396
13	293.5	164.35	-45858
14	297.5	202.9	-57351
15	301.6	248.9	-71218
16	305.6	303.3	-87837
17	309.6	367.2	-107630
18	313.6	441.9	-131061
19	317.7	528.7	-158638

The formula of Hyland and Wexler (1983), the piecewise linear fit in the current study, and the linear fit of Myers (2001) are shown in Fig. E-2.

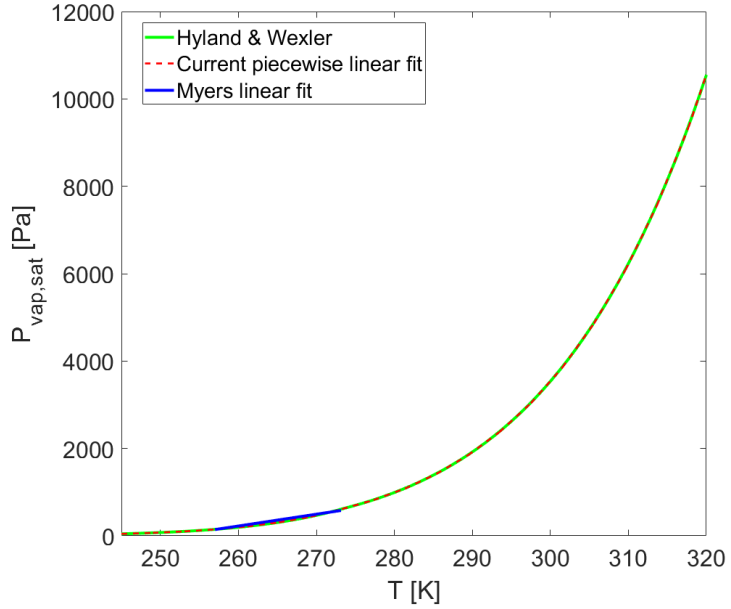

Fig. E-2 Saturation vapour pressure as a function of temperature using the empirical correlation of Hyland and Wexler (1983). The piecewise linear fit in the current work and the linear fit of Myers (2001) are also shown.

E-3 Evaporation Model Applicability

The error arising from the new piecewise linear fit is < 1% across the range specified.

The assumption in equation (E-13), that $P_{vap} \ll P_0$, is more difficult to justify, since the error incurred depends on the total pressure, temperature and relative humidity of the particular condition. The assumption is required in order to make the equation for q_{evap} a linear function of surface temperature, T_{surf}, which in turn allows the thermodynamic model (EMM-C) to be solved directly.

Firstly, the error is estimated for the experimental test cases used as validation in chapter 6. The largest error will be incurred at the highest temperature, the highest freestream relative humidity, and the lowest total pressure. In the validation cases, the total air temperature did not exceed 10 °C, the relative humidity based on total conditions did not exceed 65 %, and the total pressure was fixed throughout at 34.5 kPa. The largest error incurred in equation (E-13) is then 2.9 %.

Secondly, an upper bound for the error may be estimated for a typical engine operating condition. The largest error will be incurred just after icing is initiated, where air temperatures may still be significantly (~30 °C) above freezing, and at the lowest reasonable total pressure (i.e. cruise or top of descent). This is estimated to be 52 +/- 5 kPa, which is the interstage total pressure in the Intermediate

Pressure Compressor (IPC) at the axial location where the local air temperature is ~ 30 °C. This was estimated from data for a Trent 500 engine at top of descent, with cruise altitude in the range 30,000 – 40,000 ft. To be conservative, freestream relative humidity will be taken as 100%. From Fig. E-2, the saturation vapour pressure is ~4200 Pa. The error in using the assumption in equation (E-13) for this worst-case scenario is therefore 8.2%.

The methodology presented here for calculating the evaporative heat flux is used in several existing icing codes (Gent et al., 2000; Myers, 2001) and seems to offer sufficiently accurate results for aircraft wing icing, as assessed by comparison between predicted and measured ice shapes. In the present work, a fully turbulent boundary layer is assumed for the validation cases, with the analogy factor given by $\left(\frac{Pr}{Sc}\right)^{0.653}$. For the foreseeable future, approaches such as this will be transferred into ice crystal icing codes, due to their inherent simplicity and the complexity of modelling mass transfer within a turbomachinery environment. It is therefore important to bear in mind the limitations inherent in the derivation. The analogy factors are applicable to turbine aerofoils (thin boundary layers) rather than compressor aerofoils. The assumption of two-dimensional flow may be applicable at midspan for high aspect ratio blades, but will not be near endwalls where secondary flows and corner separations dominate; and the assumption of uniform wall temperature is unlikely to hold once icing is initiated. There is therefore significant work ahead to improve model applicability.

Appendix F Validity of Thin Water Film Assumption

The assumption of zero wall-normal heat flux in the surface water film is assessed in the following section. Consider the case of a substrate below freezing with two-layer ice and water growth (EMM-Standard). Substituting the equations for the temperature profiles in the ice layer (D-13) and water film (6-24) into the Stefan (phase change) equation (D-11):

$$\rho_i L_f \frac{\partial B}{\partial t} = k_i \frac{\partial T}{\partial z} - k_w \frac{\partial \theta}{\partial z} = k_i \frac{(T_f - T_{subs})}{B} - k_w \frac{q_2 - q_1 T_f}{k_w + h q_1} \quad \text{(F-1)}$$

The wall-normal temperature profile ($^{\partial \theta}/_{\partial z}$) in the water layer may be neglected provided that the conduction term is small, i.e. $h q_1 \ll k_w$. This assumption then gives that the net surface heat flux must be zero since $^{\partial \theta}/_{\partial z} = 0 = {}^{1}/_{k_w}(q_2 - q_1 T_f) = q_{net}$. Using equation (6-22) for q_1 and taking typical values given in Table F-1, gives $h q_1 \cong 0.0040 \ll k_w$. The assumption is therefore deemed valid.

Table F-1 Typical parameter values in ice crystal icing experiments used as validation

Parameter	*Value*
$H\ [W/m^2K]$	400
$\dot{m}_{stick,i}\ [kg/s\,m^2]$	0.20
$\dot{m}_{stick,w}\ [kg/s\,m^2]$	0.05
$\dot{m}_{run,w}\ [kg/s\,m^2]$	0.10
$L_v E_e\ [W/m^2K]$	800
$h_{film}\ [m]$	1.8 x10^{-6}

Appendix G ICICLE Sensitivity Analysis

Successive simulations were performed in ICICLE using the baseline aerodynamic and icing conditions (as given in chapter 3) and the 35° half-angle cone. The output parameter of interest was selected as the ice growth rate at 50% streamwise distance from the tip, $\dot{h}_{i,50}$. The 50% streamwise location has been chosen – in preference to the tip – so that sensitivity to terms containing a non-zero surface normal may be assessed.

Values are compared at a fixed, arbitrarily chosen time of 60 s. Ice growth rate (as opposed to overall growth rate) is subject to perturbations due to both the overall mass flux (controlled by the continuity equation) and in the relative mass fluxes of water and ice (controlled by the energy equation).

The key inputs of interest and their effect on the output are summarised in Table G-1.

Table G-1 Summary of input parameters and effect of perturbations

Input	*Model*	*Effect*
SF	EMM-C	Perturbation in ice and water mass fluxes sticking to a panel. Representative of an upstream perturbation in the trajectory, impingement and/or sticking models
K_{ero}	Erosion	Perturbation in quasi- particle kinetic energy, representative of perturbation in particle velocity and/or diameter at point of impact
η_A	Erosion	Perturbation in erosion model constant responsible for magnitude of erosive efficiency
η_C	Erosion	Perturbation in erosion model constant responsible for the dependence on surface normal angle
SH_∞	EMM-C	Perturbation in freestream specific humidity, perturbing the evaporative heat and mass transfer
H	EMM-C	Perturbation in local heat transfer coefficient, perturbing the evaporative heat and mass transfer and the convective heat transfer
T_0	EMM-C	Perturbation in freestream total temperature, perturbing fluid properties, convective heat transfer. To isolate the thermodynamic effects on EMM-C, it is assumed not to affect upstream particle melt ratio. A perturbed melt ratio at impact changes the sticking mass fluxes, covered by perturbing SF. The temperature is perturbed by 5% of its possible range, taken to be 245 – 320 K (the range of applicability of the saturation vapour pressure equation), rather than 5% relative to absolute zero.

P_0	EMM-C	Perturbation on freestream total pressure, perturbing fluid properties, evaporative heat and mass transfer. To isolate the thermodynamic effects on EMM-C it is assumed that particle trajectory and phase change is unaffected
M	EMM-C	Perturbation in freestream Mach number. The effect is limited to the heat transfer terms within EMM-C (i.e. convection, evaporation and kinetic energy of particles). It is assumed that the TWC is controlled such that the impinging mass fluxes are held constant

Fig. G-1 shows the perturbation in $\dot{h}_{i,50}$ for a positive and negative 5% perturbation in each of the inputs. Global continuity ensures that a 5% change in sticking mass flux results in a near 5% change in ice growth rate, since the other mass flux terms (evaporation and runback) are comparatively small. The second largest perturbation is due to total temperature. A positive perturbation results in an inversely proportional change in freestream density and hence Reynolds number and heat transfer coefficient. This is offset by the increased driving gas-wall temperature difference. The freestream saturation vapour pressure also increases, which, depending on the magnitude of the relative humidity, may increase or decrease the driving gas-wall mass fraction difference. At this condition, the change serves to increase the rate of condensation on the test article, increasing the heat flux to the surface. This produces the negative change in ice growth rate observed.

The perturbations in specific humidity and heat transfer coefficient result in relatively small perturbations at output. In the latter case, this is encouraging since the uncertainty is typically high even in clean (deiced) conditions. The heat transfer coefficient appears in both the convective and evaporative heat flux terms. Its effect is therefore greatest when both are of the same sign. In this case, both are positive heat fluxes to the accretion surface, so a positive perturbation in H results in a reduction in ice growth rate (with a corresponding increase in water growth rate).

Within the erosion model, the model constant responsible for the magnitude of the erosive efficiency, η_A, has the largest effect. A +5% change results in a ~0.6% reduction in ice growth rate. The quasi-particle kinetic energy term, K_{ero} gives the smallest perturbation at output for a +5% perturbation, but the fourth largest for a -5% perturbation. Since the rate of erosion is dependent upon $\log_{10}(K_{ero})$, a reduction in K_{ero} gives a greater change at output than an increase. Whilst sensitivity to K_{ero} may be relatively low overall, the perturbation could be high: K_{ero} is proportional to the cube of particle diameter, which typically has a relatively large measurement uncertainty (~ 2% at RATFac).

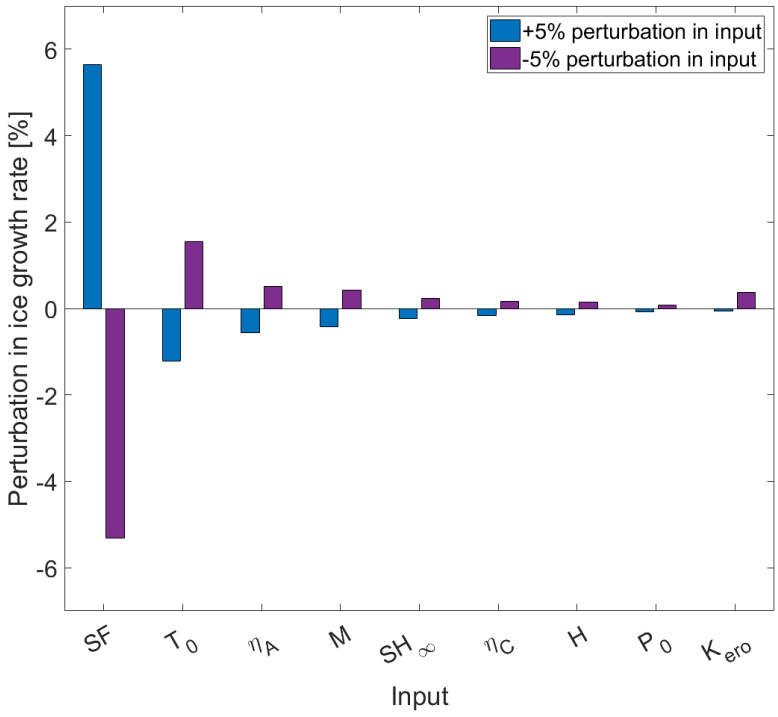

Fig. G-1 Plot of perturbation in output, the ice growth rate at 50% streamwise distance, due to +5% and -5% perturbation in each of the inputs

Appendix H Approximation of Shapes as Spheroids

Early development work on the Lagrangian particle tracking code used a simple swan-neck duct geometry to investigate particle trajectory in an environment with significant variation in both axial and radial velocity. The flowfield was solved in ANSYS Fluent using the same boundary conditions as given in Appendix A, and imported into MATLAB. Fig H-1 (a) shows a contour plot of axial velocity. An early objective was to validate that approximating particles as spheroids had limited effect on their trajectories, compared to using their 'real' shapes. Disks, cylinders and cubes were selected, and shape parameters (sphericity, crosswise sphericity, surface area and projected area) were calculated using equations for spheroids and the equations defining the individual discrete shapes. Fig H-1 (b) shows a comparison of the trajectories. Overall the difference in trajectories over the length of the domain is < 0.2 % in both the axial and radial directions.

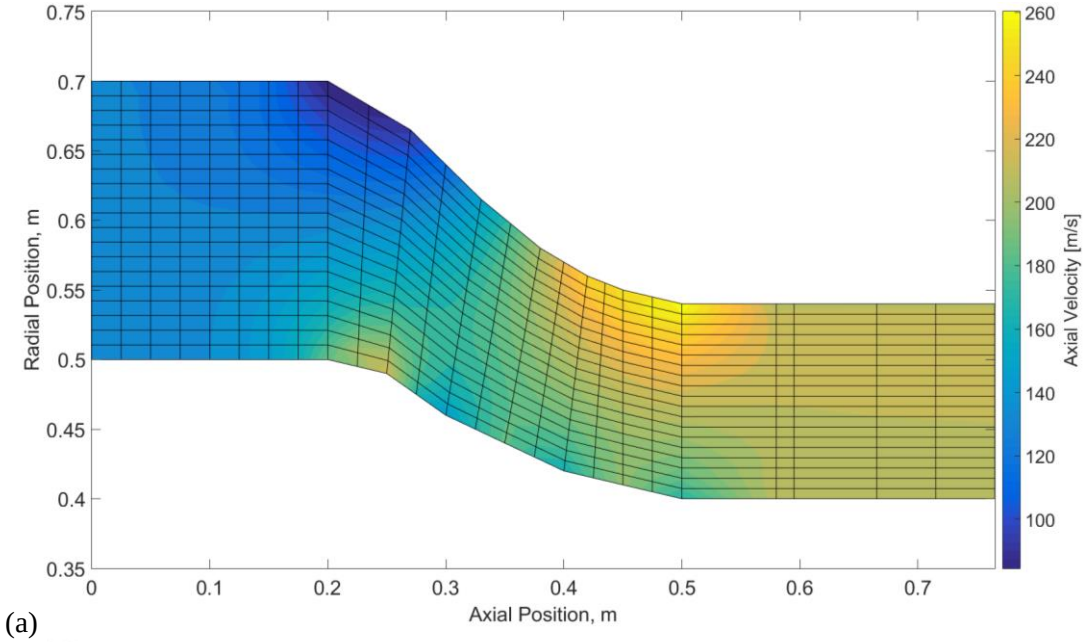

(a)

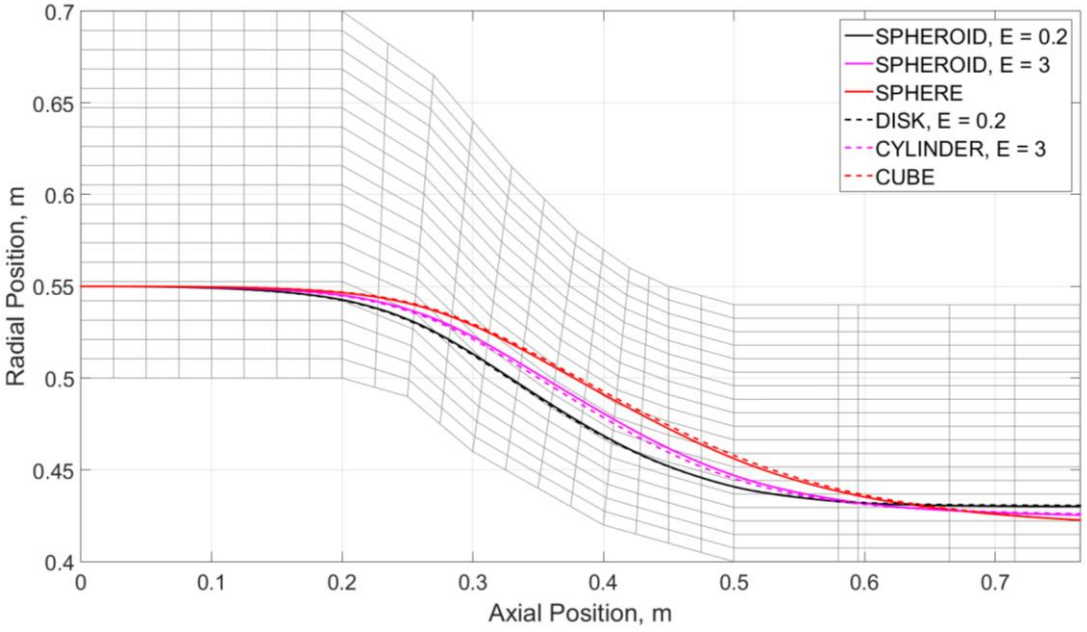

(b)

Fig. H-1 Simulation of simple swan neck duct geometry for use in development of Lagrangian particle tracking. (a) Contours of axial velocity; (b) Trajectories for a disk, cylinder and cube, and trajectories for their spheroid counterparts. Flow is left to right.

References

AGARD, 1995. Recommended practices for the assessment of the effects of atmospheric water ingestion on the performance and operability of gas turbine engines.

Al-Khalil, K., Irani, E., Miller, D., 2003. Mixed-Phase Icing Simulation and Testing at the Cox Icing Wind Tunnel. Presented at the 41st AIAA Aerospace Sciences Meeting and Exhibit, Reno, Nevada.

Aouizerate, G., Charton, V., Balland, M., Senoner, J., Trontin, P., Laurent, C., Blanchard, G., Villedieu, P., 2018. Ice Crystals Trajectory Calculations in a Turbofan Engine. Presented at the 2018 Atmospheric and Space Environments Conference, Atlanta, GA, USA.

Baumert, A., Bansmer, S.E., Bacher, M., 2015. Implementation of an innovative ice crystal generation system to the Icing Wind Tunnel Braunschweig. Presented at the 53rd AIAA Aerospace Sciences Meeting, AIAA SciTech Forum, Kissimmee, FL, USA.

Boeing Commercial Airplanes, 2018. Commercial Market Outlook 2018–2037.

Califf, C., Knezevici, D., 2014. Use of a Turbofan Engine to Measure Ice Crystal Cloud Concentration In-Flight. Presented at the 50th AIAA/ASME/SAE/ASEE Joint Propulsion Conference, Cleveland, OH, USA.

Casadevall, T.J., 1994. The 1989-1990 eruption of Mt. Redoubt volcano, Alaska: impacts on aircraft operations. J. Volcanol. Geotherm. Res. 62, 301–316.

Chambers, J.C., 1985. The 1982 encounter of British Airways 77 with the Mt. Galunggung eruption cloud. Presented at the 23rd AIAA Aerospace Sciences Meeting, Reno,NV,U.S.A.

Chandarana, D.I., Gavin, A., Wheaton, F.W., 1988. Particle/fluid interface heat transfer during aseptic processing of foods. Am. Soc. Agric. Eng. Pap. 88-6599.

Chauvin, R., Bennai, L., Trontin, P., Villedieu, P., 2018. An implicit time marching Galerkin method for the simulation of icing phenomena with a triple layer model. Finite Elem. Anal. Des. 150, 20–33.

Chrust, M., Bouchet, G., Dusek, J., 2010. Parametric study of the transition in the wake of oblate spheroids and flat cylinders. J Fluid Mech 665, 199–208.

Chung, S., 1973. Survey of Literature on Convective Heat Transfer Coefficients and Recovery Factors (No. NASA-CR-138747).

Clark, C., Orchard, D., Chevrette, G., 2018. A Guide Creating SAE AS5562 Ice Crystal, Mixed Phase and Rain Conditions in a Wind Tunnel Environment. Presented at the 2018 Atmospheric and Space Environments Conference, Atlanta, GA, USA.

Clift, R., Gauvin, W.H., 1970. The motion of particles in turbulent gas streams. Proc. Chemeca 1, 14–24.

Comer, J.K., Kleinstreuer, C., 1995. Computational analysis of convection heat transfer to non-spherical particles. Int J Heat Mass Transf 38, 3171–3180.

Connolly, J., 2018. Ice Crystal Icing in Gas Turbine Engines (Masters of Research thesis). University of Cambridge.

Crabtree, L.F., Dommett, R.L., Woodley, J.G., 1965. Estimation of Heat Transfer to Flat Plates, Cones and Blunt Bodies (No. 3637), Aeronautical Research Council Reports and Memoranda. R.A.E. Farnborough.

Crowe, C.T., Schwarzkopf, J.D., Sommerfeld, M., Tsuji, Y., 2011. Multiphase Flows with Droplets and Particles, 2nd ed.

Currie, T., Fuleki, D., Mahallati, A., 2014. Experimental Studies of Mixed-Phase and Sticking Efficiency for Ice Crystal Accretion in Jet and Engines. Presented at the 6th AIAA Atmospheric and Space Environments Conference, Atlanta, GA. https://doi.org/10.2514/6.2014-3049

Currie, T.C., Fuleki, D.M., Knezevici, D.C., MacLeod, J.D., 2013. Altitude Scaling of Ice Crystal Accretion. Presented at the 5th AIAA Atmospheric and Space Environments Conference, San Diego, California, U.S.A. https://doi.org/10.2514/6.2013-2677

Davison, C., Landreville, C., Benner, M., 2016a. Development and Validation of Compact Isokinetic Total Water Content Probe for Wind Tunnel Characterization. Presented at the 8th AIAA Atmospheric and Space Environments Conference, Washington, D.C., USA.

Davison, C., Strapp, J.W., Lilie, L.E., Ratvasky, T.P., Dumont, C., 2016b. Isokinetic TWC Evaporator Probe: Calculations and Systemic Error Analysis. Presented at the 8th AIAA Atmospheric and Space Environments Conference, Washington, D.C., USA.

Dawood, B., Giuffre, C., Bastawros, A.F., 2018. Fracture Mechanics Based Approach for Ice Adhesion Characterization. Presented at the 10th Atmospheric and Space Environments Conference, Atlanta, GA, USA.

Day, I., Williams, J., Freeman, C., 2008. Rain Ingestion in Axial Flow Compressors at Part Speed. ASME J. Turbomach. 130.

Dunn, M.G., 2012. Operation of Gas Turbine Engines in an Environment Contaminated With Volcanic Ash. J Turbomach 134.

EASA, 2010. Certification Specifications for Engines CS-E (No. Amendment 3).

Eckert, E.R.G., Sakamato, H., Simon, T.W., 2001. The heat/mass transfer analogy factor, Nu/Sh, for boundary layers on turbine blade profiles. Int. J. Heat Mass Transf. 44, 1223–1233.

Federal Air Transport Agency of Russia, n.d. "Damage to Airbridge Cargo GEnx Engine" (in Russian).

Feulner, M., Liao, S., Rose, B., Liu, X., 2015. Ice Crystal Ingestion in a Turbofan Engine. SAE Tech. Pap. 2015-01-2146. https://doi.org/10.4271/2015-01-2146

FlightGlobal, 2016. Flight Fleet Forecast's engine outlook.

Forsyth, P.R., 2017. High Temperature Particle Deposition with Gas Turbine Applications (PhD). University of Oxford, Oxford, UK.

Frossling, N., 1938. The evaporation of falling drops. Gerlands Beitrage Zur Geophys. 52, 170–216.

Fuleki, D., Chalmers, J.L., Galeote, B., 2015. Technique for Ice Crystal Particle Size Measurements and Results for the National Research Council of Canada Altitude Ice Crystal Test System. SAE Tech. Pap. 2015-01-2125. https://doi.org/10.4271/2015- 01-2125

Fuleki, D.M., MacLeod, J.D., 2010. Ice Crystal Accretion Test Rig Development For A Compressor Transition Duct. Presented at the 2010 Atmospheric and Space Environments Conference, Toronto, CA.

Ganser, G.H., 1993. A rational approach to drag prediction of spherical and nonspherical particles.

Gent, R.W., 1994. TRAJICE2: a combined water droplet and ice accretion prediction code for aerofoils (No. TR90054), RAE Technical Reports. Royal Aircraft Establishment.

Gent, R.W., Dart, N.P., Cansdale, J.T., 2000. Aircraft icing. Phil Trans R Soc Lond 358, 2873–2911.

Guégan, P., Othman, R., Lebreton, D., Pasco, F., Villedieu, P., Meyssonnier, J., Wintenberger, S., 2012. Critical impact velocity for ice fragmentation. J. Mech. Eng. Sci. 228.

Guégan, P., Othman, R., Lebreton, D., Pasco, F., Villedieu, P., Meyssonnier, J., Wintenberger, S., 2011. Experimental investigation of the kinematics of post-impact ice fragments. Int. J. Impact Eng. 38, 786–795.

Guha, A., 2008. Transport and Deposition of Particles in Turbulent and Laminar Flow. Annu. Rev. Fluid Mech. 40, 311–341.

Haider, A., Levenspiel, O., 1989. Drag Coefficient and Terminal Velocity of Spherical and Nonspherical Particles. Powder Technol. 58, 63–70.

Häring, M., Weigand, B., 1995. A New Analogy Function For The Naphthalene Sublimation Technique To Measure Heat Transfer Coefficients on Turbine Aerofoils. Presented at the International Gas Turbine and Aeroengine Congress and Exposition, Houston, TX, USA.

Hauk, T., Bonaccurso, E., Villedieu, P., Trontin, P., 2016. Theoretical and Experimental Investigation of the Melting Process of Ice Particles. J. Thermophys. Heat Transf. 30, 946–954.

Hauk, T., Roisman, I., Tropea, C., 2014. Investigation of the Impact Behaviour of Ice Particles. 6th AIAA Atmospheric Space Environ. Conf. 16-20 June 2014 Atlanta GA.

Higa, M., Arakawa, M., Maeno, N., 1998. Size Dependence of Restitution Coefficients of Ice in Relation to Collision Strength. Icarus 133, 310–3210.

Holzer, A., Sommerfeld, M., 2008. New simple correlation formula for the drag coefficient of non-spherical particles. Powder Technol. 184, 361–365.

Hyland, R.W., Wexler, A., 1983. Formulations for the thermodynamic properties of dry air from 173.15 K to 473.15 K, and of saturated moist air from 173.15 K to 372.15 K, at pressures to 5 MPa. ASHRAE Transactions.

IATA, 2017. 2036 Forecast Reveals Air Passengers Will Nearly Double to 7.8 Billion.

ICAO, 2013. ICAO 2013 Yearly Aviation Monitor. Webpage. Available at http://www.icao.int/sustainability/Documents/Yearly-Monitor.pdf. Accessed 3/8/15.

Institute of Mechanical Engineers, 2010. Volcanic Ash: To Fly or Not to Fly?

Iuliano, E., Montreuil, E., Norde, E., Van der Weide, E., Hoeijmakers, H., 2015. Modelling of Non-Spherical Particle Evolution for Ice Crystals Simulation with an Eulerian Approach, in: SAE Technical Paper 2015-01-2138. https://doi.org/10.4271/2015-01-2138

Jeck, R.K., 2002. Icing Design Envelopes (14 CFR Parts 25 and 29, Appendix C) Converted to a Distance-Based Format. Federal Aviation Administration, Atlantic City, USA.

Jones, G., 2015a. Ice Crystal Engine Research (ICER). Presentation, Oxford University.

Jones, G., 2015b. DFDR Data Analysis of IB6845 Ice Crystal Icing Event on 15th November 2006.

Knezevici, D.C., Fuleki, D., MacLeod, J., 2011. Development and Commissioning of a Linear Compressor Cascade Rig for Ice Crystal Research. SAE Tech Pap Ser SAE-2011-38-0079. https://doi.org/10.4271/2011-38-0079

Knezevici, D.C., Fuleki, D.M., Currie, T.C., MacLeod, J.D., 2012. Particle Size Effects on Ice Crystal Accretion. Presented at the 4th AIAA Atmospheric and Space Environments Conference, New Orleans, Louisiana, USA. https://doi.org/10.2514/6.2012-3039

Lawson, R.P., Angus, L.J., Heymsfield, A.J., 1998. Cloud Particle Measurements in Thunderstorm Anvils and Possible Weather Threat to Aviation.

Leith, D., 1987. Drag on Nonspherical Objects. Aerosol Sci. Technol. 6, 153–161.

Leroy, D., Fontaine, E., Schwarzenboeck, A., Strapp, J.W., Korolev, A., McFarquhar, G., Dupuy, R., Gourbeyre, C., Lilie, L., Protat, A., Delanoe, J., Dezitter, F., Grandin, A., 2017. Ice Crystal Sizes in High Ice Water Content Clouds. Part II: Statistics of Mass Diameter Percentiles in Tropical Convection Observed during the HAIC/HIWC Project. J. Atmospheric Ocean. Technol. 34, 117–136.

Leroy, D., Fontaine, E., Schwarzenboeck, A., Strapp, J.W., Lilie, L., Delanoe, J., Protat, A., Dezitter, F., Grandin, A., 2015. HAIC/HIWC Field Campaign - Specific Findings on PSD Microphysics in High IWC Regions from In Situ Measurements: Median Mass DDiameter, Particle Size Distribution Characteristics and Ice Crystal Shapes. SAE Tech. Pap. 2015-01-2087.

Lilie, L., Emery, E., Strapp, J., Emery, J., 2005. A Multiwire Hot-Wire Device for Measurement of Icing Severity, Total Water Content, Liquid Water Content, and Droplet Diameter. Presented at the 43rd AIAA Aerosp. Sci. Meet. Exhib.

Lou, D., Hammond, D.W., 2011. Heat and Mass Transfer for Ice Particle Ingestion Inside Aero-Engine.

Mack, P., 2013a. DOLOMITI II: Development of a Model to Predict the Severity of Ice Crystal Deposits in the Compressor (No. FSG90726).

Mack, P., 2013b. Analysis of test data from Ice Crystal tests performed at NRC by the ICC in January/February 2012.

Mason, B.J., 1956. On the Melting of Hailstones. Q. J. R. Meterological Soc. 82, 209–216.

Mason, J.G., Chow, P., Fuleki, D.M., 2010. Understanding Ice Crystal Accretion and Shedding Phenomenon in Jet Engines Using a Rig Test. J. Eng. Gas Turbines Power 133, 041201-041201–8. https://doi.org/10.1115/1.4002020

Mason, J.G., Strapp, J.W., Chow, P., 2006. The Ice Particle Threat to Engines in Flight. Presented at the 44th AIAA Aerospace Sciences Meeting and Exhibit, Reno, Nevada.

Mazzawy, R.S., 2007. Modeling of Accretion and Shedding in Turbofan Engines with Mixed Phase/Glaciated (Ice Crystals) Conditions. Presented at the SAE Aircraft and Engine International Icing Conference, Seville, Spain.

McClain, S.T., Vargas, M., Tsao, J., Broeren, A.P., 2018. Ice Roughness and Thickness Evolution on a Business Jet Airfoil. Presented at the AIAA Aviation Forum, Atlanta, GA, USA.

Messinger, B.L., 1953. Equilibrium Temperature of an Unheated Icing Surface as a Function of Air Speed. J Aeronaut Sci 120, 29–42.

Motwani, D.G., Gaitonde, U.N., Sukhatme, S.P., 1985. Heat Transfer From Rectangular Plates Inclined at Different Angles of Attack and Yaw to an Air Stream. J. Heat Transf. 107, 307–312.

Myers, T.G., 2001. Extension to the Messinger Model for Aircraft Icing. AIAA J 39, 211–218.

Neilson, J.H., Gilchrist, A., 1968. Erosion by a Stream of Solid Particles. J. Wear 11, 111–122.

Nilamdeen, S., Habashi, W., 2011. Multiphase Approach Toward Simulating Ice Crystal Ingestion in Jet Engines. AIAA J. Propuls. Power 27.

NTSB, 1996. Aircraft Accident Report. In-flight Icing encounter and loss of control. ATR Model 72-212, Roselawn, Indiana, October 31 1994. Volume 1: Safety Board Report.

Oliver, M.J., 2014. Validation Ice Crystal Icing Engine Test in the Propulsion Systems Laboratory at NASA Glenn Research Centre. 6th AIAA Atmospheric Space Environ. Conf. 16-20 June 2014 Atlanta GA.

Ozgen, S., Canibek, M., 2008. Ice Accretion Simulation on Multi-Element Airfoils Using Extended Messinger Model. Heat Mass Transf 45, 305–322.

Pan, H., Render, P.M., 1996. Impact characteristics of hailstones simulating ingestion by turbofan aeroengines. J. Propuls. Power 12, 457–462.

Rasmussen, R., Pruppacher, H.R., 1982. A Wind Tunnel and Theoretical Study of the Melting Behavior of Atmospheric Ice Particles. I: A Wind Tunnel Study of Frozen Drops of Radius < 500 μm. J. Atmospheric Sci. 39, 152–158.

Render, P.M., Pan, H., 1995. Experimental studies into hail impact characteristics. J. Propuls. Power 11, 1124–1230.

Richter, A., Nikrityuk, P.A., 2012. Drag forces and heat transfer coefficients for spherical, cuboidal and ellipsoidal particles in cross flow at sub-critical Reynolds numbers. Int. J. Heat Mass Transf. 55, 1343–1354.

Rosin, P., Rammler, E., 1933. The Laws Governing the Fineness of Powdered Coal. J. Inst. Fuel 7, 29–36.

Savitsky, A., Golay, M.J.E., 1964. Smoothing and Differentiation of Data by Simplified Least Squares Procedures. Anal. Chem. 36, 1627–1639.

Shin, J., 1996. Characteristics of surface roughness associated with leading-edge ice accretion. J. Aircr. 33, 316–321.

Struk, P.M., Bartkus, T., Bencic, T., King, M., Ratvasky, T.P., Van Zante, J., Tsao, J., 2017. An Initial Study of the Fundamentals of Ice Crystal Icing Physics in the NASA Propulsion Systems Laboratory. Presented at the 9th AIAA Atmospheric and Space Environments Conference, Denver, Colorado.

Struk, P.M., Bartkus, T., Tsao J., 2015a. Ice Accretion Measurements on an Airfoil and Wedge in Mixed-Phase Conditions. SAE Tech. Pap. 2015-01-2116. https://doi.org/10.4271/2015-01-2116

Struk, P.M., Bartkus, T., Tsao J., 2015b. A Method to Interpret Mixed-Phase Measurements using the SEA Multi-Wire Probe in Select Icing Test Facilities.

Struk, P.M., Broeren A.P. Tsao J. Vargas M., Wright, W.B., Currie T. Knezevici D. Fuleki D., 2012. Fundamental Ice Crystal Accretion Physics Studies. SAE Tech. Pap. Prep. Int. Conf. Aircr. Engine Icing Ground Deicing Chic. Ill. June 13–17 2011.

Struk, P.M., Lynch, C.J., 2012. Ice Growth Measurements from Image Data to Support Ice-Crystal and Mixed-Phase Accretion Testing. Presented at the 4th AIAA Atmospheric and Space Environments, New Orleans, Louisiana, USA. https://doi.org/10.2514/6.2012-3036

Struk, P.M., Wright, W.B., Broeren, A.P., Tsao, J., Vargas, M., Currie, T., Knezevici, D., Fuleki, D.M., 2011. Fundamental Ice Crystal Accretion Physics Studies. Presented at the International Conference on Aircraft and Engine Icing and Ground Deicing, Chicago, Illinois.

Sutherland, W., 1893. The viscosity of gases and molecular force. Philos. Mag. 36, 507–531.

Thomas, Q.P., 2015. NASA Glenn Propulsion Systems Lab (PSL) Icing Facility Update. Presented at the SAE 2015 International Conference on Icing of Aircraft, Engines, and Structures, Prague, Czech Republic.

Thompson, T.L., Clark, N.N., 1991. A holistic approach to particle drag prediction. Powder Technol. 67, 57–66.

Tilly, G.P., 1973. A Two Stage Mechanism of Ductile Erosion. Wear 23, 87–96.

Trontin, P., Blanchard, G., Villedieu, P., 2016. A Comprehensive Numerical Model for Mixed Phase and Glaciated Icing Conditions. Presented at the 8th AIAA Atmospheric and Space Environments Conference, Washington, D.C., USA.

Uhlmann, M., Doychev, T., 2014. Sedimentation of a dilute suspension of rigid spheres at intermediate Galileo numbers: the effect of clustering upon the particle motion. J Fluid Mech 752, 310–348.

Veillard, X., Habashi, W., Aubé, M.S., Baruzzi, G.S., 2009. FENSAP-ICE: Ice Accretion in Multi-stage Jet Engines. Presented at the 19th AIAA Computational Fluid Dynamics, San Antonio, TX, USA.

Veres, J.P., Jorgenson, P.C.E., Jones, S.M., 2016. Modeling of Highly Instrumented Honeywell Turbofan Engine Tested with Ice Crystal Ingestion in the NASA Propulsion System Laboratory. Presented at the 8th AIAA Atmospheric and Space Environments Conference, Washington, D.C., USA.

Veres, J.P., Jorgenson, P.C.E., Jones, S.M., Nili, S., 2017. Modeling of a Turbofan Engine With Ice Crystal Ingestion in the NASA Propulsion System Laboratory. Presented at the ASME Turbo Expo 2017: Turbomachinery Technical Conference and Exposition, Charlotte, NC, USA.

Vidaurre, G., Hallett, J., 2008. Particle impact and breakup in aircraft measurement. J. Atmospheric Ocean. Technol. 26, 972–983.

Villedieu, P., Trontin, P., Chauvin, R., 2014. Glaciated and mixed-phase ice accretion modeling using ONERA 2D icing suite. Presented at the 6th AIAA Atmospheric and Space Environments Conference, Atlanta, GA. https://doi.org/10.2514/6.2014-2199

Wadell, H., 1935. Volume, Shape and Roundness of Quartz Particles. J. Geol. 43, 250–280.

Wang, G., 2008. Thin water films driven by air through surface roughness (PhD). Iowa State.

Wright, W.B., 1995. Users manual for the improved NASA Lewis ice accretion code LEWICE 1.6 (CR 198355). NASA.

Wright, W.B., Gent, R.W., Guffond, D., 1997. DRA/NASA/ONERA Collaboration on Icing Research. Part 2; Prediction of Airfoil Ice Accretion (No. NASA-CR-202349).

Wright, W.B., Jorgenson, P.C.E., Veres, J.P., 2010. Mixed Phase Modeling in GlennICE with Application to Engine Icing. Presented at the AIAA Atmospheric and Space Environments Conference, Toronto, Ontario Canada. https://doi.org/10.2514/6.2010-7674

Young, J., Leeming, A., 1997. A theory of particle deposition in turbulent pipe flow. J Fluid Mech 340, 129–159.